JAIST Repository
https://dspace.jaist.ac.jp/

Title	コハク酸の選択的水素化を指向したCuPdバイメタル触媒に関する研究
Author(s)	LE, Dinh Son
Citation	
Issue Date	2021-03
Type	Thesis or Dissertation
Text version	ETD
URL	http://hdl.handle.net/10119/17486
Rights	
Description	Supervisor:西村　俊, 先端科学技術研究科, 博士

JAIST
JAPAN
ADVANCED INSTITUTE OF
SCIENCE AND TECHNOLOGY

Japan Advanced Institute of Science and Technology

Studies on CuPd Bimetallic Catalysts for Selective Hydrogenation of Succinic Acid

LE DINH SON

Japan Advanced Institute of Science and Technology

Doctoral Dissertation

Studies on CuPd Bimetallic Catalysts for Selective Hydrogenation of Succinic Acid

LE DINH SON

Supervisor : Associate Professor Shun NISHIMURA

Graduate School of Advanced Science and Technology

Japan Advanced Institute of Science and Technology

Material Science

March, 2021

Copyright © 2021 by LE DINH SON

Abstract

Succinic acid (SA) was identified as one of the most potentially bio-derived platform chemicals which can be converted to a number of value-added products via hydrogenation, esterification, and amination reactions. Among these main three conversion routes of SA, the hydrogenation is by far the most investigated transformation due to the importance of its products including γ-butyrolactone (GBL), tetrahydrofuran (THF), and 1,4-butanediol (BDO). However, the selective hydrogenation of SA is generally a challenging reaction due to the low electrophilicity of the carbonyl group and the complexity in its reaction pathways, which have provided a strong spur for chemists to design effective catalysts for this transformation. Despite that, the heavy dependence on precious metals such as Pd, Pt, Re, Ir, Ru, and Rh in previously reported catalysts is economically disadvantageous, which possibly limits them from industrial applications. Therefore, the studies embodied in this thesis aim to develop efficient earth-abundant metal-based bimetallic catalysts for selective hydrogenation of SA to BDO, THF, and GBL.

In the initial attempt to search for a suitable catalyst system, hydroxyapatite (HAP) supported Cu_xPd_y ($x + y = 10$ wt%) was found to be potential bimetallic catalysts for the production of BDO from SA. The effect of metal ratio was examined and the Cu_8Pd_2/HAP was found to be the best catalyst, affording a high selectivity of BDO (>80%) at a quantitative conversion of SA. A strong Cu–Pd interaction resulted from alloying formation led to an enhanced catalytic activity to the intermediate GBL, compared to that over the Cu_{10}/HAP monometallic catalyst. While on the other hand, the Cu-rich CuPd nanoparticles (NPs) suppressed the over-reactivity of Pd, preventing the side reaction to butyric acid (BA), which is typically encountered in the Pd_{10}/HAP monometallic catalyst. Subsequently, the Cu species that existed closely to CuPd alloying NPs promoted further hydrogenation of GBL, achieving BDO with high yield.

Since the metal–support interaction can have pronounced effects on the catalyst structures and thus their catalytic performances, the influences of various supports i.e., SiO_2, TiO_2, and γ-Al_2O_3, on the constructions of Cu-rich CuPd alloy nanoparticles (NPs) were investigated. In-depth characterizations revealed that randomly homogeneous CuPd NPs were prevalently constructed on TiO_2 and SiO_2, whereas the heterogeneous CuPd alloy NPs with a great extent of Cu segregation were dominantly formed on γ-Al_2O_3. As a result, the catalytic activity and product selectivity are distinctly different among these catalysts. Particularly, a selectivity of GBL (90%) can be attained over the CuPd/TiO_2 catalyst at 73% conversion of SA, which was attributed to the presence of large CuPd NPs preventing further hydrogenation of GBL and lowering the catalytic activity. On the other hand, higher activity and selectivity toward BDO of CuPd/SiO_2 were ascribed to its small CuPd NPs and the presence of isolated Cu species which promoted the formation of BDO at a high yield of 86%. Notably, the strong Lewis acid sites in the CuPd/γ-Al_2O_3 was revealed as the decisive factor in the formation of highly selective THF with 97% at a quantitative conversion of SA.

To broaden knowledge in the γ-Al_2O_3 supported CuPd catalysts, the influence metal ratio on the catalytic performance has been extended. Excellent catalytic performance toward THF was achieved over the Cu-rich Cu_6Pd_4/γ-Al_2O_3 and Cu_8Pd_2/γ-Al_2O_3 catalysts, achieving the product yield and selectivity of 85–90%. In addition, the present catalyst can maintain its high activity and selectivity for several recycling runs under high temperature and pressure conditions. Extensive characterization methods revealed that major factors that were responsible for the superior performance and stability of this catalyst for THF production include CuPd alloy NPs with isolated Cu species and strong Lewis acid sites of the γ-Al_2O_3 support. The strong interaction in CuPd alloy NPs resulted in the enhanced reactivity compared to that of the monometallic Cu, while the Cu-rich component helped to restrain the strong reactivity of Pd species which favors the formation of BA. Alternatively, the Cu-rich CuPd NPs were proposed to promote the formation of the intermediate BDO which was easily converted to THF via cyclodehydration under the influence of strong Lewis acid sites in the support γ-Al_2O_3.

Finally, the influence of the capping agent on the catalytic performance of CuPd NPs was studied for SA hydrogenation. A highly efficient PVP-capped CuPd NPs constructed on HAP was discovered for selective hydrogenation of SA to GBL. The inhibition effect of the capping agent PVP was revealed to play a key role in the formation of GBL with excellent selectivity. The catalyst was able to proceed at extremely low hydrogen pressure from 1 MPa while maintaining high selectivity of GBL ($>90\%$). Besides, the catalyst showed remarkable reusability, offering the catalyst with enormous potential for applying to the hydrogenation of not only SA but also other oxygen-rich biomass resources from laboratory to industrial scale.

In conclusion, the present thesis provides feasible and versatile methods to design effective CuPd bimetallic catalysts for selective hydrogenation of SA. Depending on the purpose, the product selectivity toward a specific product including BDO, THF, and GBL can be controlled by adjusting the Cu:Pd ratio, changing the catalyst support, and stabilizing with capping agent. The important findings derived from the present thesis might be useful to apply and design other earth-abundant bimetallic catalysts for hydrogenation reactions of other carboxylic acids.

Keywords: Succinic acid, CuPd alloy, Gamma-butyrolactone, 1,4-butanediol, Tetrahydrofuran

Acknowledgments

The research studies embodied in this doctoral dissertation have been conducted at the Graduate School of Advanced Science and Technology, Japan Advanced Institute of Science and Technology (JAIST) under the supervision of *Associate Professor Dr. Nishimura Shun* from April 2018 to March 2021.

First and foremost, I wish to express a deep sense of gratitude to my principal supervisor, *Associate Professor Dr. Nishimura Shun* for his careful guidance, constructive discussion with valuable suggestions, and unceasing support, which provided me with a strong impetus for the completion of this study. He is not only a professional advisor but also a true mentor who helped me to get most of the research skills/techniques in catalysis at the beginning of my Ph.D. journey. Furthermore, as a foreign student living abroad, I appreciate his genuine understanding and empathy for me on a personal level.

Second, I would like to express my heartfelt appreciation to my second supervisor *Professor Yamaguchi Masayuki* and the members of the Review Committee, *Professor Kaneko Tatsuo, Professor Matsumi Noriyoshi, Professor Taniike Toshiaki* from JAIST and *Associate Professor Ohyama Junya* from Kumamoto University, for their precious time reading, verifying, and making constructive comments and suggestions which certainly improve the quality of this dissertation.

Various characterization techniques described in this dissertation have been performed with the help and support from professors and technicians in and outside JAIST. First, I wish to thank *Mr. Higashimine Koichi, Ms. Kobayashi Shoko, and Professor Oshima Yoshifumi* (JAIST) for their great help in STEM-HAADF with EDS mapping/line-analysis techniques. Second, I am grateful to *Associate Professor Ohyama Junya* (Kumamoto University) and the technicians at SAGA Light Source (SAGA-LS, BL07, 11, and 15) for their valuable advice and technical assistance during the XAFS measurements. Third, I greatly appreciate *Mr. Hideki Numata* (Katsukitarohsukesyoten Co. Ltd., Japan) for his professional expertise to support me in the AAS measurements.

Financial supports and research and travel grants are indispensable for the completion of any research project. In this context, I gratefully acknowledge the scholarship from JAIST Doctoral Research Fellowship (DRF), JAIST Research Grant (Houga) for Potential Research Project, and JAIST Research Grant for Attending International Conferences. Also, I wish to extend my sincere gratitude to the monetary support from JAIST which covered the expenditure on my outside research activities at SAGA-LS.

During the doctoral course, I am grateful to work with my lab members, *Ms. Chu Xueting, Mr. Inuduka Sho, Ms. Li Xinyue* and visiting researcher *Dr. Abdallah I.M. Rabee*. Besides, I wish to express my sincere gratitude to Vietnamese friends at JAIST, *Dr. Doan Duy, Dr. Ton Nu Thanh Nhan, Mr. Le Cong Duy, Ms. Mai Thi Minh Anh, Mr. Nguyen Tan Viet Tuyen, Ms. Nguyen Thi Thuy, and Ms. Nguyen Thu Trang*, for their warm friendships and cheerful times together. Also, I am thankful to be a member of the Vietnamese Tennis Club at JAIST where I can play and relax after long hours studying at the lab. Special thanks to *Dr. Pham Van Cu* and *Mr. Nguyen Dai Duong* for their generous and timely help to me and my family, occasionally and in urgent situations.

Last but not least, I deeply thank my wife and my baby daughter who always stand by my side at every moment of this challenging journey. Their unconditional love, understanding, and faith make me recovered and stronger to complete this dissertation. This is also an opportunity for me to show my genuine appreciation to my father, my big family, and friends in Vietnam, who constantly support and encourage me during the fulfillment of this thesis. Finally, to my mother in heaven, who sacrificed everything for me, this work is dedicated to you.

Le Dinh Son
Ishikawa, Japan 2021

Contents

List of Figures

List of Schemes

List of Tables

Chapter 1

General Introduction

1.1 Succinic Acid as a Renewable Platform Chemical

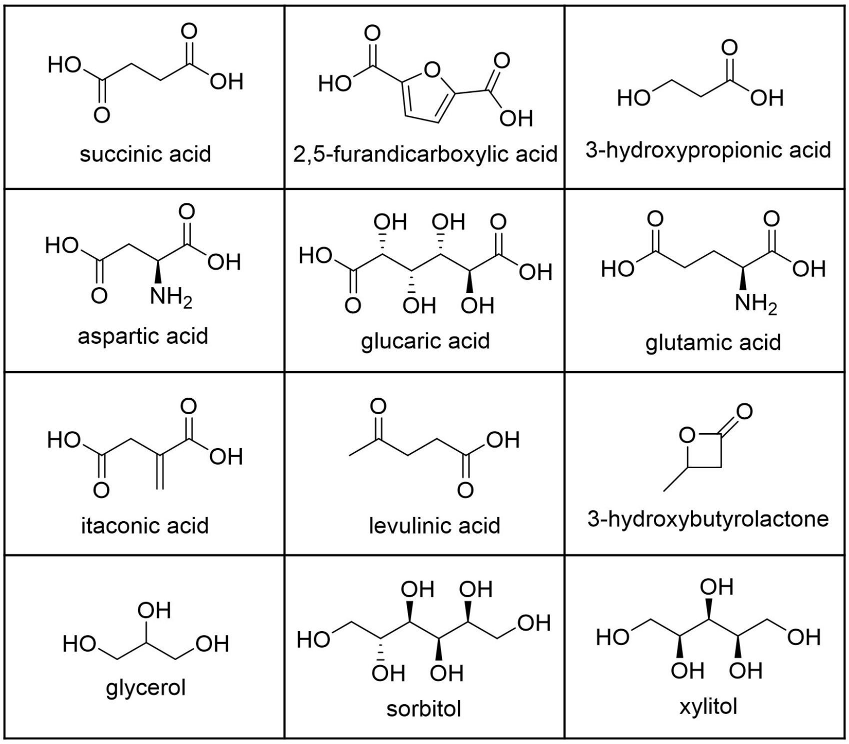

Figure 1.1: Top twelve building block chemicals [1]

Depleting fossil-based resources associated with severe environmental impacts have provided a strong spur for utilizing renewable carbon which is available in biomass-based materials, and recycled products. In the context of chemistry, particularly the chemical industry, considerable efforts have been devoted to searching for petro-equivalent or new building block chemicals. The top twelve sugar-based building block chemicals identified by the U.S. Department of Energy are shown in Figure 1.1 [1].

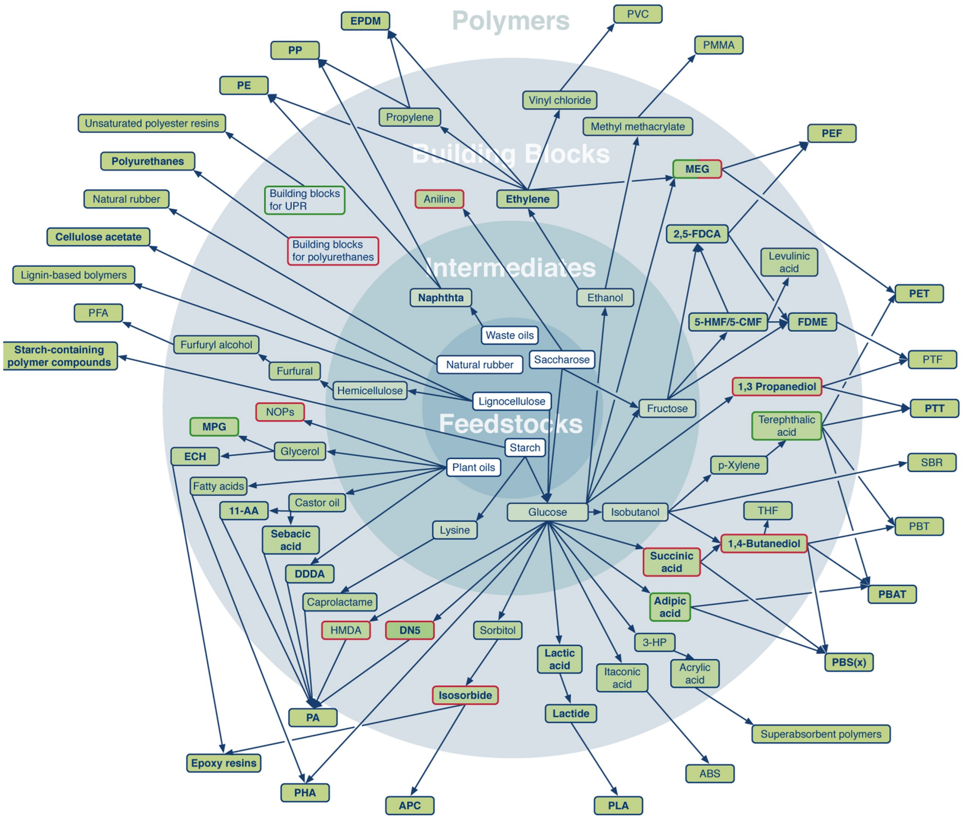

Figure 1.2: Routes to bio-based polymers [2]

These platform chemicals are mainly used to prepare polymers and plastics and a variety of fine and specialty chemicals (Figure 1.2). In the conversions of building blocks from plant feedstocks, biological transformations are mainly used, while chemical transformations account for the major routes from building blocks to value-added chemicals. Although it is technically possible to substitute fossil-based chemicals with their bio-based counterparts, the costs in both mentioned conversion routes in many cases exceeds the production cost of existing petrochemicals, limiting them from commercializing. Also, in terms of sustainable and green chemistry, selective conversions of bio-based materials to desired chemicals still stand as a challenge.

1.1.1 Production of Renewable Succinic Acid

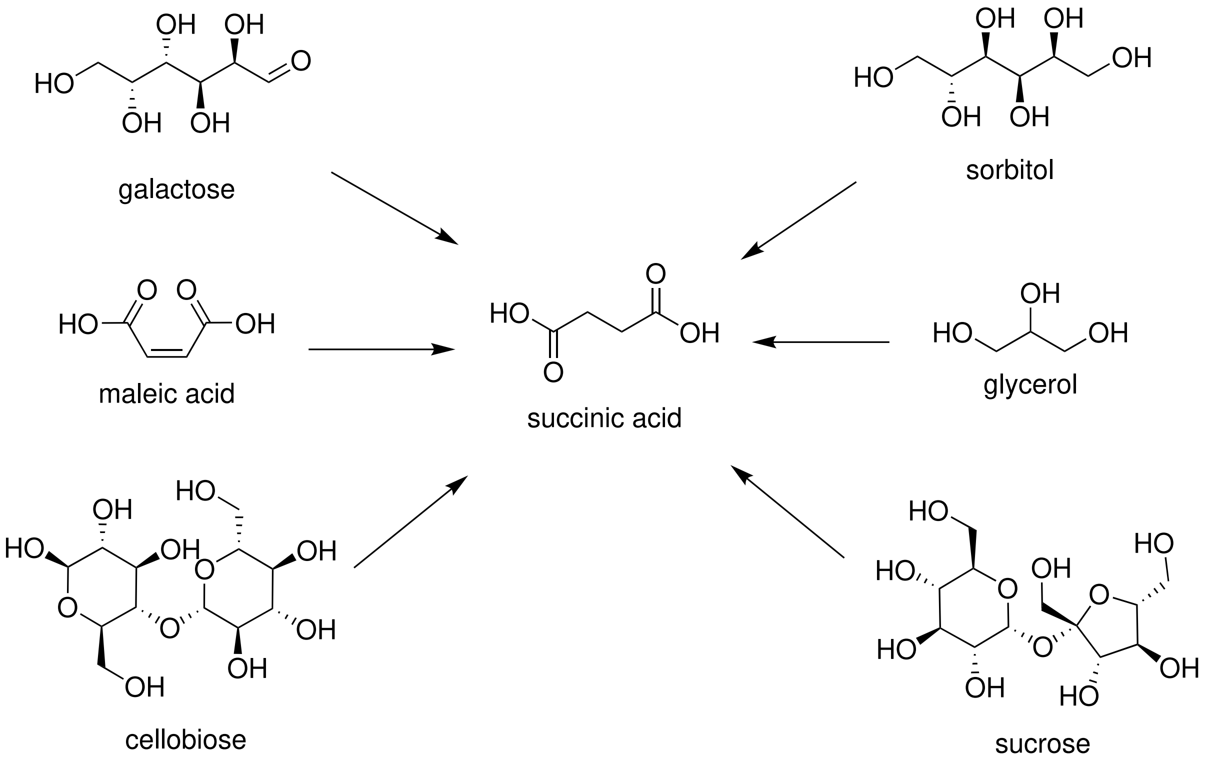

Scheme 1.1: Catalytic routes from renewable chemicals to succinic acid [3]

Succinic acid (SA) is one of the few renewable chemicals that are available in the market as a competitive supply to the petroleum-based maleic anhydride C_4 platform [4]. The renewable SA can be converted from different renewable bulk chemicals via chemical routes, while another method is based on the microbial succinate production via fermentation of various renewable carbon sources such as glucose, sucrose, and glycerol (Scheme 1.1) [3]. The current market of SA is based on fossil-derived maleic anhydride by several major companies such as Mitsubishi Chemical, Kawasaki Kasei, and Gadiv Petrochemical with the total production capacity of about 40 KT in 2013 [5]. The price of SA in the market is approximately US$ 2.40–2.60 per kg depending largely on the purity, whereas the price of maleic anhydride is about US$ 1.25–1.65 per kg [6]. Although the current market price of SA produced by the petrochemical process is profitable [7], high raw material cost about half the price of SA together with a large amount of greenhouse gas emission has stimulated researchers and companies to search for a more feasible, sustainable, and cost-effective bio-based process.

Renewable bulk chemicals for production of succinic acid

The first example on this conversion route indicates the use of maleic acid (MA) which can be synthesized from lignocellulose-derived furans [8]. An earlier study by Muzumdar et al. reported the electrochemical reduction of MA on a reusable TiO_2 cathode, affording SA with >90% yield [9]. Another study by Li et al. examined the use of HY-Al_2O_3 supported NiPt bimetallic catalysts which efficiently catalyzed the hydrogenation of MA to SA with a quantitative yield at mild reaction temperature and hydrogen pressure [10]. The second example on the production of SA using biomass-derived furans was introduced by Ebitani's group [11, 12]. Their studies described a facial method to synthesize SA from furan carbonyls (furfural, 5-hydroxymethyl-2-furaldehyde, furoic acid) using Amberlyst-15 as a solid catalyst and H_2O_2 as a green oxidant under mild reaction conditions.

Fermentative succinic acid production

The bio-SA that is available in the market is currently produced by fermentation processes by several renewable chemistry companies such as Myriant, BioAmber, Succinity, Reverdia, and Mitsubishi Chemical [13–17]. The total capacity for annual production of bio-SA contributed from these companies is ranging from 76.6–86.6 KT [18]. While the bio-SA market was estimated at US$ 175.7 million in 2017 and is anticipated to grow approximately 20% annually reaching a global revenue of more than US$ 900 million by 2026 [19]. Compared to petroleum-based SA, the cost of glucose for producing bio-based SA is cheaper approximately US$ 0.66–0.98 per kg [20]. ALso, the bio-based production of SA is a greater energy-efficient process, selective with fewer by-products, and more environmentally-friendly. Although the current price of bio-SA (US$ 2.86–3.00/kg) is higher than that of the petroleum-based SA (US$ 2.40–2.60) due to the high cost in the complex downstream process [21], the features offered by bio-SA have caught great attention from companies and researchers worldwide.

Since the first recognition of fermentation process for bio-SA production in 1980 by

Zeikus, various microorganisms including gram-positive bacteria, fungi, and yeast have been screened and studied [22]. The most intensive studies on bacteria have focused on the use of *A. succinogenes*, *A. succiniciproducens* and *M. succiniciproducens*, which are considered as the most promising candidates that can produce SA naturally. The metabolic engineering of bacteria generally includes the glucose specific phosphotransferase, the pyruvate formate lyase, and the fermentative lactate dehydrogenase systems [23]. The growth of these bacteria depends on carbon sources including glucose, glycerol, sucrose, and CO_2. However, due to the pathogenicity-associated potential, poor cell viability, and intolerance to high acidity and osmotic sock, manufacturing on an industrial scale is limited on these bacterial hosts [7, 24]. At the same time, studies on filamentous fungi (molds) such as *A. niger*, *A. fumigatus*, *B. nivea*, *L. degener*, *P. varioti*, and *P. viniferum* for SA production have also been pursued [15, 25, 26]. The drawbacks that might come from these production processes include technical difficulties in fermentation causing low productivities and tedious downstream processes [14].

The downstream processing can be simplified while reducing the risk of microbial contamination by lowering the pH [27]. Thus, the use of yeast for SA production is highly desirable due to its high tolerance to acid environments. Several groups of yeasts including *S. cerevisiae* [28–35], *Y. lipolytica* [36–44] and others, i.e., *Pichia* and *Candida* have been investigated for production of bio-SA. Among these studies, *Y. lipolytica* has emerged as the most potential candidate which can produce 209.7 g/L SA titer in fed-batch cultivation without pH control [43]. The advancements of this process compared to normal metabolic routes to succinate at low pH is that it prevents the formation of acetate [41]. Although the fermentative production of bio-SA has shown great potential to completely substitute petroleum-SA, it is admitted that the development of a high-performance strain remains as the major challenge that needs the contribution of not only companies and researcher but also the suitable policy worldwide.

1.1.2 Succinic Acid to Material, Chemicals and Fuels

Holding an enormous potential of a renewable platform chemical, SA together with MA would replace the fossil-based C_4 platform chemical in the foreseeable future [3]. SA itself is a suitable and profitable source for preparing fine chemicals, additives in cosmetics and foods, de-icer, coolants, neutralizing agents, plasticize, and many others [15]. Also, as a versatile compound SA can be converted into many useful derivative, as described in Scheme 1.2 [1, 4, 45].

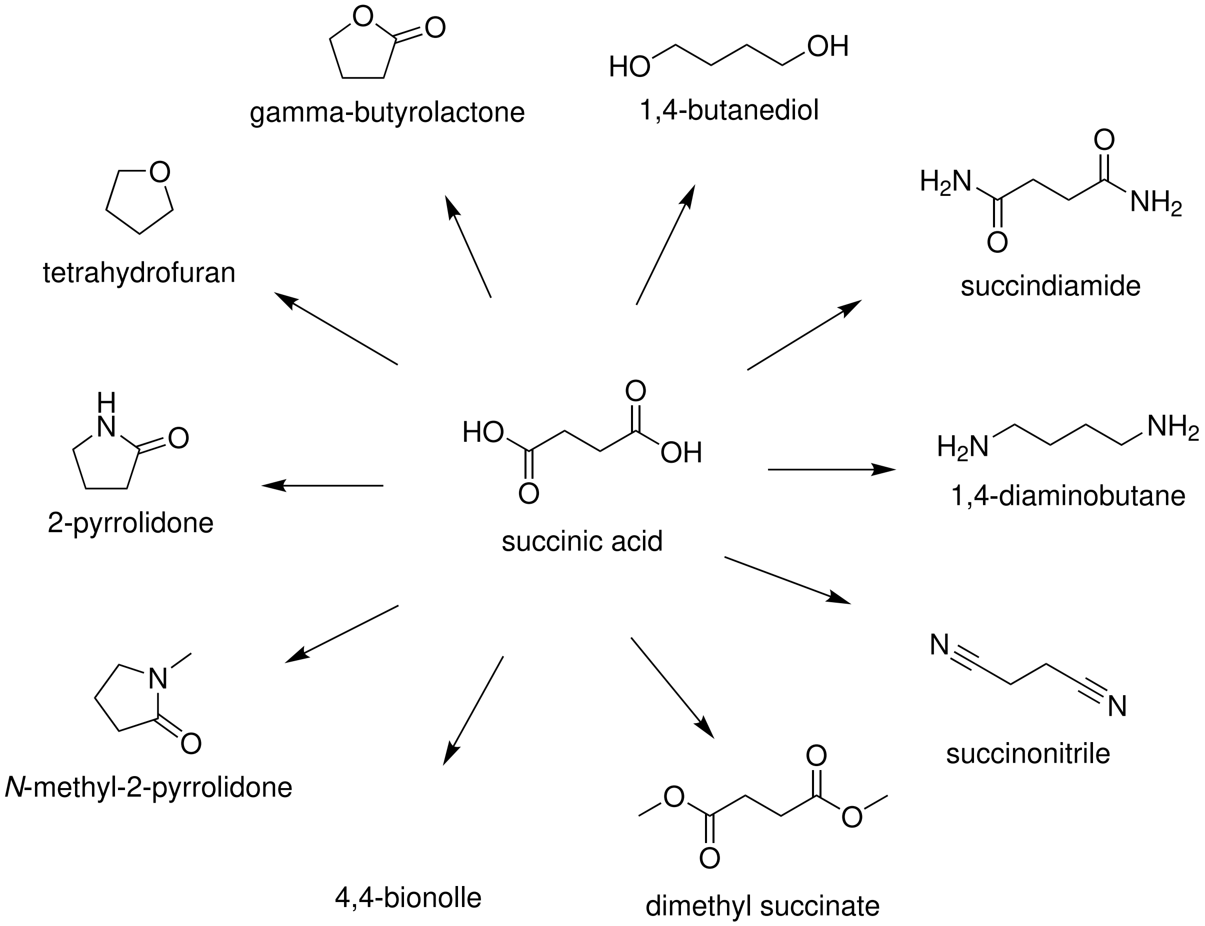

Scheme 1.2: Transformation of succinic acid to value-added chemicals [1]

Succinic acid to bio-based polymers

The bio-based polymer market is accounted for a major part of the SA production. The first important bio-based polymer is polybutene succinate (PBS) which is known as a biodegradable aliphatic polyester with properties that are comparable to polypropylene

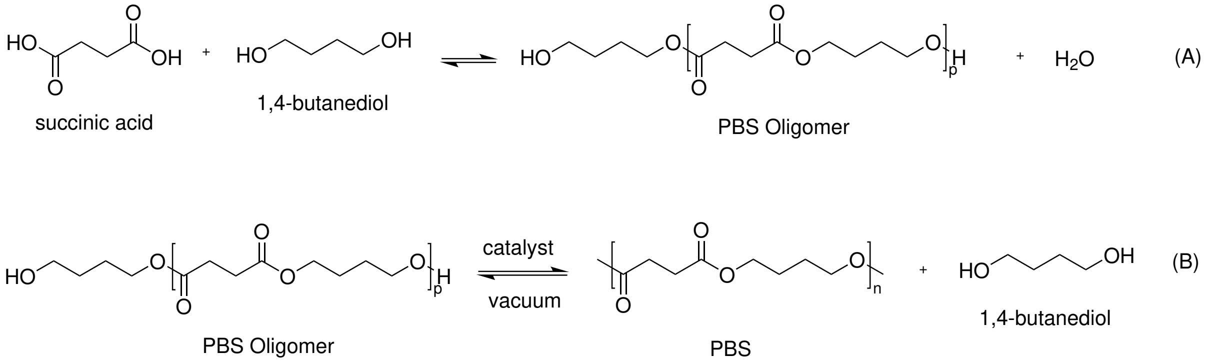

Scheme 1.3: Succinic acid for synthesis of polybutylene succinate (PBS) [47]

or polyethylene terephthalate (PET) [46]. PBS can be prepared by direct esterification of SA with 1,4-butanediol (BDO). The synthesis can be done via two steps as described in Scheme 1.3 [47]. In the first step, an excess amount of BDO is allowed to react with SA to form the PBS oligomers along with water elimination (Scheme 1.3A). The second step is trans-esterification which is proceeded by, for example, organometal-(Ti, Zr, Sn, Hf, and Bi) and metal oxide-(Ge and Sb) based catalysts under vacuum to form a polymer with high molar mass (Scheme 1.3B).

Recent developments have witnessed the generations of novel succinate-derived polymers such as poly(propylene succinate) (PPS) [48], poly(butylene succinate-*co*-butylene sulfonated succinate) (PBSxSSy) [49], acylated poly(glycerolsuccinate) (PGSC) [50–52], succinyl polyxylosides (SPx) [53], and succinyl polyesters (PHxS) [54, 55]. These polymers offer wide range of melting points (44–114 ℃), and molecular weights (2800–70000 g mol^{-1}), stronger but also highly bio-degradable, making them potential candidates in many applications such as natural fiber in composite materials and drug carrier in medical applications.

Catalytic conversions of succinic acid

Among the main three conversion routes of SA, i.e., hydrogenation, esterification, and amination, hydrogenation reaction has attracted considerable attention due to the importance of its products including γ-butyrolactone (GBL), tetrahydrofuran (THF), and BDO [3]. GBL is a fine chemical intermediate that is used in the syntheses of BDO, THF, *N*-Methyl-2-pyrrolidone (NMP), and *N*-vinylpyrrolidone [56–59]. GBL can also be found in a wide range of applications such as a solvent in polymer, paint, and pharmaceutical industries [60, 61]. With the growing demand, the global market of GBL was valued at US$ 622.62 million in 2019 and is predicted to increase 5.47% annually and reach US$ 903.92 million by 2026 [62]. While, the major applications of THF include polyesters, polyurethane elastomers, and polytetrahydrofuran (PTMEG) [63–65]. THF can also be used as a solvent in the production of polyvinyl chloride (PVC) and paints [66]. In terms of value, the global THF market was estimated at US$ 1.5 billion in 2018 and projected to grow annually at a rate of 7.8% and reach at US$ 2.8 billion by 2026 [67]. This high rate of growth can be ascribed to the increasing demand for the PTMEG which is used as a raw material for various Spandex fibers in the textile industry. BDO is probably the most important product that can be converted by hydrogenation of SA. It is employed as an important precursor for the polybutylene terephthalate (PBT) which is widely used in the automobile and electronic industries [68, 69]. Other polymers that can be prepared with the use of BDO include PBS and poly(butylene succinate-*co*-butylene terephthalate) (PBST) which can be used in melt-spinning fiber and yarns [70–72]. The global market size of BDO was valued at US$ 6.19 billion in 2015 and expected to reach US$ 12.6 billion by 2025 with an annual growth rate of 7.7% [73].

1.2 Supported Metal Catalysts for Hydrogenation of Succinic Acid

1.2.1 Metal catalysts: General aspects

Catalyst design is the main focus of the modern chemical industry since the value that is created from the conversion of raw materials to value-added products such as fuels and chemicals is much higher compared to the spend on catalysts [74]. The hydrogenation reactions catalyzed by heterogeneous metal catalysts are at the heart of petrochemical, coal chemical, fine chemical, and environmental industries [75–78]. The selective catalysts for hydrogenation reactions favor specific transformations while preventing others in the same catalytic system. Despite the fact that the catalysts for hydrogenations had been widely investigated, many of the fundamental aspects regarding both the catalyst synthesis and structure–property relationship are yet not fully understood [79]. For the hydrogenations to fine chemicals, both homogeneous and heterogeneous catalysts have been used. The homogeneous catalysts referring to metal–ligand complexes typically offer high selectivity due to the steric and electronic effects of the ligands. However, this kind of catalyst generally suffers from difficulties in separation and reusability. Therefore, in the context of industrial chemistry, heterogeneous catalysts are more favorable, though it is challenging to rationally design the catalysts which offer high selectivity without compromising the activity.

Since the catalysis consists of adsorption, transformation, and desorption processes of the reactant, intermediate, and products on the catalyst surface [80], the first requirement for catalyst design is the control of their adsorption position, strength, and configuration on the active sites. On the other hand, for the hydrogenation reaction, in particular, the adsorption and activation of H_2 by metal catalysts are other key steps. Both of the mentioned processes are fundamentally important for catalytic hydrogenations, which can be optimized by constructing the catalysts with specific electronic and geometric structures [81, 82]. However, this is undoubtedly not a mean task since many factors define the catalyst structures and they often interfere with each other in a catalyst system. Nevertheless, it would be easier to begin considering all the possible factors individually.

Size of metal ensembles

Figure 1.3 illustrates the electronic and geometric structures on the size of metal ensembles ranging from a single atom to cluster and to nanoparticles (NPs) [83]. It can be seen that when the size of metal particles is less than 1 nm, the electron levels are strongly quantized, as indicated by the discrete energy values. While as the increase of the metal size (>2 nm), a continuous energy level is formed. The dependence of Au particle size on the electronic structure thus the work function can serve as a representative example for this aspect [84].

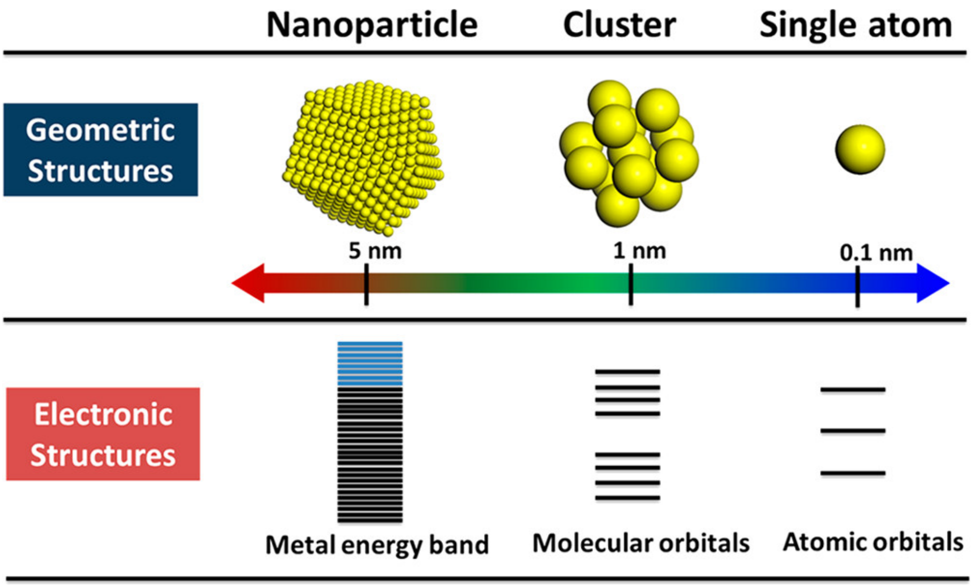

Figure 1.3: The dependence of geometric and electronic structures on the size of metal ensembles [83]

In this case, it was reported that the work function fluctuated greatly in the Au cluster size while it showed slight changes in the Au NPs (> 1.5 nm). The geometric structures, on the other hand, also vary depending on the particle size. For example, in the single atoms supported on inorganic supports such as metal oxides and zeolites, limited geometric transformations are observed [83]. While for the cluster size particles, several possible topological structures can be formed, depending on the support, reactant, and reaction conditions. For the metal NPs, the geometric structure was found relatively stable even though the geometric configuration might change due to the exposure of surface atoms, i.e., facet, corner, edge, metal–support interface, to the reaction environment [85].

Coordination environment

The coordination environments that can influence the electronic and geometric structures of heterogeneous metal catalysts consist of the following three fundamental interactions: (i) metal–metal, (ii) metal–support, and (iii) metal–capping ligand.

(i) Metal–metal interaction: When more than one metal is mixed together, multi-metallic NPs can be formed within a single catalyst. Bimetallic catalysts, however, have appeared as the common catalysts in many reactions such as hydrogenolysis, hydrogenation, oxidation, and reforming [86–89]. The four popular type of bimetallic catalysts are illustrated in Figure 1.4 [90]. The formation of these systems can be affected by several factors [90], for examples, the relative strength of the bond between the two different metals (M_1–M_2) and the pure metals (M_1–M_1 and M_2–M_2), the relative atomic size, surface energy, charge transfer, and specific electronic/magnetic effects. In general, these bimetallic systems showed unique properties compared to those of the monometallic ones, which are often ascribed to synergistic effects caused by alloying formation. In fact, the synergies generated in bimetallic catalysts result from the modifications of (a) electronic structure via the ligand effects and (b) geometry by the neighboring metal via the strain effects and lattice defects [87, 91].

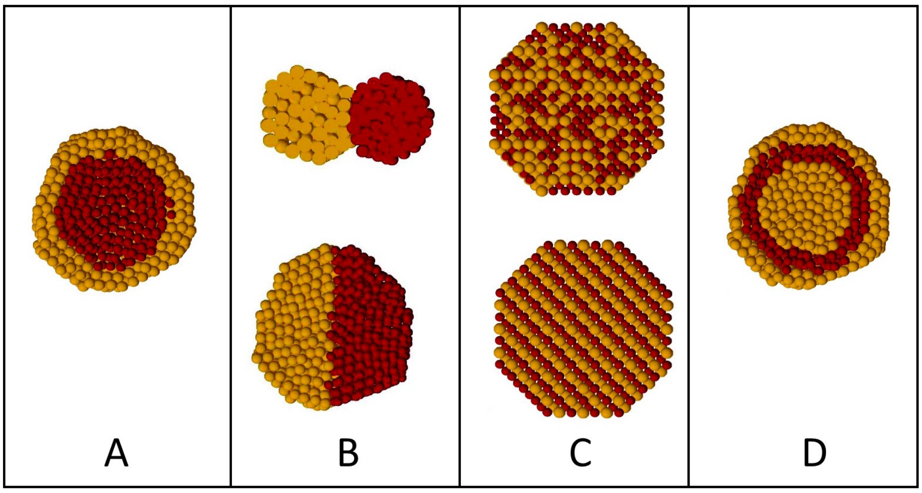

Figure 1.4: Schematic representation of some possible mixing patterns in bimetallic systems: (A) core-shell, (B) subcluster segregated, (C) random homogeneous and ordered, and (D) multishell alloys [90]

(ii) Metal–support interaction: The importance of metal–support interactions (MSI) has been recognize by Tauster et al. since the late 1970s [92, 93]. In heterogeneous catalysts, the MSI can affect the catalytic performance and therefore can serve as options for catalyst design [94]. Figure 1.5 shows typical forms of MSI and as discussed earlier, these are often entangled with each other and with other factors in the same catalyst system [94].

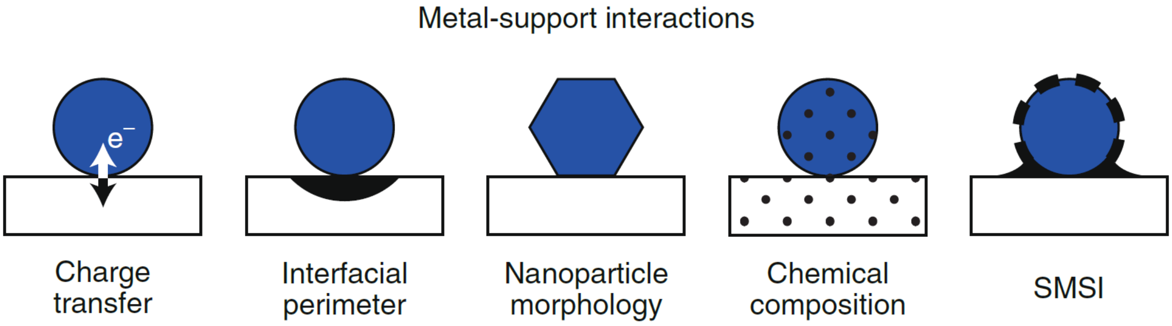

Figure 1.5: Typical metal–support interactions [94]

(a) Charge transfer. The unbalance in the electron density between metal NPs and its support can result in a redistribution of electrons at the metal–support interface [95]. Depending on the relative difference in the Fermi levels between metal NPs and the support, the magnitude and direction of the charge transfer can be different. In addition, the nature of metal and its size, support morphology and defects, and other surrounding matters such as the neighboring metal, capping/stabilizing agent, substrate [96, 97], can be relevant to the charge transfer between metal and support, which ultimately influences the electronic structure of the whole catalyst system.

(b) Interfacial perimeter. The interface sites marked by perimeters of supported metal NPs are unique environments where NPs, support, and reactant are directly in contact. This area also favors the accumulation of excess charge if charge transfer occurs, which enhances the adsorption of reactants/intermediates [98]. In addition, the spillovers of hydrogen can be initiated at the metal active sites and then the molecules can subsequently be transferred via the interfacial perimeter to other surfaces (support, metal) [94, 99].

(c) NP morphology. Depending on the adhesion energy of the support to the metal NPs, the metal shape and crystal structure can be different [100]. The strong adhesion generally leads to more faceted NPs and even raft-like shapes [101]. It is worth mentioning that the adhesion energy can be increased by decreasing the size of metal NPs [102].

(d) Chemical composition. The difference in relative adhesive energies between support and different metal components can affect the local composition of alloyed metal NPs [103]. For example, in the supported M_1-M_2 alloying NPs, if the support–M_1 interaction is stronger than the support–M_2, the fraction of M_1 in the M_1-M_2 alloy can be reduced, while the isolated M_1 NPs would be found in the support surface with the increasing frequency. If the difference is significant, the initially uniform composition of a bimetallic NPs may be turned into core-shell or segregated sub-cluster structure [90].

(e) Strong metal–support interaction (SMSI). The term refers to the metal–support that interacts strongly due to the enclosed suboxides around metal NPs and the support interface [92, 93, 104]. These suboxides can be generated in reducible supports under the reducing conditions. The extensive coverage of metal NPs by these suboxides is detrimental to the catalytic performance since it may prevent the accessibility of substrates to the active sites. However, the existence of a proper suboxide layer can modify the electronic structure of the metal surface, which may act as Lewis acid sites, enhancing the catalytic performance [105].

(iii) Metal–capping ligand interaction. In many cases, the supported metal catalysts are prepared by the colloidal approach where the colloidal NPs are synthesized in a solution first and subsequently be immobilized on a support [106]. By this approach, the influence of support on the formation of metal NPs can be excluded or minimized. The colloidal NPs is typically prepared by employing organic ligands (Figure 1.6A) under a reducing environment. The use of organic ligands may help to prevent the aggregation, coalescence and unlimited growth of metal NPs [107], which, therefore, offers an effective method to control the size and shape of the synthesized NPs.

In general, the interactions between capping ligands and metal NPs occur at the metallic surface with the coordination of the head group of the ligand molecules [108]. Depending on the type of capping ligand, metal NPs can be stabilized by either electrostatic or steric interactions (Figure 1.6B) [109]. Also, the strength of these interactions can be varied

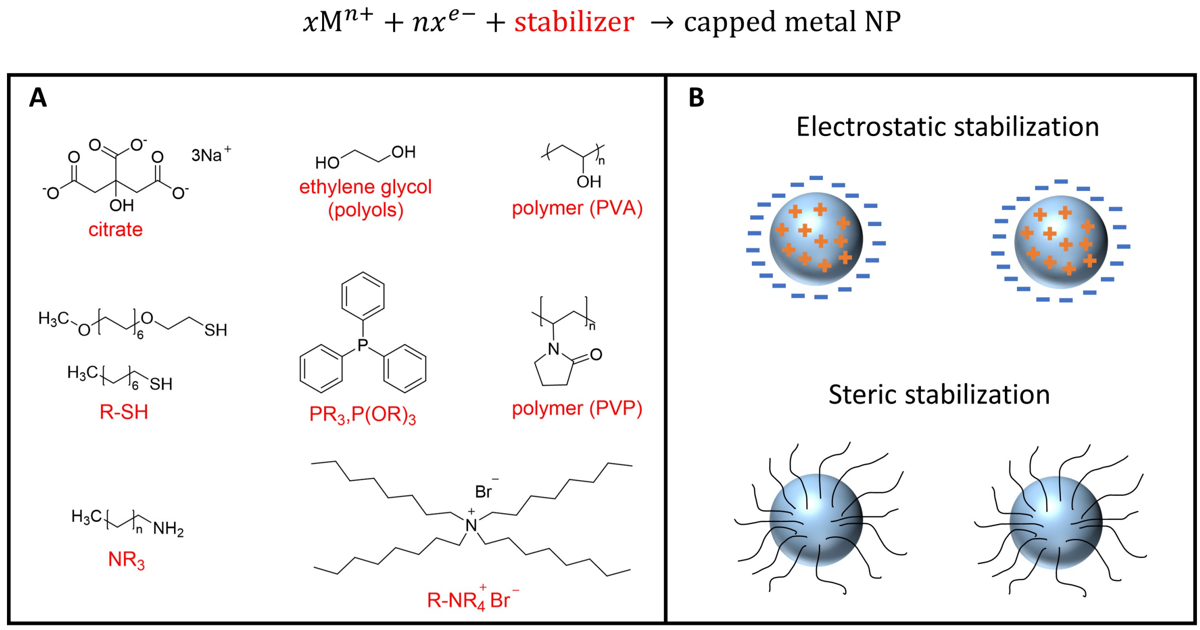

Figure 1.6: (A) Common capping ligands used in colloidal NPs for catalysis and (B) types of interactions between capping ligands and metal NPs [108]

depending on the binding affinity of ligand molecules to the metallic surface. Typically, the strong metal–ligand interaction can help to prepare more uniform NPs with narrow size distribution. By controlling the passivated layer of capping ligands around the metal NPs, the catalytic performance can be enhanced due to the electronic effects. Furthermore, the steric effect of capping ligands can be used as a tool to control the selectivity toward a certain product by preventing the accessibility of reactant/intermediates to a specific site of the metal surface. On the other hand, it should be noted that the strong metal–ligand interaction can cause adverse impacts on the catalytic performance by passivating active sites and poisoning the catalyst surface [110]. Nevertheless, the weak interaction may cause the detachment of the capping ligand from the metal surface during the reaction, leading to metal sintering and thus decreasing the catalyst activity and stability.

Activation of H_2

In hydrogenation, the hydrogen adsorption and activation is critically important since the effectiveness of these steps can affect both the catalytic activity and selectivity [89].

Depending on the electron density around the metal, a hydrogen atom can be adsorbed and dissociated in different manners, i.e., homolysis or heterolysis (Figure 1.7, [111]). The reduction ability can be different among different types of H species and substrates.

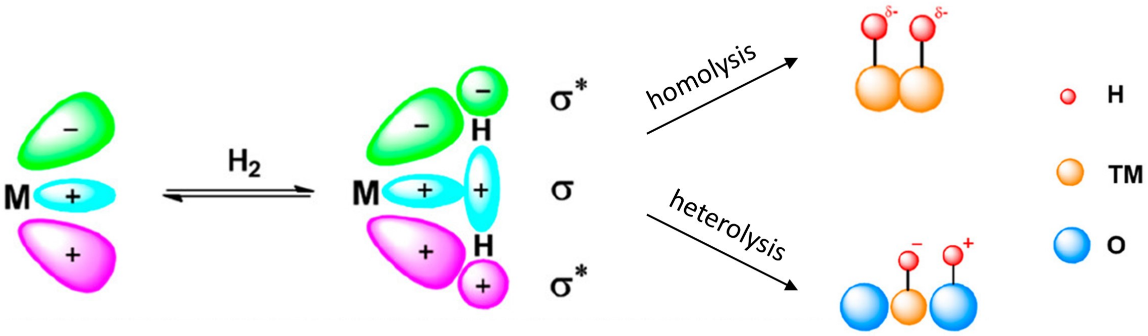

Figure 1.7: Types of hydrogen dissociations [111]

(i) Homolytic dissociation of hydrogen: The precious metal such as Pt, Pd, and Rh can easily dissociate H_2 by destabilizing the σ^* anti-bonding orbital of H_2, while at the same time accept the σ electrons of H_2. As a result, the hydrogen bonding is weakened and subsequently cleaved, forming $H^{\delta+}$ and $H^{\delta-}$ hydrides species via homolytic dissociation [111]. Since this kind of dissociation requires the donation of d-electrons from metal, increasing the electron density at the metal active sites by coordinating with electron-rich components such as a secondary metal, support, and capping ligand can enhance the activation steps of hydrogen atoms.

(ii) Heterolytic dissociation of hydrogen: The metal active sites with electron deficiency tend to cleave hydrogen via the heterolytic pathway. This kind of dissociation, however, requires the involvement of the catalyst support or additive/promoter where the electropositive metal accepts the H^- species, while the electronegative heteroatom from support accepts the H^+ species [89]. Since the polarization degree of metal–heteroatom can be changed depending on the support or additive, the dissociation of H_2 and ultimately the hydrogenation rate can be enhanced. In addition, it was reported that the H^+/H^- species kinetically favor the reduction of polar groups rather than the non-polar ones, indicating that the chemoselectivity in hydrogenation reaction can be increased by controlling the H_2 dissociation steps [112].

1.2.2 Hydrogenation of succinic acid

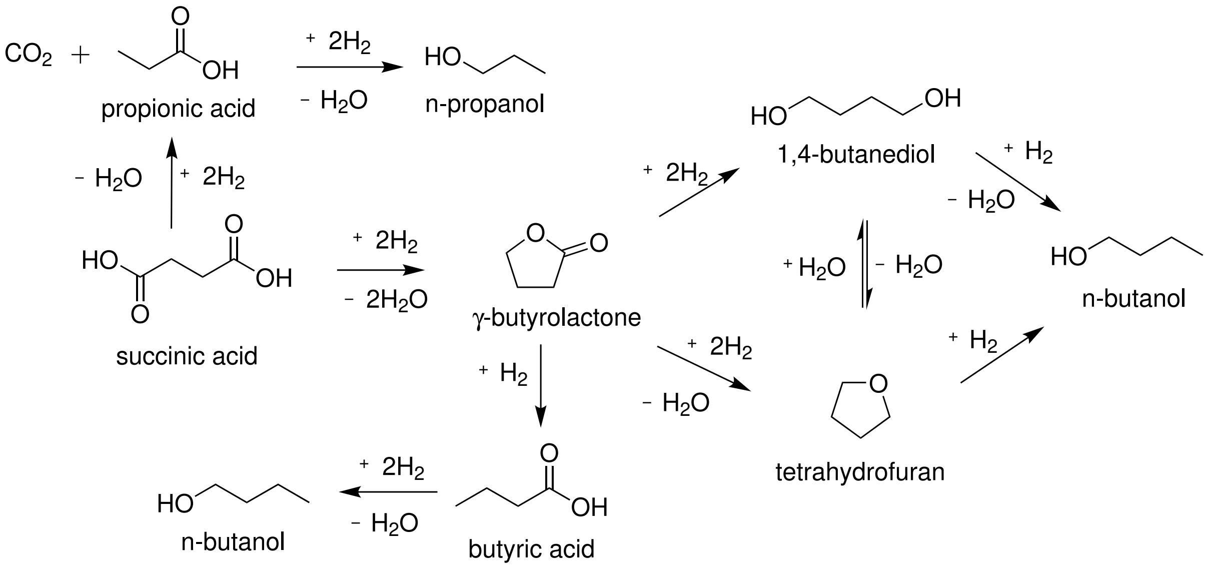

Scheme 1.4: Reported reaction pathways of succinic acid hydrogenolysis [113, 114]

The hydrogenation of carboxylic acid is an industrially important reaction in the context of upgrading renewable carbon sources [115]. For SA in particular, the hydrogenation reaction is by far the most investigated route [3] (Scheme 1.4). The potential use of SA as a starting feedstock for the production of BDO, PBS, and PBST is the main driver for this increasing attraction in the SA hydrogenation [116]. The catalytic conversion of SA and dicarboxylic acid is generally a challenging transformation that can be attributed to the low electrophilicity of the carbonyl group and the difficulties allied to the polarization of this group [117]. In addition, the conversion can be more difficult since carboxylic acids and their esters, lactones might interconvert under applied reaction conditions [115]. As a result, the product distribution in the hydrogenation of dicarboxylic acid, i.e., SA, may vary depending on the extent of interconversion. The resistance of SA and their esters, lactones toward reduction have provided a spur for designing effective catalysts for selective hydrogenation of SA.

1.2.3 Monometallic catalysts for hydrogenation of succinic acid

Table 1.1: Recent studies on the SA hydrogenation over monometallic catalysts

Catalyst	Solvent	Temp. /°C	P H_2 /MPa	Conv. /%	Selectivity /% GBL	BDO	THF	Ref.
Pd/Al_2O_3	Dioxane	170	3	70	95	1	0	[118]
Re/C-4%^{a}	H_2O	240	8	48	90	1	9	[119]
Re/C-8%^{a}	H_2O	240	8	95	20	7	67	[119]
Re/MC-0.4^b	Dioxane	240	8	100	27	5	38	[120]
Re/MC-0^b	Dioxane	240	8	80	62	3	7	[120]
Pd/MCM-41	EtOH + H_2O	250	10	60	32	53	15	[121]
Pd/SBA-15	EtOH + H_2O	250	10	65	39	36	25	[121]
Pd/SiO_2	EtOH + H_2O	250	10	57	27	25	48	[121]
Ru/Starbon®	EtOH + H_2O	100	1	90	30	10	60	[61]
Pt/Starbon®	EtOH + H_2O	100	1	78	15	85	0	[61]
Pd/Starbon®	EtOH + H_2O	100	1	75	30	70	0	[61]
Rh/Starbon®	EtOH + H_2O	100	1	60	10	90	0	[61]

[a] Re/C–X, X = Re loading (wt%)
[b] Re/MC–X, X = concentration of H_2SO_4 treated (M)

Recent research on the hydrogenation of SA over monometallic catalysts published in the open literature are listed in Table 1.1. Luque et al. reported several Starbon®-supported precious metal (Pt, Pd, Rh, Ru) catalysts for the SA hydrogenation in aqueous ethanol under middle reaction conditions [61]. The SA conversion varied among 60–90% while the product selectivity was found depending on the metal employed. For example, Starbon®-Pd, Pt, Rh catalysts promoted the formation of BDO as the major product, while the Ru-Starbon® favored the THF formation. GBL can be observed in all these catalysts with the selectivity ranging from 15–30%. Chung et al. studied the SA hydrogenation over MCM-41 and SBA-15 supported Pd catalysts [121]. It was found that the large Pd particles and small pore size in Pd/MCM-41 were responsible for enhanced the BDO selectivity but relatively low SA conversion. Whereas the small Pd particles constructed on Pd/SBA-15 was preferable for the formations of GBL and THF. However, it is noted that in all these reported Pd catalysts, the product selectivities are less than 50% with medium SA conversion (<65%).

GBL with higher selectivities can be achieved over rhenium supported on H_2SO_4-treated mesoporous carbon (Re/MC-X) [120] prepared by precipitation method. The product selectivities were influenced by the concentration (XM) of treated H_2SO_4. Particularly, without H_2SO_4 treatment, the Re/MC-0 can produce GBL with 77.4% selectivity at high SA conversion (80.4%). Increasing the concentration of H_2SO_4 treated, THF selectivity was observed at higher selectivity (38.3%) over the Re/MC-0.4; however, GBL still remained as a comparable product over this catalyst. Re/C catalysts prepared by a microwave-assisted thermolytic method were also reported as efficient catalysts for SA hydrogenation to GBL and THF [119]. The product selectivities can be controlled by monitoring the irradiation time and the concentration of the precursor $Re_2(CO)_{10}$. Accordingly, a high selectivity was achieved with a short irradiation time (3 min) and a lower concentration ratio of the precursor to the support (2%). In contrast, longer time irradiation (5 min) and high concentration of precursor (8%) favored the formation of THF.

In terms of catalytic efficiency at mild conditions, the Pd/Al_2O_3 catalyzed SA hydrogenation to GBL is a notable example [118]. The study showed that an excellent GBL selectivity (95%) can be achieved at relatively high SA conversion ($< 70\%$). The reaction can proceed at mild hydrogen pressures (1.5–3.0 MPa) and reaction temperatures (140–170 ℃). The choice of support and the size of Pd particles were revealed as crucial factors for the catalytic performance. In particular, the high surface area and low acidity of Pd/Al_2O_3 that was prepared by the co-precipitation method resulting in a more uniform distribution of Pd were responsible for the superior catalytic activity and selectivity of this catalyst.

1.2.4 Bimetallic catalysts for hydrogenation of succinic acid

Besides the development of monometallic catalysts, the uses of bimetallic catalysts with well-defined core-shell, alloyed or intermetallic structures have been emerging as a central topic in hydrogenation reaction [86]. Compared to the monometallic analogs, bimetallic catalysts have been reported to offer unique properties stemmed from synergistic effects

Table 1.2: Recent studies on the SA hydrogenation over bimetallic catalysts

Catalyst	Solvent	Temp. /°C	P H_2 /MPa	Conv. /%	Selectivity /% BDO	GBL	THF	Ref.
Ir−Re/C	H_2O	240	8	100	< 5	0	75	[123]
Pd−Cu/AX	2-propanol	190	7	72	0	94	0	[124]
Re−Ru/C	H_2O	160	8	99	70	6	6	[125]
Re3−Ru/C	H_2O	240	8	99	3	5	60	[125]
Pd−Re/AC	H_2O	180	10	100	67	0	14	[126]
Pt−Sn/AC	H_2O	180	10	100	51	15	13	[126]
Ru−Sn/AC	H_2O	180	10	100	67	23	13	[126]
Re−Ru/BMC	H_2O	200	8	100	65	34	3	[127]
Re−Pd/SiO_2	Dioxane	140	8	100	89	3	0	[128]
Pd−5 FeO_x/C	H_2O	200	5	100	70	-	-	[114]
Re−Ru/MC	Dioxane	200	8	100	71	18	11	[129]
Pd−Re/C	H_2O	240	8	89	4	-	73	[130]
Pd−Re/TiO_2	H_2O	160	15	100	83	0	-	[131]
Pd−Re/C	H_2O	160	15	100	66	0	-	[132]

AX: alumina xerogel, AC: activated carbon, MC: mesoporous carbon, BMC: boron-modified mesoporous carbon

between the two metals [122]. Also, the use of secondary metals in many cases can be economically advantageous since it can reduce the dependence on the precious metals which are typical used in the catalysts for hydrogenation reactions. Recent research on the hydrogenation of SA to GBL, BDO, and THF published in the open literature is listed in Table 1.2.

In most studies, Re-based bimetallic catalysts were used for the liquid phase hydrogenation of SA. In an earlier study by Ly et al., the Pd−Re/TiO_2 was found to be a potential bimetallic catalyst for the hydrogenation of SA in an aqueous phase, affording BDO with high selectivity of 83% at quantitative conversion [131]. It was proposed that the synergy between Pd and Re species enhanced the activity compared to the monometallic catalysts which generally favored the GBL formation. However, a high loading amount of Re (>3.5 wt%) was required for achieving the best performance. Re−Pd/SiO_2 catalysts prepared by different reduction methods were also examined for hydrogenations of several dicarboxylic acids [128]. A higher BDO yield (89%) was achieved in the SA hydrogenation over the *ex situ* liquid-phase reduced catalyst, compared to the *in situ* one. Characterizations revealed that in the presence of dicarboxylic acid, the reduction of Re species to Re^0 was suppressed leaving much amount of Re^{n+} species on the catalyst prepared by in situ reduction. The unbalance between these two components led to the low activity of hydrogenation of dicarboxylic acids. Other bimetallic catalysts such as boron-modified mesoporous carbon (BMC) supported Re–Ru [127], Ru−Sn/AC [126], and Re−Ru/C were also reported for SA hydrogenation to afford BDO with high yield and selectivity.

Liang et al. studied activated carbon-supported Pd–Re and Pd–Ir catalysts for aqueous-phase hydrogenation of SA, achieving THF with high selectivity [123, 130]. The research found that the SA hydrogenation over both the monometallic catalysts Ir/C and Pd/C showed low SA conversions with high selectivities of GBL. The additions of small amounts of Re in the bimetallic catalysts resulted in the enhancements of GBL yield, whereas a larger Re amount can facilitate the THF formation. Di et al. examined the role of Re and Ru in Re–Ru/C catalysts for SA hydrogenation. The 1:1 wt% of Re–Ru catalyst was found to be an appropriate ratio favoring the formation of BDO with a selectivity of 70% at nearly quantitative conversion. While the addition of Re in the Re3–Ru/C led to a sharp increase in the THF selectivity. Compared to the Re monometallic catalyst which was also reported to favor the THF formation [119], the Re3–Ru/C bimetallic catalyst enhanced both the THF selectivity and yield.

Earth-abundant metals such as Fe and Cu in combination with Pd were also reported for the SA hydrogenation [114, 124]. For example, Liu et al. reported $Pd{-}5\,FeO_x/C$ as efficient catalyst for aqueous hydrogenation of SA to afford >70% BDO yield under 200 ℃ and 5 MPa H_2. The Fe species were proposed to enhance the catalytic activity while altering the product selectivity toward either THF or BDO. The plausible reason behind this improvement can be explained by several factors, for example, the increase in acidity of introduced Fe species, the well-dispersed Pd species, and the synergy that existed between these two metals. Another example in this category is the alumina xerogel (AX) supported Pd–Cu catalyzed SA hydrogenation in isopropyl alcohol [124]. A high selectivity of GBL (94%) at 72% SA conversion can be achieved ever the 2.5%Pd-2.5%Cu/AX at 190 ℃ and 7 MPa H_2. The Cu component in this catalyst was suggested to suppress the reactivity of Pd, preventing further hydrogenation of GBL to BDO and THF.

1.3 Research Gaps

The availability of bio-based SA and the increasing demand for its derivatives led to great attention in the hydrogenation of SA recently. [3, 16]. However, since literature referring to this reaction can be found mainly in the patent, information on the promoting, doping, and synergistic effects of between metals and kinetic data are limited [4]. The open literature published during the last decade, to some extent, have recorded significant achievements. In most reports, the role of metals and synergy between metal species have been clarified. To identify the reaction network and determine the optimum reaction conditions toward a certain product, kinetic studies were also performed in several research [118, 125, 128, 133]. However, it is worth mentioning that the kinetic models, specifically, the reaction order, observed in this complex reaction containing multiple steps/pathways might not practically important due to the influences of many factors in the whole reaction [134].

Despite that, most catalysts reported in previous studies limited to the uses of precious metals such as Ir, Rh, Pt, Re, and Ru. The heavy dependence on these rare-earth metals is economically disadvantageous, possibly limiting them from industrial applications. The uses of earth-abundant and cheaper alternatives, i.e, the first-row transition metals Cu [124] and Fe [114], were reported, however, controlling the catalytic activity or product selectivity seems to be difficult. Furthermore, leaching issue to the reaction media which is generally associated with the use of transition metal is difficult to avoid. For example, leaching of Fe (∼5%) was observed Pd−FeO$_x$/C, causing approximately 30% loss in the SA conversion [114].

The construction of metal species can be influenced by the catalyst support [74, 83]. Also, the support itself can also affect a certain step in the hydrogenation of SA. To restrain these influences by supports, which simplifies the evaluation of the metal roles, inert support, i.e., carbon has generally been used as a support for the hydrogenation of SA. The main disadvantage of this catalyst support lies in the formation of carbon fine during the reaction [4]. As a result, the void spaces in the catalyst can be plugged leading to decreases in the catalytic activity.

1.4 Research Motivation and Objectives

The limitation regarding the uses of noble metals has motivated me to develop efficient earth-abundant metal-based bimetallic catalysts that can catalyze the hydrogenation of SA to either BDO, THF, or GBL with high yield and selectivity. The metals were carefully searched with referring to the findings from previous research on the hydrogenation of dicarboxylic acids, esters, and lactones. For example, Pd/Al_2O_3 showed an excellent catalytic activity to the formation of GBL from SA. While on the other hand, Cu-based bimetallic catalysts were reported as efficient catalysts for the hydrogenation of GBL to BDO with excellent yields [135, 136]. Thus, Cu–Pd bimetallic catalysts are expected to promote the BDO formation from direct hydrogenation of SA.

The catalyst support can also be considered given the previous reports on the hydrogenation reactions. Hydroxyapatite (HAP) has emerged as a suitable support for the hydrogenation of levulinic acid (LA) [137, 138]. For example, Sudhakar et al. reported HAP supported Ru as an efficient catalyst for the LA hydrogenation, producing >99% yield of γ-valerolactone at mild reaction conditions. The supported Pt–Mo bimetallic catalysts were also studied for the LA hydrogenation [138]. The catalyst activity and product selectivity were influenced by not only the metal ratio but also the catalyst support. While the Pt–Mo/HAP exhibited superior catalytic activity toward 1,4-pentanediol (1,4-PeD) with 93% yield, Pt–Mo supported on other materials, i.e., SiO_2, TiO_2, CeO_2, and MgO showed lower 1,4-PeD yield and higher GVL selectivity. Therefore, on the one hand, HAP supported Cu–Pd can be a potential catalyst for the hydrogenation of SA to BDO. On the other hand, in order to tune the product selectivity, the influences of metal ratio and catalyst support are highly desirable to be studied.

The construction of metal species in supported bimetallic catalysts can be governed by not only the metal–metal and metal–suports interactions but also the metal–capping agent conjugation. It provides a useful tool to design nanomaterials with precise size, shape, and surface composition, which are crucial factors controlling the catalytic activity and selectivity [108]. Furthermore, the metal species can be stabilized via electrostatic and/or steric effects with capping agents [108, 139, 140], which might help to prevent metal leaching issues. In addition, selectivity toward a certain product can be tuned in the presence of a capping agent which is presumably due to the inhibition of substrate accessibility to specific sites [141]. Therefore, the effects of capping agents on the construction of metals and their contributions to the catalytic activity and product selectivity are also pursued.

1.5 Thesis Outline

In Chapter 1, a general introduction regarding the current advancement of bio-based SA and its importance for the manufacture of valuable products including fine chemicals, solvent polymers, plastics, etc., is presented. The chapter also provides an outlook on the development in the catalyst design for SA hydrogenation during the last decade. By emphasizing the significant achievements while carefully revising the shortcomings encountered in the previous research, the motivation and objectives for performing the research embodied in this thesis are formulated.

Chapter 2 presents the study on Cu–Pd/HAP catalysts for the highly selective synthesis of BDO by direct hydrogenation of SA. In this chapter, the effect of Cu:Pd ratio which is able to tune the catalytic activity and product selectivity is described. By carefully evaluating the catalytic performance with regard to its properties characterized by extensive techniques, the synergy between Cu and Pd species is revealed.

Chapter 3 shows an intensive study on the effects of several supports on the construction of CuPd NPs. The essential roles of metal–metal and metal-support on the formation CuPd NPs are investigated. In addition, the nature of support in the overall catalytic performance is also examined and presented in this chapter. Accordingly, this chapter shows an effective catalyst for the production of highly selective THF from SA, that is CuPd/γ-Al_2O_3.

To broaden knowledge in the γ-Al_2O_3 supported CuPd catalysts, the influence metal ratio on the catalytic performance is extended in Chapter 4. This chapter aims to provide a comprehensive picture of the CuPd bimetallic catalysts, where competitive effects between the roles of metal species and the supports for the overall catalytic activity and selectivity, are discussed.

In Chapter 5, the influence of capping agent, i.e., poly(*N*-vinyl-2-pyrrolidone) (PVP), on the formation of CuPd NPs is demonstrated. This chapter provides a feasible method to prepare an efficient catalyst, that is the CuPd−PVP/HAP, for the production of highly selective GBL under mild hydrogen pressure.

The achievements represented in the main four chapters are summarized in Chapter 6. Therein, the key findings and significance of this thesis which contribute to the field of catalyst and catalysis are highlighted.

References

(1) Werpy, T.; Petersen, G. *Top Value Added Chemicals from Biomass: Volume I–Results of Screening for Potential Candidates from Sugars and Synthesis Gas*; tech. rep.; National Renewable Energy Lab., Golden, CO (US), 2004.

(2) Chinthapalli, R.; Skoczinski, P.; Carus, M.; Baltus, W.; de Guzman, D.; Käb, H.; Raschka, A.; Ravenstijn, J. Biobased Building Blocks and Polymers—Global Capacities, Production and Trends, 2018–2023. *Ind. Biotechnol. (New Rochelle N Y)* **2019**, *15*, 237–241.

(3) Mazière, A.; Prinsen, P.; García, A.; Luque, R.; Len, C. A Review of Progress in (Bio)Catalytic Routes from/to Renewable Succinic Acid. *Biofuels, Bioprod. Biorefining* **2017**, *11*, 908–931.

(4) Delhomme, C.; Weuster-Botz, D.; Kühn, F. E. Succinic Acid from Renewable Resources as a C_4 Building-Block Chemical–a Review of the Catalytic Possibilities in Aqueous Media. *Green Chem.* **2009**, *11*, 13–26.

(5) Taylor, R.; Nattrass, L.; Alberts, G.; Robson, P.; Chudziak, C.; Bauen, A.; Libelli, I.; Lotti, G.; Prussi, M.; Nistri, R., et al. *From the Sugar Platform to Biofuels and Biochemicals: Final Report for the European Commission Directorate-General Energy*; tech. rep.; E4tech/Re-CORD/Wageningen UR, 2015.

(6) Maleic Anhydride Market-Segmented by Type, End-user Industry, and Geography-Growth, Trends, and Forecast (2018–2023), https://www.mordorintelligence.com/, Accessed: 2020-11-18.

(7) Song, H.; Lee, S. Y. Production of Succinic Acid by Bacterial Fermentation. *Enzyme Microb. Technol.* **2006**, *39*, 352–361.

(8) Wojcieszak, R.; Santarelli, F.; Paul, S.; Dumeignil, F.; Cavani, F.; Gonçalves, R. V. Recent Developments in Maleic Acid Synthesis from Bio-based Chemicals. *Sustain. Chem. Process* **2015**, *3*, 9.

(9) Muzumdar, A. V.; Sawant, S. B.; Pangarkar, V. G. Reduction of maleic acid to succinic acid on titanium cathode. *Org. Process Res. Dev.* **2004**, *8*, 685–688.

(10) Li, J.; Tian, W.-P.; Shi, L. Highly Active and Selective Nickel–Platinum Catalyst for the Low Temperature Hydrogenation of Maleic Anhydride to Succinic Anhydride and Synthesis of Succinic Acid at 40 ℃. *Catal. Lett.* **2011**, *141*, 565–571.

(11) Choudhary, H.; Nishimura, S.; Ebitani, K. Highly Efficient Aqueous Oxidation of Furfural to Succinic Acid Using Reusable Heterogeneous Acid Catalyst with Hydrogen Peroxide. *Chem. Lett.* **2012**, *41*, 409–411.

(12) Choudhary, H.; Nishimura, S.; Ebitani, K. Metal-free Oxidative Synthesis of Succinic Acid from Biomass-derived Furan Compounds using a Solid Acid Catalyst with Hydrogen Peroxide. *Appl. Catal. A Gen.* **2013**, *458*, 55–62.

(13) Cok, B.; Tsiropoulos, I.; Roes, A. L.; Patel, M. K. Succinic Acid Production Derived from Carbohydrates: An Energy and Greenhouse Gas Assessment of a Platform Chemical toward a Bio-based Economy. *Biofuel Bioprod. Biorefin.* **2014**, *8*, 16–29.

(14) Jansen, M. L.; van Gulik, W. M. Towards Large Scale Fermentative Production of Succinic Acid. *Curr. Opin. Biotechnol.* **2014**, *30*, 190–197.

(15) Ahn, J. H.; Jang, Y.-S.; Lee, S. Y. Production of Succinic Acid by Metabolically Engineered Microorganisms. *Curr. Opin. Biotechnol.* **2016**, *42*, 54–66.

(16) Nghiem, N.; Kleff, S.; Schwegmann, S. Succinic Acid: Technology Development and Commercialization. *Fermentation* **2017**, *3*, 26–40.

(17) Saxena, R.; Saran, S.; Isar, J.; Kaushik, R. In *Current Developments in Biotechnology and Bioengineering*; Elsevier: 2017, pp 601–630.

(18) Li, C.; Ong, K. L.; Cui, Z.; Sang, Z.; Li, X.; Patria, R. D.; Qi, Q.; Fickers, P.; Yan, J.; Lin, C. S. K. Promising advancement in fermentative succinic acid production by yeast hosts. *J. Hazard. Mater.* **2020**, *401*, 123414.

(19) Bio-based Succinic Acid Market, `https://www.transparencymarketresearch.com/bio-succinic-acid.html`, Accessed: 2020-11-18.

(20) Pinazo, J. M.; Domine, M. E.; Parvulescu, V.; Petru, F. Sustainability Metrics for Succinic Acid Production: A Comparison between Biomass-based and Petrochemical Routes. *Catalysis Today* **2015**, *239*, 17–24.

(21) Tan, J. P.; Jahim, J. M.; Harun, S.; Wu, T. Y. Overview of the Potential of Bio-Succinic Acid Production from Oil Palm Fronds. *J. Phys. Sci.* **2017**, *28*.

(22) Zeikus, J. Chemical and Fuel Production by Anaerobic Bacteria. *Annu. Rev. Microbiol.* **1980**, *34*, 423–464.

(23) Thakker, C.; Martínez, I.; San, K.-Y.; Bennett, G. N. Succinate Production in Escherichia Coli. *Biotechnol. J.* **2012**, *7*, 213–224.

(24) Cheng, H.-Y.; Yu, R.-C.; Chou, C.-C. Increased Acid Tolerance of Escherichia Coli O157: H7 as Affected by Acid Adaptation Time and Conditions of Acid Challenge. *Food Res. Int.* **2003**, *36*, 49–56.

(25) Beauprez, J. J.; De Mey, M.; Soetaert, W. K. Microbial Succinic Acid Production: Natural versus Metabolic Engineered Producers. *Process Biochem.* **2010**, *45*, 1103–1114.

(26) Dessie, W.; Zhang, W.; Xin, F.; Dong, W.; Zhang, M.; Ma, J.; Jiang, M. Succinic Acid Production from Fruit and Vegetable Wastes Hydrolyzed by On-site Enzyme Mixtures through Solid State Fermentation. *Bioresour. Technol.* **2018**, *247*, 1177–1180.

(27) Joglekar, H.; Rahman, I.; Babu, S.; Kulkarni, B.; Joshi, A. Comparative Assessment of Downstream Processing Options for Lactic Acid. *Sep. Purif. Technol.* **2006**, *52*, 1–17.

(28) Kubo, Y.; Takagi, H.; Nakamori, S. Effect of Gene Disruption of Succinate Dehydrogenase on Succinate Production in a Sake Yeast Strain. *J. Biosci. Bioeng.* **2000**, *90*, 619–624.

(29) Camarasa, C.; Grivet, J.-P.; Dequin, S. Investigation by ^{13}C−NMR and Tricarboxylic Acid (TCA) Deletion Mutant Analysis of Pathways for Succinate Formation in Saccharomyces Cerevisiae during Anaerobic Fermentation. *Microbiol.* **2003**, *149*, 2669–2678.

(30) Raab, A. M.; Gebhardt, G.; Bolotina, N.; Weuster-Botz, D.; Lang, C. Metabolic Engineering of Saccharomyces Cerevisiae for the Biotechnological Production of Succinic Acid. *Metab. Eng.* **2010**, *12*, 518–525.

(31) Agren, R.; Otero, J. M.; Nielsen, J. Genome-scale Modeling Enables Metabolic Engineering of Saccharomyces Cerevisiae for Succinic Acid Production. *J. Ind. Microbiol. Biotechnol.* **2013**, *40*, 735–747.

(32) Otero, J. M.; Cimini, D.; Patil, K. R.; Poulsen, S. G.; Olsson, L.; Nielsen, J. Industrial Systems Biology of Saccharomyces Cerevisiae Enables Novel Succinic Acid Cell Factory. *PloS one* **2013**, *8*, e54144.

(33) Ito, Y.; Hirasawa, T.; Shimizu, H. Metabolic Engineering of Saccharomyces Cerevisiae to Improve Succinic Acid production Based on Metabolic Profiling. *Biosci. Biotechnol. Biochem.* **2014**, *78*, 151–159.

(34) Yan, D.; Wang, C.; Zhou, J.; Liu, Y.; Yang, M.; Xing, J. Construction of Reductive Pathway in Saccharomyces Cerevisiae for Effective Succinic Acid Fermentation at Low pH Value. *Bioresour. Technol.* **2014**, *156*, 232–239.

(35) Franco-Duarte, R.; Bessa, D.; Gonçalves, F.; Martins, R.; Silva-Ferreira, A. C.; Schuller, D.; Sampaio, P.; Pais, C. Genomic and Transcriptomic Analysis of Saccharomyces Cerevisiae Isolates with Focus in Succinic Acid Production. *FEMS Yeast Res.* **2017**, *17*.

(36) Kamzolova, S. V.; Yusupova, A. I.; Vinokurova, N. G.; Fedotcheva, N. I.; Kondrashova, M. N.; Finogenova, T. V.; Morgunov, I. G. Chemically Assisted Microbial Production of Succinic Acid by the Yeast Yarrowia Lipolytica Grown on Ethanol. *Appl. Microbiol. Biotechnol.* **2009**, *83*, 1027–1034.

(37) Yuzbashev, T. V.; Yuzbasheva, E. Y.; Sobolevskaya, T. I.; Laptev, I. A.; Vybornaya, T. V.; Larina, A. S.; Matsui, K.; Fukui, K.; Sineoky, S. P. Production of Succinic Acid at Low pH by a Recombinant Strain of the Aerobic Yeast Yarrowia Lipolytica. *Biotechnol. Bioeng.* **2010**, *107*, 673–682.

(38) Jost, B.; Holz, M.; Aurich, A.; Barth, G.; Bley, T.; Müller, R. A. The Influence of Oxygen Limitation for the Production of Succinic Acid with Recombinant Strains of Yarrowia Lipolytica. *Appl. Microbiol. Biotechnol.* **2015**, *99*, 1675–1686.

(39) Gao, C.; Yang, X.; Wang, H.; Rivero, C. P.; Li, C.; Cui, Z.; Qi, Q.; Lin, C. S. K. Robust Succinic Acid Production from Crude Glycerol using Engineered Yarrowia Lipolytica. *Biotechnol. Biofuels* **2016**, *9*, 1–11.

(40) Yuzbashev, T. V.; Bondarenko, P. Y.; Sobolevskaya, T. I.; Yuzbasheva, E. Y.; Laptev, I. A.; Kachala, V. V.; Fedorov, A. S.; Vybornaya, T. V.; Larina, A. S.; Sineoky, S. P. Metabolic Evolution and ^{13}C Flux Analysis of a Succinate Dehydrogenase Deficient Strain of Yarrowia Lipolytica. *Biotechnol. Bioeng.* **2016**, *113*, 2425–2432.

(41) Cui, Z.; Gao, C.; Li, J.; Hou, J.; Lin, C. S. K.; Qi, Q. Engineering of Unconventional Yeast Yarrowia Lipolytica for Efficient Succinic Acid Production from Glycerol at Low pH. *Metab. Eng.* **2017**, *42*, 126–133.

(42) Yang, X.; Wang, H.; Li, C.; Lin, C. S. K. Restoring of Glucose Metabolism of Engineered Yarrowia Lipolytica for Succinic Acid Production via a Simple and Efficient Adaptive Evolution Strategy. *J. Agric. Food Chem.* **2017**, *65*, 4133–4139.

(43) Li, C.; Gao, S.; Yang, X.; Lin, C. S. K. Green and Sustainable Succinic Acid Production from Crude Glycerol by Engineered Yarrowia Lipolytica via Agricultural Residue based *in situ* Fibrous Bed Bioreactor. *Bioresour. Technol.* **2018**, *249*, 612–619.

(44) Li, C.; Gao, S.; Li, X.; Yang, X.; Lin, C. S. K. Efficient Metabolic Evolution of Engineered Yarrowia Lipolytica for Succinic Acid Production using a Glucose-based Medium in an *in situ* fibrous Bioreactor under Low-pH Condition. *Biotechnol. Biofuels* **2018**, *11*, 236.

(45) Corma, A.; Iborra, S.; Velty, A. Chemical Routes for the Transformation of Biomass into Chemicals. *Chem. Rev.* **2007**, *107*, 2411–2502.

(46) Choi, S.; Song, C. W.; Shin, J. H.; Lee, S. Y. Biorefineries for the Production of Top Building Block Chemicals and Their Derivatives. *Metab. Eng.* **2015**, *28*, 223–239.

(47) Jacquel, N.; Freyermouth, F.; Fenouillot, F.; Rousseau, A.; Pascault, J. P.; Fuertes, P.; Saint-Loup, R. Synthesis and Properties of Poly(Butylene Succinate): Effi-

ciency of Different Transesterification Catalysts. *J. Polym. Sci. A Polym. Chem.* **2011**, *49*, 5301–5312.

(48) Bikiaris, D. N.; Papageorgiou, G. Z.; Papadimitriou, S. A.; Karavas, E.; Avgoustakis, K. Novel Biodegradable Polyester Poly(Propylene Succinate): Synthesis and Application in the Preparation of Solid Dispersions and Nanoparticles of a Water-Soluble Drug. *AAPS PharmSciTech* **2009**, *10*, 138–146.

(49) Bautista, M.; De Ilarduya, A. M.; Alla, A.; Muñoz-Guerra, S. Poly(Butylene Succinate) Ionomers with Enhanced Hydrodegradability. *Polymers* **2015**, *7*, 1232–1247.

(50) Agach, M.; Delbaere, S.; Marinkovic, S.; Estrine, B.; Nardello-Rataj, V. Synthesis, Characterization, Biodegradability and Surfactant Properties of Bio-sourced Lauroyl Poly(Glycerol-Succinate) Oligoesters. *Colloids Surf. A Physicochem. Eng. Asp.* **2013**, *419*, 263–273.

(51) Khongphow, C.; Theerakul, J.; Puttamat, S.; Singkhonrat, J. Characterisation of Poly(Glycerol-Succinate) Oligomers as Bio-based Non-ionic Surfactants by Nuclear Magnetic Resonance and Mass Spectrometry. *Colloids Surf. A Physicochem. Eng. Asp.* **2015**, *468*, 301–308.

(52) Agach, M.; Marinkovic, S.; Estrine, B.; Nardello-Rataj, V. Acyl Poly (Glycerol-Succinic Acid) Oligoesters: Synthesis, Physicochemical and Functional Properties, and Biodegradability. *J. Surfactants Deterg.* **2016**, *19*, 933–941.

(53) Renault, B.; Portella, C.; Marinkovic, S.; Estrine, B. Synthesis and Surface Properties of Succinic Acid End-Capped Alkyl-Polyxylosides. *J. Surfactants Deterg.* **2012**, *15*, 191–198.

(54) Shi, Z.; Zhou, Y.; Yan, D. Facile Fabrication of pH-Responsive and Size-Controllable Polymer Vesicles From a Commercially Available Hyperbranched Polyester. *Macromol. Rapid Commun.* **2008**, *29*, 412–418.

(55) Zhou, Y.; Huang, W.; Liu, J.; Zhu, X.; Yan, D. Self-Assembly of Hyperbranched Polymers and Its Biomedical Applications. *Adv. Mater.* **2010**, *22*, 4567–4590.

(56) Bechthold, I.; Bretz, K.; Kabasci, S.; Kopitzky, R.; Springer, A. Succinic Acid: A New Platform Chemical for Biobased Polymers from Renewable Resources. *Chem. Eng. Technol.* **2008**, *31*, 647–654.

(57) Budroni, G.; Corma, A. Gold and Gold–Platinum as Active and Selective Catalyst for Biomass Conversion: Synthesis of γ-Butyrolactone and One-pot Synthesis of Pyrrolidone. *J. Catal.* **2008**, *257*, 403–408.

(58) Lammens, T. M.; Franssen, M. C.; Scott, E. L.; Sanders, J. P. Synthesis of Biobased *N*-Methylpyrrolidone by One-pot Cyclization and Methylation of γ-Aminobutyric Acid. *Green Chem.* **2010**, *12*, 1430–1436.

(59) Lanzafame, P.; Centi, G.; Perathoner, S. Catalysis for Biomass and CO_2 Use through Solar Energy: Opening New Scenarios for a Sustainable and Low-Carbon Chemical Production. *Chem. Soc. Rev.* **2014**, *43*, 7562–7580.

(60) Pillai, U. R.; Sahle-Demessie, E.; Young, D. Maleic Anhydride Hydrogenation over Pd/Al_2O_3 Catalyst under Supercritical CO_2 Medium. *Appl. Catal. B Environ.* **2003**, *43*, 131–138.

(61) Luque, R.; Clark, J. H.; Yoshida, K.; Gai, P. L. Efficient Aqueous Hydrogenation of Biomass Platform Molecules using Supported Metal Nanoparticles on Starbons®. *Chem. Commun.* **2009**, 5305–5307.

(62) Global Gamma-Butyrolactone Market, 2020–2026, https://www.industryresearch.biz/global-gamma-butyrolactone-butyrolactone-gbl-cas-96-48-0-market-15739305, Accessed: 2020-11-18.

(63) Küksal, A.; Klemm, E.; Emig, G. Reaction Kinetics of the Liquid-phase Hydrogenation of Succinic Anhydride on CuZnO-Catalysts with Varying Copper-to-Zinc Ratios in a Three-phase Slurry Reactor. *Appl. Catal. A Gen.* **2002**, *228*, 237–251.

(64) Müller, S. P.; Kucher, M.; Ohlinger, C.; Kraushaar-Czarnetzki, B. Extrusion of Cu/ZnO Catalysts for the Single-Stage Gas-phase Processing of Dimethyl Maleate to Tetrahydrofuran. *J. Catal.* **2003**, *218*, 419–426.

(65) Rocco, J. A. F. F.; Lima, J. E. S.; Lourenço, V. L.; Batista, N. L.; Botelho, E. C.; Iha, K. Dynamic Mechanical Properties for Polyurethane Elastomers Applied in Elastomeric Mortar. *J. Appl. Polym. Sci.* **2012**, *126*, 1461–1467.

(66) Hong, U. G.; Kim, J. K.; Lee, J.; Lee, J. K.; Song, J. H.; Yi, J.; Song, I. K. Hydrogenation of Succinic Acid to Tetrahydrofuran (THF) over Ruthenium–Carbon Composite (Ru–C) Catalyst. *Appl. Catal. A Gen.* **2014**, *469*, 466–471.

(67) Global Market Study on Tetrahydrofuran (THF): Increasing Demand for PTMEG from Spandex Manufacturing Expected to Drive Revenue Growth, `https://www.persistencemarketresearch.com/market-research/tetrahydrofuran-market.asp`, Accessed: 2020-11-18.

(68) Gallezot, P. Conversion of Biomass to Selected Chemical Products. *Chem. Soc. Rev.* **2012**, *41*, 1538–1558.

(69) Sun, D.; Sato, S.; Ueda, W.; Primo, A.; Garcia, H.; Corma, A. Production of C_4 and C_5 Alcohols from Biomass-Derived Materials. *Green Chem.* **2016**, *18*, 2579–2597.

(70) Wojtczak, M.; Dutkiewicz, S.; Galeski, A.; Piorkowska, E. Structure and Characterization of Random Aliphatic–Aromatic Copolyester. *Eur. Polym. J.* **2014**, *55*, 86–97.

(71) Jacquel, N.; Saint-Loup, R.; Pascault, J.-P.; Rousseau, A.; Fenouillot, F. Bio-based Alternatives in the Synthesis of Aliphatic–Aromatic Polyesters Dedicated to biodegradable Film Applications. *Polymer* **2015**, *59*, 234–242.

(72) Wojtczak, M.; Dutkiewicz, S.; Galeski, A.; Gutowska, A. Classification of Aliphatic-Butylene Terephthalate Copolyesters in Relation to Aliphatic/Aromatic Ratio. *Polymer* **2017**, *113*, 119–134.

(73) 1,4-Butanediol Market Size, Share & Trends Analysis By Application (Tetrahydrofuran (THF), Polybutylene Terephthalate (PBT), Gamma-Butyrolactone (GBL), Polyurethane (PU)), By Region, And Segment Forecasts, 2018–2025, `https://www.grandviewresearch.com/industry-analysis/1-4-butanediol-market`, Accessed: 2020-11-18.

(74) Munnik, P.; De Jongh, P. E.; De Jong, K. P. Recent Developments in the Synthesis of Supported Catalysts. *Chem. Rev.* **2015**, *115*, 6687–6718.

(75) Wang, W.; Wang, S.; Ma, X.; Gong, J. Recent Advances in Catalytic Hydrogenation of Carbon Dioxide. *Chem. Soc. Rev.* **2011**, *40*, 3703–3727.

(76) Wang, D.; Astruc, D. The Golden Age of Transfer Hydrogenation. *Chem. Rev.* **2015**, *115*, 6621–6686.

(77) Meemken, F.; Baiker, A. Recent Progress in Heterogeneous Asymmetric Hydrogenation of C=O and C=C Bonds on Supported Noble Metal Catalysts. *Chem. Rev.* **2017**, *117*, 11522–11569.

(78) Alig, L.; Fritz, M.; Schneider, S. First-Row Transition Metal (De)Hydrogenation Catalysis Based On Functional Pincer Ligands. *Chem. Rev.* **2018**, *119*, 2681–2751.

(79) Mondloch, J. E.; Bayram, E.; Finke, R. G. A Review of the Kinetics and Mechanisms of Formation of Supported-Nanoparticle Heterogeneous Catalysts. *J. Mol. Catal. A Chem.* **2012**, *355*, 1–38.

(80) Védrine, J. C. Heterogeneous Catalysis on Metal Oxides. *Catalysts* **2017**, *7*, 341.

(81) Lear, T.; Marshall, R.; Antonio Lopez-Sanchez, J.; Jackson, S. D.; Klapötke, T. M.; Bäumer, M.; Rupprechter, G.; Freund, H.-J.; Lennon, D. The Application of Infrared Spectroscopy to Probe the Surface Morphology of Alumina-Supported Palladium Catalysts. *J. Chem. Phys.* **2005**, *123*, 174706.

(82) Hamm, G.; Schmidt, T.; Breitbach, J.; Franke, D.; Becker, C.; Wandelt, K. The Adsorption of Ethene on Pd(111) and Ordered Sn/Pd(111) Surface Alloys. *Z. Phys. Chem.* **2009**, *223*, 209–232.

(83) Liu, L.; Corma, A. Metal Catalysts for Heterogeneous Catalysis: From Single Atoms to Nanoclusters and Nanoparticles. *Chem. Rev.* **2018**, *118*, 4981–5079.

(84) Boronat, M.; Leyva-Pérez, A.; Corma, A. Theoretical and Experimental Insights into the Origin of the Catalytic Activity of Subnanometric Gold Clusters: Attempts to Predict Reactivity with Clusters and Nanoparticles of Gold. *Acc. Chem. Res.* **2014**, *47*, 834–844.

(85) Schauermann, S.; Hoffmann, J.; Johánek, V.; Hartmann, J.; Libuda, J.; Freund, H.-J. Catalytic Activity and Poisoning of Specific Sites on Supported Metal Nanoparticles. *Angew. Chem. Int. Ed.* **2002**, *41*, 2532–2535.

(86) Sankar, M.; Dimitratos, N.; Miedziak, P. J.; Wells, P. P.; Kiely, C. J.; Hutchings, G. J. Designing Bimetallic Catalysts for A Green and Sustainable Future. *Chem. Soc. Rev.* **2012**, *41*, 8099–8139.

(87) Yu, W.; Porosoff, M. D.; Chen, J. G. Review of Pt-Based Bimetallic Catalysis: From Model Surfaces to Supported Catalysts. *Chem. Rev.* **2012**, *112*, 5780–5817.

(88) Ruppert, A. M.; Weinberg, K.; Palkovits, R. Hydrogenolysis Goes Bio: From Carbohydrates and Sugar Alcohols to Platform Chemicals. *Angew. Chem. Int. Ed.* **2012**, *51*, 2564–2601.

(89) Zhang, L.; Zhou, M.; Wang, A.; Zhang, T. Selective Hydrogenation over Supported Metal Catalysts: From Nanoparticles to Single Atoms. *Chem. Rev.* **2019**, *120*, 683–733.

(90) Ferrando, R.; Jellinek, J.; Johnston, R. L. Nanoalloys: From Theory to Applications of Alloy Clusters and Nanoparticles. *Chem. Rev.* **2008**, *108*, 845–910.

(91) Wu, J.; Li, P.; Pan, Y.-T. F.; Warren, S.; Yin, X.; Yang, H. Surface Lattice-Engineered Bimetallic Nanoparticles and Their Catalytic Properties. *Chem. Soc. Rev.* **2012**, *41*, 8066–8074.

(92) Tauster, S.; Fung, S.; Garten, R. L. Strong Metal–Support Interactions. Group 8 Noble Metals Supported on Titanium Dioxide. *J. Am. Chem. Soc.* **1978**, *100*, 170–175.

(93) Tauster, S.; Fung, S. Strong Metal-Support Interactions: Occurrence among the Binary Oxides of Groups IIA–VB. *J. Catal.* **1978**, *55*, 29–35.

(94) Van Deelen, T. W.; Mejía, C. H.; de Jong, K. P. Control of Metal–Support Interactions in Heterogeneous Catalysts to Enhance Activity and Selectivity. *Nat. Catal.* **2019**, 1–16.

(95) Pacchioni, G.; Freund, H.-J. Controlling the Charge State of Supported Nanoparticles in Catalysis: Lessons from Model Systems. *Chem. Soc. Rev.* **2018**, *47*, 8474–8502.

(96) Pacchioni, G. Electronic Interactions and Charge Transfers of Metal Atoms and Clusters on Oxide Surfaces. *Phys. Chem. Chem. Phys.* **2013**, *15*, 1737–1757.

(97) Ruiz Puigdollers, A.; Schlexer, P.; Tosoni, S.; Pacchioni, G. Increasing Oxide Reducibility: The Role of Metal/Oxide Interfaces in the Formation of Oxygen Vacancies. *ACS Catal.* **2017**, *7*, 6493–6513.

(98) Farnesi Camellone, M.; Negreiros Ribeiro, F.; Szabová, L.; Tateyama, Y.; Fabris, S. Catalytic Proton Dynamics at the Water/Solid Interface of Ceria-Supported Pt Clusters. *J. Am. Chem. Soc.* **2016**, *138*, 11560–11567.

(99) Karim, W.; Spreafico, C.; Kleibert, A.; Gobrecht, J.; VandeVondele, J.; Ekinci, Y.; van Bokhoven, J. A. Catalyst Support Effects on Hydrogen Spillover. *Nature* **2017**, *541*, 68–71.

(100) Roldan Cuenya, B. Metal Nanoparticle Catalysts Beginning to Shape-up. *Acc. Chem. Res.* **2013**, *46*, 1682–1691.

(101) Karim, A. M.; Prasad, V.; Mpourmpakis, G.; Lonergan, W. W.; Frenkel, A. I.; Chen, J. G.; Vlachos, D. G. Correlating Particle Size and Shape of Supported

Ru/γ-Al_2O_3 Catalysts with NH_3 Decomposition Activity. *J. Am. Chem. Soc.* **2009**, *131*, 12230–12239.

(102) Ahmadi, M.; Behafarid, F.; Cuenya, B. R. Size-Dependent Adhesion Energy of Shape-Selected Pd and Pt Nanoparticles. *Nanoscale* **2016**, *8*, 11635–11641.

(103) Zafeiratos, S.; Piccinin, S.; Teschner, D. Alloys in catalysis: phase separation and surface segregation phenomena in response to the reactive environment. *Catal. Sci. Technol.* **2012**, *2*, 1787–1801.

(104) Tauster, S.; Fung, S.; Baker, R.; Horsley, J. Strong Interactions in Supported–Metal Catalysts. *Science* **1981**, *211*, 1121–1125.

(105) Chen, M.; Goodman, D. Interaction of Au with Titania: The Role of Reduced Ti. *Top Catal.* **2007**, *44*, 41–47.

(106) Semagina, N.; Kiwi-Minsker, L. Recent Advances in the Liquid-Phase Synthesis of Metal Nanostructures with Controlled Shape and Size for Catalysis. *Catal. Rev.* **2009**, *51*, 147–217.

(107) Thanh, N. T.; Maclean, N.; Mahiddine, S. Mechanisms of nucleation and growth of nanoparticles in solution. *Chem. Rev.* **2014**, *114*, 7610–7630.

(108) Rossi, L. M.; Fiorio, J. L.; Garcia, M. A.; Ferraz, C. P. The Role and Fate of Capping Ligands in Colloidally Prepared Metal Nanoparticle Catalysts. *Dalton Trans.* **2018**, *47*, 5889–5915.

(109) Ott, L. S.; Finke, R. G. Transition-Metal Nanocluster Stabilization for Catalysis: A Critical Review of Ranking Methods and Putative Stabilizers. *Coord. Chem. Rev.* **2007**, *251*, 1075–1100.

(110) Collins, G.; Davitt, F.; O'Dwyer, C.; Holmes, J. D. Comparing Thermal and Chemical Removal of Nanoparticle Stabilizing Ligands: Effect on Catalytic Activity and Stability. *ACS Appl. Nano Mater.* **2018**, *1*, 7129–7138.

(111) Frey, G. D.; Lavallo, V.; Donnadieu, B.; Schoeller, W. W.; Bertrand, G. Facile Splitting of Hydrogen and Ammonia by Nucleophilic Activation at a Single Carbon Center. *Science* **2007**, *316*, 439–441.

(112) Mitsudome, T.; Mikami, Y.; Matoba, M.; Mizugaki, T.; Jitsukawa, K.; Kaneda, K. Design of a Silver–Cerium Dioxide Core–Shell Nanocomposite Catalyst for Chemoselective Reduction Reactions. *Angew. Chem. Int. Ed.* **2012**, *51*, 136–139.

(113) Deshpande, R.; Buwa, V.; Rode, C.; Chaudhari, R.; Mills, P. Tailoring of Activity and Selectivity Using Bimetallic Catalyst in Hydrogenation of Succinic Acid. *Catal. Commun.* **2002**, *3*, 269–274.

(114) Liu, X.; Wang, X.; Xu, G.; Liu, Q.; Mu, X.; Liu, H. Tuning the Catalytic Selectivity in Biomass-Derived Succinic Acid Hydrogenation on FeO_x-Modified Pd Catalysts. *J. Mater. Chem. A* **2015**, *3*, 23560–23569.

(115) Pritchard, J.; Filonenko, G. A.; Van Putten, R.; Hensen, E. J.; Pidko, E. A. Heterogeneous and Homogeneous Catalysis for the Hydrogenation of Carboxylic Acid Derivatives: History, Advances and Future Directions. *Chem. Soc. Rev.* **2015**, *44*, 3808–3833.

(116) Bio-succinic Acid Market Size, Share & Trends Analysis Report By Application (BDO, Polyester Polyols, PBS/PBST, Plasticizers, Alkyd Resins), By Region (North America, Europe, APAC), And Segment Forecast, 2014–2020, `https://www.grandviewresearch.com/industry-analysis/bio-succinic-acid-market`, Accessed: 2020-11-19.

(117) Clayden, J.; Geeves, N.; Warren, S., *Organic Chemistry*, 2nd ed.; Oxford University Press: 2012, p 1264.

(118) Yakabi, K.; Jones, A.; Buchard, A.; Roldan, A.; Hammond, C. Chemoselective Lactonization of Renewable Succinic Acid with Heterogeneous Nanoparticle Catalysts. *ACS Sustain. Chem. Eng.* **2018**, *6*, 16341–16351.

(119) Di, X.; Shao, Z.; Li, C.; Li, W.; Liang, C. Hydrogenation of Succinic Acid over Supported Rhenium Catalysts Prepared by the Microwave-Assisted Thermolytic Method. *Catal. Sci. Technol.* **2015**, *5*, 2441–2448.

(120) Hong, U. G.; Park, H. W.; Lee, J.; Hwang, S.; Yi, J.; Song, I. K. Hydrogenation of Succinic Acid to Tetrahydrofuran (THF) over Rhenium Catalyst Supported on H_2SO_4-Treated Mesoporous Carbon. *Appl. Catal. A Gen.* **2012**, *415*, 141–148.

(121) Chung, S.-H.; Park, Y.-M.; Kim, M.-S.; Lee, K.-Y. The Effect of Textural Properties on the Hydrogenation of Succinic acid Using Palladium Incorporated Mesoporous Supports. *Catal. Today* **2012**, *185*, 205–210.

(122) Astruc, D. Introduction: Nanoparticles in Catalysis. *Chem. Rev.* **2020**, *120*, 461–463.

(123) Keels, J. M.; Chen, X.; Karakalos, S.; Liang, C.; Monnier, J. R.; Regalbuto, J. R. Aqueous-Phase Hydrogenation of Succinic Acid Using Bimetallic Ir–Re/C Catalysts Prepared by Strong Electrostatic Adsorption. *ACS Catal.* **2018**, *8*, 6486–6494.

(124) Patankar, S. C.; Sharma, A. G.; Yadav, G. D. Biobased Process Intensification in Selective Synthesis of γ-Butyrolactone from Succinic Acid via Synergistic Palladium–Copper Bimetallic Catalyst Supported on Alumina Xerogel. *Clean Technol. Environ. Policy* **2018**, *20*, 683–693.

(125) Di, X.; Li, C.; Zhang, B.; Qi, J.; Li, W.; Su, D.; Liang, C. Role of Re and Ru in Re-Ru/C Bimetallic Catalysts for the Aqueous Hydrogenation of Succinic Acid. *Ind. Eng. Chem. Res.* **2017**, *56*, 4672–4683.

(126) Vardon, D. R.; Settle, A. E.; Vorotnikov, V.; Menart, M. J.; Eaton, T. R.; Unocic, K. A.; Steirer, K. X.; Wood, K. N.; Cleveland, N. S.; Moyer, K. E.; Michener, W. E.; Beckham, G. T. Ru–Sn/AC for the Aqueous-Phase Reduction of Succinic Acid to 1,4-Butanediol under Continuous Process Conditions. *ACS Catal.* **2017**, *7*, 6207–6219.

(127) Kang, K. H.; Han, S. J.; Lee, J. W.; Kim, T. H.; Song, I. K. Effect of Boron Content on 1,4-Butanediol Production by Hydrogenation of Succinic Acid over Re–Ru/BMC (Boron-Modified Mesoporous Carbon) Catalysts. *Appl. Catal. A Gen.* **2016**, *524*, 206–213.

(128) Takeda, Y.; Tamura, M.; Nakagawa, Y.; Okumura, K.; Tomishige, K. Hydrogenation of Dicarboxylic Acids to Diols over Re–Pd Catalysts. *Catal. Sci. Technol.* **2016**, *6*, 5668–5683.

(129) Kang, K. H.; Hong, U. G.; Bang, Y.; Choi, J. H.; Kim, J. K.; Lee, J. K.; Han, S. J.; Song, I. K. Hydrogenation of Succinic Acid to 1,4-Butanediol over Re–Ru Bimetallic Catalysts Supported on Mesoporous Carbon. *Appl. Catal. A Gen.* **2015**, *490*, 153–162.

(130) Shao, Z.; Li, C.; Di, X.; Xiao, Z.; Liang, C. Aqueous-Phase Hydrogenation of Succinic Acid to γ-Butyrolactone and Tetrahydrofuran over Pd/C, Re/C, and Pd–Re/C Catalysts. *Ind. Eng. Chem. Res.* **2014**, *53*, 9638–9645.

(131) Ly, B. K.; Minh, D. P.; Pinel, C.; Besson, M.; Tapin, B.; Epron, F.; Especel, C. Effect of Addition Mode of Re in Bimetallic Pd−Re/TiO_2 Catalysts Upon the Selective Aqueous-Phase Hydrogenation of Succinic Acid to 1,4-Butanediol. *Top Catal.* **2012**, *55*, 466–473.

(132) Minh, D. P.; Besson, M.; Pinel, C.; Fuertes, P.; Petitjean, C. Aqueous-Phase Hydrogenation of Biomass-Based Succinic Acid to 1,4-Butanediol over Supported Bimetallic Catalysts. *Top Catal.* **2010**, *53*, 1270–1273.

(133) Heisig, C.; Diedenhoven, J.; Jensen, C.; Gehrke, H.; Turek, T. Selective Hydrogenation of Biomass-Derived Succinic Acid: Reaction Network and Kinetics. *Chem. Eng. Technol.* **2020**, *43*, 484–492.

(134) Bamford, C. H.; Tipper, C. F. H., *The Theory of Kinetics*; Elsevier: 1969; Vol. 2.

(135) Huang, Z.; Barnett, K. J.; Chada, J. P.; Brentzel, Z. J.; Xu, Z.; Dumesic, J. A.; Huber, G. W. Hydrogenation of γ-Butyrolactone to 1,4-Butanediol over CuCo/TiO_2 Bimetallic Catalysts. *ACS Catal.* **2017**, *7*, 8429–8440.

(136) Wu, J.; Gao, G.; Sun, P.; Long, X.; Li, F. Synergetic Catalysis of Bimetallic CuCo Nanocomposites for Selective Hydrogenation of Bioderived Esters. *ACS Catal.* **2017**, *7*, 7890–7901.

(137) Sudhakar, M.; Kantam, M. L.; Jaya, V. S.; Kishore, R.; Ramanujachary, K.; Venugopal, A. Hydroxyapatite as a Novel Support for Ru in the Hydrogenation of Levulinic Acid to γ-Valerolactone. *Catal. Commun.* **2014**, *50*, 101–104.

(138) Mizugaki, T.; Nagatsu, Y.; Togo, K.; Maeno, Z.; Mitsudome, T.; Jitsukawa, K.; Kaneda, K. Selective Hydrogenation of Levulinic Acid to 1,4-Pentanediol in Water using a Hydroxyapatite-Supported Pt–Mo Bimetallic Catalyst. *Green Chem.* **2015**, *17*, 5136–5139.

(139) Manojkumar, K.; Sivaramakrishna, A.; Vijayakrishna, K. A Short Review on Stable Metal Nanoparticles using Ionic Liquids, Supported Ionic Liquids, and Poly(Ionic Liquids). *J. Nanoparticle Res.* **2016**, *18*, 103.

(140) Heuer-Jungemann, A.; Feliu, N.; Bakaimi, I.; Hamaly, M.; Alkilany, A.; Chakraborty, I.; Masood, A.; Casula, M. F.; Kostopoulou, A.; Oh, E., et al. The Role of Ligands in the Chemical Synthesis and Applications of Inorganic Nanoparticles. *Chem. Rev.* **2019**, *119*, 4819–4880.

(141) Liu, P.; Qin, R.; Fu, G.; Zheng, N. Surface Coordination Chemistry of Metal Nanomaterials. *J. Am. Chem. Soc.* **2017**, *139*, 2122–2131.

Chapter 2

Highly Selective Synthesis of 1,4-Butanediol via Hydrogenation of Succinic Acid with Supported Cu–Pd Alloy Nanoparticles

Abstract

Hydroxyapatite (HAP)-supported Cu–Pd catalysts, denoted as Cu–Pd/HAP, have been discovered to be the efficient catalysts for hydrogenation of bio-derived succinic acid (SA) in which the products are selectively tunable by adjusting the mixing ratio of Cu and Pd. Optimal performance toward 1,4-butanediol (BDO) is observed with the Cu–Pd/HAP prepared with 8 wt%-Cu and 2 wt%-Pd, affording the selectivity of 82% at quantitative conversion. In contrast, the monometallic Cu and Pd catalysts are unable to produce BDO as the major product, but only the γ-butyrolactone (GBL) with a low yield of 16% and butyric acid (BA) with a considerable yield of 78%, respectively, are formed. The formation of well-dispersed bimetallic alloy nanoparticles (NPs) is revealed by a transmission electron microscopy with energy-dispersive spectroscopy, H_2-temperature programed reduction, X-ray diffraction, and X-ray absorption spectroscopy studies. It

is found that the fine alloying structure with high Cu contents is significant in favoring the formation of BDO via the ring-opening step of GBL rather than the hydrogenation of GBL to the non-target product of BA. In addition, the CuPd alloy catalyst exhibits a good recycling ability in four consecutive runs without significant loss in its activity.

2.1 Introduction

Until the end of the 18th century, the world's economy had been primarily agricultural. However, since the arrival of the industrial revolution, fossil fuels including coal, petroleum, and natural gas were established as the main resources [1]. Over centuries of industrial exploitation with fast and heavy consumption, these non-renewable raw materials have become severely depleted. In addition, the massive increase in demand associated with the unequal distribution of these resources not only causes several adverse effects on the economy but also raises the possibility of geopolitical disputes [2, 3]. Furthermore, the consumption of fossil fuels is often linked to the increase of greenhouse gas emission, in particular, carbon dioxide, attributing to global warming and climate change. The raised issues make the development of alternative feedstock imperative. Among various renewable resources, biomass has emerged as a promising candidate, offering a great opportunity to improve the overall economic and sustainable chemistry [4–7].

Generally, key building-block chemicals can be produced via biological or chemical conversions from biomass materials, which subsequently are converted to a number of high valued bio-based chemicals. Succinic acid (SA) has been identified as one of twelve platform chemicals by the U.S. Department of Energy since 2004 [8]. Conventionally, SA was mostly manufactured by catalytic hydrogenation of maleic anhydride, which is a fossil-based chemical. However, the production of petroleum-based SA posed problems of carbon footprint emissions and price volatility, which subsequently lead to the development of bio-based SA. Recent breakthroughs in bio-fermentation technology make SA more abundant and competitive supply [9–12]. However, while there has been an increase of interest in various renewable chemicals such as glucose [5, 13], fructose [14, 15], and levulinic acid (LA) [16, 17], only scant attention has been paid for the catalytic conversion of SA despite that a large number of value-added products can be converted from it; i.e.., γ-butyrolactone (GBL), 1,4-butanediol (BDO), tetrahydrofuran (THF), N-methyl-2-pyrrolidone (NMP), and several other derivatives [18, 19]. Among these potential products, the conversion of bio-derived SA to BDO has been recognized as one of the most important industrial processes. Particularly, BDO can be utilized as a starting material for various commodity compounds and combined with SA to prepare polybutylene succinate (PBS) and poly(butylene succinate-*co*-butylene terephthalate), which are known as biodegradable plastics [20].

The hydrogenation of SA is typically carried out at high pressure of hydrogen using metallic catalysts on various inert supports [1]. The catalyst can be either monometallic or bimetallic catalysts, which are mainly noble metals. For example, various Starbons® supported metal nanoparticles including Pt, Pd, and Rh were reported as efficient catalysts for hydrogenation of SA with moderate to good conversion and high selectivity toward BDO [21]. Supported Ru [21] and Re [22] catalysts were also employed, however, GBL and THF were produced as main products. In fact, the uses of bimetallic catalysts are more favorable because the additional metal could minimize the use of precious metals and/or influence the selectivity towards certain products by altering the effect of the first metal for a certain purpose [1]. Di et al. reported that the strong intermetallic interactions in Re–Ru/C bimetallic catalysts were contributed to the high selectivity of BDO, while THF, GBL, and propionic acid were formed as the main products over monometallic Re/C and Ru/C [23]. The nature of metals is an important factor but the catalyst support, preparation method, and reaction parameters are also considered to be of great importance. For example, Takeda et al. reported that the structure of Re-based catalysts is significantly influenced by the reduction method [24]. Particularly, high BDO yield was achieved using the *ex-situ* liquid-phase reduced catalyst, while the *in-situ* liquid-phase reduced catalyst showed low activity.

To reduce the heavy dependence on noble metals for the direct hydrogenation of SA, it is highly desirable to develop efficient earth-abundant heterogeneous catalyst systems.

In this chapter, supported Cu-based bimetallic catalysts are studied for the direct hydrogenation of SA to BDO. The Cu-based bimetallic catalyst would be a promising system since it is reported as one of the effective catalysts for hydrogenation of molecules containing C=O double bonds [25–27]. Recently, it is reported as a potential catalyst for the hydrogenation of GBL to BDO with excellent yield [28–30]. However, to the best of our knowledge, the direct hydrogenation of SA to BDO with a great selectivity has not been conducted over Cu-based bimetallic catalysts with high Cu contents.

Hydroxyapatite (HAP), which is a calcium orthophosphate with an apatite structure [31], has attracted great attention because it offers a wide range of applications. As the main mineral constituent of human bones and teeth, it is generally applied in orthopedic and dentistry as biocompatibility materials [32]. In catalysis field, HAP is known as a nonporous catalyst support with the coexistence of weak acidic and basic sites, which help to avoid mass transfer limitations and prevent side reactions [31].Furthermore, owning a high specific area and superior ion exchangeability make HAP a promising support by immobilizing metals on the surface or incorporating them into the apatite framework [33, 34]. Utilizing these properties, HAP-supported metal nanoparticles were reported as efficient catalysts for various hydrogenation reactions. For example, HAP-supported monometallic catalysts, i.e., Ru, Pt, Pd, Ni were investigated for hydrogenation of LA with good to excellent yields of γ-valerolactone [35]. Taking advantage of concerted effects between multimetallic species, HAP-supported Pt–Mo bimetallic nanoparticles can accelerate LA to 1,4-pentanediol with excellent yield [36]. Inspiration derived from these research, HAP-supported Cu-based bimetallic catalysts with high Cu contents are studied for the direct hydrogenation of SA to BDO.

2.2 Experimental Section

2.2.1 Materials

All the chemicals and their details are listed in Table 2.1 below:

Table 2.1: List of chemicals used in this research

No.	Name	Formula	Supplier
1	1,4-butanediol (BDO)	$C_4H_{10}O_2$	Wako
2	1,4-dioxane	$C_4H_8O_2$	Wako
3	1-butanol (BuOH)	C_4H_9OH	Wako
4	2-propanol	C_3H_8O	Wako
5	Aluminum nitrate nonahydrate	$Al(NO_3)_3 \cdot 9\,H_2O$	Wako
6	Butyric acid (BA)	$C_4H_8O_2$	Sigma Aldrich
7	Cerium (III) nitrate hexahydrate	$Ce(NO_3)_3 \cdot 6\,H_2O$	Wako
8	Cobalt (II) nitrate hexahydrate	$Co(NO_3)_2 \cdot 6\,H_2O$	Wako
9	Copper (II) nitrate trihydrate	$Cu(NO_3)_2 \cdot 3\,H_2O$	Wako
10	Copper oxide	CuO	STREM
11	Ethanol	C_2H_5OH	Kanto
12	Hydroxyapatite (HAP)	$Ca_{10}(PO_4)_6(OH)_2$	Kanto
13	Nickel (II) nitrate hexahydrate	$Ni(NO_3)_2 \cdot 6\,H_2O$	Wako
14	Norit® "SX Plus"	C	Wako
15	Palladium (II) nitrate	$Pd(NO_3)_2$	Wako
16	Ruthenium (III) chloride hydrate	$RuCl_3 \cdot x\,H_2O$	Wako
17	Silicon dioxide, G-6, 3µm	SiO_2	Fuji Silysia
18	Succinic acid (SA)	$C_4H_6O_4$	Kanto
19	Tetrahydrofuran (THF)	C_4H_8O	Wako
20	Titanium dioxide (rutile form)	TiO_2	Kanto
21	Zinc nitrate hexahydrate	$Zn(NO_3)_2 \cdot 6\,H_2O$	Wako
22	α-alumina	α-Al_2O_3	Kanto
23	γ-butyrolactone (GBL)	$C_4H_6O_2$	Wako

2.2.2 Catalyst Preparation

The Cu–M/HAP catalysts were prepared by the co-impregnation method with modifications based on the previous papers [36, 37]. In a typical procedure, $Cu(NO_3)_2 \cdot 3\,H_2O$ and a secondary metal precursor, e.g. $Pd(NO_3)_2$, were added simultaneously into a round-bottom flask with 150 mL distilled water. Subsequently, HAP was gradually added to the solution and the mixture was stirred at room temperature for 12 h. The solid was obtained after removing water by a rotary evaporator. The obtained powder was further dried in an oven at 110 ℃ for 12 h and calcined in a furnace at 500 ℃ for 4 h. Finally, the calcined sample was reduced in a flow of 5% H_2/N_2 at the flow rate of 60 mL min^{-1} at 500 ℃ for 2 h.

2.2.3 Catalyst Characterization

The crystal structure was obtained by the powder X-ray diffraction (XRD) method using a Rigaku Smart Lab X-ray diffractometer (Rigaku Co.) with a Cu Kα radiation (λ= 0.154 nm) at 40 kV and 30 mA. The diffraction patterns were analyzed using the database of the Joint Committee of Powder Diffraction Standard. The morphology was acquired by the transmission electron microscopy (TEM) using an H-7100 TEM (Hitachi) operated at 100 kV. Images from the high-angle annular dark-field scanning transmission electron microscopy (HAADF-STEM) with the energy dispersive X-ray spectroscopy (EDS) were recorded by using a JEM-ARM200F (JEOL USA, Inc.) operated at 200 kV. The temperature programmed reduction (TPR) experiments were carried out on a BELCat II (MicrotracBEL, Corp.) to investigate the Pd–Cu interaction of the bimetallic catalysts. The gaseous mixture of 10% H_2/Ar was introduced to the sample at the flow rate of 30 mL min^{-1}, while the temperature was increased from 50 ℃ to 750 ℃ at a ramping rate of 10 ℃ min^{-1}. The H_2 quantification was performed on the basis of H_2 consumption of CuO (99.999%) as an TPR standard.

The electronic state of Cu–Pd on HAP was analyzed by X-ray photoelectron spectroscopy (XPS) using an Axis-Ultra DLD spectrometer system (Shimadzu Co. and Kratos Analytical Ltd.) with the monochromatic Al Kα (1486 eV) X-ray resources. The binding energies (BE) were calibrated using the C 1*s* spectrum of adventitious carbon contamination as an internal standard. Actual compositions of Cu and Pd in fresh and used catalysts were determined by atomic absorption spectroscopy (AAS) using a ZA3700 Polarized Zeeman Atomic Absorption Spectrophotometer (Hitachi, Ltd.). For the quantification, the absorption wavelengths of 324.8 nm and 247 nm are respectively monitored for Cu and Pd elements. N_2-adsorption/desorption experiments were conducted on BELSORP-mini analyzer (MicrotracBEL Corp.). Surface areas of samples were calculated based on the Brunauer-Emmett-Teller (BET) theory.

The X-ray absorption spectroscopy (XAS) experiments were conducted at the BL07 (Pd K-edge) and BL15 (Cu K-edge) stations at SAGA light source under the proposal nos.

11901136T and 1901135R, respectively. The storage ring was operated at 1.4 GeV and Si (220) and Si (111) single crystals were employed to obtain a monochromatic X-ray beam for Pd K-edge and Cu K-edge measurements, respectively. All the samples were ground finely and pressed to pellets with a diameter of 10 mm. Analyses of X-ray absorption near edge spectra (XANES) and extended X-ray absorption fine structure (EXAFS) were performed by using Athena and Artemis software (Demeter package ver. 0.9.26).

2.2.4 Catalyst Evaluation

Hydrogenation of SA was performed in a stainless-steel autoclave reactor (Taiatsu Technol., Japan) with an internal glass vessel (50 mL vol.). In a typical experiment, 10 mL of 1,4-dioxane solvent including SA (0.1 g) and the as-prepared catalyst (0.1 g) were loaded into the vessel along with a magnetic stirrer bar. The reactor was then sealed and purged with pure H_2 (99.999%) three times before being pressurized to 8.0 MPa at room temperature. After that, the reactor was placed into an aluminum block bath heated at 200 ℃ and then kept for 96 h under vigorous stirring (780 rpm). After an appropriate period of reaction, the reactor was cooled to the room temperature and centrifugated. Subsequently, the obtained products were analyzed using gas chromatography (Shimadzu GC-2014) with a polar DB-FFAP column (Agilent). The GC column temperature was increased from 50 ℃ (2 min) to 240 ℃ (5 min) at a rate of 20 ℃ min^{-1}. The injection and detector temperatures were 250 ℃ and 280 ℃, respectively. The conversion of SA was analyzed by using a high-performance liquid chromatography (HPLC, Water 2414) equipped with a refractive index detector (RID). An Aminex HPX-87H column (Bio-Rad) was used for the separation at 50 ℃. The aqueous solution of 10 mM H_2SO_4 was employed as the eluent at a flow rate of 0.5 mL min^{-1}.

2.3 Results and Discussion

2.3.1 Catalyst Evaluation and Reaction Pathways and Optimization

In an attempt to find out a potential catalytic system for SA hydrogenation, various catalysts were examined in 1,4-dioxane solvent (Table 2.2). Among the tested Cu-based bimetallic catalysts, the Cu_xPd_y/HAP ($x = y = 5$ wt%) emerged as a promising catalyst for the formation of BDO, while the other catalysts produced GBL as the main product. Particularly, a 23% yield of BDO was achieved over the present catalyst.

Table 2.2: Screening Cu_5M_5/HAP for SA hydrogenation[a]

Catalyst	GBL	BDO	THF	BuOH	BA	SA conv.
Cu_5Ru_5/HAP	5	0	0	0	0	5
Cu_5Ce_5/HAP	6	0	0	0	0	8
Cu_5Zn_5/HAP	14	0	0	0	0	31
Cu_5Pd_5/HAP	25	23	4	2	35	100
Cu_5Al_5/HAP	26	0	0	0	0	61
Cu_5Ni_5/HAP	34	0	0	0	0	48
Cu_5Co_5/HAP	63	4	0	0	0	96

[a] Reaction conditions: SA (0.1 g), catalyst (0.1 g), 1,4-dioxane (10 mL), temperature (200 ℃), H_2 pressure (8 MPa), reaction time (96 h).

Subsequently, the effect of Cu/Pd ratios in the Cu_xPd_y/HAP catalysts was further examined while the total metal loading ($x + y$) was fixed at 10 wt%. As shown in Figure 2.1A, it is observed that the monometallic Pd_{10}/HAP and Cu_{10}/HAP catalysts were unable to produce BDO. A low conversion of SA (16%) to GBL with an absolute selectivity was obtained over the Cu_{10}/HAP catalyst, whereas a full conversion of SA to butyric acid (BA) as the major product with a 78% yield and GBL as minor product with a 11% yield were observed with the Pd_{10}/HAP catalyst. Interestingly, as the increases in the Cu contents in the Cu_xPd_y/HAP catalysts, the yields of BA were gradually reduced while BDO were increased to be the major product along with various by-products such as THF and 1-butanol (BuOH). As a result, the maximum yield of BDO at 82% was achieved over the Cu_8Pd_2/HAP catalyst with a complete conversion of SA. It is noteworthy that the

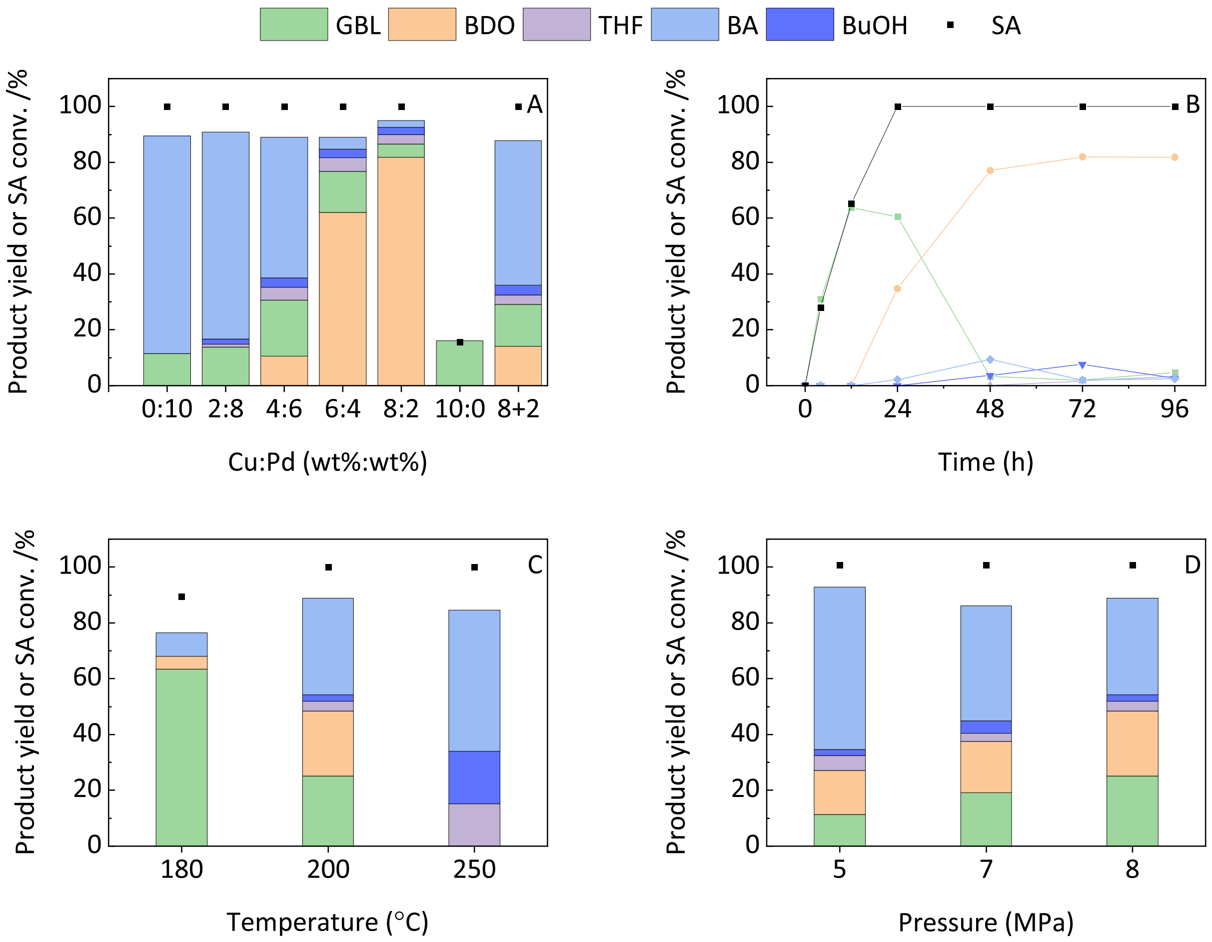

Figure 2.1: (A) Hydrogenation of SA over Cu_xPd_y/HAP catalysts ($x + y = 10$ wt%), (B) time-based reaction progression over the Cu_8Pd_2/HAP, (C–D) effects of temperature H_2 pressure on the catalytic acitivty of Cu_5Pd_5/HAP. Reaction conditions: SA (0.1 g), catalyst (0.1 g), 1,4-dioxane (10 mL), temperature (200 ℃), H_2 pressure (8 MPa), reaction time (96 h).

physical mixture of theCu_8/HAP and Pd_2/HAP monometallic catalysts was unable to produce BDO with such a high selectivity: only 14% selectivity of BDO was provided at the same reaction conditions. Accordingly, close interactions between Cu and Pd atoms: e.g. alloying, would be a crucial factor enhancing the catalytic activity for the highly selective hydrogenation of SA to BDO. To figure out the underlying reason, simple experiments were carried out using monometallic catalysts (Table 2.3). When the GBL was chosen as the starting material, the Pd_2/HAP catalyst was favorable for the formation of BA as the main product with 88% in selectivity, while the Cu_8/HAP catalyst was able to catalyze the reaction toward BDO with ca. 91% in selectivity. Considering the hydrogenation of SA that the Cu_{10}/HAP catalyst was unable to further hydrogenate

Table 2.3: Hydrogenation of GBL using HAP supported monometallic catalysts[a]

Entry	Catalyst	Conv. /%	Selectivity /%			
			BDO	THF	BuOH	BA
1	Pd_2/HAP	100	0	0	<1	88
2	Cu_8/HAP	97	91	3	<1	0

[a] Reaction conditions: GBL (0.1 g), catalyst (0.1 g), 1,4-dioxane (10 mL), temperature (200 °C), H_2 pressure (8 MPa), reaction time (96 h).

GBL to BDO (Figure 2.1A), it is believed that there was an inhibition effect of SA to the ring-opening step of GBL over the Cu active centers. In fact, the hydrogenation of GBL over the Cu_8/HAP catalyst in the presence of different concentrations of SA served crucial results (Table 2.4). The results show that the Cu_8/HAP itself possesses the catalytic ability for the transformation of GBL to BDO; however, such ring-opening step from GBL to BDO is inhibited when the concentration of SA is significant to GBL. From these pieces of evidence, it is highly expected that in the physical mixture of the two monometallic catalysts, the Pd_2/HAP plays a role in decreasing the concentration of SA via the transformation into GBL, whereas the Cu_8/HAP promotes the step of ring-opening GBL to BDO. As an overall result, the production of BDO could be detected with 14% yield from SA as the substrate (Figure 2.1A).

Table 2.4: Hydrogenation of GBL in the presence of SA over the Cu_8/HAP catalyst[a]

Entry	Starting materials			Products	
	SA /mmol	GBL /mmol	GBL:SA ratio /wt%	BDO /mmol	GBL /mmol
1	0.0	1.2	100:0	1.0	0.0
2	0.2	0.9	80:20	1.0	0.0
3	0.4	0.6	50:50	0.1	0.8

[a] Reaction conditions: substrates (0.1 g), catalyst (0.1 g), 1,4-dioxane (10 mL), temperature (200 °C), H_2 pressure (8 MPa), reaction time (96 h).

To draw a comprehensive reaction pathway in this catalytic system, the time-based reaction was implemented and the results are plotted in Figure 2.1B. In accordance with previous reports [38, 39], the present research shows that in the first step of SA hydrogenation, GBL was formed as the intermediate which was successively converted to BDO

Table 2.5: Cu_8Pd_2/HAP catalyzed reactions with different substrates[a]

Entry	Substrate	Conv. /%	BDO /%	GBL /%	THF /%	BuOH /%	BA /%
1	GBL	88, 98[b]	80, 84[b]	–	0, 2[b]	0, 4[b]	2, 2[b]
2	BDO	6	-	2	3	0	0
3	THF	0	0	0	-	0	0
4	BA	9	0	0	0	8	-
5	BuOH	2	0	0	0	-	0

[a] Reaction conditions: substrates (0.1 g), catalyst (0.1 g), 1,4-dioxane (10 mL), temperature (200 ℃), H_2 pressure (8 MPa), reaction time (24 h).

[b] Reaction time (48 h).

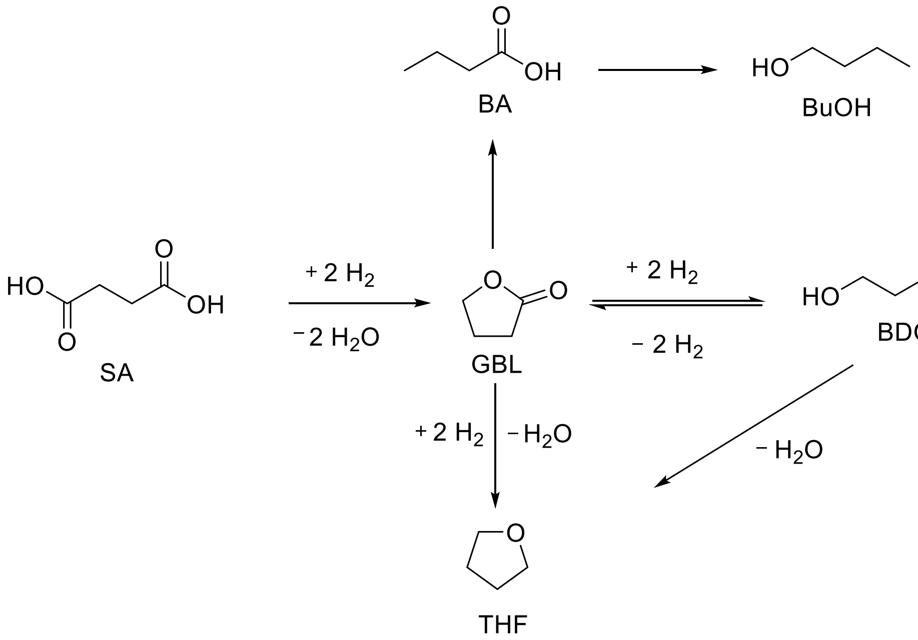

Scheme 2.1: Proposed reaction pathways for SA hydrogenation over the Cu_8Pd_2/HAP catalyst

along with the formations of other non-target products such as BA and BuOH in small quantities. The hydrogenation reactions with different starting materials were carried out to understand the conversion of each compound under the same conditions (Table 2.5). The results revealed that the hydrogenation of GBL over the Cu_8Pd_2/HAP catalyst produced BDO as the main products with 80% yield (entry 1). However, BDO can further undergo hydrogenation to THF (3% yield) or dehydrogenation to GBL (2% yield) (entry 2). BA, which formed as a by-product from GBL hydrogenation, can also be reduced to

BuOH as the final product (8% yield) (entry 4). As a summary of these results, the main reaction pathway is proposed as described in Scheme 2.1.

The optimization of reaction conditions such as temperature, H_2 pressure are important to investigate for any catalytic system, especially for the present process consisting of multiple reaction paths [1]. It is known that the conversion of SA at low temperature favors the formation of GBL, while BDO or THF is the major product at high reaction temperature and pressure [39]. However, in comparison to THF, the formation of BDO is favored at lower temperature and higher pressure [23, 24]. Thus, proper H_2 pressure and temperature for achieving high yields of BDO were examined. In agreement with the previous reports, at the lower temperature, GBL was dominantly formed, while THF, BA, and BuOH appeared as the major products at the higher temperature (Figure 2.1C). In this case, the high concentration of BA which further converts to BuOH can be attributed to the loss of Cu sites at elevated temperature. Whereas, as shown in Figure 2.1D, the yield of GBL and BDO growth with the increase of H_2 pressure. However, BA yield significantly decreases, which can be attributed to the increase in the ability of Cu sites for dissociation of H_2, in competing with Pd sites.

2.3.2 Structure–Activity Relationship

It is worth noting that the hydrogenation of GBL to BA using bimetallic catalysts was minimized with the increase of wt% of Cu, while the formation of BDO was accelerated, which implies new active sites were generated via intermetallic interactions. Therefore, several characterizations were conducted to gain better insight into the catalyst structures. Figure 2.2 illustrates the H_2-TPR profiles of the calcined catalyst precursors. Apparently, the TPR profile of HAP support itself shows no obvious reduction peak from 50 ℃ to 750 ℃. However, when Pd was introduced, a negative at about 85 ℃ and two other positively broad peaks appeared at 360 ℃ and 560 ℃. According to various reports [40–42], at a certain partial pressure, H_2 can be absorbed by the reduced Pd at room temperature, forming β-phase Pd hydride. This phase is unstable at $T > 80$ ℃, releasing H_2 which

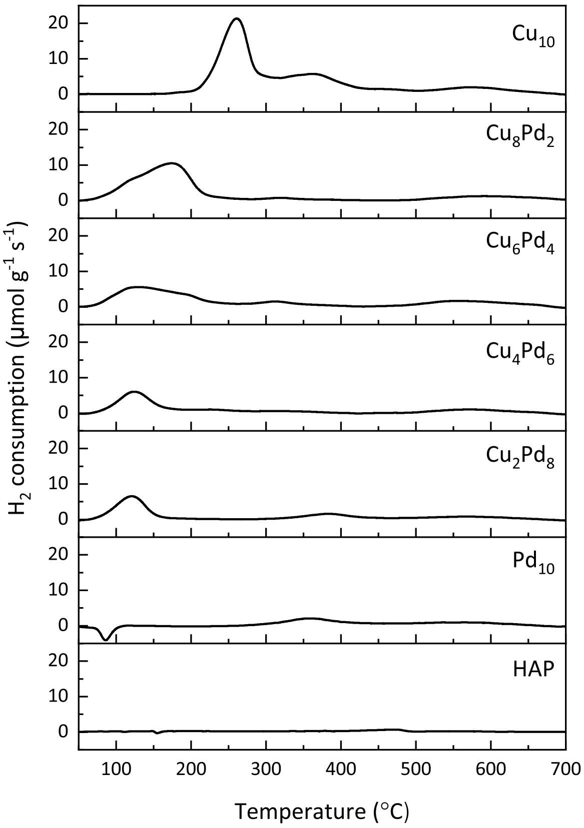

Figure 2.2: H_2-TPR profiles of the calcined Cu_xPd_y/HAP catalysts

caused the negative peak in the profile of the Pd_{10}/HAP. Besides, the first positive peaks at about 360 ℃ can be seen in the cases of the catalyst with high Pd content ($\geq$ 8 wt%), which might be explained by the reduction of a two-dimensional PdO on the surface of support [43, 44]. While, the reduction of palladium species embedded in the structure of support can be responsible for the second positive peak at higher temperature of 560 ℃.

By introducing Cu into the catalysts, there was no negative peak detected, while positive peaks emerged at about 120 ℃ in the TPR profiles of the Cu_xPd_y/HAP. As the Cu content increased, it could have altered the active surface of Pd by the alloying effect to form several mixed oxides Pd_xCu_yO during the calcination at 500 ℃ for 4 h in the preparation of catalysts. These mixed oxides suppressed the H_2 adsorption of Pd and led to the shifts in TPR profiles from lower temperature 120 ℃ to the higher temperature 170 ℃ [45–47]. In the Cu_{10}/HAP, there are three reduction peaks at lower temperature than 500 ℃, which can be characterized as the reduction copper species on the surface

[48, 49], while the peak appears around 570 ℃ can be assigned to the reduction of copper species coordinated in the HAP framework or in solid phase-libethenite denoted as $Cu_2(OH)(PO_4)$ [34, 50]. Particularly, the peak at around 260 ℃ and its shoulder at about 360 ℃ can be ascribed to the reduction of highly dispersed Cu^{2+} and bulk Cu^{2+} with large particle size [51–54]. Therefore, in the Cu_6Pd_4/HAP and Cu_8Pd_2/HAP with high loading Cu content, the reduction peaks are broader than other bimetallic catalysts, contributing to the reduction of well-dispersed isolated CuO species in close vicinity with the mixed oxides. Based on the actual loading amount of metal determined by AAS, the extent of reduction was calculated (Table 2.7, *vide infra*). The results show that with the increase of Pd, the reduction degree significantly decreases to about 50%. This is due to the increase of Pd_xCu_yO mixed oxides (share of oxygen) while decrease of the isolated CuO species in bimetallic catalyst with higher Pd content.

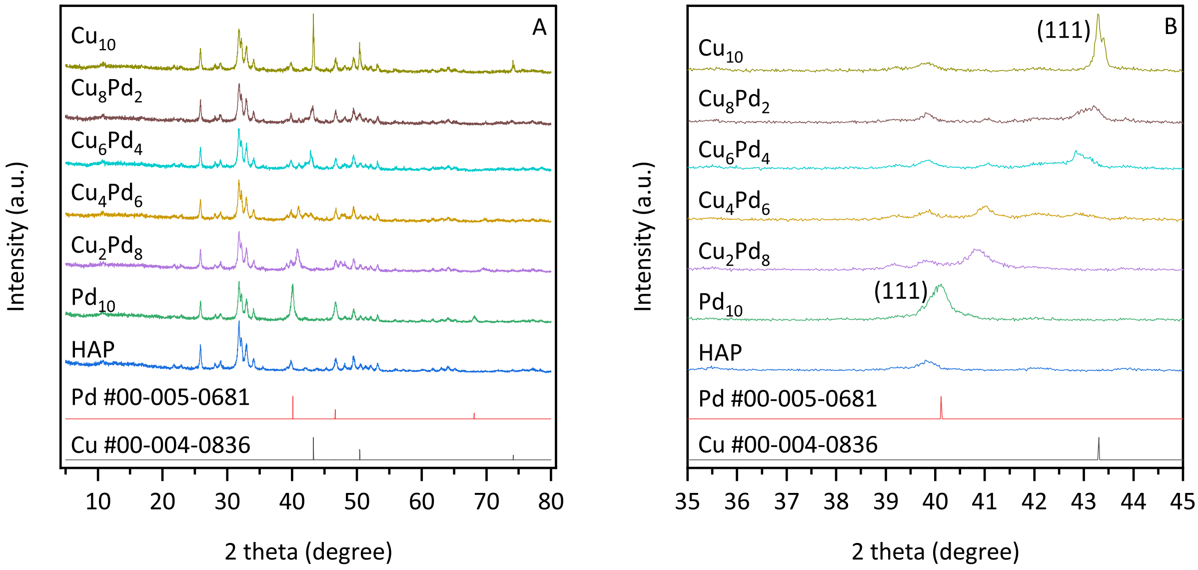

Figure 2.3: XRD patterns of the reduced Cu_xPd_y/HAP in the 2θ range of (A) 5–80° and (B) range-enlargement of 35–45°

The XRD patterns of the support and reduced catalysts are shown in Figure 2.3. Although the peaks of HAP are at high intensity, peaks of the metals are still recognizable. The XRD pattern of Cu_{10}/HAP exhibits peaks at 43.3°, 50.4°, and 74.1°, while those of Pd_{10}/HAP are at 40.1°, 46.7°, and 68.1°, respectively, corresponding to the (111), (200), and (220) planes of their face-centered cubic (*fcc*) metal structure. Taking a closer look at the patterns (Figure 2.3B), it is observed that the shift in the (111) plane of monometallic Pd/HAP catalyst toward higher 2θ values together with the increases of Cu contents indicates the substitution of Cu into the Pd lattice to form bimetallic alloy [55–57]. However, it is pointed out that it is not only one but two phases are formed and their diffraction peaks are easily visualized if the concentration of Cu is significant. This might be rationalized by the low concentration of Pd compared to Cu in the present catalyst system which is rapidly occupied by Cu. Accordingly, once the equilibrium is reached, Cu will no longer substitute into the Pd lattice of the *fcc* structure but forming a new structure, possibly a body-centered cubic (*bcc*) structure, which coexists with the *fcc* structure in the CuPd alloy [58, 59]. As a result, no obvious shift toward higher the 2θ value in the diffraction peak at about 41° was seen when the Cu content increased from 4 to 8 wt%; instead, the peak at about 43° clearly emerged and shifted to a higher 2θ value with the increase in the Cu content from 6 to 8 wt%. The dependence of the bimetallic structure on the metal concentration was previously reported in various reports [60, 61]. For example, a research group of Marakatti et al. recently reported that the effect of the concentration of Pd and Cu on the structural formation [61]. In their study, the Pd_xCu_{1-x} with $x = 0$, 0.25, 0.75, and 1.0 showed an *fcc* structure of PdCu alloy, while a mixed-phase containing both *bcc* and *fcc* of PdCu intermetallic was formed with $x = 0.4$ and 0.6. In our catalyst system, however, the mixed-phase might be formed easily due to the high metal loading.

To have insights into the oxidation state and clarify whether charge transfer occurs between Cu and Pd, XPS studies on the Cu_xPd_y/HAP were performed. The Cu $2p_{3/2}$ spectrum of the monometallic catalyst can be deconvoluted into three components at 932.7 eV, 934.5 eV, and 941.1–943.1 eV, corresponding to Cu^0 in Cu–Cu, Cu^{2+} in Cu–O, and Cu^{2+} satellite peaks [62, 63] (Figure 2.4A). It can be observed that as the increase in Pd content in the bimetallic catalysts, the core-level are shifted to lower binding energy (BE). This result is in good agreement with previous reports that confirmed charge transfer as an outcome of alloying effect between Cu and Pd [63, 64]. It is noticed that in the bimetallic catalysts with higher Pd content, the Cu–Pd interaction becomes stronger, resulted in broader peaks in Cu $2p_{3/2}$ regions [64]. While, during the preparation for the

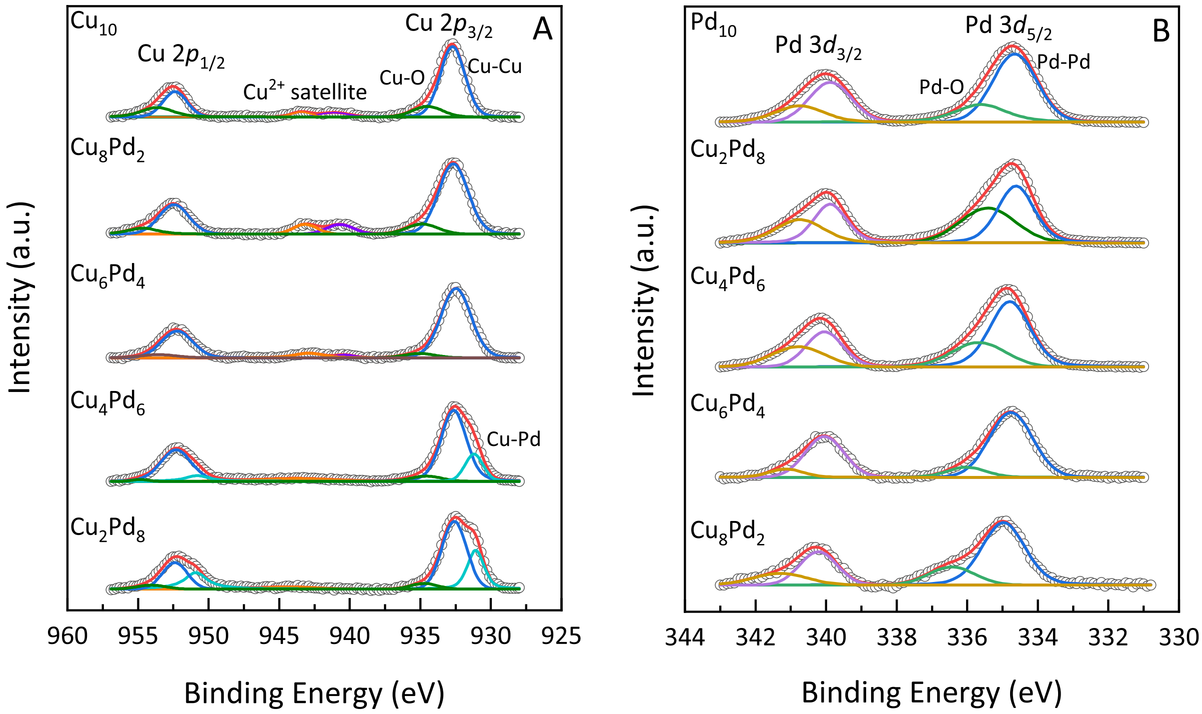

Figure 2.4: XPS spectra of the reduced Cu_xPd_y/HAP catalysts at (A) Cu 2p and (B) Pd 3d regions

XPS experiments, the reduced catalysts were exposed to the air, causing small peaks of CuO and their satellites, owning to the partial oxidation of Cu species on the surface. However, with the increase of Pd content, these peaks become weaker, indicating that the Cu–Pd interaction prevents the oxidation of Cu species [56, 61, 64]. In the Pd 3d spectra of the catalyst samples are shown in Figure 2.4B. The Pd 3$d_{5/2}$ of the monometallic catalyst can be fitted with two peaks at 334.7 eV and 336.1, corresponding to Pd^0 in Pd–Pd and Pd^{2+} in Pd–O, which are close to previous reports [65–68]. Similarly, when Pd interacts with Cu in the bimetallic catalyst, a new peak which can be attributed to Pd–Cu interaction appeared [64]. This peak becomes stronger as the increase of Cu content and finally overlaps the Pd–Pd peak. Accordingly, the corporation of Pd and Cu leads to a shift in higher binding energy, revealing the partial charge transfer from Cu to Pd as the result of Cu–Pd alloying formation [64, 69, 70]. It is noticed that the relative intensities of Cu 2p are intense compared to those of Pd 3d, suggesting a partial enrichment of Cu species on the surface of the present nanoalloy particles [71, 72].

For getting more details about the electronic states and insights into structures of

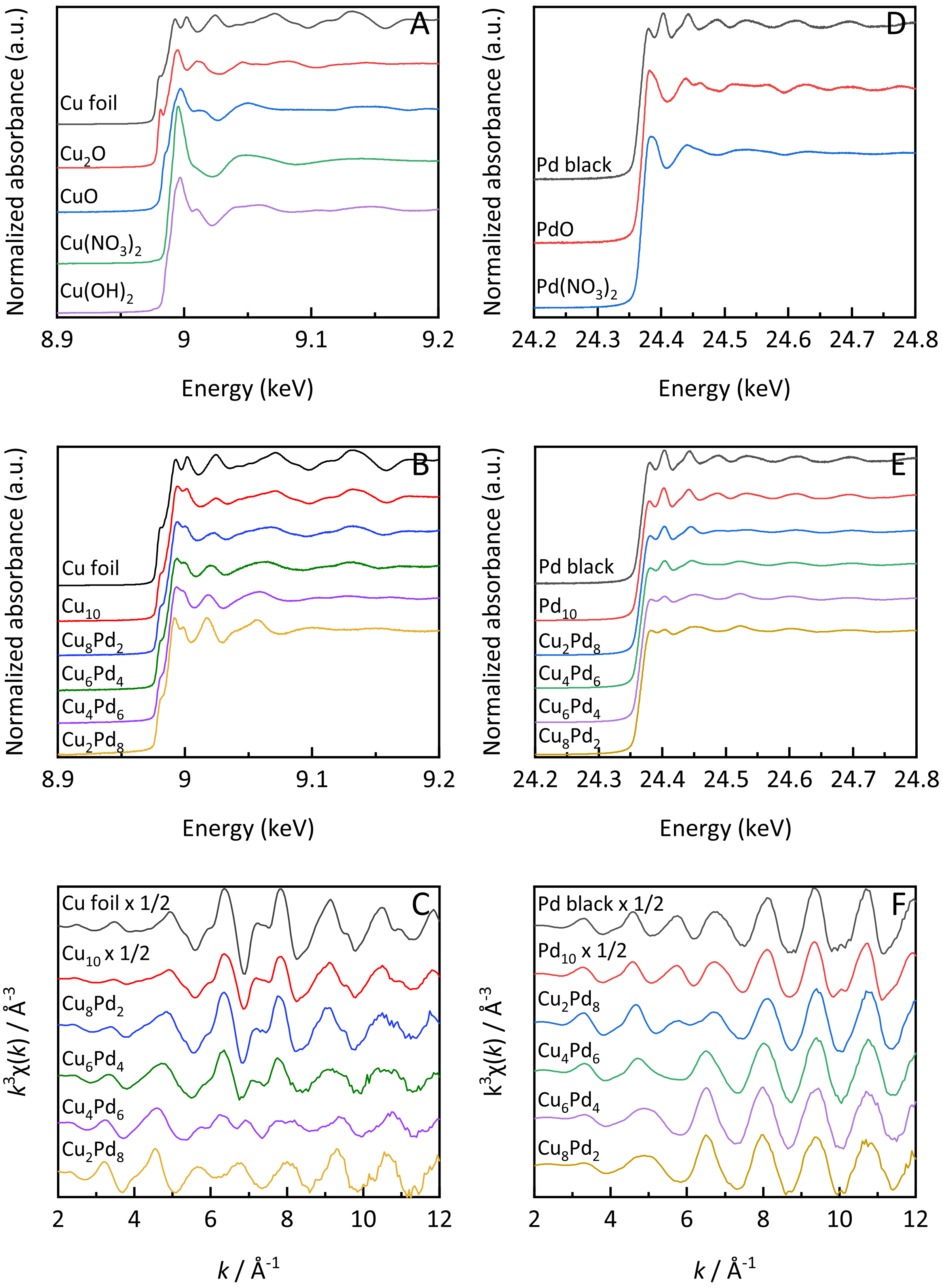

Figure 2.5: XANES features of references and Cu_xPd_y/HAP catalysts and k^3-weighted EXAFS spectra at (A–C) Cu K-edge and (D–F) Pd K-edge

the bimetallic catalysts, XAFS inspections were carried out for the reduced catalysts. Figure 2.5 shows the Cu K-edge and Pd K-edge of both the catalysts and their relevant references. It is clear that the XANES features of both the Cu K-edge and Pd K-edges are similar to their corresponding purely metallic references of Cu foil (Cu^0) and Pd black (Pd^0), indicating the presence of zero-valent metals as the influential state in the catalysts [73]. To estimate the changes in the bimetallic structures compared to the monometallic ones, further interpretations of the data on the EXAFS were performed. The k^3-weighted EXAFS and Fourier transform (FT) spectra at the Cu K-edge and Pd K-edge are demonstrated in Figure 2.5C&F and Figure 2.6, respectively. At the Cu K-edge, little information about the intermetallic interactions can be observed via the changes in oscillations (Figure 2.5C) and shapes of the shells (Figure 2.6A) if the ratio (wt%) of the neighboring atom to the atom of interest was low (Pd $<$ 4 wt%). However, when the ratio significantly increases (Pd $>$ 6 wt%), these changes are clearly observed as the humps instead of the single peaks in the FT spectra. In contrast, for the Pd K-edge, the differences in oscillations are clearly visible even at the low mentioned ratios (Figure 2.5F), which might be attributed to the low concentration of Pd loaded in the bimetallic catalyst, as in accordance with the XRD and AAS results (Table 2.7, *vide infra*). In a clearer view, the FT of the k^3-weighted Pd K-edge EXAFS of the Pd reference and Pd_{10}/HAP displayed a broad peak at about 2.5 Å; however, as the addition of Cu, the shape of peak greatly changes to a hump at first (Cu = 2 wt%) and then to broad peaks (Cu $>$ 4 wt%) with shifts to the lower distance at about 2.1 Å (Figure 2.6B).

The EXAFS fitting was then performed to determine the structural parameters of the bimetallic catalysts: i.e., coordination number (CN) and interatomic distance (r). In order to eliminate all multiple scattering effects and reduce the number of independent variables, only the first coordination shells were involved in the fits. The amplitude reduction factors, which were determined from the fit of the Cu and Pd reference data, were constrained to the fits of all the catalysts of the corresponding edges. Other factors including the change to the interatomic distance and the mean spare relative displacement were either fitted independently or constrained to be the same for all paths in certain shells to optimize

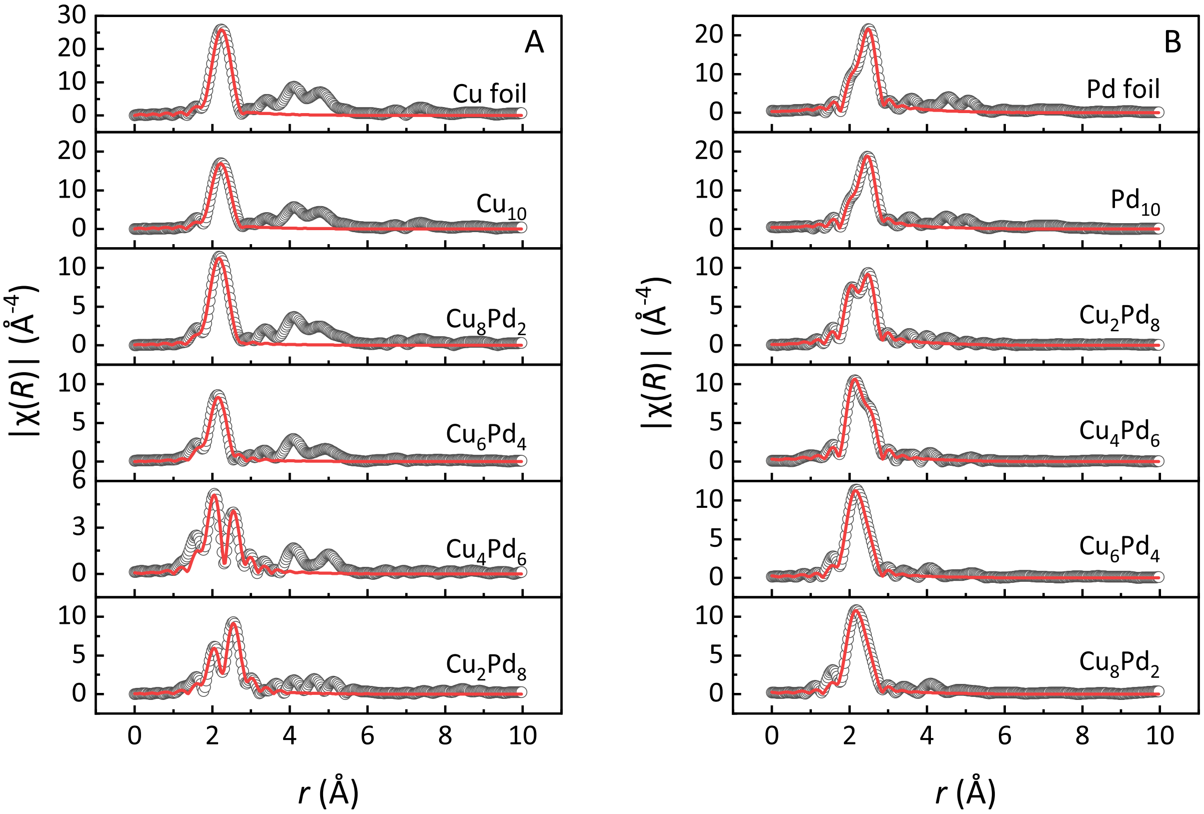

Figure 2.6: FT EXAFS spectra of raw (grey open circles) and fitting (red solid line) data of the Cu_xPd_y/HAP at (A) Cu K-edge and (B) Pd K-edge

the fits. In all fits the k^3-weighted was used. The EXAFS spectra including both raw and fitting data are demonstrated in Figure 2.6 while the detailed results are listed in Table 2.6. To improve the visualization, the CNs obtained from the fits are illustrated in Figures 2.7A&B. The results confirm that the metals in the bimetallic catalysts are alloyed with the neighboring atom of Cu or Pd. Particularly, as the content of the neighboring atoms increases, the CNs of Pd–Cu and Cu–Pd increase, indicating the growth in the alloying degree of these bimetallic catalysts. Furthermore, the total metal–metal (M–M) CNs obtained from all interactions for individual metal can reveal information about the core-shell structure or homogeneous alloy structure of the bimetallic catalysts [74, 75]. In a previous research [76], by comparing the CNs of Pt–M and Pd–M (in the Pd–Pt (1:1) and Pd–Pt (4:1) bimetallic catalyst, Toshima et al. reported that as the increase of Pd content, the CN of Pd–M was also increased, while that of the Pt–M was not distinctly different, indicating the existence of a Pt core surrounded by Pd monolayer.

Table 2.6: EXAFS fitting results of the reduced Cu_xPd_y/HAP catalysts at Cu and Pd K-edges

Sample	Cu K-edge			Pd K-edge		
	Path	CN	R (Å)	Path	CN	R (Å)
Cu foil	Cu–Cu	12	2.542 ± 0.002	-	-	-
Cu_{10}	Cu–Cu	7.8 ± 1.4	2.532 ± 0.011	-	-	-
Cu_8Pd_2	Cu–Cu	6.7 ± 2.1	2.544 ± 0.027	Pd–Pd	3.1 ± 1.3	2.697 ± 0.024
	Cu–Pd	0.8 ± 1.4	2.604 ± 0.135	Pd–Cu	6.9 ± 1.6	2.566 ± 0.016
Cu_6Pd_4	Cu–Cu	4.0 ± 1.2	2.465 ± 0.021	Pd–Pd	3.3 ± 1.0	2.693 ± 0.016
	Cu–Pd	2.0 ± 0.4	2.409 ± 0.055	Pd–Cu	7.6 ± 1.2	2.564 ± 0.016
Cu_4Pd_6	Cu–Cu	1.9 ± 0.9	2.509 ± 0.024	Pd–Pd	6.5 ± 1.3	2.662 ± 0.013
	Cu–Pd	4.5 ± 0.8	2.539 ± 0.027	Pd–Cu	4.0 ± 0.7	2.573 ± 0.011
Cu_2Pd_8	Cu–Cu	2.3 ± 0.4	2.613 ± 0.021	Pd–Pd	7.6 ± 0.6	2.693 ± 0.006
	Cu–Pd	6.7 ± 1.5	2.639 ± 0.010	Pd–Cu	3.7 ± 0.5	2.631 ± 0.009
Pd_{10}	-	-	-	Pd–Pd	11.3 ± 0.6	2.739 ± 0.003
Pd black	-	-	-	Pd–Pd	12	2.751 ± 0.002

In the present catalyst system, however, it is observed that when the concentration of neighboring atom, i.e., Pd and Cu, increased, the CNs of Cu–M and Pd–M were similar within the uncertainty. These results might suggest that rather than a core-shell, the homogeneous alloy structures are favorable to form [75].

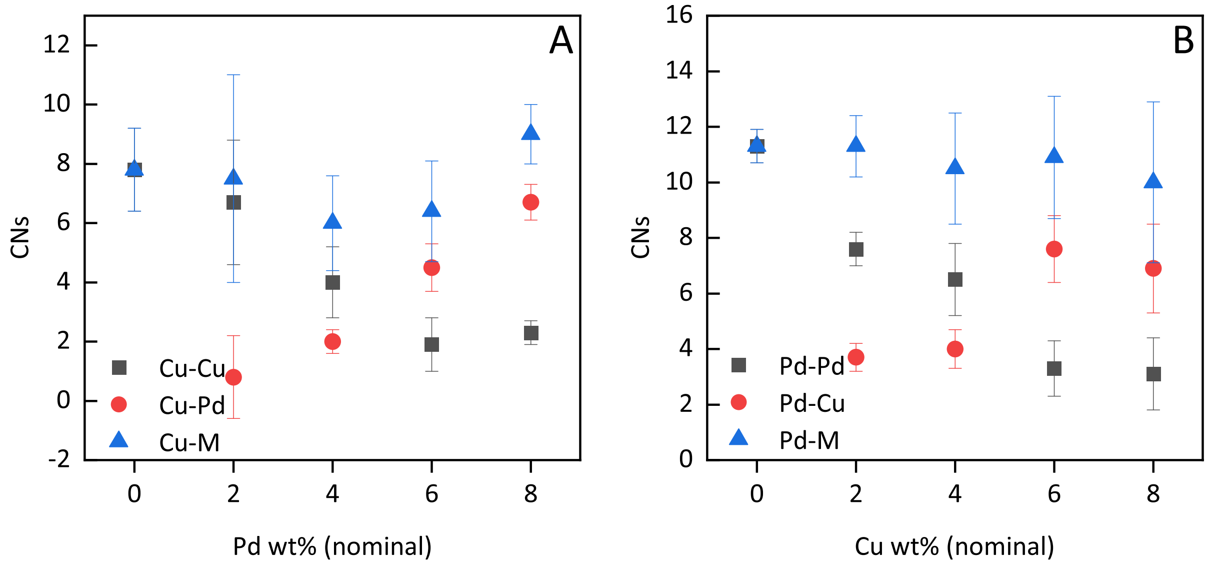

Figure 2.7: CNs obtained from fitting results at (A) Cu K-edge and (B) Pd K-edge of the reduced Cu_xPd_y/HAP

To further study the internal structure and compositional distribution of the nanoparticles, the TEM techniques for the most active catalyst of the reduced Cu_8Pd_2/HAP were

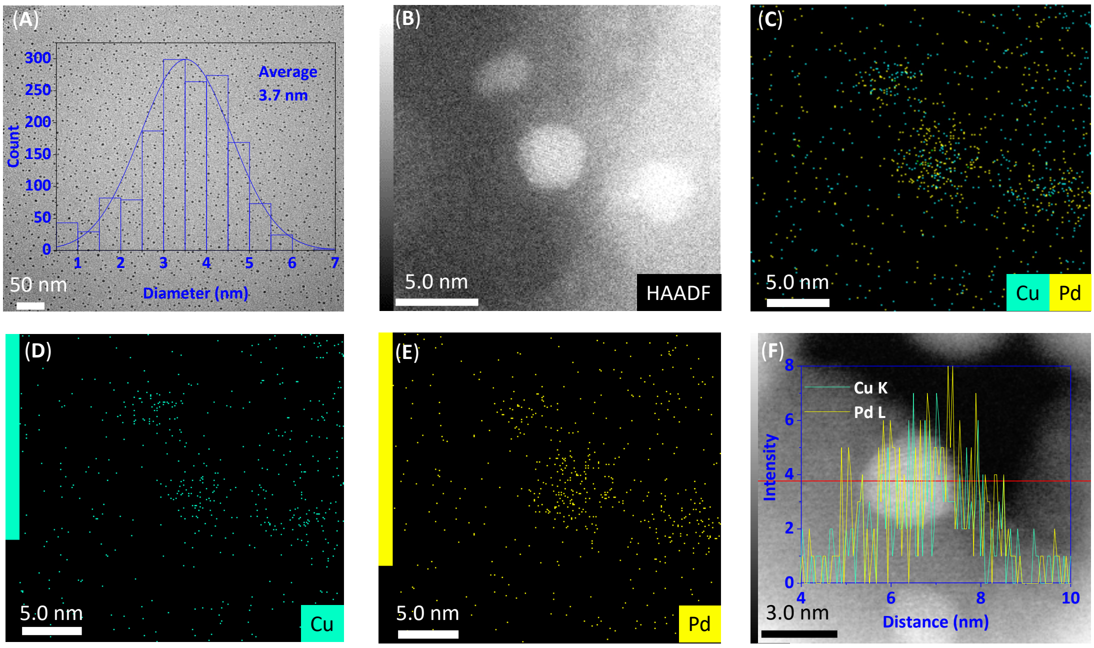

Figure 2.8: (A) TEM image and particle size distribution of the reduced Cu_8Pd_2/HAP catalyst, (B–E) HAADF-STEM image with EDS elemental mapping images, and (F) EDS-line analysis

conducted (Figure 2.8). The TEM result clearly shows that the metals were well-dispersed on the surface of HAP. The average diameter of the particles was then estimated using numerous counting particles, which is 3.7 nm (Figure 2.8A). Subsequently, the STEM with the HAADF imaging technique, which provides structural and chemical information at atomic resolution was performed [77, 78]. It is known that an image Z-contrast for the bimetallic catalyst system possessing a significant difference in atomic numbers such as Cu ($Z = 29$) and Pd ($Z = 46$) would be noticeable provided that the elemental segregation, i.e., core-shell structure or phase-separation, occurred [56, 79]. Figure 2.8B exhibits a regular brightness spot without any contrast, indicating the absence of elemental-segregation. Whereas, the EDS elemental mapping results elementally identify the particles which show that both Cu (jade green) and Pd (yellow) were homogeneously and randomly distributed throughout the particle, as shown in Figure 2.8C–E. The EDS line analysis for the major particles in average sizes visually exhibits Cu and Pd in a similar intensity (Figure 2.8F, which is different from the actual atomic ratio determined on the basis of AAS results, which are Cu-89% and Pd-11%. Therefore, the different analysis on a larger particle was also performed as shown in Figure 2.9. It was observed that the larger particle (ca. 11.9 nm in diameter) was composed of CuPd alloy with higher Cu content. Although the Cu-rich alloy with larger nanoparticles is not dominant in the present catalyst, it might be an important component in the production of BDO from the intermediate GBL. Accordingly, when the Cu was leached during the recycling runs, the overall catalytic reactivity toward BDO decreased, which will be discussed later in this chapter.

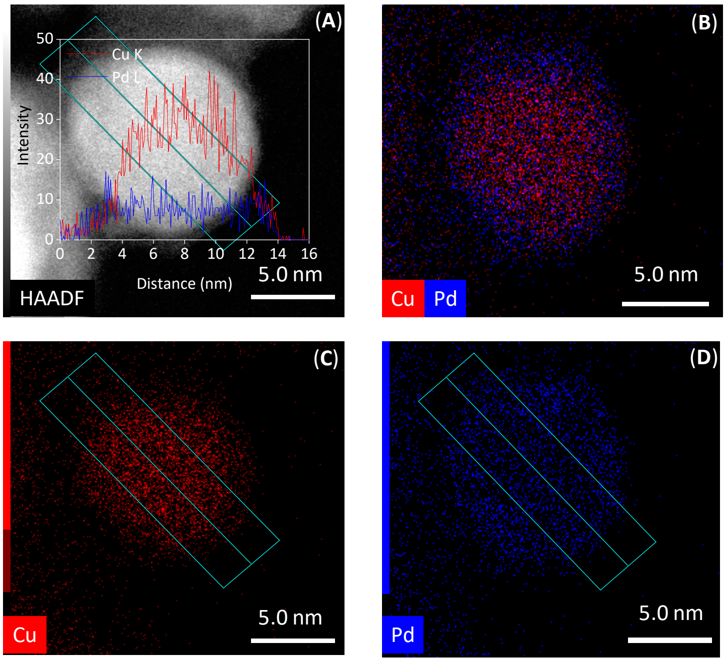

Figure 2.9: (A) STEM-HAADF image of a larger particle observed in the Cu_8Pd_2/HAP catalyst with line analysis and (B) elemental mapping images

2.3.3 Stability of Catalysts

As discussed elsewhere, the requirements for a high-performance heterogeneous catalyst are not only the active metals species but also the support [80]. Accordingly, the active species need to be formed precisely with strong interaction on the support surface [81]. HAP, which was reported as the effective support for many reactions due to its strong interaction with metallic species [33, 82–84], was chosen for the present catalyst system. In order to evaluate the actual stability and reusability of the catalyst, after the first run,

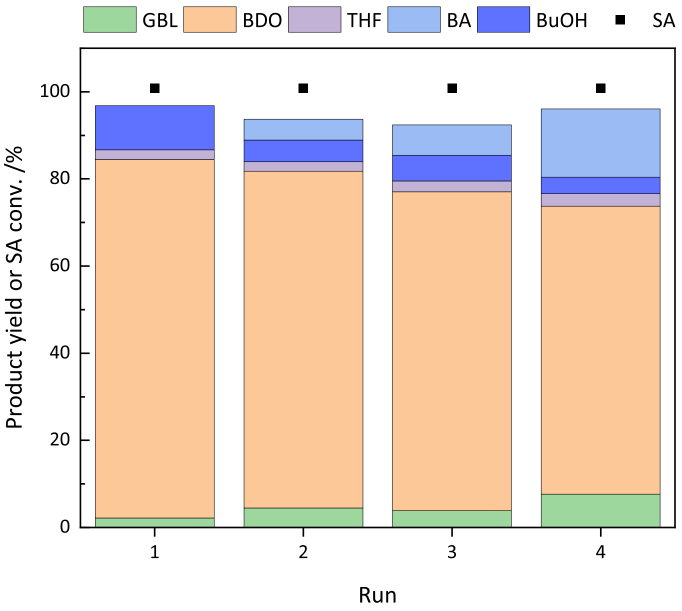

Figure 2.10: Reusability capacity of the Cu_8Pd_2/HAP catalyst for the SA hydrogenation. Reaction conditions: SA (0.1 g), catalyst (0.1 g), 1,4-dioxane (10 mL), H_2 pressure (8 MPa), temperature (200 ℃), reaction time (48 h).

Table 2.7: Actual metal loadings and textural properties of the samples[a,b,c]

Sample	Cu wt%	Pd wt%	Cu/Pd molar ratio	Surface area $m^2\ g^{-1}$	Extent of reduction /%
Cu_{10}/HAP	10.6	n.d.	-	35	109
Cu_8Pd_2/HAP	8.5	1.8	8.1	53	97
Cu_8Pd_2/HAP-used	7.1	1.4	8.5	n.d.	n.d.
Cu_6Pd_4/HAP	6.3	3.9	2.7	47	84
Cu_4Pd_6/HAP	4.1	6.1	1.1	47	78
Cu_2Pd_8/HAP	2.1	7.4	0.5	53	52
Pd_{10}/HAP	n.d.	8.3	-	53	62
HAP	n.d.	n.d.	-	44	n.d.

[a] The Cu and Pd contents of the reduced catalyst samples were determined by AAS method.

[b] The BET surface area of the calcined catalyst samples were determined by N_2 adsorption/desorption method.

[c] The extent of reduction was calculated based on the actual H_2 consumption from TPR and the H_2 consumption in the assumption that all the loading metals (from AAS) were reduced.

the Cu_8Pd_2/HAP was simply centrifugated, washed with 1,4-dioxane solvent and dried in vacuum before using for the next run. As shown in Figure 2.10, it was clearly observed that the catalyst could be recycled for 4 consecutive runs without noticeable loss in its activity. It is noticed that the selectivity of BA gradually increases during recycling runs. As discussed previously, Cu is the dominant factor for the production of BDO, whereas Pd is the key for the production of BA from the intermediate GBL. Accordingly, the increase in BA seems to be attributed to the decrease of Cu active sites due to the metal leaching issue. In comparison with the fresh sample, the AAS results of the used catalyst evidence that a significant decrease in the Cu content (1.4 wt%) compared to that of Pd (0.4 wt%) was observed, which is possibly responsible for the decrease in the selectivity of BDO (Table 2.7).

2.4 Conclusion

In summary, this chapter demonstrates the direct hydrogenation of SA to BDO with high selectivity using the Cu–Pd/HAP as highly effective bimetallic catalysts. While the monometallic Pd/HAP catalyst could not produce the target product, the addition of the optimized Cu content (8 wt%) in the bimetallic catalyst facilitates the reduction of SA to BDO, affording 82% yield with complete conversion of SA. Simple experiments using monometallic catalysts for the hydrogenation of GBL revealed that the Pd sites favor the formation of BA, whereas the Cu sites promote the generation of BDO. A wide range of characterization techniques was employed to deepen understanding of the present catalyst system. The obtained data discloses a synergistic effect between Cu and Pd as a result of alloying formation, leading to its remarkable reactivity compared to the monometallic catalysts. Notably, as suggested from XPS and AAS results, the Cu-rich alloy particles in the present catalyst are determined as important components toward the high selectivity of BDO. Therefore, the superior performance of the HAP supported CuPd bimetallic catalysts with high Cu loading makes it efficient in direct hydrogenation of SA to BDO.

References

(1) Delhomme, C.; Weuster-Botz, D.; Kühn, F. E. Succinic Acid from Renewable Resources as a C_4 Building-Block Chemical–a Review of the Catalytic Possibilities in Aqueous Media. *Green Chem.* **2009**, *11*, 13–26.

(2) Gandini, A. The Irruption of Polymers from Renewable Resources on the Scene of Macromolecular Science and Technology. *Green Chem.* **2011**, *13*, 1061–1083.

(3) Luterbacher, J.; Alonso, D. M.; Dumesic, J. Targeted Chemical Upgrading of Lignocellulosic Biomass to Platform Molecules. *Green Chem.* **2014**, *16*, 4816–4838.

(4) Huber, G. W.; Iborra, S.; Corma, A. Synthesis of Transportation Fuels from Biomass: Chemistry, Catalysts, and Engineering. *Chem. Rev.* **2006**, *106*, 4044–4098.

(5) Chheda, J. N.; Huber, G. W.; Dumesic, J. A. Liquid-Phase Catalytic Processing of Biomass-Derived Oxygenated Hydrocarbons to Fuels and Chemicals. *Angew. Chem., Int. Ed.* **2007**, *46*, 7164–7183.

(6) Zhou, C.-H. C.; Beltramini, J. N.; Fan, Y.-X.; Lu, G. M. Chemoselective Catalytic Conversion of Glycerol as a Biorenewable Source to Valuable Commodity Chemicals. *Chem. Soc. Rev.* **2008**, *37*, 527–549.

(7) Mika, L. T.; Cséfalvay, E.; Németh, Á. Catalytic Conversion of Carbohydrates to Initial Platform Chemicals: Chemistry and Sustainability. *Chem. Rev.* **2018**, *118*, 505–613.

(8) Werpy, T.; Petersen, G. *Top Value Added Chemicals from Biomass: Volume I–Results of Screening for Potential Candidates from Sugars and Synthesis Gas*; tech. rep.; National Renewable Energy Lab., Golden, CO (US), 2004.

(9) Yang, S.-T.; Liu, X.; Zhang, Y. In *Bioprocessing for Value-Added Products from Renewable Resources*; Elsevier: 2007, pp 73–118.

(10) Goldberg, I.; Rokem, J. In *Encyclopedia of Microbiology (Third Edition)*, Schaechter, M., Ed., Third Edition; Academic Press: Oxford, 2009, pp 421–442.

(11) Matano, C.; Meiswinkel, T. M.; Wendisch, V. F. In *Wheat and Rice in Disease Prevention and Health*, Watson, R. R., Preedy, V. R., Zibadi, S., Eds.; Academic Press: San Diego, 2014, pp 493–505.

(12) Nghiem, N.; Kleff, S.; Schwegmann, S. Succinic Acid: Technology Development and Commercialization. *Fermentation* **2017**, *3*, 26–40.

(13) Huber, G. W.; Corma, A. Synergies between Bio- and Oil Refineries for the Production of Fuels from Biomass. *Angew. Chemie Int. Ed.* **2007**, *46*, 7184–7201.

(14) Huang, R.; Qi, W.; Su, R.; He, Z. Integrating Enzymatic and Acid Catalysis to Convert Glucose into 5-Hydroxymethylfurfural. *Chem. Commun.* **2010**, *46*, 1115–1117.

(15) Ma, Y.; Qing, S.; Wang, L.; Islam, N.; Guan, S.; Gao, Z.; Mamat, X.; Li, H.; Eli, W.; Wang, T. Production of 5-Hydroxymethylfurfural from Fructose by a Thermo-Regulated and Recyclable Brønsted Acidic Ionic Liquid Catalyst. *RSC Adv.* **2015**, *5*, 47377–47383.

(16) Osatiashtiani, A.; Lee, A. F.; Wilson, K. Recent Advances in the Production of γ-valerolactone from Biomass-Derived Feedstocks via Heterogeneous Catalytic Transfer Hydrogenation. *J. Chem. Technol. Biotechnol.* **2017**, *92*, 1125–1135.

(17) Dutta, S.; Iris, K.; Tsang, D. C.; Ng, Y. H.; Ok, Y. S.; Sherwood, J.; Clark, J. H. Green Synthesis of Gamma-Valerolactone (GVL) through Hydrogenation of Biomass-Derived Levulinic Acid Using Non-Noble Metal Catalysts: A Critical Review. *Chem. Eng. J.* **2019**, *372*, 992–1006.

(18) Corma, A.; Iborra, S.; Velty, A. Chemical Routes for the Transformation of Biomass into Chemicals. *Chem. Rev.* **2007**, *107*, 2411–2502.

(19) Mazière, A.; Prinsen, P.; García, A.; Luque, R.; Len, C. A Review of Progress in (Bio)Catalytic Routes from/to Renewable Succinic Acid. *Biofuels, Bioprod. Biorefining* **2017**, *11*, 908–931.

(20) Bechthold, I.; Bretz, K.; Kabasci, S.; Kopitzky, R.; Springer, A. Succinic Acid: A New Platform Chemical for Biobased Polymers from Renewable Resources. *Chem. Eng. Technol.* **2008**, *31*, 647–654.

(21) Luque, R.; Clark, J. H.; Yoshida, K.; Gai, P. L. Efficient Aqueous Hydrogenation of Biomass Platform Molecules using Supported Metal Nanoparticles on Starbons®. *Chem. Commun.* **2009**, 5305–5307.

(22) Hong, U. G.; Park, H. W.; Lee, J.; Hwang, S.; Yi, J.; Song, I. K. Hydrogenation of Succinic Acid to Tetrahydrofuran (THF) over Rhenium Catalyst Supported on H_2SO_4-Treated Mesoporous Carbon. *Appl. Catal. A Gen.* **2012**, *415*, 141–148.

(23) Di, X.; Li, C.; Zhang, B.; Qi, J.; Li, W.; Su, D.; Liang, C. Role of Re and Ru in Re-Ru/C Bimetallic Catalysts for the Aqueous Hydrogenation of Succinic Acid. *Ind. Eng. Chem. Res.* **2017**, *56*, 4672–4683.

(24) Takeda, Y.; Tamura, M.; Nakagawa, Y.; Okumura, K.; Tomishige, K. Hydrogenation of Dicarboxylic Acids to Diols over Re–Pd Catalysts. *Catal. Sci. Technol.* **2016**, *6*, 5668–5683.

(25) Zhu, Y.; Kong, X.; Li, X.; Ding, G.; Zhu, Y.; Li, Y.-W. Cu Nanoparticles Inlaid Mesoporous Al_2O_3 As a High-Performance Bifunctional Catalyst for Ethanol Synthesis via Dimethyl Oxalate Hydrogenation. *ACS Catal.* **2014**, *4*, 3612–3620.

(26) Wang, Y.; Shen, Y.; Zhao, Y.; Lv, J.; Wang, S.; Ma, X. insight into the Balancing Effect of Active Cu Species for Hydrogenation of Carbon–Oxygen Bonds. *ACS Catal.* **2015**, *5*, 6200–6208.

(27) Li, W.; Cui, X.; Junge, K.; Surkus, A.-E.; Kreyenschulte, C.; Bartling, S.; Beller, M. General and Chemoselective Copper Oxide Catalysts for Hydrogenation Reactions. *ACS Catal.* **2019**, *9*, 4302–4307.

(28) Huang, Z.; Barnett, K. J.; Chada, J. P.; Brentzel, Z. J.; Xu, Z.; Dumesic, J. A.; Huber, G. W. Hydrogenation of γ-Butyrolactone to 1,4-Butanediol over CuCo/TiO_2 Bimetallic Catalysts. *ACS Catal.* **2017**, *7*, 8429–8440.

(29) Wu, J.; Gao, G.; Sun, P.; Long, X.; Li, F. Synergetic Catalysis of Bimetallic CuCo Nanocomposites for Selective Hydrogenation of Bioderived Esters. *ACS Catal.* **2017**, *7*, 7890–7901.

(30) Wu, J.; Gao, G.; Li, Y.; Sun, P.; Wang, J.; Li, F. Highly Chemoselective Hydrogenation of Lactone to Diol over Efficient Copper-Based Bifunctional Nanocatalysts. *Appl. Catal. B Environ.* **2019**, *245*, 251–261.

(31) Xu, G.; Zhang, Y.; Fu, Y.; Guo, Q. Efficient Hydrogenation of Various Renewable Oils over Ru-HAP Catalyst in Water. *ACS Catal.* **2017**, *7*, 1158–1169.

(32) Elliott, J. C., *Structure and Chemistry of the Apatites and Other Calcium Orthophosphates*; Elsevier: 2013.

(33) Sun, H.; Su, F.-Z.; Ni, J.; Cao, Y.; He, H.-Y.; Fan, K.-N. Gold Supported on Hydroxyapatite as a Versatile Multifunctional Catalyst for the Direct Tandem Synthesis of Imines and Oximes. *Angew. Chem. Int. Ed.* **2009**, *48*, 4390–4393.

(34) Tounsi, H.; Djemal, S.; Petitto, C.; Delahay, G. Copper Loaded Hydroxyapatite Catalyst for Selective Catalytic Reduction of Nitric Oxide with Ammonia. *Appl. Catal. B Environ.* **2011**, *107*, 158–163.

(35) Sudhakar, M.; Kantam, M. L.; Jaya, V. S.; Kishore, R.; Ramanujachary, K.; Venugopal, A. Hydroxyapatite as a Novel Support for Ru in the Hydrogenation of Levulinic Acid to γ-Valerolactone. *Catal. Commun.* **2014**, *50*, 101–104.

(36) Mizugaki, T.; Nagatsu, Y.; Togo, K.; Maeno, Z.; Mitsudome, T.; Jitsukawa, K.; Kaneda, K. Selective Hydrogenation of Levulinic Acid to 1,4-Pentanediol in Water using a Hydroxyapatite-Supported Pt–Mo Bimetallic Catalyst. *Green Chem.* **2015**, *17*, 5136–5139.

(37) Cai, B.; Zhou, X.-C.; Miao, Y.-C.; Luo, J.-Y.; Pan, H.; Huang, Y.-B. Enhanced Catalytic Transfer Hydrogenation of Ethyl Levulinate to γ-Valerolactone over a Robust Cu–Ni Bimetallic Catalyst. *ACS Sustain. Chem. Eng.* **2017**, *5*, 1322–1331.

(38) Deshpande, R.; Buwa, V.; Rode, C.; Chaudhari, R.; Mills, P. Tailoring of Activity and Selectivity Using Bimetallic Catalyst in Hydrogenation of Succinic Acid. *Catal. Commun.* **2002**, *3*, 269–274.

(39) Liu, X.; Wang, X.; Xu, G.; Liu, Q.; Mu, X.; Liu, H. Tuning the Catalytic Selectivity in Biomass-Derived Succinic Acid Hydrogenation on FeO_x-Modified Pd Catalysts. *J. Mater. Chem. A* **2015**, *3*, 23560–23569.

(40) Neri, G.; Musolino, M. G.; Milone, C.; Pietropaolo, D.; Galvagno, S. Particle Size Effect in the Catalytic Hydrogenation of 2,4-Dinitrotoluene over Pd/C Catalysts. *Appl. Catal. A Gen.* **2001**, *208*, 307–316.

(41) Nag, N. K. A Study on the Formation of Palladium Hydride in a Carbon-Supported Palladium Catalyst. *J. Phys. Chem. B* **2001**, *105*, 5945–5949.

(42) Amorim, C.; Keane, M. A. Palladium Supported on Structured and Nonstructured Carbon: A Consideration of Pd Particle Size and the Nature of Reactive Hydrogen. *J. Colloid Interface Sci.* **2008**, *322*, 196–208.

(43) Barrera, A.; Viniegra, M.; Fuentes, S.; Díaz, G. The Role of Lanthana Loading on the Catalytic Properties of $Pd/Al_2O_3-La_2O_3$ in the NO Reduction with H_2. *Appl. Catal. B Environ.* **2005**, *56*, 279–288.

(44) Babu, N. S.; Lingaiah, N.; Gopinath, R.; Sankar Reddy, P. S.; Sai Prasad, P. Characterization and Reactivity of Alumina-Supported Pd Catalysts for the Room-Temperature Hydrodechlorination of Chlorobenzene. *J. Phys. Chem. C* **2007**, *111*, 6447–6453.

(45) Meshesha, B. T.; Barrabés, N.; Llorca, J.; Dafinov, A.; Medina, F.; Föttinger, K. PdCu Alloy Nanoparticles on Alumina as Selective Catalysts for Trichloroethylene Hydrodechlorination to Ethylene. *Appl. Catal. A Gen.* **2013**, *453*, 130–141.

(46) Hamid, S.; Bae, S.; Lee, W. Novel Bimetallic Catalyst Supported by Red Mud for Enhanced Nitrate Reduction. *Chem. Eng. J.* **2018**, *348*, 877–887.

(47) Yang, Q.; Hou, R.; Sun, K. Tuning Butene Selectivities by Cu Modification on Pd-Based Catalyst for the Selective Hydrogenation of 1,3-Butadiene. *J. Catal.* **2019**, *374*, 12–23.

(48) Jemal, J.; Tounsi, H.; Djemel, S.; Pettito, C.; Delahay, G. Characterization and DeNO$_x$ Activity of Copper-Hydroxyapatite Catalysts Prepared by Wet Impregnation. *React. Kinet., Mech. Catal.* **2013**, *109*, 159–165.

(49) Qu, Z.; Sun, Y.; Chen, D.; Wang, Y. Possible Sites of Copper Located on Hydroxyapatite Structure and the Identification of Active Sites for Formaldehyde Oxidation. *J. Mol. Catal. A: Chem.* **2014**, *393*, 182–190.

(50) Wen, C.; Cui, Y.; Chen, X.; Zong, B.; Dai, W.-L. Reaction Temperature Controlled Selective Hydrogenation of Dimethyl Oxalate to Methyl Glycolate and Ethylene Glycol over Copper-Hydroxyapatite Catalysts. *Appl. Catal. B Environ.* **2015**, *162*, 483–493.

(51) Chen, L.-F.; Guo, P.-J.; Zhu, L.-J.; Qiao, M.-H.; Shen, W.; Xu, H.-L.; Fan, K.-N. Preparation of Cu/SBA-15 Catalysts by Different Methods for the Hydrogenolysis of Dimethyl Maleate to 1,4-Butanediol. *Appl. Catal. A Gen.* **2009**, *356*, 129–136.

(52) Nishimura, S.; Shishido, T.; Ebitani, K.; Teramura, K.; Tanaka, T. Novel Catalytic Behavior of Cu/Al$_2$O$_3$ Catalyst Against Daily Start-up and Shut-down (DSS)-like Operation in the Water Gas Shift Reaction. *Appl. Catal. A Gen.* **2010**, *387*, 185–194.

(53) Jemal, J.; Tounsi, H.; Chaari, K.; Petitto, C.; Delahay, G.; Djemel, S.; Ghorbel, A. NO Reduction with NH$_3$ under Oxidizing Atmosphere on Copper Loaded Hydroxyapatite. *Appl. Catal. B Environ.* **2012**, *113*, 255–260.

(54) Guo, J.; Yu, H.; Dong, F.; Zhu, B.; Huang, W.; Zhang, S. High Efficiency and Stability of Au–Cu/Hydroxyapatite Catalyst for the Oxidation of Carbon Monoxide. *RSC Adv.* **2017**, *7*, 45420–45431.

(55) Toshima, N.; Wang, Y. Preparation and Catalysis of Novel Colloidal Dispersions of Copper/Noble Metal Bimetallic Clusters. *Langmuir* **1994**, *10*, 4574–4580.

(56) Yin, Z.; Zhou, W.; Gao, Y.; Ma, D.; Kiely, C. J.; Bao, X. Supported Pd–Cu Bimetallic Nanoparticles That Have High Activity for the Electrochemical Oxidation of Methanol. *Chem. Eur. J.* **2012**, *18*, 4887–4893.

(57) Di, L.; Xu, W.; Zhan, Z.; Zhang, X. Synthesis of Alumina Supported Pd–Cu Alloy Nanoparticles for CO Oxidation via a Fast and Facile Method. *RSC Adv.* **2015**, *5*, 71854–71858.

(58) Bradley, J. S.; Via, G. H.; Bonneviot, L.; Hill, E. W. Infrared and EXAFS Study of Compositional Effects in Nanoscale Colloidal Palladium-Copper Alloys. *Chem. Mater.* **1996**, *8*, 1895–1903.

(59) Guy, K. A.; Xu, H.; Yang, J. C.; Werth, C. J.; Shapley, J. R. Catalytic Nitrate and Nitrite Reduction with Pd–Cu/PVP Colloids in Water: Composition, Structure, and Reactivity Correlations. *J. Phys. Chem. C* **2009**, *113*, 8177–8185.

(60) Friedrich, M.; Armbrüster, M. Crystallite Size Controls the Crystal Structure of $Cu_{60}Pd_{40}$ Nanoparticles. *Chem. Mater.* **2009**, *21*, 5886–5891.

(61) Marakatti, V. S.; Sarma, S. C.; Joseph, B.; Banerjee, D.; Peter, S. C. Synthetically Tuned Atomic Ordering in PdCu Nanoparticles with Enhanced Catalytic Activity toward Solvent-Free Benzylamine Oxidation. *ACS Appl. Mater. Interfaces* **2017**, *9*, 3602–3615.

(62) Fulajtárova, K.; Soták, T.; Hronec, M.; Vávra, I.; Dobročka, E.; Omastová, M. Aqueous Phase Hydrogenation of Furfural to Furfuryl Alcohol over Pd–Cu Catalysts. *Appl. Catal. A Gen.* **2015**, *502*, 78–85.

(63) Mhadmhan, S.; Franco, A.; Pineda, A.; Reubroycharoen, P.; Luque, R. Continuous Flow Selective Hydrogenation of 5-Hydroxymethylfurfural to 2,5-Dimethylfuran Using Highly Active and Stable Cu–Pd/Reduced Graphene Oxide. *ACS Sustain. Chem. Eng.* **2019**, *7*, 14210–14216.

(64) Castegnaro, M. V.; Gorgeski, A.; Balke, B.; Alves, M. C. M.; Morais, J. Charge Transfer Effects on the Chemical Reactivity of Pd_xCu_{1-x} Nanoalloys. *Nanoscale* **2016**, *8*, 641–647.

(65) Kim, K. S.; Gossmann, A. F.; Winograd, N. X-ray Photoelectron Spectroscopic Studies of Palladium Oxides and the Palladium-Oxygen Electrode. *Anal. Chem.* **1974**, *46*, 197–200.

(66) Umpierre, A. P.; Machado, G.; Fecher, G. H.; Morais, J.; Dupont, J. Selective Hydrogenation of 1,3-Butadiene to 1-Butene by Pd(0) Nanoparticles Embedded in Imidazolium Ionic Liquids. *Adv. Synth. Catal.* **2005**, *347*, 1404–1412.

(67) Bernardi, F.; Alves, M. C. M.; Traverse, A.; Silva, D. O.; Scheeren, C. W.; Dupont, J.; Morais, J. Monitoring Atomic Rearrangement in Pt_xPd_{1-x} (x=1, 0.7, or 0.5) Nanoparticles Driven by Reduction and Sulfidation Processes. *J. Phys. Chem. C* **2009**, *113*, 3909–3916.

(68) Kilian, A. S.; Bernardi, F.; Pancotti, A.; Landers, R.; de Siervo, A.; Morais, J. Atomic Structure of Cr_2O_3/Ag(111) and Pd/Cr_2O_3/Ag(111) Surfaces: a Photoelectron Diffraction Investigation. *J. Phys. Chem. C*, 20452–20460.

(69) Chen, D.; Sun, P.; Liu, H.; Yang, J. Bimetallic Cu–Pd Alloy Multipods and Their Highly Electrocatalytic Performance for Formic Acid Oxidation and Oxygen Reduction. *J. Mater. Chem. A* **2017**, *5*, 4421–4429.

(70) Sarkar, C.; Koley, P.; Shown, I.; Lee, J.; Liao, Y.-F.; An, K.; Tardio, J.; Nakka, L.; Chen, K.-H.; Mondal, J. Integration of Interfacial and Alloy Effects to Modulate Catalytic Performance of Metal-Organic-Framework-Derived Cu–Pd Nanocrystals

toward Hydrogenolysis of 5-Hydroxymethylfurfural. *ACS Sustain. Chem. Eng.* **2019**, *7*, 10349–10362.

(71) Huang, Y.; Cai, J.; Zheng, S.; Guo, Y. Fabrication of a High-Performance Pb–PtCu/CNT Catalyst for Methanol Electro-Oxidation. *J. Power Sources* **2012**, *210*, 81–85.

(72) Cai, J.; Zeng, Y.; Guo, Y. Copper@Palladium–Copper Core–Shell Nanospheres as a Highly Effective Electrocatalyst for Ethanol Electro-Oxidation in Alkaline Media. *J. Power Sources* **2014**, *270*, 257–261.

(73) Choudhary, H.; Nishimura, S.; Ebitani, K. Hydrothermal Preparation of a Robust Boehmite-Supported *N*,*N*-Dimethyldodecylamine *N*-Oxide-Capped Cobalt and Palladium Catalyst for the Facile Utilization of Formic Acid as a Hydrogen Source. *ChemCatChem* **2015**, *7*, 2361–2369.

(74) Knecht, M. R.; Weir, M. G.; Frenkel, A. I.; Crooks, R. M. Structural Rearrangement of Bimetallic Alloy PdAu Nanoparticles within Dendrimer Templates to Yield Core/Shell Configurations. *Chem. Mater.* **2008**, *20*, 1019–1028.

(75) Myers, S. V.; Frenkel, A. I.; Crooks, R. M. X-ray Absorption Study of PdCu Bimetallic Alloy Nanoparticles Containing an Average of 64 Atoms. *Chem. Mater.* **2009**, *21*, 4824–4829.

(76) Toshima, N.; Harada, M.; Yonezawa, T.; Kushihashi, K.; Asakura, K. Structural Analysis of Polymer-Protected Palladium/Platinum Bimetallic Clusters as Dispersed Catalysts by using Extended X-ray Absorption Fine Structure Spectroscopy. *J. Phys. Chem.* **1991**, *95*, 7448–7453.

(77) Nellist, P.; Pennycook, S. Accurate Structure Determination from Image Reconstruction in ADF STEM. *J. Microsc.* **1998**, *190*, 159–170.

(78) James, E.; Browning, N. Practical Aspects of Atomic Resolution Imaging and Analysis in STEM. *Ultramicroscopy* **1999**, *78*, 125–139.

(79) Da Silva, F. P.; Fiorio, J. L.; Gonçalves, R. V.; Teixeira-Neto, E.; Rossi, L. M. Synergic Effect of Copper and Palladium for Selective Hydrogenation of Alkynes. *Ind. Eng. Chem. Res.* **2018**, *57*, 16209–16216.

(80) Kaneda, K.; Mizugaki, T. Design of High-Performance Heterogeneous Catalysts using Apatite Compounds for Liquid-Phase Organic Syntheses. *ACS Catal.* **2017**, *7*, 920–935.

(81) Corma, A. Heterogeneous Catalysis: Understanding for Designing, and Designing for Applications. *Angew. Chem. Int. Ed.* **2016**, *55*, 6112–6113.

(82) Kaneda, K.; Mizugaki, T. Development of Concerto Metal Catalysts using Apatite Compounds for Green Organic Syntheses. *Energy Environ. Sci.* **2009**, *2*, 655–673.

(83) Zhang, P.; Wu, T.; Jiang, T.; Wang, W.; Liu, H.; Fan, H.; Zhang, Z.; Han, B. Ru–Zn Supported on Hydroxyapatite as an Effective Catalyst for Partial Hydrogenation of Benzene. *Green Chem.* **2013**, *15*, 152–159.

(84) Xu, G.; Guo, J.; Zhang, Y.; Fu, Y.; Chen, J.; Ma, L.; Guo, Q. Selective Hydrogenation of Phenol to Cyclohexanone over Pd–HAP Catalyst in Aqueous Media. *ChemCatChem* **2015**, *7*, 2485–2492.

Chapter 3

Effect of Support on the Formation of CuPd Alloy Nanoparticles for the Hydrogenation of Succinic Acid

Abstract

Three kinds of supported CuPd catalysts are studied for the hydrogenation of succinic acid (SA) to value-added chemicals including γ-butyrolactone (GBL), 1,4-butanediol (BDO), and tetrahydrofuran (THF). The strength of metal–support interaction played an essential role in the construction of CuPd nanoparticles (NPs), inducing different catalytic activity and selectivity. In-depth characterizations revealed that while homogeneous alloys were dominantly constructed on TiO_2 and SiO_2 supports, heterogeneous alloy with a great extent of Cu segregation was preferably formed on γ-Al_2O_3. Although a high GBL selectivity was achieved over CuPd/TiO_2, large particles with the least Cu segregation caused a lower SA conversion while preventing it from further hydrogenation. In contrast, smaller CuPd NPs with a minority of Cu segregation on SiO_2 made it a superior catalyst in the BDO production. Notably, strong Lewis acid sites on γ-Al_2O_3 occupied a major role in the formation of highly selective THF with a nearly quantitative yield.

3.1 Introduction

Heterogeneous catalysis using functional nanomaterials plays an indispensable role in our modern energy and chemical transformations [1, 2]. The unique properties of nanomaterials as catalysts derive from their specific reactivities due to the enhanced relative surface areas and quantum effects [3]. These effects coupled with structural and morphological changes thus render nanomaterials potential candidates in various fields including catalysis [4]. In the past few decades, major research efforts were devoted to the investigation of metal-based nanocatalysts [5]. The use of metallic nanocatalysts was mainly based on the inherently electronic [6] and magnetic [7] properties of metals, leading to their high catalytic efficiencies and selectivities compared to bulk metals and molecules [8, 9]. On the basis of nanoscience, it has been well known that the catalysis performance can be highly sensitive to the particle size and shape at the nanoscale [10]. On the other hand, the intrinsic composition of metallic NPs has also been recognized as one of the crucial factors to control reactivity and selectivity on specific catalytic reactions [3]. Thus, besides the development of monometallic catalysts, bimetallic nanocrystals with well-defined core-shell, alloyed, or intermetallic structures has been emerging as a topic of choice in heterogeneous catalysis [11]. In comparison with monometallic analogues, bimetallic catalysts are expected to not only offer extended and distinct properties due to synergistic effects [12] upon alloying but also minimize the use of precious metal for advancements toward green nanocatalysis [13]. Although the nature of metals plays an essential role in catalytic performance, the support, via its properties and interaction with the NPs, can be considered as an integral part in controlling the stability, size, and shape of active metal species [14]. Besides the engagement with catalyst active sites which reduces their mobility then prevents them from sintering [15–17], synergistic effects between catalysts and supports such as electron transfer have also been reported in many catalyst systems[18–22]. Overall, offering unique and superior reactivity, selectivity, and stability due to synergism between the metals themselves and/or with the supports, supported metal nanocatalysts, therefore, have been extensively used in the synthesis of fuel [23] and bio-based chemicals [24].

Advancements in science and technology after all is for ensuring a healthy and productive life in harmony with nature [25]. In other words, the development is to fulfill the human's needs without comprising the environment. In the chemistry context, as important as the catalyst which is considered as a fundamental pillar, the utilization of benign and renewable feedstocks holds the essential role to advance the goals of green and sustainable chemistry [26]. Indeed, as the growing scarcity, uncertain price, and often associated with environmental issues of fossil hydrocarbons, the importance of alternative resources of energy and organic carbon has become more evident. Biomass carbohydrates, which are diversely available and renewable resources, have emerged as an ideal candidate to reduce the heavy dependence on petroleum and natural gas resources [27–30]. Succinic acid (SA) has been listed among the new bio-derived key building block chemicals that can transform into a variety of high-value chemicals, as a replacement of the maleic acid platform [27, 28, 31]. However, not until recently when the considerable advancements in bio-fermentation and purification technologies have been successfully made for the production of bio-based SA, it starts to become an economically attractive and competitive supply [32, 33]. Hydrogenation of carboxylic acids and their derivatives currently becomes the subject of intense research in terms of upgrading bio-based feedstocks to a vast number of platform chemicals and intermediates [34]. As for SA, it undergoes catalytic reduction over metal-based catalysts to commodity chemicals such as γ-butyrolactone (GBL), 1,4-butanediol (BDO), and tetrahydrofuran (THF), which widely used in the manufactures of important polymers and industrial solvents [35]. In general, the low electrophilicity associated with polarization of the carbonyl carbon makes difficulties in the hydrogenation of carboxylic acids and their derivatives [36]. For hydrogenation of SA in particular, harsh conditions or long reaction time are necessary due to the low reactivity of SA compared to its analogues [37, 38].

The product selectivity was reported to be strongly influenced by catalyst and reaction conditions. Extensive work has been done on the hydrogenation of SA which revealed that GBL was the main product over monometallic catalysts, while the addition of secondary metal promoter in the bimetallic catalysts facilitated the conversion of SA and increased the selectivity of BDO [39–41] or THF [42–44]. For example, the addition of Ru in Re–Ru supported on mesoporous carbon favors the formation of BDO [39], whereas the Ir–Re/C bimetallic catalyst promotes the production of THF [44]. The use of bimetallic based on earth-abundant metals such as Fe and Cu was also reported for the SA hydrogenation. Liu et al. reported that Fe can be an efficient promoter in Pd$-$5FeO$_x$/C for the SA hydrogenation, which not only enhanced the catalytic activity but also able to control the product distribution [45]. Whereas the Pd–Cu supported on alumina xerogel was found to be an efficient bimetallic catalyst for highly selective GBL [46]. In chapter 2, the hydroxyapatite (HAP) supported CuPd bimetallic catalysts for the hydrogenation of SA were reported [47]. The study discovered that the hydrogenation products can be selectively controlled by simply adjusting the Cu:Pd metal ratio. Extensive characterization techniques revealed that the Cu rich CuPd alloying nanoparticles (NPs): in particular, 8 wt%-Cu and 2 wt%-Pd composition, served as the most potential catalyst for the SA hydrogenation toward highly selective BDO. Since the metal–support interaction greatly affects the nanostructure of metal catalysts and catalytic behaviors for certain reactions, further investigation on the support effect for the unique Cu rich CuPd catalyst system is an attractive subject. Therefore, in the present chapter, to deepen our understanding of the CuPd bimetallic catalysts, the effects of catalyst supports on the construction of the CuPd nanostructures as well as their own contributions to the hydrogenation of SA, are further studied.

3.2 Experimental Section

3.2.1 Materials

All the chemicals and their details are listed in Table 3.1 below:

Table 3.1: List of chemicals used in this research

No.	Name	Formula	Supplier
1	1,4-butanediol (BDO)	$C_4H_{10}O_2$	Wako
2	1,4-dioxane	$C_4H_8O_2$	Wako
3	1-butanol (BuOH)	C_4H_9OH	Wako
4	2-propanol	C_3H_8O	Wako
5	Butyric acid (BA)	$C_4H_8O_2$	Sigma Aldrich
6	Copper (II) nitrate trihydrate	$Cu(NO_3)_2 \cdot 3\,H_2O$	Wako
7	Copper oxide	CuO	STREM
8	Palladium (II) nitrate	$Pd(NO_3)_2$	Wako
9	Silicon dioxide, G-6, 3µm	SiO_2	Fuji Silysia
10	Succinic acid (SA)	$C_4H_6O_4$	Kanto
11	Tetrahydrofuran (THF)	C_4H_8O	Wako
12	Titanium dioxide (rutile form)	TiO_2	Kanto
13	γ-alumina, JRC-ALO-8	γ-Al_2O_3	Sumitomo Chemical
14	γ-butyrolactone (GBL)	$C_4H_6O_2$	Wako

3.2.2 Catalyst Preparation

TiO_2 support was pretreated at 750 ℃ for 4 h, while γ-Al_2O_3 and SiO_2 supports were used without any pretreatment. Supported CuPd bimetallic catalysts were synthesized by adapting a previously reported protocol [47]. In general, the precursor solution was prepared by dissolving $Cu(NO_3)_2 \cdot 3\,H_2O$ and $Pd(NO_3)_2$ into a round-bottom flask containing 150 mL deionized water. Subsequently, the support was gradually added to the solution and stirred thoroughly at room temperature for 12 h. The impregnated sample was then evaporated to remove water and dried at 110 ℃ for 12 h. The obtained dried solid was further calcined in at 500 ℃ for 4 h and finally reduced in a flow of 5% H_2/N_2 (60 mL min^{-1}) at 500 ℃ for 2 h. The samples were typically characterized or used for reactions as quick as possible after reduction, however, it is inevitable that the samples were contacted with air during weighing and transportation. It is noted that on the basis of the previous study [47], the weights of metal precursors and supports were adjusted to nominally obtain 8 wt% of Cu and 2 wt% of Pd in the final supported CuPd catalyst samples.

3.2.3 Catalyst Characterization

In general, the reduced samples were used for the following characterizations, unless otherwise mentioned. Powder X-ray diffraction (XRD) was conducted to study the crystal structures of the prepared catalyst samples. The measurements were performed on a Rigaku Smart Lab X-ray diffractometer (Rigaku Co.) with a Cu Kα radiation ($\lambda = 0.154$ nm) at 40 kV and 30 mA. The diffraction patterns were analyzed using the database of the Joint Committee of Powder Diffraction Standard. The catalyst morphologies were observed by transmission electron microscopy (TEM) using an H-7100 (Hitachi) and H-7650 (Hitachi) operated at 100 kV. High-resolution TEM (HRTEM) and energy-dispersive X-ray spectroscopy (EDS) line scanning analysis were performed by using a JEM-ARM200F (JEOL Ltd., Japan). X-ray photoelectron spectra (XPS) were acquired using an Axis-Ultra DLD spectrometer system (Shimadzu Co. and Kratos Analytical Ltd.) with the monochromatic Al Kα (1486 eV) X-ray resources. The binding energies (BE) were calibrated using the C 1s spectrum of adventitious carbon contamination as an internal standard. Peak deconvolutions were performed using the XPSPEAK4.1 software.

X-ray absorption fine structure (XAFS) spectra were recorded at the BL07 (for Pd K-edge) and BL11 (for Cu K-edge) stations of the SAGA light source under the proposal no. 1910092R. The storage ring was operated at 1.4 GeV and Si (220) and Si (111) single crystals were employed to obtain a monochromatic X-ray beam for Pd K-edge and Cu K-edge measurements, respectively, in transmission mode. To optimize the signal at each target edge, XAFS samples were individually prepared by grinding to fine powders and pressing in air to pellets with diameter of 10 mm from the same lots of catalysts. Analyses of X-ray absorption near edge spectra (XANES) and extended X-ray absorption fine structure (EXAFS) were processed on the Athena and Artemis software of the Demeter suite version 0.9.26.

Temperature programmed reduction (TPR) and desorption (TPD) experiments were conducted on a BELCat II (MicrotracBEL, Corp.). For H_2-TPR measurements, samples were arranged in between quartz wool fixed inside a quartz triple cell. The samples were heated from 50 ℃ to 700 ℃ at a ramping rate of 10 ℃ min^{-1} in a gaseous mixture of 10% H_2/Ar with a flow of 30 mL min^{-1}. A molecular sieve (4A 1/16) trap was attached to prevent water from passing through the detector. The hydrogen consumption was monitored by a thermal conductivity detector (TCD) and quantified by means of calibration with pure CuO standard (99.999%). While for NH_3-TPD, the samples were loaded in the same type of quartz cell and treated at 500 ℃ in a flow of He for 1 h before the adsorption of NH_3 at 100 ℃ for 1 h. The NH_3 saturated samples were then treated with water vapor for 3 times in an attempt to remove physically adsorbed ammonia. The amount of desorbed NH_3 was monitored by a linked quadrupole mass spectrometer (BELMASS SII) at a temperature range of 100–550 ℃ at a heating rate of 10 ℃ min^{-1}. Analyses on the acid density and peak deconvolution were performed on the ChemMaster version 1.4.16.

Infrared spectroscopy (IR) spectra of adsorbed pyridine were recorded in a range of 4000–400 cm^{-1} with a JASCO-4700 FTIR spectrometer. A 10 mm diameter of the self-supporting pellet was prepared and pretreated in situ at 500 ℃ under vacuum for 1 h. After cooling the IR cell to room temperature, pyridine was dosed onto the sample for 30 min, followed by evacuation at the same temperature for 1 h to remove the physically excessively adsorbed pyridine and at 120 ℃ for 1 h to remove stronger adsorbed sites. N_2-adsorption/desorption experiments were conducted on a BELSORP-mini analyzer (MicrotracBEL, Corp.). Surface areas of samples were calculated based on the Brunauer–Emmett–Teller (BET) theory.

3.2.4 Catalyst Evaluation

In a typical catalytic test, a solution including 1,4-dioxane solvent (10 mL), SA (0.1 g), and the reduced supported CuPd catalyst (0.1 g) was loaded into a 50 mL glass vessel together with a magnetic stirrer bar. The vessel was then inserted inside a stainless-steel autoclave reactor (Taiatsu Tech., Japan) and firmly sealed. The reactor was purged from the remaining air by pure H_2 (99.999%) several times before being pressurized to 8.0 MPa at room temperature. Thereafter, the reactor was set into an aluminum heating block at 200 ℃ under vigorous stirring (780 rpm) for 96 h reaction.

After a designated reaction period, the reactor was removed from the heater and cooled to the ambient air temperature. The reaction slurry was then centrifugated (Kubota centrifuge 2410) to separate from the catalyst. The isolated reaction mixture was subsequently analyzed by gas chromatography (GC, Shimadzu GC-2014) with a polar DB-FFAP column (Agilent). The column temperature program was set to increase from 50 ℃ (2 min) to 240 ℃ (5 min) at a rate of 20 ℃ min^{-1} while the injection and detector temperatures were 250 ℃ and 280 ℃, respectively. The conversion of SA was analyzed by means of high-performance liquid chromatography (Water 2414) equipped with a refractive index detector. An aqueous solution of H_2SO_4 (10 mM) was used as an eluent pumped at a flow rate of 0.5 mL min^{-1} through an Aminex HPX-87H column (Bio-Rad) operated at 50 ℃.

3.3 Results and discussion

3.3.1 Effect of Support on the Catalytic Performance

The activity of CuPd NPs on several supports including SiO_2, γ-Al_2O_3, and TiO_2 was investigated for the hydrogenation of SA, as shown in Figure 3.1A. In general, all these bimetallic catalysts exhibited good to excellent activity since more than 60% conversion of SA was attained. It is noteworthy mentioning that the catalytic activity was apparently different depending on the support since quantitative conversions of SA were achieved over SiO_2 and γ-Al_2O_3 supported CuPd, while that figure over the CuPd/TiO_2 catalyst was only 73% at the same reaction conditions. Interestingly, excellent selectivities toward different products were observed: particularly, the selectivities of 86% for BDO, 97% for THF, and 90% for GBL were afforded at over the SiO_2, γ-Al_2O_3, and TiO_2 supported CuPd bimetallic catalysts, respectively. Quantitative conversion of SA can be achieved over CuPd/TiO_2 at longer reaction time of 120 h. However, at this conversion, the

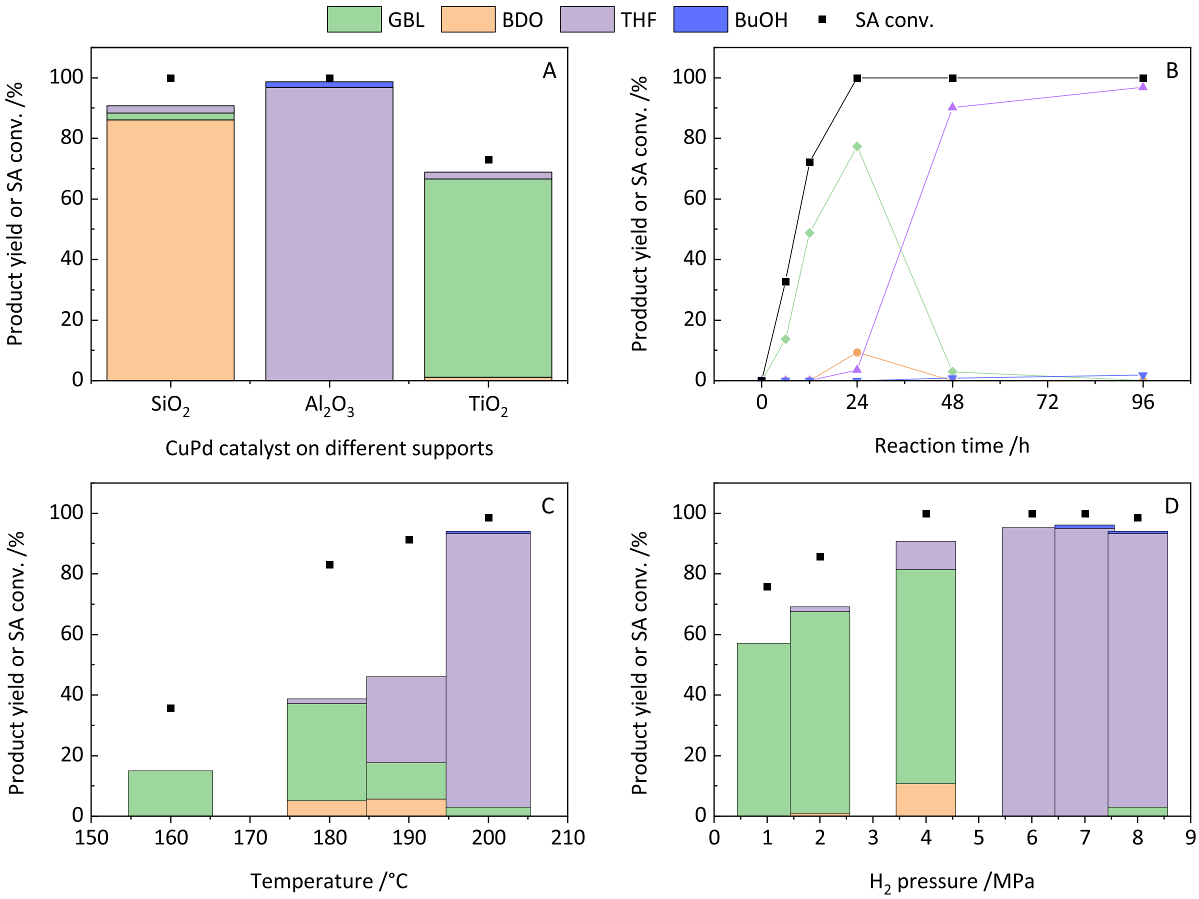

Figure 3.1: (A) Hydrogenation of SA over different supported CuPd bimetallic catalysts and (B–D) studies of reaction parameters. Reaction conditions: SA (0.1 g), supported CuPd catalyst (0.1 g), 1,4-dioxane (10 mL), temperature (200 °C, for A, B, and D), H_2 pressure (8 MPa, for A, B, and C), reaction time (96 h for A, 48 h for C and D). γ-Al_2O_3 supported CuPd catalyst was used in B, C, and D.

GBL selectivity was significantly decreased to 62% due to a significant loss of products to gaseous phase, which can be contributed to the formation of light products via side reactions such as C–C bond cleavage [40].

To confirm the superior performance of the present bimetallic catalysts, the hydrogenation of SA over the bare catalyst supports and monometallic catalysts were carried out and the results are shown in Table 3.2. Obviously, in the absence of metal components, the bare supports were failed to accelerate the SA hydrogenation since none of the target products could be observed. On the other hand, the supported Cu monometallic catalysts show modest activity as only 16% yield of GBL was obtained over the Cu/γ-Al_2O_3. In contrast, the supported Pd monocatalysts exhibited higher activities since >90% conver-

Table 3.2: Hydrogenation of SA over bare supports and monometallic catalysts[a]

Catalyst/support	SA conversion /%	Product yield /%				
		GBL	BDO	THF	BA	BuOH
γ-Al_2O_3	39	0	0	0	0	0
SiO_2	21	0	0	0	0	0
TiO_2	13	0	0	0	0	0
Cu/γ-Al_2O_3	86	16	0	0	0	0
Cu/SiO_2	16	0	0	0	0	0
Cu/TiO_2	22	0	0	0	0	0
Pd/γ-Al_2O_3	100	0	0	0	54	30
Pd/SiO_2	90	67	0	1	11	0
Pd/TiO_2	100	28	0	0	31	17

[a] The monometallic catalysts were prepared using 10 wt% of metals.

sion of SA was achieved. In this momometallic catalyst system, the product selectivity was also found to be influenced by the support. Particularly, the hydrolysis to butyric acid and further reduction to 1-butanol (BuOH) were dominantly observed over the Pd/γ-Al_2O_3, and Pd/TiO_2, while the formation of the intermediate GBL was prevalent over the Pd/SiO_2.

Considering the existence of much research on synthesis of BDO while lesser reports on open literatures for the production of THF from SA [48], hereafter, only results on the optimization of the reaction parameters for THF production are presented. Figure 3.1B demonstrates time-progression on the hydrogenation of SA over CuPd/γ-Al_2O_3. It is clear that SA conversion and the formation of GBL increased rapidly during the first 12 h, while none of the other products was detected. After 24 h, when quantitative conversion of SA was reached together with the highest point in the yield of GBL, BDO and THF were observed with less than 10% selectivities. Afterwards, while both GBL and BDO dropped significantly to less than 5% in selectivity or completely transformed, that figure for THF climbed rapidly to more than 90%. Further prolonging the reaction time can slightly increase the selectivity of THF, affording 97% as the maximum.

The appearance of BDO and THF as indicated in Figure 3.1B suggested that these products can form concurrently. Moreover, while the BDO yield maintained similarly, the

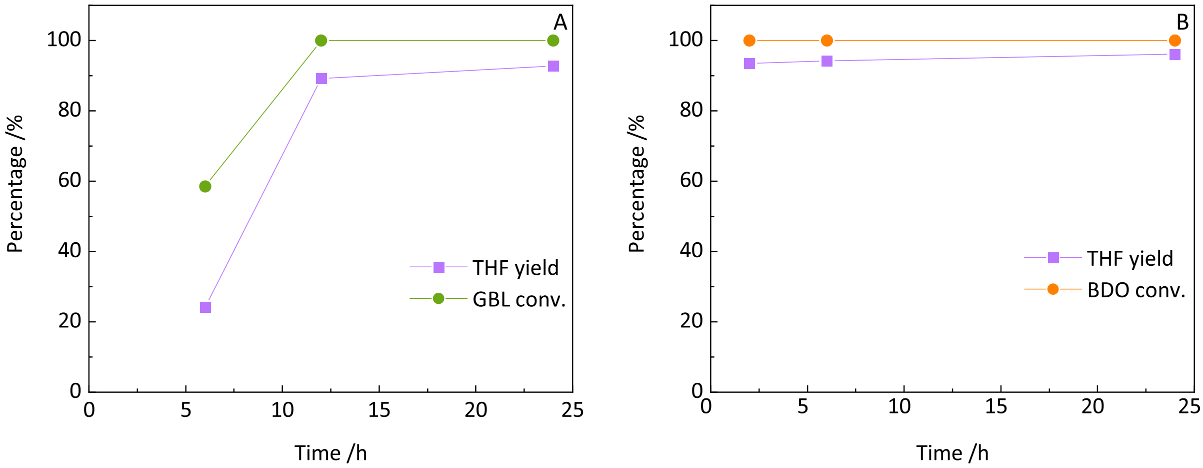

Figure 3.2: CuPd/γ-Al_2O_3 catalyzed (A) hydrogenation of GBL and (B) dehydration of BDO. *Reaction conditions:* substrate (0.1 g), catalyst (0.1 g), 1,4-dioxane (10 mL), temperature (200 ℃), H_2 pressure (8 MPa).

THF yield increased with the decrease of GBL, as described in Figure 3.1C. In addition, a small amount of THF can be detected at lower pressure (Figure 3.1D) suggested that THF can be directly converted from GBL. Additional experiments were carried out using GBL as starting material, which showed that GBL was transformed into THF directly without the detection of BDO (Figure 3.2A), further confirming the aforementioned suggestion. Nevertheless, we cannot rule out the possibility that THF can be converted partly by dehydration, as indicated in Figure 3.1B, since BDO yield gradually went down along with the growth of THF. The experiment using BDO as starting material showed that the dehydration of BDO proceeded very fast under the present catalyst system, affording the THF yield of 93% after only 2 h reaction (Figure 3.2B). Therefore, we suggest that THF can be either converted from direct hydrogenation of GBL or dehydration of BDO under the present catalyst system and conditions.

As reported elsewhere [49], elevated temperature and pressure are required to have high selectivity toward THF from SA. This is applicable for the present catalyst system since the high temperature of 200 ℃ is necessary for the formation of THF. Lower temperature gives lower conversion of SA and selectivity of THF due to the formation of gaseous by-products via side reactions [40]. Higher temperatures than 200 ℃ might not bring improvement on the selectivity but can give rise to undesired hydrolysis products [50] and might not practically desirable [51]. Fair to excellent activity and good selectivity toward GBL was obtained at the lower pressures of H_2. However, high selectivity of THF was only achieved at higher pressure than 6 MPa in the present catalyst system. It is noted that even though much lower H_2 pressure was reported for the dehydration of BDO to THF [51], the direct conversion of SA required harder conditions due to the needs to form intermediate GBL and to overcome the substrate inhibitory effects [31]. Additionally, in comparison with BDO which is formed through an equilibrium reaction with GBL under lower temperature and higher pressure, THF formation is favored higher temperatures and lower pressures [52, 53]. Therefore, to maximize the yield of THF via hydrogenation of SA, careful optimization of the reaction conditions is highly desirable.

3.3.2 Analysis and Discussion on the Structure-Activity Relationship

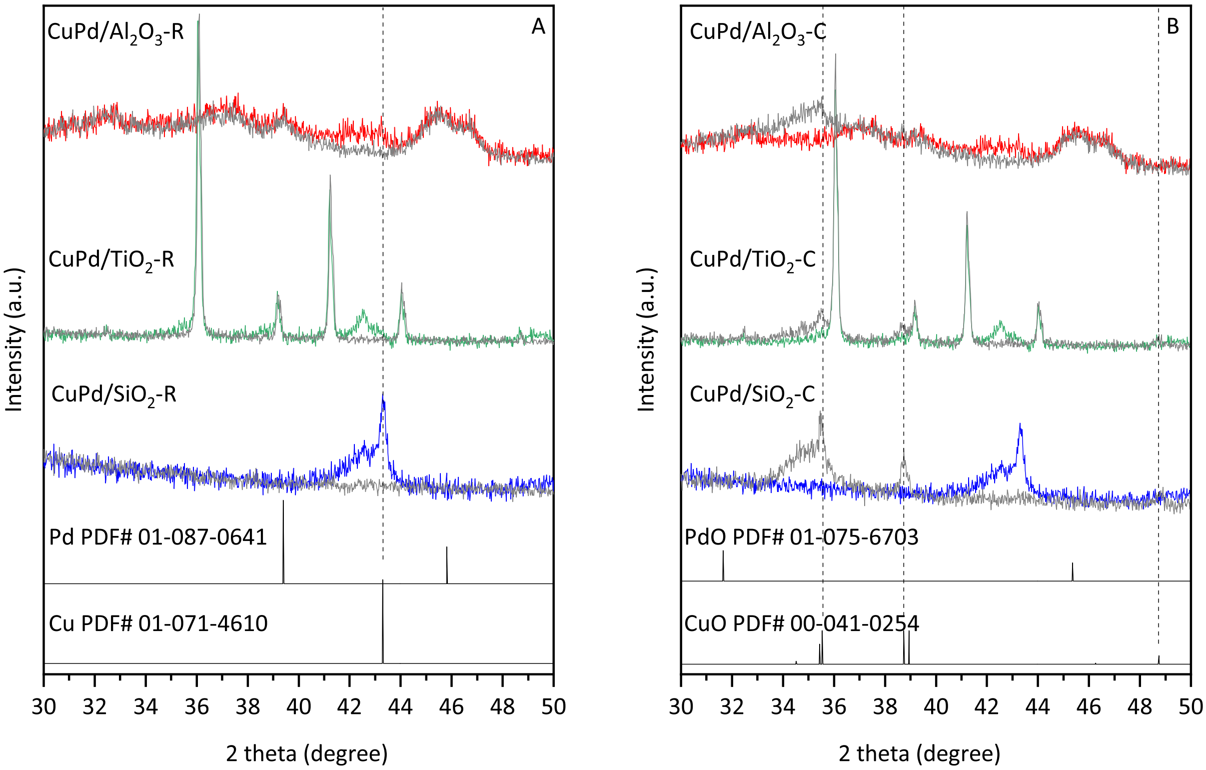

Figure 3.3: XRD patterns of the reduced CuPd catalysts (vivid color) with (A) their corresponding supports (grey color) or (B) their calcined catalysts (grey color)

Figure 3.3A shows comparisons between the XRD patterns of the reduced catalyst sample with their corresponding supports. A closer look at the 2θ of 43.3° of SiO_2 supported CuPd nanoparticles gives us evidence about the existence of isolated metallic Cu. Whereas, the adjacent peak shifted to the lower degree suggests a formation of CuPd alloys. In the case of TiO_2 supported CuPd, the peaks indicated metallic Cu are not apparent, while a clear peak appears at 42.5° might be attributed to CuPd alloy which is dominant compared to isolated metallic Cu phase. It is noted that while the diffraction peaks of NPs on SiO_2 and TiO_2 can be apparently distinguishable from their supports, no distinct diffraction peak was observed on the CuPd/γ-Al_2O_3 but mainly the typical pattern of the support. This can be ascribed to the highly amphoteric nature of γ-Al_2O_3 and/or the uniform dispersion of small nanoparticles on the support [54, 55]. Nevertheless, a broad and dispersed peak observed at the lower 2θ position than 43.3° might suggest the existence of CuPd alloy and/or highly dispersed Cu in close contact. The peaks indicating metallic Pd are not observable due to its low concentration in these bimetallic catalyst samples. Figure 3.3B shows comparisons between the calcined and reduced CuPd catalyst. In all the calcined samples, CuO diffraction peaks can be observed at the 2θ of 35.5°, 38.7°, and 48.7°. Adjacently broad peaks shift to lower 2θ ranging from 33.1° to 35.5° can be assigned to the Cu_xPd_yO mixed oxides which formed during the calcination step. These diffraction peaks disappeared after reducing, indicating that the calcined catalyst samples were completely reduced.

TEM images and the corresponding particle size distributions of the reduced CuPd NPs on different support are presented in Figure 3.4. A relatively narrow size distribution between 2 and 4 nm with an area-weighted average diameter of 3.0 nm was observed for the γ-Al_2O_3 supported CuPd NPs. Thus, this result is perfectly consistent with the XRD since it is typically reported that the particles with smaller sizes than 5 nm do not show apparent diffraction patterns [56, 57]. In contrast, wide ranges of size distributions with average diameters of 6.0 and 7.7 nm were obtained for the CuPd NPs on SiO_2, and TiO_2 supports, respectively. The difference in the sizes of NPs in this catalyst system can possibly be influenced by the characteristics of supports, i.e., surface area and/or acidity influence the support–metal interactions. Particularly, the more strong metals

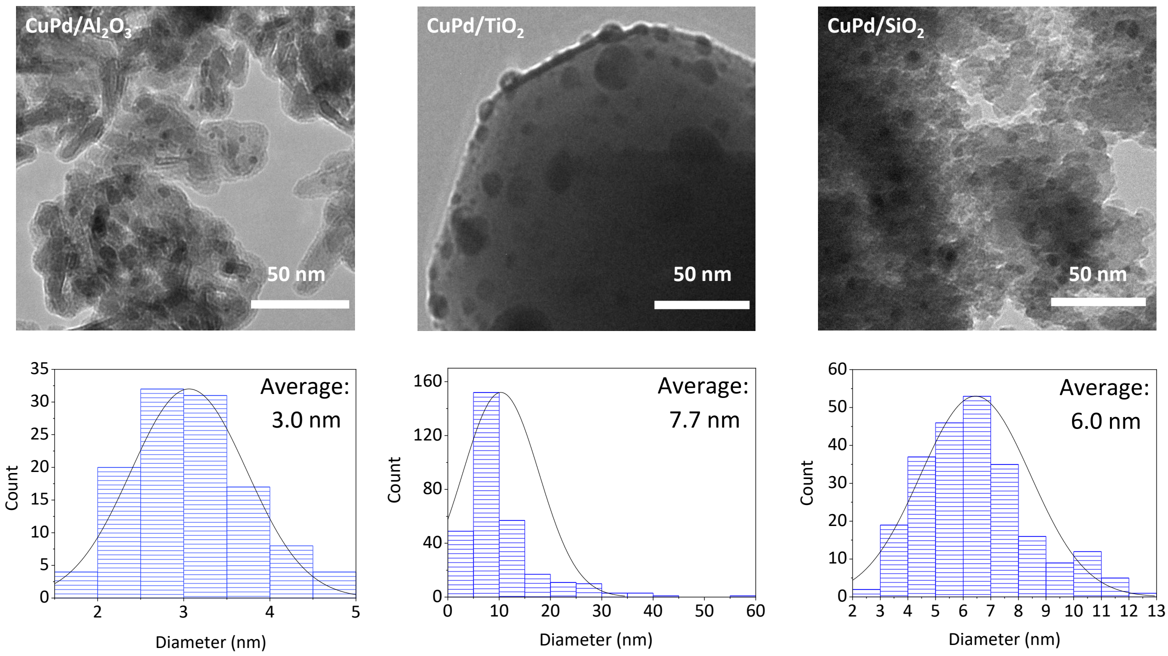

Figure 3.4: Representative TEM images (top) and particle size distributions (bottom) of CuPd NPs on different supports

are attached to the supports, the more weakly they bind together and the less sintering they are in the catalysts [17]. In particular, the stronger interaction between Cu and the γ-Al$_2$O$_3$ support, possibly related to the OH group on the support surface [58], induced a weaker interaction with Pd, compared to that of the other supports. In addition, the effect of supports on the NP sizes and the morphology-dependent catalytic activity was reported widely [59–62]. Therefore, to some extent, the lower activity of CuPd/TiO$_2$ catalyst on the hydrogenation of SA can result from its greater sintering to larger particles. To further study on the compositional structures, HRTEM and line EDS line scanning were performed, and the results are shown in Figure 3.5A–F. The observed lattice fringes of all the bimetallic catalysts are about 2.13–2.17 Å, which fall in between the *d*-spacing of the (111) planes of Cu (2.088 Å, PDF #01-071-4610) and Pd (2.285 Å, PDF #01-087-0641). In addition, the line scanning results show that both Cu and Pd are distributed throughout the particles, which visually indicate the existence of CuPd alloying NPs.

XPS spectra at Cu 2*p* and Pd 3*d* regions for the reduced catalyst samples were collected and illustrated in Figure 3.6. The Cu 2$p_{3/2}$ spectra of CuPd NPs on different supports

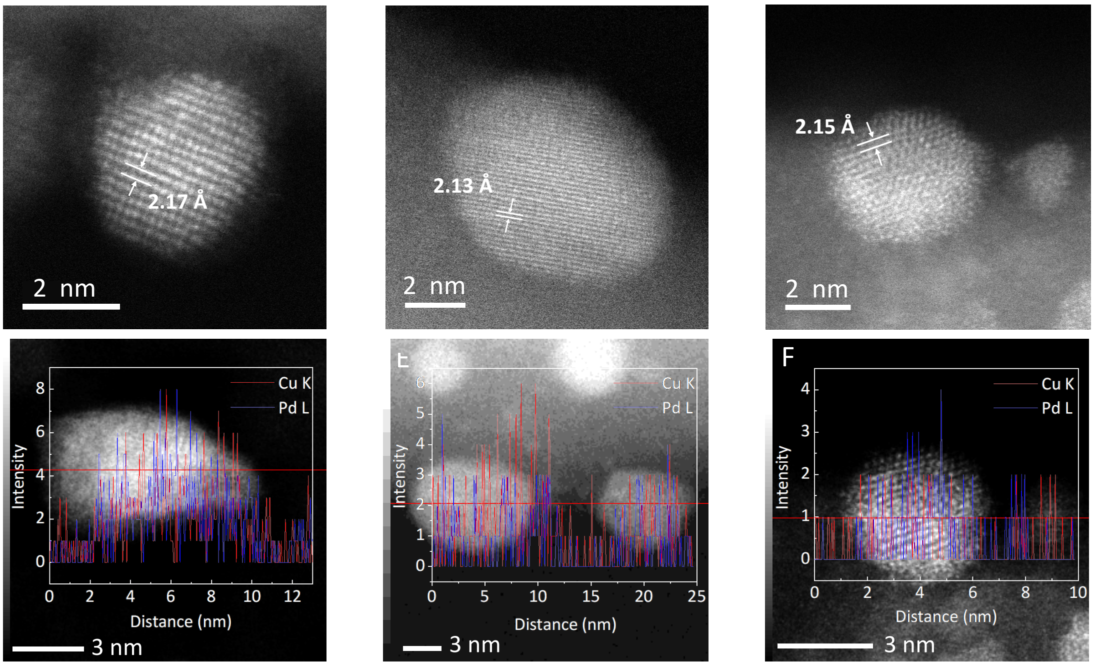

Figure 3.5: HRTEM of (A) CuPd/γ-Al_2O_3, (B) CuPd/TiO_2, and (C) CuPd/SiO_2 and (D–F) their corresponding line scanning results

can be deconvoluted into three components at 932.2–933.2 eV and 933.7–935.9 eV (Figure 3.6A), corresponding to the peaks of Cu–Cu in Cu^0 and Cu–O in CuO [63, 64]. In comparison with previous reports [65–67] for the BE of Cu $2p_{3/2}$ at ca. 933.5 eV, chemical shifts of approximately 0.3–1.3 eV for Cu $2p_{3/2}$ were observed in these CuPd bimetallic catalysts. In accordance with other researches [68–71], these variations in the BE revealed the strong interaction between Cu and Pd as a result of alloying. Moreover, the presence of satellite peaks diffused around 941–944 eV indicated that during the preparation for XPS measurements, the reduced samples were partially re-oxidized [54]. Noticeably, the fraction of Cu^{2+} on the surface of CuPd/TiO_2 is dominant compared to the Cu^0, indicating the ease of oxidation on this sample. Similar results on Pd $3d_{5/2}$ was obtained as the peak of Pd^{2+} also existed at a large quantity.

The XRD results indicated the formation of alloy NPs in these different supported CuPd NPs, generally offering strong resistance toward oxidation [69, 70, 72]. Therefore, the difference in oxidation resistance of these samples can be explained by additional factors, i.e., the morphology of the catalyst sample. In agreement with the TEM results,

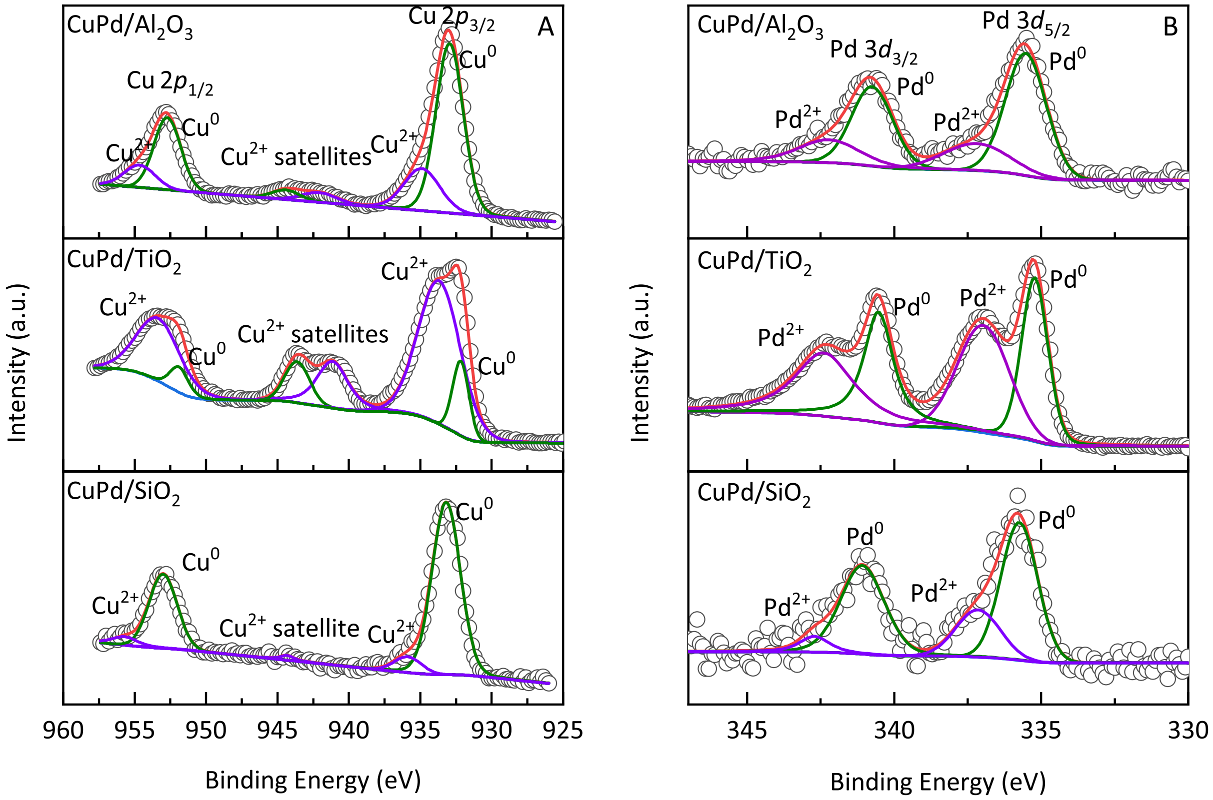

Figure 3.6: Deconvoluted XPS spectra at (A) Cu 2*p* and (B) Pd 3*d* regions of different supported CuPd catalysts

the weaker interaction with the TiO$_2$ support resulted in the large particle size of CuPd NPs which have a tendency to locate at the edge of its support can be a reason for its susceptibility to oxidation. As for the γ-Al$_2$O$_3$ and SiO$_2$ supports, stronger metal—support interactions dramatically enhanced oxidation resistance of CuPd NPs, despite the lesser extent of alloying in these two catalysts as suggested by XRD. The Pd 3$d_{5/2}$ can be fitted into two peaks at 335.2–336.1 eV and 337.0–337.6 eV (Figure 3.6B), with respect to Pd^0 and Pd^{2+} components [73–76]. Similarly, chemical shifts about 0.2–1.1 eV compared to the reported Pd 3$d_{5/2}$ BE value of 336.3 eV were determined. The XPS experiments comparing between the monometallic and bimetallic NPs on the same supports were also carried out (Figure 3.7A–C). The results show that the BE at Pd 3d core-level of all the bimetallic catalysts shifted to higher value compared to those of the monometallic catalysts, clearly confirming the formation of CuPd alloy leading to the partial charge transfer between the two metals [69, 71, 77].

Figure 3.8A describes Cu K-edge XANES spectra of different supported CuPd catalysts

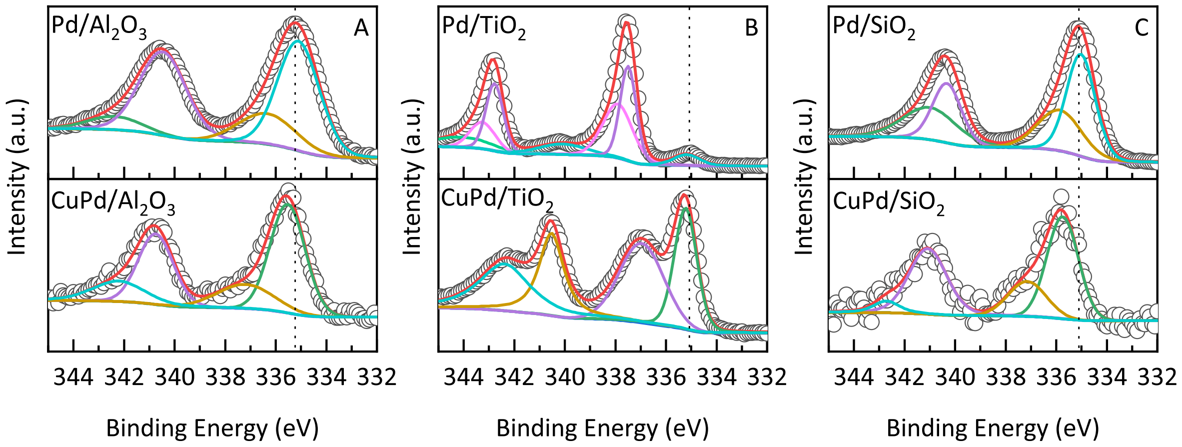

Figure 3.7: XPS spectra of (A) γ-Al$_2$O$_3$, (B) TiO$_2$, and (C) SiO$_2$ supported monometallic and their corresponding bimetallic catalysts at Pd 3d regions.

in comparison with that of the Cu references. There are relatively weak white lines that can be observed in the CuPd/SiO$_2$ and CuPd/TiO$_2$ catalysts. The peak shape of the former is generally similar to that of the Cu foil, indicating the dominant of metallic Cu. However, the first two peaks of the later tend to merge into one which resembles the peak shape of CuO. A stronger white line can be seen in the CuPd/γ-Al$_2$O$_3$, suggesting a larger amount of oxidized Cu [57, 78, 79]. Accordingly, it is envisaged that the oxidized CuO might result in a considerable fraction of Cu unavailable for alloying with Pd [80].

The first-derivative of $\chi\mu$(E) function of XANES can be used to determine the maximum point of the first peak in the rising edge step for Cu foil, Cu$_2$O, and CuO, which are 8978, 8979, and 8982 eV, respectively (Figure 3.8B). These shakedown-like features of the tested catalyst samples are broader and lower in their intensities, suggesting decreases in the zero-valence component of Cu and increases in the oxidized Cu species. This finding was qualitatively confirmed by the linear combination fit (LCF) and peak fitting of Fourier transformed (FT) EXAFS at R-space and visualized in Figure 3.8C. It should be noted that although there are variations between the dominant phase of Cu species on γ-Al$_2$O$_3$ determined by XAFS and XPS due to longer air exposing time in the sample pelletizing step of the former technique, the information derived from analysis at Cu K-edge is valuable for elucidating the differences in the structures among these catalysts. Particularly, the dominance of CuO species confirms that more Cu was unable to combine

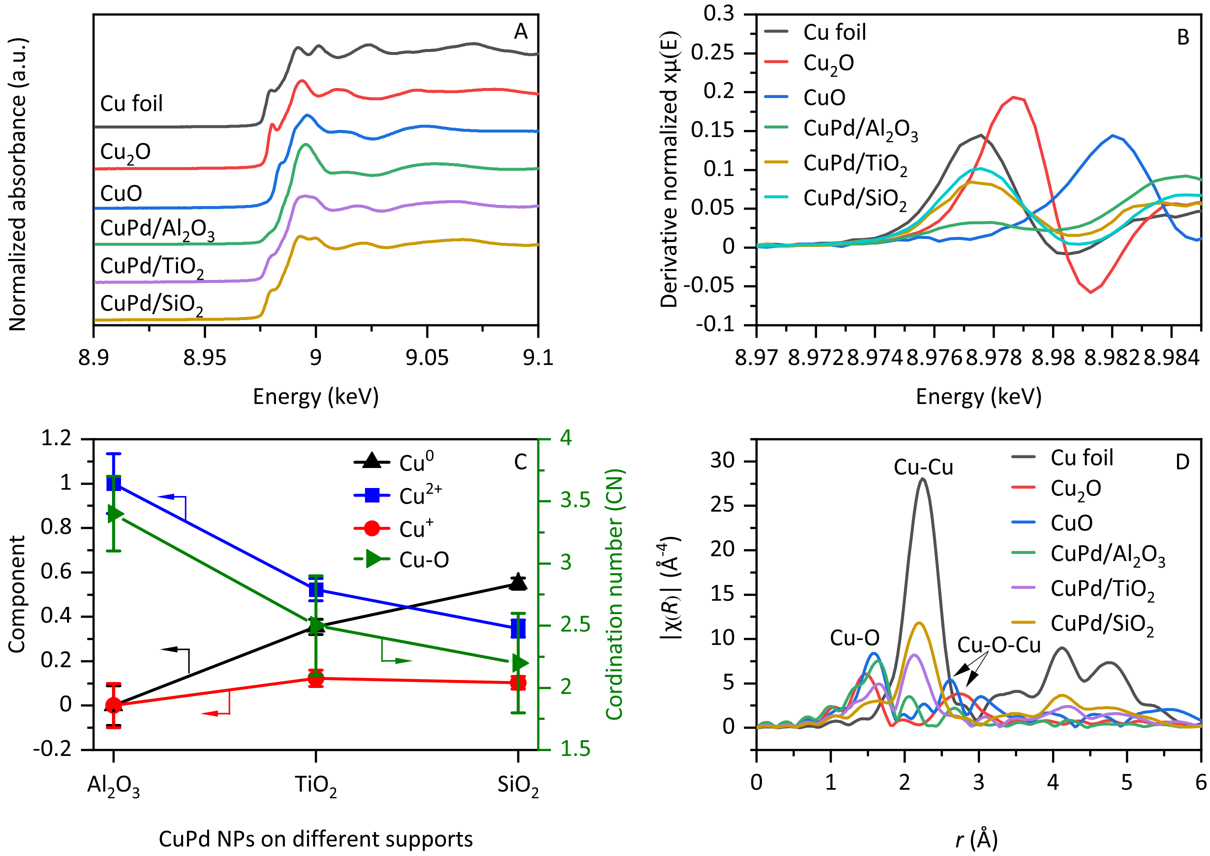

Figure 3.8: (A) XANES features, (B) first-derivative spectra, (C) LCF and results of CN fitting in R-space, and (D) FT EXAFS spectra of supported CuPd catalysts with references at Cu K-edge

with Pd to form CuPd alloy on the γ-Al_2O_3 support, which is revealed later by the fitting results at Pd K-edge.

Figure 3.8D demonstrates FT EXAFS spectra of Cu references and CuPd NPs on different supports. Except for γ-Al_2O_3 supported CuPd catalyst which shows a notable scattering for O neighbor at 1.9 Å (phase-corrected), all the catalysts exhibit a strong scattering at 2.5 Å which represents Cu neighbor (Table 3.3). The enrichment of Cu on the γ-Al_2O_3 support can be ascribed to its strong interaction due to the large difference in surface energy between Cu and Pd [81–83]. The peak intensities associated with these catalysts are apparently smaller compared to that of the Cu foil, qualitatively indicating the decrease in the coordination with Cu neighboring atoms. The fitting results are displayed in Table 3.3, which shows the coordination numbers (CNs) and bond distances at Cu K-edge. The CNs of Cu–Cu of these two catalysts are similar within the uncertainty.

Additionally, the bond distances and disordered terms are not much different from Cu foil. These results can possibly be explained by the low Pd/Cu fraction in the catalyst which causes weak perturbations in Cu oscillations. However, the presence of Cu–Pd scattering is still sufficient to involve in the fit, implying the existence of the Cu–Pd bonds in these catalysts.

Table 3.3: EXAFS fitting results of CuPd NPs on different supports at Cu K-edge

Sample	Cu–Cu	Cu–O	Cu–Pd	R_{Cu-Cu}	R_{Cu-O}	R_{Cu-Pd}
Cu foil	12.0	–	–	2.542	n.d.	–
CuPd/γ-Al_2O_3	n.d.	3.4 ± 0.3	n.d.	n.d.	1.942	n.d.
CuPd/TiO_2	4.6 ± 0.9	2.5 ± 0.4	1.5 ± 0.6	2.553	1.953	2.612
CuPd/SiO_2	6.1 ± 1.1	2.2 ± 0.4	0.5 ± 0.6	2.537	1.972	2.588

To further study the interaction of Cu–Pd, the catalysts were measured at Pd K-edge (Figure 3.9). The first two peaks of XANES spectra of CuPd bimetallic catalysts are generally similar in shape, possibly suggesting the prevailing of the metallic Pd among other oxidized states (Figure 3.9A). Accordingly, the maximum peaks in the first-derivative XANES spectra at Pd K-edge of the catalysts show similar features of Pd foil (Figure 3.9B). However, the shifts to the higher energy of these peaks envisage that the bond distance between Pd–Pd is shorter compared to that of the Pd foil [78]. The differences in the environment around Pd atoms in these bimetallic are further demonstrated in Figure 3.9C. Apparently, the k^3-weighted EXAFS oscillations of the bimetallic catalysts, especially on the TiO_2 and SiO_2 supports, are significantly different from that of the Pd foil in terms of shape and magnitude. The results reveal that the presence of Cu in the CuPd bimetallic catalysts modified the local structure of Pd atoms, conceivably causing a decrease in the Pd neighbors while an increase in the Cu by the alloying effect. Additionally, the characteristics of supports can contribute to the difference in the construction of the catalyst structure.

The raw and fitted data of the FT EXAFS at Pd K-edge for CuPd catalysts are visually demonstrated in Figure 3.9D, whereas details on fitting results are listed in Table 3.4. It is apparently observed that the metallic peaks of the bimetallic catalysts are considerably

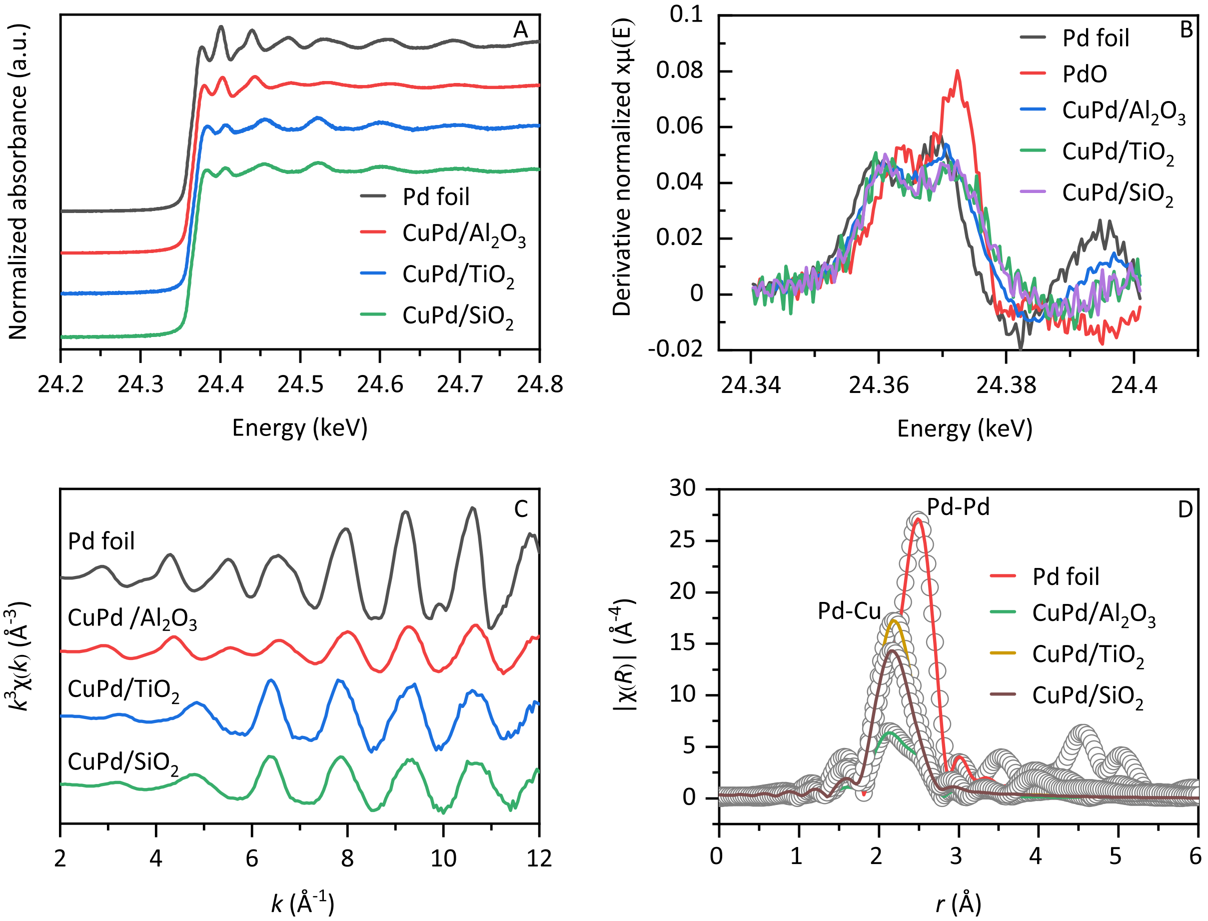

Figure 3.9: (A) XANES features, (B) first-derivative of XANES spectra, (C) k^3-weighted EXAFS spectra, and (D) FT EXAFS spectra of raw data (open circles) and fitted data (solid lines) at Pd K-edge

shifted to lower r values (2.68–2.70 Å) compared to that of the Pd foil (2.74 Å), indicating the presence of Cu as neighboring atoms. Additionally, the r values of Pd–Cu bonds (2.58–2.59 Å) are larger than that of the Cu–Cu bond (2.54 Å) but smaller than that of the Pd–Pd (2.74 Å), suggesting that during the formation of CuPd alloy, Pd would be dispersed into the Cu lattice. Besides, the total CN of Pd–M (M = Pd or Cu) are 10.0 ± 1.1, 7.9 ± 1.5, and 5.9 ± 0.9 for TiO$_2$, SiO$_2$, and γ-Al$_2$O$_3$ supported CuPd, respectively. These results also visually agree with the order in peak intensities (Figure 3.9D) and the mean particle sizes as revealed by the TEM technique (Figure 3.4). On the other hand, the total CNs of CuPd/TiO$_2$ and CuPd/SiO$_2$ at Pd K-edge are larger than those at Cu K-edge (6.1 ± 1.5 and 6.6 ± 1.7) suggesting that, at a certain extent, segregation of Cu atoms to the surface of the NPs existed [80, 84, 85]. Nevertheless, only single peaks

Table 3.4: EXAFS fitting results of CuPd NPs on different supports at Pd K-edge

Sample	Pd–Pd	Pd–Cu	$R_{Pd–Pd}$	$R_{Pd–Cu}$
Pd foil	12.0	–	2.741	–
CuPd/γ-Al_2O_3	2.6 ± 0.5	3.3 ± 0.4	2.685	2.589
CuPd/TiO_2	1.6 ± 0.5	8.4 ± 0.6	2.702	2.587
CuPd/SiO_2	1.5 ± 0.7	6.4 ± 0.8	2.679	2.577

were observed, indicating the prevalence of randomly homogeneous alloy compared to the heterogeneous alloy with Cu rich on the surface in these catalysts. In contrast, the extent of Cu segregation in CuPd/γ-Al_2O_3 seems greater since it has significant Cu–O scattering as indicated in the Cu K-edge. Furthermore, as visualized in FT EXAFS spectra at Pd K-edge, not only the peak indicating Pd–Cu bond was observed but also a shoulder peak at high r value can be seen. This result possibly suggests that in this case, relatively large amounts of Pd atoms are present in the interior, leading to the comparable Pd–Pd CN with the Pd–Cu CN (Table 2.6). It is noted that the nominal atomic ratio of Pd to Cu is about 1÷6.7, thus $\frac{CN_{Pd-Pd}}{CN_{Cu-Cu}} \gg \frac{x_{Pd}}{x_{Cu}}$, indicating a positive tendency to clustering within the bimetallic nanoparticles [84]. In other words, there exists either inter-particle or intra-particle segregation in this catalyst. The difference in the total CN suggests that the elemental distribution of the NPs is different, probably due to the interaction strength between the metal NPs and these supports. Cu was known to interact strongly with γ-Al_2O_3 stemmed from the lower surface free energy compared to that of Pd, driving a predominance of Cu on the surface of the catalyst. As reported, this also happened in the other supports [86–88], however, at lesser extent due to the similar interaction of both Pd and Cu to the supports, resulted in the formation of randomly homogeneous CuPd alloys.

For getting more inside into the metal–metal and metal–support interactions, H_2-TPR profiles of the calcined CuPd catalysts were characterized and demonstrated in Figure 3.10. It is experimentally observed that the pure CuO was reduced at about 345 ℃, while it is reported that, for example, PdO/γ-Al_2O_3 is easily reduced at room temperature [54]. Accordingly, it is expected that the addition of Pd to the Cu structure in CuPd alloy

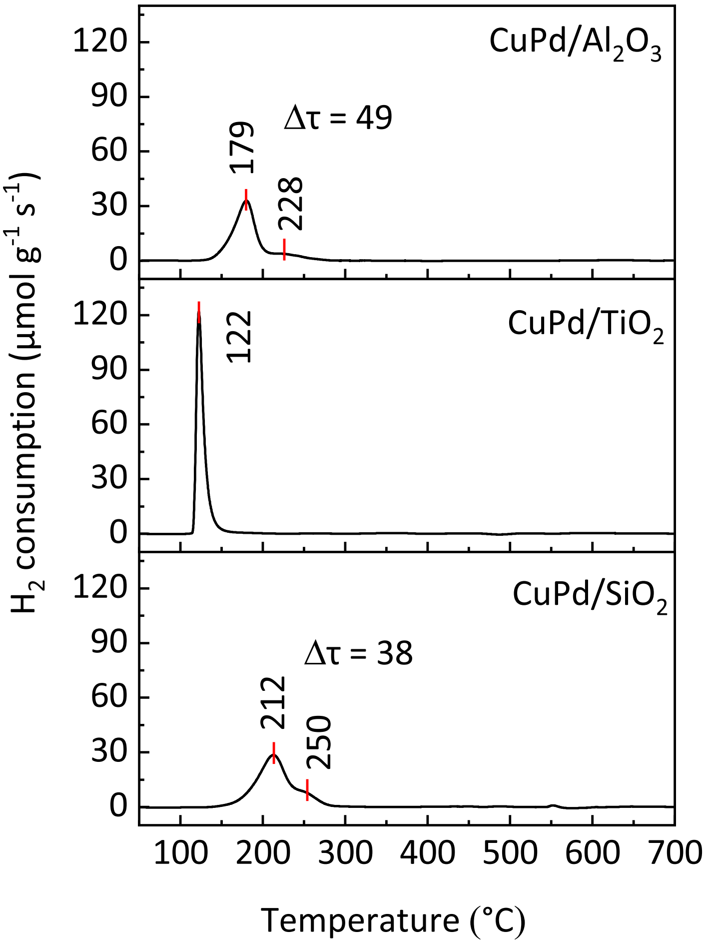

Figure 3.10: H$_2$-TPR profiles of calcined CuPd NPs on different supports

induces changes in the reduction profiles [88–92]. In the present catalysts system, the reduction peaks appeared between 122–212 ℃, which can be assigned to the reaction of Cu and Pd from the mixed oxide Cu_xPd_yO. These results are perfectly consistent with the previous studies on the CuPd NPs on γ-Al_2O_3 and other supports [47, 93]. Furthermore, it was reported that in addition to the influence of Pd, the nature of support which has a decisive impact on the metal–support interaction can simultaneously affect the reduction of the Cu species [58]. Particularly, the strength of metal–support interaction can induce the differences in these CuPd bimetallic catalysts [94]. Accordingly, the weakest interaction with TiO_2 of highly alloying CuPd NPs makes it the most reducible catalyst. The single reduction peak at 122 ℃ in CuPd/TiO_2 can possibly assign to the reduction of mixed oxide, which is in good agreement with the highest degree of alloying for this catalyst, as pointed out by its CN from EXAFS fitting results. On the other hand, the highest reduction temperature for CuPd/SiO_2 can plausibly be attributed to the strongest interaction of CuPd NPs with the support. Besides the peak at 212 ℃ assigned to the reduction of the mixed oxide, the shoulder peak emerged at 250 ℃ can be assignable to the isolated CuO species which is in close vicinity with the mixed oxides, as revealed in Figure 3.3B. Similarly, there exists an adjacently broad peak at higher temperature beside the main reduction peak, as observed in the CuPd/γ-Al_2O_3 catalyst.

However, it is noteworthy mentioning that, the temperature difference ($\Delta\tau$) between these two peaks is larger compared to that of the CuPd/SiO_2, confirming the stronger interaction between Cu and γ-Al_2O_3 comparison with SiO_2 [58]. This also agrees with the previous report on the CuAu bimetallic catalyst system that while the CuO_x on alumina tends to migrate away from the Au NPs, it formed a small cluster located near the Au NPs on silica [79]. The close distance between CuO_x species and CuPd alloying NPs in SiO_2 can improve the oxidation resistance, thus led to a small Cu^{2+} fraction, compared with that of the γ-Al_2O_3 support, which further supports the XPS results. The appearances of a single reduction peak in TiO_2 support, as well as two peaks but in closer contact in SiO_2 support, can also support the EXAFS results that in these cases the homogeneous alloys were influential; whereas, it is highly likely that more Cu atoms were segregated and/or isolated in the γ-Al_2O_3 supported CuPd catalyst.

It is reported that the support acidity is important in controlling the selectivity of THF because it facilitates the dehydration step of BDO [95, 96]. For example, Sato et al. reported that the cyclization of BDO to THF is favorable over the strong acid catalyst such as alumina. Therefore, further characterizations to determine the support acidity, as well as the total acidity of the catalyst samples, were performed. The total acid amounts of the supports and reduced catalysts samples were estimated using the NH_3-TPD profiles (Figure 3.11). Table 3.5 presents similar acid densities, ca., 0.01 mmol g^{-1} in TiO_2 and SiO_2 supports, while that figure for γ-Al_2O_3 is substantially larger with 0.07 mmol g^{-1}. The trend in the acidity amounts observed in this research is well consistent with the results reported from previous studies [97]. It is interesting to note that the deposition of CuPd NPs resulted in changes in the support acid sites, which eventually altered the total acidity of the catalyst samples. An eightfold increase in the acid density was observed in $CuPd/SiO_2$, which possibly attributed to the generation of new acid sites, in accordance with the IR results (Figure 3.12, *vide infra*). However, it caused scarcely impact on the THF formation over the $CuPd/SiO_2$ (Table S3, *vide infra*). In contrast, a considerable amount of acid was vanished by loading CuPd NPs onto γ-Al_2O_3 and TiO_2, which can be rationalized by their low surface areas (Table 3.5).

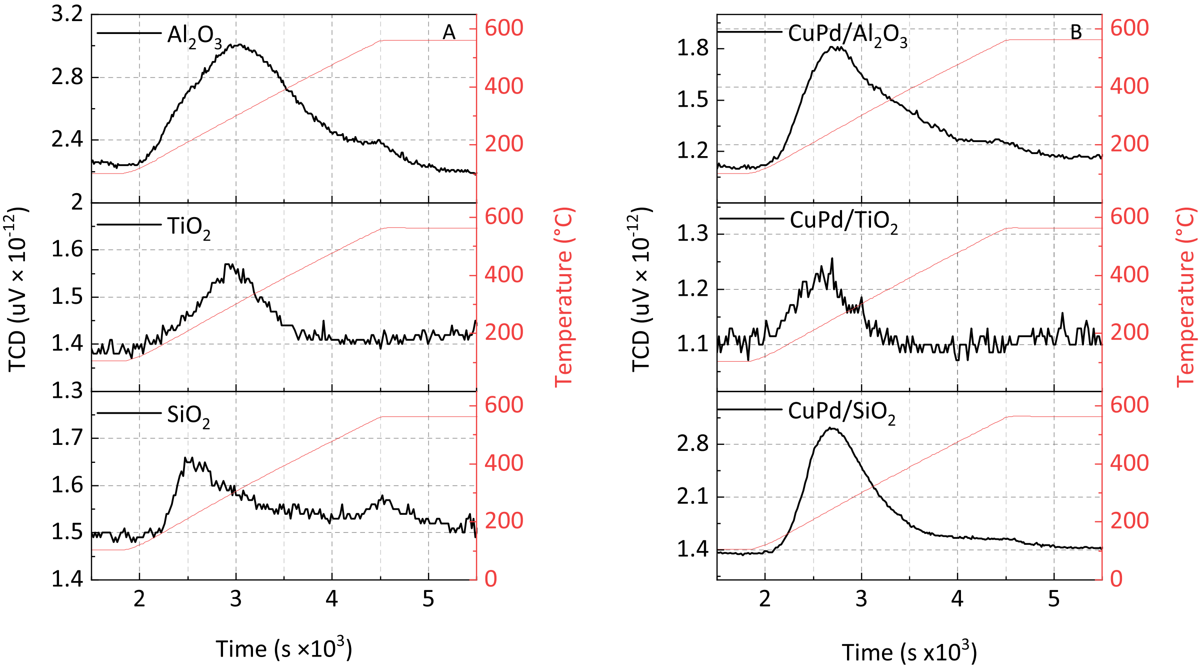

Figure 3.11: NH_3-TPD profiles of supports and reduced CuPd catalysts

Table 3.5: Acid amount and surface area of the plain supports and CuPd catalysts

Support	Acid amount[a] (mmol g^{-1})		BET surface area[b] (m^2 g^{-1})	
	Plain support	CuPd-supported catalyst	Plain support	CuPd-supported catalyst
TiO_2	0.010	0.004	6	7
SiO_2	0.012	0.101	480	386
γ-Al_2O_3	0.073	0.050	170	142

[a] Acidity of the plain supports and reduced samples were measured using NH_3-TPD with water vapor treatment.

[b] Surface area of the plain support and calcined samples were determined by N_2 adsorption/desorption method.

Since the NH_3 is a strong base (p$K_b \approx 5$) which is ready to react with extremely weak

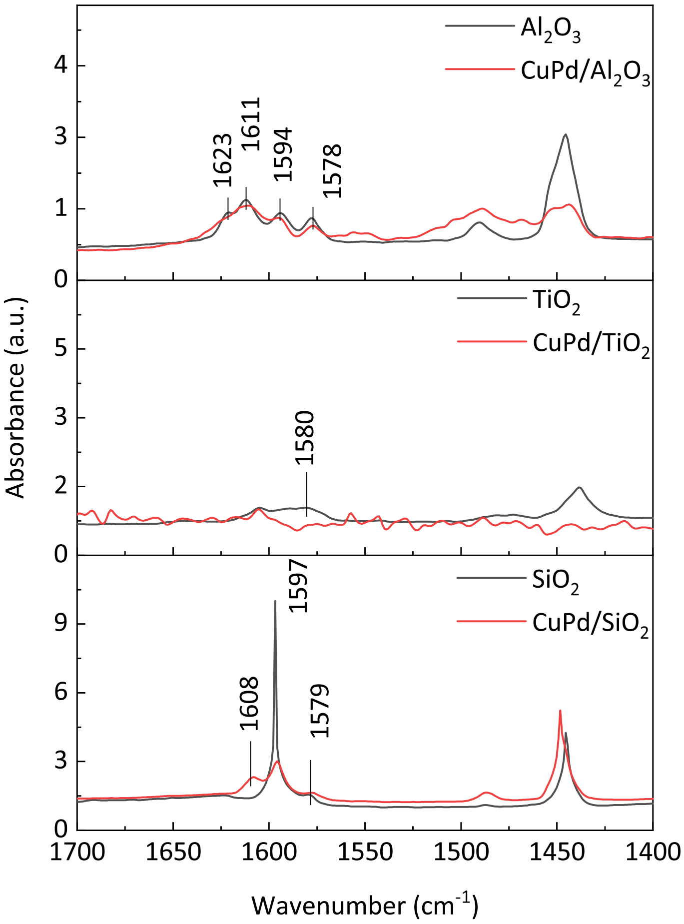

Figure 3.12: Pyridine adsorbed IR spectra of the support (black lines) and the corresponding reduced catalysts (red lines). For γ-Al$_2$O$_3$ and SiO$_2$ groups, the spectra were recorded after desorption at room temperature

acid sites [98], the determination of the strength of protonic sites in the NH$_3$-TPD profile, as indicated in Figure 3.11, was subjected to some interference. Therefore, the IR studies of adsorbed pyridine were further performed in the 1400–1700 cm^{-1} region, as presented in Figures 3.12 and 3.13. The former spectra indicated that there exist several groups of Lewis sites with different acid strength on the surface of γ-Al$_2$O$_3$. In previous reports [98–100], different temperatures in the evacuation of pyridine were investigated to delineate the acid strength of γ-Al$_2$O$_3$ Lewis sites. The same tendency was also observed in our experiments (Figure 3.13A); that is, after desorption at 120 ℃, the band at 1623 cm^{-1}, which can be assigned to strong Lewis acid sites was almost the same, while the band at 1611 cm^{-1}, assigned to medium Lewis acid sites, was decreased in their intensities

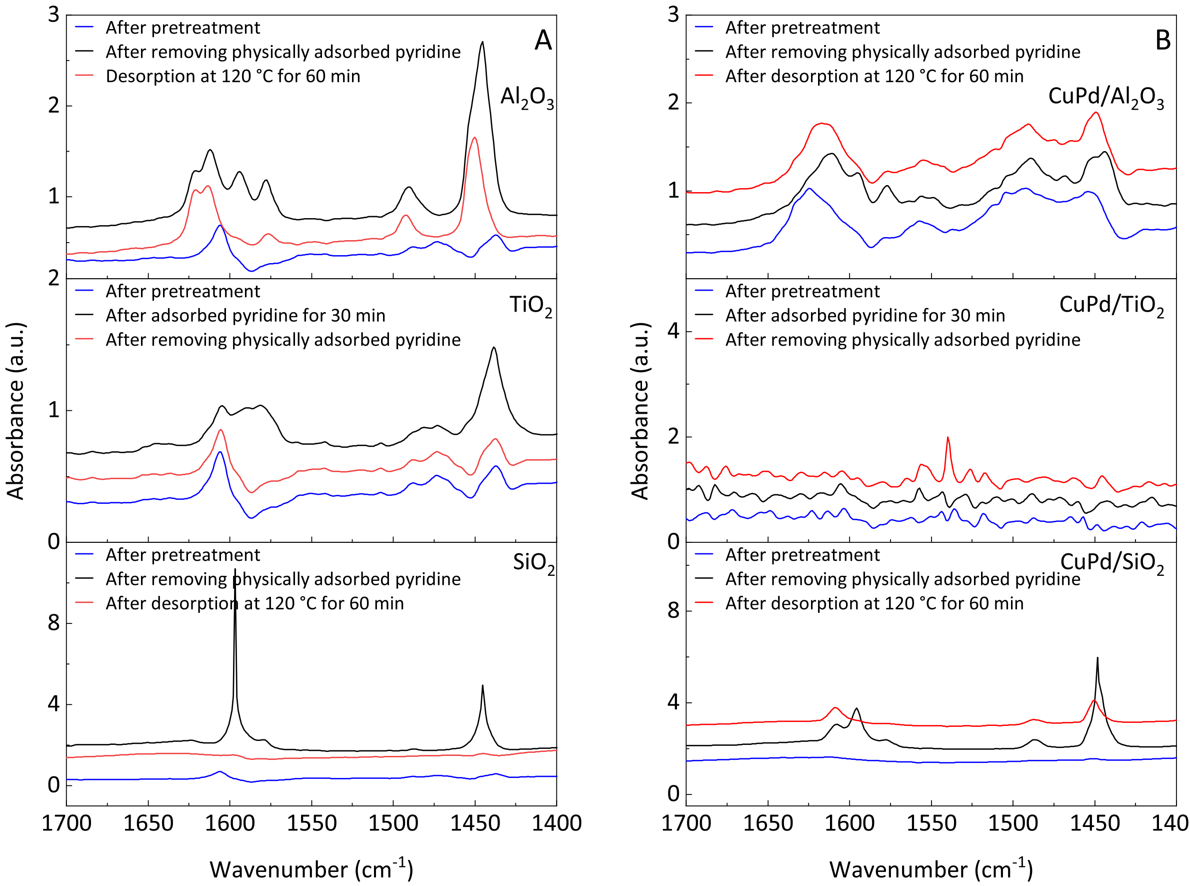

Figure 3.13: Pyridine adsorbed IR spectra of supports and reduced catalysts

after evacuation [101]. A significant decrease in intensity was observed for the band at 1594 cm^{-1}, implying the less resistance to the high temperature of the hydrogen-bonded pyridine band. The band at 1578 cm^{-1} also decreased its intensity after evacuation at high temperature, but at a lesser extent, which can be assignable to all coordinately bonded pyridine [102, 103]. It is noted that the Brønsted acid sites with the characteristic IR band of 1540 cm^{-1}, was not found in γ-Al$_2$O$_3$ support, as in accordance with previous reports [98, 100, 104]. By tracking the changes in the acid sites before and after loading metals, the decrease in the strong Lewis acid site was revealed to be a plausible reason for the decrease in the total acid amount, as estimated by NH$_3$-TPD. The SiO$_2$ support, however, contains only two bands at 1579 and 1597 cm^{-1}, which represent the vibration of coordinated pyridine on the surface and pyridine linked to OH groups of the support, respectively. These peaks were almost disappeared upon desorption at 120 ℃ (Figure 3.13A). In accordance with the NH$_3$-TPD results, the addition of metals generated Lewis acid sites at 1608 cm^{-1}, which increases the acid strength and amount of the CuPd/SiO_2. This band characterizes medium Lewis sites which is rather persistent after desorption at 120 ℃ (Figure 3.13B). A noisy spectrum was observed both in the cases of TiO_2 support and CuPd/TiO_2 catalyst due to the small number of acid site on the limited surface area of the support. The coordinated pyridine band at 1580 cm^{-1} immediately disappeared after evacuating at room temperature (Figure 3.13A). It should be noted that a tiny peak at 1542 cm^{-1} in the IR spectrum of TiO_2 can be observed upon enlargement. However, since the noise is also increased, it is difficult to confirm whether it is a real characteristic band of Brønsted acid sites. Furthermore, in comparison with other peaks in the spectrum, it is less likely that the contribution of this peak can significantly affect the total acidity of TiO_2.

Table 3.6: Controlled experiments using different catalysts/supports catalyzed different starting materials

Starting material	Catalyst/support	Conversion /%	THF /%	BDO /%
GBL	γ-Al_2O_3	23	0	0
GBL	CuPd/γ-Al_2O_3	100	93	0
GBL	CuPd/SiO_2	97	1	87
GBL	CuPd/TiO_2	65	2	62
BDO	γ-Al_2O_3	96[b]	82[b]	-
BDO	SiO_2	16	0	-
BDO	TiO_2	8	3	-
BDO	CuPd/γ-Al_2O_3	100[b]	93[b]	-
BDO	None	6	0	-

[a] Reaction conditions: substrate (0.1 g), catalyst or support (0.1 g), 1,4-dioxane (10 mL), H_2 pressure (8 MPa), temperature (200 ℃), reaction time (24 h)

[b] Reaction time (2 h)

Controlled experiments on the dehydration of BDO over different support were performed to confirm the importance of the support acidity on the formation of THF (Table 3.6). Over the weak and low acid amount of the pure SiO_2 and TiO_2, the BDO conversions were significantly low, with 16% and 8%, respectively, while less than 5% yields of THF were attained after 24 h reaction. In contrast, having strong Lewis acid sites as determined by pyridine adsorbed IR and an apparently larger amount of acid due to larger surface area, the pure γ-Al_2O_3 facilitated the reaction with a nearly quantitative conversion of BDO to afford a good yield of 82% of THF only after 2 h reaction. However, it is noted that a quantitative conversion of SA and an excellent THF yield of 93% can only achieve over the CuPd/γ-Al_2O_3, implying the added impact of CuPd NPs on the final catalytic performance for this reaction, despite the fact that it decreased the total acidity of the catalyst.

The hydrogenation of GBL over γ-Al_2O_3 was also performed to evaluate the influence of acidity on the THF formation (Table 3.6. However, a low conversion of GBL without any THF was detected after 24 h. The hydrogenation reaction over CuPd/γ-Al_2O_3 catalyst gave a quantitative conversion of GBL and a 93% yield of THF but at a slower rate compared to the dehydration reaction of BDO to THF, indicating the indispensable role of CuPd NPs on the catalytic performance. On the other hand, the SiO_2 and TiO_2 supported CuPd catalyzed the hydrogenation reaction converting 97% and 65% of GBL into 87% and 62% BDO, respectively, while less than 3% yields of THF was obtained. Since the monometallic Cu catalyst was reported to effectively catalyze the hydrogenation of GBL affording excellent yield of BDO (Table 2.3, Chapter 2), the superior catalytic performance of CuPd/SiO_2 can also be attributed to the minor but reactive Cu rich CuPd NPs on SiO_2, in comparison with the highly homogeneous CuPd alloy on TiO_2 support. Furthermore, the crucial role of strong Lewis acid in γ-Al_2O_3 was emphasized for the selective production of THF from the intermediate GBL.

3.4 Conclusions

A systematic set of experiments were performed and analyzed thoroughly driving out to these important findings:

(i) Metal–support interaction plays a key role in controlling the structure of the supported CuPd alloy catalysts. Even though a small amount of Cu rich CuPd NPs exist, randomly homogeneous CuPd NPs were found to be prevailing in TiO_2 and SiO_2 due to either weak or strong metal–support interactions. Whereas heterogeneous CuPd alloy with a high degree of Cu segregation and/or isolated Cu atoms was dominantly constructed on the γ-Al_2O_3 support as a result of strong Cu–Al_2O_3 interaction only.

(ii) Large NPs on the CuPd/TiO_2 catalyst caused by sintering gave lower activity on the hydrogenation of SA, as only the intermediate GBL was achieved. While the higher activity and selectivity toward BDO of CuPd/SiO_2 can be attributed to its smaller NP size and the existence of small but effective Cu rich CuPd NPs. On the other hand, the strong Lewis acid sites in CuPd/γ-Al_2O_3 was proved to be the decisive factor in the formation of highly selective THF.

(iii) Reaction conditions can have a great influence on the catalyst activity and selectivity. Given the high resistance of SA to hydrogenation reaction, high temperature (200 ℃), H_2 pressure (6–8 MPa), and longer reaction time (48–96 h) are required to achieve high conversion and product yields.

References

(1) Huber, G. W.; Iborra, S.; Corma, A. Synthesis of Transportation Fuels from Biomass: Chemistry, Catalysts, and Engineering. *Chem. Rev.* **2006**, *106*, 4044–4098.

(2) Munnik, P.; De Jongh, P. E.; De Jong, K. P. Recent Developments in the Synthesis of Supported Catalysts. *Chem. Rev.* **2015**, *115*, 6687–6718.

(3) Philippot, K.; Serp, P. In *Nanomaterials in Catalysis*; Wiley-VCH Verlag GmbH & Co. KGaA: Weinheim, Germany, 2012; Chapter 1, pp 1–54.

(4) Altavilla, C.; Ciliberto, E., *Inorganic Nanoparticles: Synthesis, Applications, and Perspectives*, 1st; Altavilla, C., Ciliberto, E., Eds.; CRC Press: 2010, p 600.

(5) Ashik, U.; Viswan, A.; Kudo, S.; Hayashi, J.-i. In *Applications of Nanomaterials*; Elsevier: 2018; Chapter 3, pp 45–82.

(6) Balasanthiran, C.; Hoefelmeyer, J. D. In *Metal Nanoparticles for Catalysis: Advances and Applications*, Tao, F. F., Ed., 2014; Chapter 2, pp 6–29.

(7) Gubin, S. P., *Magnetic Nanoparticles*; Gubin, S. P., Ed.; John Wiley and Sons: 2009, p 466.

(8) Schmid, G. In *Nanoparticles*; Wiley-VCH Verlag GmbH & Co. KGaA: Weinheim, FRG, 2003, pp 1–3.

(9) Altavilla, C.; Ciliberto, E. In *Inorganic Nanoparticles: Synthesis, Applications, and Perspectives*, Altavilla, C., Ciliberto, E., Eds.; CRC Press: 2010; Chapter 1, pp 1–14.

(10) Bell, A. T. The Impact of Nanoscience on Heterogeneous Catalysis. *Science* **2003**, *299*, 1688–1691.

(11) Sankar, M.; Dimitratos, N.; Miedziak, P. J.; Wells, P. P.; Kiely, C. J.; Hutchings, G. J. Designing Bimetallic Catalysts for A Green and Sustainable Future. *Chem. Soc. Rev.* **2012**, *41*, 8099–8139.

(12) Ferrando, R.; Jellinek, J.; Johnston, R. L. Nanoalloys: From Theory to Applications of Alloy Clusters and Nanoparticles. *Chem. Rev.* **2008**, *108*, 845–910.

(13) Astruc, D. Introduction: Nanoparticles in Catalysis. *Chem. Rev.* **2020**, *120*, 461–463.

(14) Liu, L.; Corma, A. Metal Catalysts for Heterogeneous Catalysis: From Single Atoms to Nanoclusters and Nanoparticles. *Chem. Rev.* **2018**, *118*, 4981–5079.

(15) Campbell, C. T.; Parker, S. C.; Starr, D. E. The Effect of Size-Dependent Nanoparticle Energetics on Catalyst Sintering. *Science* **2002**, *298*, 811–814.

(16) Farmer, J. A.; Campbell, C. T. Ceria Maintains Smaller Metal Catalyst Particles by Strong Metal–support Bonding. *Science* **2010**, *329*, 933–936.

(17) Campbell, C. T. The Energetics of Supported Metal Nanoparticles: Relationships to Sintering Rates and Catalytic Activity. *Acc. Chem. Res.* **2013**, *46*, 1712–1719.

(18) Daniel, M.-C.; Astruc, D. Gold Nanoparticles: Assembly, Supramolecular Chemistry, Quantum-Size-Related Properties, and Applications toward Biology, Catalysis, and Nanotechnology. *Chem. Rev.* **2004**, *104*, 293–346.

(19) Nilius, N.; Ganduglia-Pirovano, M. V.; Brázdová, V.; Kulawik, M.; Sauer, J.; Freund, H. J. Counting Electrons Transferred Through a Thin Alumina Film into Au Chains. *Phys. Rev. Lett.* **2008**, *100*, 096802.

(20) Lin, X.; Nilius, N.; Freund, H. J.; Walter, M.; Frondelius, P.; Honkala, K.; Häkkinen, H. Quantum Well States in Two-Dimensional Gold Clusters on MgO Thin Films. *Phys. Rev. Lett.* **2009**, *102*, 206801.

(21) Vayssilov, G. N.; Lykhach, Y.; Migani, A.; Staudt, T.; Petrova, G. P.; Tsud, N.; Skála, T.; Bruix, A.; Illas, F.; Prince, K. C.; Matolín, V.; Neyman, K. M.; Libuda, J. Support Nanostructure Boosts Oxygen Transfer to Catalytically Active Platinum Nanoparticles. *Nat. Mater.* **2011**, *10*, 310–315.

(22) Lykhach, Y.; Kozlov, S. M.; Skála, T.; Tovt, A.; Stetsovych, V.; Tsud, N.; Dvořák, F.; Johánek, V.; Neitzel, A.; Mysliveček, J.; Fabris, S.; Matolín, V.; Neyman, K. M.; Libuda, J. Counting Electrons on Supported Nanoparticles. *Nat. Mater.* **2016**, *15*, 284–288.

(23) Alonso, D. M.; Wettstein, S. G.; Dumesic, J. A. Bimetallic Catalysts for Upgrading of Biomass to Fuels and Chemicals. *Chem. Soc. Rev.* **2012**, *41*, 8075–8098.

(24) Besson, M.; Gallezot, P.; Pinel, C. Conversion of Biomass into Chemicals over Metal Catalysts. *Chem. Rev.* **2014**, *114*, 1827–1870.

(25) Horváth, I. T.; Anastas, P. T. Introduction: Green chemistry. *Chem. Rev.* **2007**, *107*, 2167–2168.

(26) Anastas, P.; Eghbali, N. Green Chemistry: Principles and Practice. *Chem. Soc. Rev.* **2010**, *39*, 301–312.

(27) Corma, A.; Iborra, S.; Velty, A. Chemical Routes for the Transformation of Biomass into Chemicals. *Chem. Rev.* **2007**, *107*, 2411–2502.

(28) Serrano-Ruiz, J. C.; Luque, R.; Sepúlveda-Escribano, A. Transformations of Biomass-Derived Platform Molecules: From High Added-Value Chemicals to Fuels via Aqueous-Phase Processing. *Chem. Soc. Rev.* **2011**, *40*, 5266–5281.

(29) Zhang, X.; Wilson, K.; Lee, A. F. Heterogeneously Catalyzed Hydrothermal Processing of C_5-C_6 Sugars. *Chem. Rev.* **2016**, *116*, 12328–12368.

(30) Mika, L. T.; Cséfalvay, E.; Németh, Á. Catalytic Conversion of Carbohydrates to Initial Platform Chemicals: Chemistry and Sustainability. *Chem. Rev.* **2018**, *118*, 505–613.

(31) Delhomme, C.; Weuster-Botz, D.; Kühn, F. E. Succinic Acid from Renewable Resources as a C_4 Building-Block Chemical–a Review of the Catalytic Possibilities in Aqueous Media. *Green Chem.* **2009**, *11*, 13–26.

(32) Mazière, A.; Prinsen, P.; García, A.; Luque, R.; Len, C. A Review of Progress in (Bio)Catalytic Routes from/to Renewable Succinic Acid. *Biofuels, Bioprod. Biorefining* **2017**, *11*, 908–931.

(33) Nghiem, N.; Kleff, S.; Schwegmann, S. Succinic Acid: Technology Development and Commercialization. *Fermentation* **2017**, *3*, 26–40.

(34) Pritchard, J.; Filonenko, G. A.; Van Putten, R.; Hensen, E. J.; Pidko, E. A. Heterogeneous and Homogeneous Catalysis for the Hydrogenation of Carboxylic Acid Derivatives: History, Advances and Future Directions. *Chem. Soc. Rev.* **2015**, *44*, 3808–3833.

(35) Weissermel, K.; Arpe, H.-J., *Industrial Organic Chemistry*, 4th ed.; Wiley-VCH: 2003, p 491.

(36) Clayden, J.; Geeves, N.; Warren, S., *Organic Chemistry*, 2nd ed.; Oxford University Press: 2012, p 1264.

(37) Toba, M.; Tanaka, S. I.; Niwa, S. I.; Mizukami, F.; Koppány, Z.; Guczi, L.; Cheah, K. Y.; Tang, T. S. Synthesis of Alcohols and Diols by Hydrogenation of Carboxylic

Acids and Esters over Ru-Sn-Al_2O_3 Catalysts. *Appl. Catal. A Gen.* **1999**, *189*, 243–250.

(38) Corbel-Demailly, L.; Ly, B.-K.; Minh, D.-P.; Tapin, B.; Especel, C.; Epron, F.; Cabiac, A.; Guillon, E.; Besson, M.; Pinel, C. Heterogeneous Catalytic Hydrogenation of Biobased Levulinic and Succinic Acids in Aqueous Solutions. *ChemSusChem* **2013**, *6*, 2388–2395.

(39) Kang, K. H.; Hong, U. G.; Bang, Y.; Choi, J. H.; Kim, J. K.; Lee, J. K.; Han, S. J.; Song, I. K. Hydrogenation of Succinic Acid to 1,4-Butanediol over Re–Ru Bimetallic Catalysts Supported on Mesoporous Carbon. *Appl. Catal. A Gen.* **2015**, *490*, 153–162.

(40) Vardon, D. R.; Settle, A. E.; Vorotnikov, V.; Menart, M. J.; Eaton, T. R.; Unocic, K. A.; Steirer, K. X.; Wood, K. N.; Cleveland, N. S.; Moyer, K. E.; Michener, W. E.; Beckham, G. T. Ru–Sn/AC for the Aqueous-Phase Reduction of Succinic Acid to 1,4-Butanediol under Continuous Process Conditions. *ACS Catal.* **2017**, *7*, 6207–6219.

(41) Di, X.; Li, C.; Zhang, B.; Qi, J.; Li, W.; Su, D.; Liang, C. Role of Re and Ru in Re-Ru/C Bimetallic Catalysts for the Aqueous Hydrogenation of Succinic Acid. *Ind. Eng. Chem. Res.* **2017**, *56*, 4672–4683.

(42) Hong, U. G.; Kim, J. K.; Lee, J.; Lee, J. K.; Song, J. H.; Yi, J.; Song, I. K. Hydrogenation of Succinic Acid to Tetrahydrofuran (THF) over Ruthenium–Carbon Composite (Ru–C) Catalyst. *Appl. Catal. A Gen.* **2014**, *469*, 466–471.

(43) Shao, Z.; Li, C.; Di, X.; Xiao, Z.; Liang, C. Aqueous-Phase Hydrogenation of Succinic Acid to γ-Butyrolactone and Tetrahydrofuran over Pd/C, Re/C, and Pd–Re/C Catalysts. *Ind. Eng. Chem. Res.* **2014**, *53*, 9638–9645.

(44) Keels, J. M.; Chen, X.; Karakalos, S.; Liang, C.; Monnier, J. R.; Regalbuto, J. R. Aqueous-Phase Hydrogenation of Succinic Acid Using Bimetallic Ir–Re/C Cat-

alysts Prepared by Strong Electrostatic Adsorption. *ACS Catal.* **2018**, *8*, 6486–6494.

(45) Liu, X.; Wang, X.; Xu, G.; Liu, Q.; Mu, X.; Liu, H. Tuning the Catalytic Selectivity in Biomass-Derived Succinic Acid Hydrogenation on FeO$_x$-Modified Pd Catalysts. *J. Mater. Chem. A* **2015**, *3*, 23560–23569.

(46) Patankar, S. C.; Sharma, A. G.; Yadav, G. D. Biobased Process Intensification in Selective Synthesis of γ-Butyrolactone from Succinic Acid via Synergistic Palladium–Copper Bimetallic Catalyst Supported on Alumina Xerogel. *Clean Technol. Environ. Policy* **2018**, *20*, 683–693.

(47) Le, S. D.; Nishimura, S. Highly Selective Synthesis of 1,4-Butanediol via Hydrogenation of Succinic Acid with Supported Cu–Pd Alloy Nanoparticles. *ACS Sustain. Chem. Eng.* **2019**, *7*, 18483–18492.

(48) Sun, D.; Sato, S.; Ueda, W.; Primo, A.; Garcia, H.; Corma, A. Production of C$_4$ and C$_5$ Alcohols from Biomass-Derived Materials. *Green Chem.* **2016**, *18*, 2579–2597.

(49) Chaudhari, R. V.; Rode, C. V.; Deshpande, R. M.; Jaganathan, R.; Leib, T. M.; Mills, P. L. Kinetics of Hydrogenation of Maleic Acid in a Batch Slurry Reactor using a Bimetallic Ru–Re/C Catalyst. *Chem. Eng. Sci.* **2003**, *58*, 627–632.

(50) Di, X.; Shao, Z.; Li, C.; Li, W.; Liang, C. Hydrogenation of Succinic Acid over Supported Rhenium Catalysts Prepared by the Microwave-Assisted Thermolytic Method. *Catal. Sci. Technol.* **2015**, *5*, 2441–2448.

(51) Aghaziarati, M.; Kazemeini, M.; Soltanieh, M.; Sahebdelfar, S. Evaluation of Zeolites in Production of Tetrahydrofuran from 1,4-Butanediol: Performance Tests and Kinetic Investigations. *Ind. Eng. Chem. Res.* **2007**, *46*, 726–733.

(52) Thomas, D. J.; Stammbach, M. R.; Cant, N. W.; Wainwright, M. S.; Trimm, D. L. Hydrogenolysis of Dimethyl Succinate over Raney Copper Catalyst: A Correction. *Ind. Eng. Chem. Res.* **1990**, *29*, 204–208.

(53) Schlander, J. H.; Turek, T. Gas-phase Hydrogenolysis of Dimethyl Maleate to 1,4-Butanediol and γ- Butyrolactone over Copper/Zinc Oxide Catalysts. *Ind. Eng. Chem. Res.* **1999**, *38*, 1264–1270.

(54) Batista, J.; Pintar, A.; Mandrino, D.; Jenko, M.; Martin, V. XPS and TPR examinations of γ-alumina-supported Pd–Cu catalysts. *Appl. Catal. A Gen.* **2001**, *206*, 113–124.

(55) Sanchez-Escribano, V.; Arrighi, L.; Riani, P.; Marazza, R.; Busca, G. Characterization of Pd–Cu Alloy Nanoparticles on γ-Al_2O_3-Supported Catalysts. *Langmuir* **2006**, *22*, 9214–9219.

(56) Seshu Babu, N.; Lingaiah, N.; Sai Prasad, P. S. Characterization and Reactivity of Al_2O_3 Supported Pd–Ni Bimetallic Catalysts for Hydrodechlorination of Chlorobenzene. *Appl. Catal. B Environ.* **2012**, *111-112*, 309–316.

(57) Caldas, P. C.; Gallo, J. M. R.; Lopez-Castillo, A.; Zanchet, D.; Bueno, J. M. C. The Structure of the Cu–CuO Sites Determines the Catalytic Activity of Cu Nanoparticles. *ACS Catal.* **2017**, *7*, 2419–2424.

(58) Molenbroek, A. M.; Haukka, S.; Clausen, B. S. Alloying in Cu/Pd Nanoparticle Catalysts. *J. Phys. Chem. B* **1998**, *102*, 10680–10689.

(59) Goodman, D. W. Model Studies in Catalysis Using Surface Science Probes. *Chem. Rev.* **1995**, *95*, 523–536.

(60) Valden, M.; Lai, X.; Goodman, D. W. Onset of Catalytic Activity of Gold Clusters on Titania with the Appearance of Nonmetallic Properties. *Science* **1998**, *281*, 1647–1650.

(61) Rodriguez, J. A.; Liu, P.; Hrbek, J.; Evans, J.; Pérez, M. Water Gas Shift Reaction on Cu and Au Nanoparticles Supported on $CeO_2(111)$ and $ZnO(000\bar{1})$: Intrinsic Activity and Importance of Support Interactions. *Angew. Chem. Int. Ed.* **2007**, *46*, 1329–1332.

(62) Bruix, A.; Rodriguez, J. A.; Ramírez, P. J.; Senanayake, S. D.; Evans, J.; Park, J. B.; Stacchiola, D.; Liu, P.; Hrbek, J.; Illas, F. A New Type of Strong Metal-Support Interaction and the Production of H_2 through the Transformation of Water on Pt/CeO_2(111) and Pt/CeO_x/TiO_2(110) Catalysts. *J. Am. Chem. Soc.* **2012**, *134*, 8968–8974.

(63) Fulajtárova, K.; Soták, T.; Hronec, M.; Vávra, I.; Dobročka, E.; Omastová, M. Aqueous Phase Hydrogenation of Furfural to Furfuryl Alcohol over Pd–Cu Catalysts. *Appl. Catal. A Gen.* **2015**, *502*, 78–85.

(64) Mhadmhan, S.; Franco, A.; Pineda, A.; Reubroycharoen, P.; Luque, R. Continuous Flow Selective Hydrogenation of 5-Hydroxymethylfurfural to 2,5-Dimethylfuran Using Highly Active and Stable Cu–Pd/Reduced Graphene Oxide. *ACS Sustain. Chem. Eng.* **2019**, *7*, 14210–14216.

(65) Gervasini, A.; Manzoli, M.; Martra, G.; Ponti, A.; Ravasio, N.; Sordelli, L.; Zaccheria, F. Dependence of Copper species on the Nature of the Support for Dispersed CuO Catalysts. *J. Phys. Chem. B* **2006**, *110*, 7851–7861.

(66) He, Z.; Lin, H.; He, P.; Yuan, Y. Effect of Boric Oxide Doping on the Stability and Activity of a $Cu-SiO_2$ Catalyst for Vapor-Phase Hydrogenation of Dimethyl Oxalate to Ethylene Glycol. *J. Catal.* **2011**, *277*, 54–63.

(67) Zhu, Y.; Kong, X.; Li, X.; Ding, G.; Zhu, Y.; Li, Y.-W. Cu Nanoparticles Inlaid Mesoporous Al_2O_3 As a High-Performance Bifunctional Catalyst for Ethanol Synthesis via Dimethyl Oxalate Hydrogenation. *ACS Catal.* **2014**, *4*, 3612–3620.

(68) Boucher, M. B.; Zugic, B.; Cladaras, G.; Kammert, J.; Marcinkowski, M. D.; Lawton, T. J.; Sykes, E. C. H.; Flytzani-Stephanopoulos, M. Single Atom Alloy Surface Analogs in $Pd_{0.18}Cu_{15}$ Nanoparticles or Selective Hydrogenation Reactions. *Phys. Chem. Chem. Phys.* **2013**, *15*, 12187.

(69) Castegnaro, M. V.; Gorgeski, A.; Balke, B.; Alves, M. C. M.; Morais, J. Charge Transfer Effects on the Chemical Reactivity of Pd_xCu_{1-x} Nanoalloys. *Nanoscale* **2016**, *8*, 641–647.

(70) Marakatti, V. S.; Sarma, S. C.; Joseph, B.; Banerjee, D.; Peter, S. C. Synthetically Tuned Atomic Ordering in PdCu Nanoparticles with Enhanced Catalytic Activity toward Solvent-Free Benzylamine Oxidation. *ACS Appl. Mater. Interfaces* **2017**, *9*, 3602–3615.

(71) Sarkar, C.; Koley, P.; Shown, I.; Lee, J.; Liao, Y.-F.; An, K.; Tardio, J.; Nakka, L.; Chen, K.-H.; Mondal, J. Integration of Interfacial and Alloy Effects to Modulate Catalytic Performance of Metal-Organic-Framework-Derived Cu–Pd Nanocrystals toward Hydrogenolysis of 5-Hydroxymethylfurfural. *ACS Sustain. Chem. Eng.* **2019**, *7*, 10349–10362.

(72) Yin, Z.; Zhou, W.; Gao, Y.; Ma, D.; Kiely, C. J.; Bao, X. Supported Pd–Cu Bimetallic Nanoparticles That Have High Activity for the Electrochemical Oxidation of Methanol. *Chem. Eur. J.* **2012**, *18*, 4887–4893.

(73) Kim, K. S.; Gossmann, A. F.; Winograd, N. X-ray Photoelectron Spectroscopic Studies of Palladium Oxides and the Palladium-Oxygen Electrode. *Anal. Chem.* **1974**, *46*, 197–200.

(74) Umpierre, A. P.; Machado, G.; Fecher, G. H.; Morais, J.; Dupont, J. Selective Hydrogenation of 1,3-Butadiene to 1-Butene by Pd(0) Nanoparticles Embedded in Imidazolium Ionic Liquids. *Adv. Synth. Catal.* **2005**, *347*, 1404–1412.

(75) Bernardi, F.; Alves, M. C. M.; Traverse, A.; Silva, D. O.; Scheeren, C. W.; Dupont, J.; Morais, J. Monitoring Atomic Rearrangement in Pt_xPd_{1-x} (x=1, 0.7, or 0.5) Nanoparticles Driven by Reduction and Sulfidation Processes. *J. Phys. Chem. C* **2009**, *113*, 3909–3916.

(76) Kilian, A. S.; Bernardi, F.; Pancotti, A.; Landers, R.; de Siervo, A.; Morais, J. Atomic Structure of Cr_2O_3/Ag(111) and Pd/Cr_2O_3/Ag(111) Surfaces: a Photoelectron Diffraction Investigation. *J. Phys. Chem. C*, 20452–20460.

(77) Chen, D.; Sun, P.; Liu, H.; Yang, J. Bimetallic Cu–Pd Alloy Multipods and Their Highly Electrocatalytic Performance for Formic Acid Oxidation and Oxygen Reduction. *J. Mater. Chem. A* **2017**, *5*, 4421–4429.

(78) Kugai, J.; Miller, J. T.; Fox, E. B.; Song, C. In-situ X-ray Absorption Study of Ceria-Supported Pd–Cu Nanoparticles for Oxygen-Enhanced Water Gas Shift. *Appl. Catal. A Gen.* **2016**, *528*, 67–73.

(79) Destro, P.; Kokumai, T. M.; Scarpellini, A.; Pasquale, L.; Manna, L.; Colombo, M.; Zanchet, D. The Crucial Role of the Support in the Transformations of Bimetallic Nanoparticles and Catalytic Performance. *ACS Catal.* **2018**, *8*, 1031–1037.

(80) Goulas, K. A.; Sreekumar, S.; Song, Y.; Kharidehal, P.; Gunbas, G.; Dietrich, P. J.; Johnson, G. R.; Wang, Y. C.; Grippo, A. M.; Grabow, L. C.; Gokhale, A. A.; Toste, F. D. Synergistic Effects in Bimetallic Palladium-Copper Catalysts Improve Selectivity in Oxygenate Coupling Reactions. *J. Am. Chem. Soc.* **2016**, *138*, 6805–6812.

(81) Batista, J.; Pintar, A.; Gomilšek, J. P.; Kodre, A.; Bornette, F. On the Structural Characteristics of γ-Alumina-Supported Pd–Cu Bimetallic Catalysts. *Appl. Catal. A Gen.* **2001**, *217*, 55–68.

(82) Hungría, A. B.; Iglesias-Juez, A.; Martínez-Arias, A.; Fernández-García, M.; Anderson, J. A.; Conesa, J. C.; Soria, J. Effects of Copper on the Catalytic Properties of Bimetallic Pd–Cu/(Ce,Zr)O_x/Al_2O_3 and Pd–Cu/(Ce,Zr)O_x Catalysts for CO and NO Elimination. *J. Catal.* **2002**, *206*, 281–294.

(83) Lambert, S.; Heinrichs, B.; Brasseur, A.; Rulmont, A.; Pirard, J. P. Determination of Durface Composition of Alloy Nanoparticles and Relationships with Catalytic

Activity in Pd–Cu/SiO_2 Cogelled Xerogel Catalysts. *Appl. Catal. A Gen.* **2004**, *270*, 201–208.

(84) Frenkel, A. I. Applications of Extended X-ray Absorption Fine-Structure Spectroscopy to Studies of Bimetallic Nanoparticle Catalysts. *Chem. Soc. Rev.* **2012**, *41*, 8163–8178.

(85) Frenkel, A. I.; Wang, Q.; Sanchez, S. I.; Small, M. W.; Nuzzo, R. G. Short Range Order in Bimetallic Nanoalloys: An Extended X-ray Absorption Fine Structure Study. *J. Chem. Phys.* **2013**, *138*, 064202.

(86) Heinrichs, B.; Noville, F.; Schoebrechts, J.-P.; Pirard, J.-P. Palladium–Silver Sol–Gel Catalysts for Selective Hydrodechlorination of 1,2-Dichloroethane into Ethylene: II. Surface Composition of Alloy Particles. *J. Catal.* **2000**, *192*, 108–118.

(87) Benito, P.; Gregori, M.; Andreoli, S.; Fornasari, G.; Ospitali, F.; Millefanti, S.; Avila, M. S.; Garetto, T. F.; Albonetti, S. Pd–Cu Interaction in Pd/Cu-MCM-41 Catalysts: Effect of Silica Source and Metal Content. *Catal. Today* **2015**, *246*, 108–115.

(88) Ardila, A. N.; Sánchez-Castillo, M. A.; Zepeda, T. A.; Villa, A. L.; Fuentes, G. A. Glycerol Hydrodeoxygenation to 1,2-Propanediol Catalyzed by CuPd/TiO_2–Na. *Appl. Catal. B Environ.* **2017**, *219*, 658–671.

(89) Moretti, G.; Sachtler, W. M. Characterization and Catalysis of PtCu Clusters in NaY. *J. Catal.* **1989**, *115*, 205–216.

(90) Fernández-García, M.; Conesa, J. C.; Clotet, A.; Ricart, J. M.; López, N.; Illas, F. Study of the Heterometallic Bond Nature in PdCu(111) Surfaces. *J. Phys. Chem. B* **1998**, *102*, 141–147.

(91) Soares, O. S.; Órfão, J. J.; Ruiz-Martínez, J.; Silvestre-Albero, J.; Sepúlveda-Escribano, A.; Pereira, M. F. Pd–Cu/AC and Pt–Cu/AC Catalysts for Nitrate Reduction with Hydrogen: Influence of Calcination and Reduction Temperatures. *Chem. Eng. J.* **2010**, *165*, 78–88.

(92) Veldurthi, S.; Shin, C. H.; Joo, O. S.; Jung, K. D. Promotional Effects of Cu on Pt/Al_2O_3 and Pd/Al_2O_3 Catalysts During n-butane Dehydrogenation. *Catal. Today* **2012**, *185*, 88–93.

(93) Di, L.; Xu, W.; Zhan, Z.; Zhang, X. Synthesis of Alumina Supported Pd–Cu Alloy Nanoparticles for CO Oxidation via a Fast and Facile Method. *RSC Adv.* **2015**, *5*, 71854–71858.

(94) Yang, Q.; Hou, R.; Sun, K. Tuning Butene Selectivities by Cu Modification on Pd-Based Catalyst for the Selective Hydrogenation of 1,3-Butadiene. *J. Catal.* **2019**, *374*, 12–23.

(95) Sato, S.; Takahashi, R.; Sodesawa, T.; Yamamoto, N. Dehydration of 1,4-Butanediol into 3-Buten-1-ol Catalyzed by Ceria. *Catal. Commun.* **2004**, *5*, 397–400.

(96) Mi, R.; Hu, Z.; Yi, C.; Yang, B. Catalytic Dehydration of 1,4-Butanediol over Mg–Yb Binary Oxides and the Mechanism Study. *ChemCatChem* **2020**, *12*, 2859–2871.

(97) Sabu, K. R. P.; Rao, K. V. C.; Nair, C. G. R. A Comparative Study on the Acidic Properties and Catalytic Activities of TiO_2, SiO_2, Al_2O_3, $SiO_2-Al_2O_3$, SiO_2-TiO_2, $Al_2O_3-TiO_2$,and $TiO_2-SiO_2-Al_2O_3$. *Bull. Chem. Soc. Jpn.* **1991**, *64*, 1920–1925.

(98) Parry, E. P. An Infrared Study of Pyridine Adsorbed on Acidic Solids. Characterization of Surface Acidity. *J. Catal.* **1963**, *2*, 371–379.

(99) Vimont, A.; Lavalley, J. C.; Sahibed-Dine, A.; Areán, C. O.; Delgado, M. R.; Daturi, M. Infrared Spectroscopic Study on the Surface Properties of γ-Gallium Oxide as Compared to Those of γ-Alumina. *J. Phys. Chem. B* **2005**, *109*, 9656–9664.

(100) Kondo, J. N.; Nishitani, R.; Yoda, E.; Yokoi, T.; Tatsumi, T.; Domen, K. A Comparative IR Characterization of Acidic Sites on HY Zeolite by Pyridine and CO

Probes with Silica-Alumina and γ-Alumina References. *Phys. Chem. Chem. Phys.* **2010**, *12*, 11576–11586.

(101) Gafurov, M. R.; Mukhambetov, I. N.; Yavkin, B. V.; Mamin, G. V.; Lamberov, A. A.; Orlinskii, S. B. Quantitative Analysis of Lewis Acid Centers of γ-Alumina by Using EPR of the Adsorbed Anthraquinone as a Probe Molecule: Comparison with the Pyridine, Carbon Monoxide IR, and TPD of Ammonia. *J. Phys. Chem. C* **2015**, *119*, 27410–27415.

(102) Kline, C. H.; Turkevich, J. The Vibrational Spectrum of Pyridine and the Thermodynamic Properties of Pyridine Vapors. *J. Chem. Phys.* **1944**, *12*, 300–309.

(103) Morterra, C.; Chiorino, A.; Ghiotti, G.; Garrone, E. Surface Acidity of η-Alumina. Part 1.–Pyridine Chemisorption at Room Temperature. *J. Chem. Soc. Faraday Trans. 1 Phys. Chem. Condens. Phases* **1979**, *75*, 271–288.

(104) Ravenelle, R. M.; Copeland, J. R.; Kim, W. G.; Crittenden, J. C.; Sievers, C. Structural Changes of γ-Al_2O_3-Supported Catalysts in Hot Liquid Water. *ACS Catal.* **2011**, *1*, 552–561.

Chapter 4

Influence of Metal Ratio on Alumina-Supported CuPd Catalysts for the Production of Tetrahydrofuran from Succinic Acid

Abstract

The present research studies the influence of metal ratio on the construction of γ-Al_2O_3 supported Cu_xPd_y ($x+y = 10$ wt%) bimetallic catalysts for the hydrogenation of succinic acid (SA) to tetrahydrofuran (THF). Synergistic effects between Cu and Pd due to alloying formation are responsible for the enhanced activity of the bimetallic catalysts compared to the monometallic ones. The Cu-rich CuPd catalysts, particularly Cu_8Pd_2/γ-Al_2O_3 and Cu_6Pd_4/γ-Al_2O_3, have emerged as the best catalysts for the production of THF with yields of 85–90%. The key factor that distinguishes them from the rest is the presence of isolated Cu components which holds the potential for further reduction of the intermediate γ-butyrolactone while restraining the hydrogenolysis of SA to butyric acid over the Pd sites.

4.1 Introduction

The chemical industry is now in the process of switching from fossil-based reserves to biomass-based feedstocks which were identified as the more renewable and sustainable resources. Lignocellulosic biomass, in particular, was known as an abundant renewable material for the productions of biofuels and platform chemicals. However, challenges in the process of converting raw materials to platform chemicals with high selectivities and yields are the main obstacles hindering them from successful commercialization [1] Recent developments in the fermentation technology allow few renewable chemicals including succinic acid (SA) to be a competitive supply with the petroleum-based maleic anhydride platform [2]. The main three conversion routes from SA include hydrogenation, esterification, and reductive amination [3]. In the context of the upgrading of bio-bassed feedstocks, the catalytic hydrogenation of SA has been receiving great attention and becoming the most investigated route in the last decade [4]. As a result, efforts have been devoted to designing heterogeneous metal catalysts for the hydrogenation of SA to value-added chemicals. Since the conversion involves multiple steps and several possible pathways to form different products, i.e, γ-butyrolactone (GBL), 1,4-butanediol (BDO), and tetrahydrofuran (THF), the design of a catalyst that shows both high activity and selectivity can be challenged. It can be a more complex question since the effective catalysts generally consist of several functions derived from metal ratio, support, and capping/stabilizing agent, which might interfere with each other. Therefore, controlling those factors by properly combining, amplifying, or reducing the influences of certain factors is critically important for the highly selective hydrogenation of SA.

Recent developments in the catalytic hydrogenation of SA have been focusing on the production of BDO [5–8]. However, it seems that fewer studies reported effective catalysts for the production of THF in the open literature. In most cases, bimetallic catalysts those consist of rare-earth elements such as Re, Ir, Pd, and Ru, have been reported. For example, Liang et al. described that the strong Pd–Re interaction and higher amount of Re in the Pd–Re/C catalyst were accounted for the higher SA conversion (99%) and

THF selectivity (58%) [9]. Another example reported by the same group suggested that the increase in Re:Ru wt% ratio of the Ru–Re/C led to an improvement in the THF selectivity. Accordingly, the highest selectivity of THF (60%) can be achieved at a nearly quantitative SA conversion over the Re3Ru/C catalyst [8]. More recently, they reported a further improvement in the THF production from SA using a series of Ir–Re/C bimetallic catalysts. It was reported that a bifunctional effect between Re and Ir was accounted for the superior selectivity of the bimetallic catalysts compared to the monometallic ones, producing THF with better selectivity ranging from 60–75% [10]. Attempts were made to minimize the non-target products such as BDO, 1-butanol (BuOH), and 1-propanol by decreasing Re molar fraction; however, BuOH, for example, with the selectivities of 20–30% was still observed in these catalysts.

As mentioned earlier, the catalyst support can also be an important factor that may influence the physicochemical properties and thus alters the overall catalytic activity and product selectivity in the SA hydrogenation. For example, Hong et al. reported that the modified mesoporous carbon (MC) supported Re catalysts showed different catalytic activity depending on the concentration of H_2SO_4 treated [11]. In particular, large Re particles generated on untreated MC were found to favor the production of GBL, while the genesis of small Re particles on the H_2SO_4 0.4 M treated MC was proposed to enhance the THF selectivity. Another example regarding the effect of the textural properties of supports on the SA hydrogenation over Pd catalysts was also investigated [12]. In that research, Chung et al. reported that the large pore of SBA-15 favored the construction of small Pd nanoparticles (NPs) which enhanced the production of GBL and THF. On the other hand, large Pd particles were found to form externally to the pore of MCM-41 support, which promoted the formation of BDO. The effect of support acidity for the production of THF from SA is rarely examined despite the fact that acid catalysts have been widely studied for the dehydration of BDO to THF [13–15]. For example, in an early study by Sato et al., various metal oxides such as Al_2O_3, $SiO_2-Al_2O_3$, and ZrO_2 were reported as effective solid acid catalysts for the THF formation from BDO [13]. Various types of zeolites including ZSM-5, Y, Mordenite, Ferrierite, and Beta were also found as effective catalysts for the dehydration of BDO to THF with excellent selectivity [14].

In Chapter 3, the γ-Al_2O_3 supported CuPd catalyst was discovered as a remarkably efficient catalyst for the hydrogenation of SA toward THF [16]. The study revealed that strong Lewis acid sites in the γ-Al_2O_3 support favored the formation of THF as the final product. In the present work, to broaden knowledge in the γ-Al_2O_3 supported CuPd catalysts, the influence of metal ratio on the catalytic performance has been extended for the hydrogenation of SA. In fact, controlling the metal ratio in bimetallic catalysts is a general approach to tune the catalytic activity and selectivity. This method is not only simple in preparation but also cost-effective if a fraction of precious metal can be substituted with an earth-abundant metal in a bimetallic system. For example, a $\sim$1:1 wt% of Ru–Sn [17] and a $Pd-y\,FeO_x/C$ ($y = 5$ wt%) [6] were reported as efficient catalysts for selective hydrogenation of SA to BDO. Although Chapter 2 thoroughly discussed the effect of metal ratio on the activity of hydroxyapatite (HAP) supported Cu-rich CuPd catalysts for the BDO production from SA [18], herein, for further understanding the effect under different circumstance, i.e., catalyst support, γ-Al_2O_3 supported CuPd catalysts with different metal ratios are investigate for the SA hydrogenation toward THF.

4.2 Experimental Section

4.2.1 Materials

All the chemicals and materials used in the current chapter are listed in Table 3.1, Chapter 3.

4.2.2 Catalyst Preparation

γ-Al_2O_3 supported CuPd catalysts with different metal ratio, denoted as Cu_xPd_y/γ-Al_2O_3 ($x + y = 10$ wt%) were prepared by the conventional impregnation method. In general, aqueous solution of Cu and Pd precursors and γ-Al_2O_3 were stirred in a round-bottom flask in ambient temperature for 12 h. The slurry was evaporated under reduced pressure to separate solid from the water media. The solid obtained was further dried at 110 ℃ for another 12 h before being calcined at 500 ℃ for 4 h. The samples were activated by being reduced in a flow of 5% H_2/N_2 (60 mL min^{-1}) at 500 ℃ for 2 h before using for reaction or characterization.

4.2.3 Catalyst Characterization

X-ray diffraction (XRD) patterns were obtained using a Rigaku Smart Lab X-ray diffractometer (Rigaku Co.) with a Cu Kα radiation ($\lambda = 0.154$ nm) operated at 40 kV and 30 mA. The patterns were analyzed referring to the database of Joint Committee of Powder Diffraction Standard. Transmission electron microscopy (TEM) images were acquired by an H-7650 (Hitachi) operated at 100 kV. X-ray photoelectron spectroscopy (XPS) were performed on an Axis-Ultra DLD spectrometer system (Shimadzu Co. and Kratos Analytical Ltd.) with the monochromatic Al Kα (1486 eV) X-ray resources. The binding energies (BE) were calibrated using the binding energy of C 1*s* signal from adventitious carbon contamination on the samples and the peak deconvolutions were performed using the XPSPEAK4.1 software.

X-ray absorption fine structure (XAFS) spectra were recorded in transmission mode at the BL07 (for Pd K-edge) and BL11 (for Cu K-edge) stations of the SAGA light source under the proposal nos. 1910092R and 2010105R. The storage ring was operated at 1.4 GeV where Si (220) and Si (111) single crystals were employed to generate monochromatic X-ray beams at Pd K-edge and Cu K-edge measurements, respectively. To optimize the signals, the sample weight for each target edge was individually calculated. The sampling process which contains grinding and compressing samples to 10 mm pellets was done in the air. The obtained data were analyzed by Athena and Artemis software included in the Demeter package, version 0.9.26.

Temperature programmed reduction of hydrogen (H_2-TPR) for calcined catalyst precursors were conducted on a BELCat II (MicrotracBEL, Corp.). The samples were aligned between quartz wool and placed inside a quartz triple cell. Temperature was increased from 50 ℃ to 700 ℃ at a ramping rate of 10 ℃ min^{-1} in a flow of 10% H_2 /Ar (30 mL min^{-1}). The hydrogen consumption was monitored by a thermal conductivity detector (TCD) and quantified by using a pure CuO standard (99.999%). For keeping water moisture from moving through the detector, a molecular sieve (4A 1/16) trap was employed.

4.2.4 Catalyst Evaluation

The reaction is performed in a stainless-steel autoclave reactor (Taiatsu Technol., Japan) containing a solution of 1,4-dioxane (10 mL), SA (0.1 g), and the reduced catalyst (0.1 g). To remove remaining air inside the reactor, pure H_2 (99.999%) is allowed to purged several times, followed by pressurizing to a certain pressure at room temperature. The reactor is then placed into an aluminum block (Zodiac CCX, EYELA) which was heated previously at 200 ℃ under vigorous stirring. After a certain time, it is cooled down to room temperature. The reaction mixture is centrifugated and analyzed by gas chromatography (GC, Shimadzu GC-2014) with a polar column (DB-FFAP Agilent, 30 m). The GC oven is set to rise from an initial temperature of 50 ℃ (keep for 2 min) to 240 ℃ (keep for 5 min) at a ramping rate of 20 ℃ min^{-1}, whereas the temperatures at the injection port and the detector are 250 ℃ and 280 ℃, respectively. The SA conversion is measured by using high-performance liquid chromatography (HPLC, Water 2414) equipped with a refractive index detector. An aqueous solution of H_2SO_4 (10 mM) is selected as the HPLC eluent, which is pumped at a flow rate of 0.5 mL min^{-1} passing through an Aminex HPX-87H column (Bio-Rad) operated at 50 ℃. The SA conversion, product yields and selectivities are defined as the following equations.

$$\text{Conversion of SA (\%)} = \frac{\text{mole of consumed SA}}{\text{mole of initial SA}} \times 100 \tag{4.1}$$

$$\text{Yield of product (\%)} = \frac{\text{mole of product formed}}{\text{mole of initial SA}} \times 100 \tag{4.2}$$

$$\text{Selectivity of product (\%)} = \frac{\text{mole of product}}{\text{mole of SA consumed}} \times 100 \tag{4.3}$$

4.3 Results and Discussion

4.3.1 Catalytic Performance

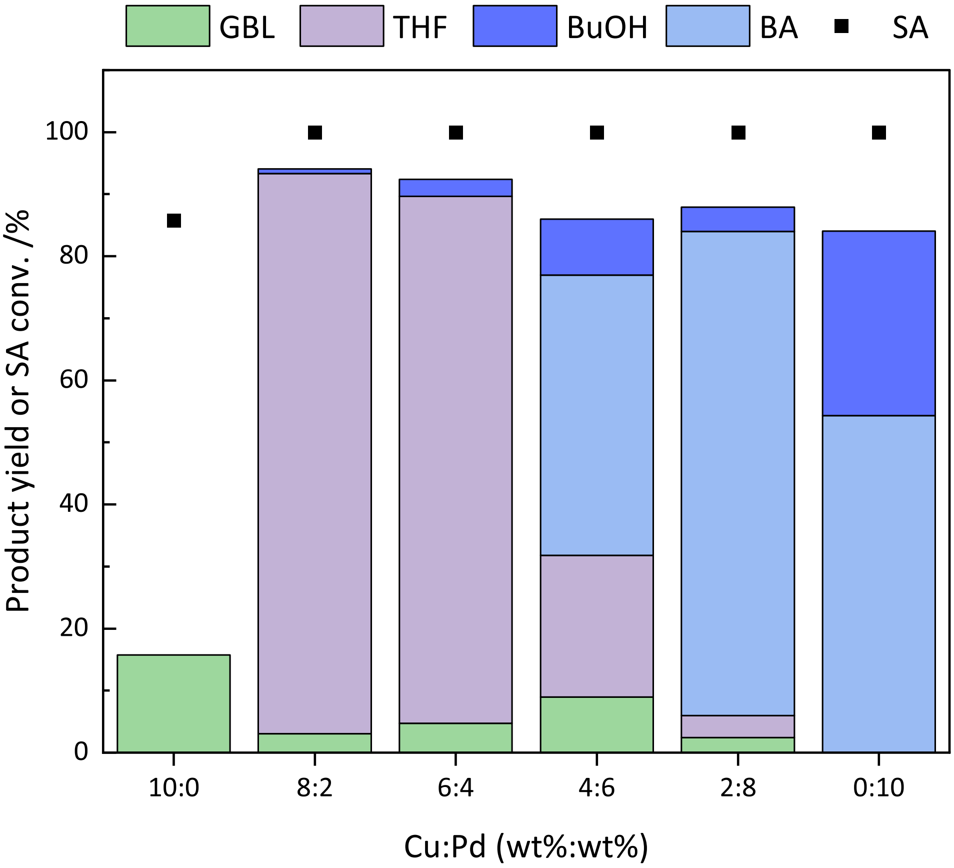

Figure 4.1: Effect of Cu:Pd wt% ratio on the catalytic activity of $Cu_xPd_y/\gamma\text{-}Al_2O_3$ for the hydrogenation of SA. Reaction conditions: SA (0.1 g), catalyst (0.1 g), 1,4-dioxane (10 mL), temperature (200 ℃), H_2 pressure (8 MPa), reaction time (48 h).

Figure 4.1 shows the hydrogenation of SA over $\gamma\text{-}Al_2O_3$ supported CuPd bimetallic catalysts with different metal ratio, while the detailed values can be found in Table 4.1. On the basis of product selectivity, these catalysts can be divided into three groups including (i) $Cu/\gamma\text{-}Al_2O_3$, (ii) Cu-rich $CuPd/\gamma\text{-}Al_2O_3$, and (iii) Pd-rich $CuPd/\gamma\text{-}Al_2O_3$ or $Pd/\gamma\text{-}Al_2O_3$. In the first group catalyst, less than 20% yield of GBL was obtained at a

Table 4.1: Detailed catalysis values for Figure 4.1

Cu_xPd_y/γ-Al_2O_3 (x:y)	Product yield /%				SA conversion /%
	GBL	THF	BA	BuOH	
10:0	16	0	0	0	86
8:2	3	90	0	1	100
6:4	5	85	0	3	100
4:6	9	23	45	9	100
2:8	2	4	78	4	100
0:10	0	0	54	30	100

high conversion of SA (86%). The low carbon balance, in this case, can be attributed to the formation of gaseous by-products via over-reduction, dehydration, or cracking reactions [17]. However, the analysis of gas-phase by micro-GC (INFICON Fusion) hardly identified any by-products derived from carbon due to the excess amount of hydrogen gas that remained after the reaction. While the addition of the Pd element in the bimetallic catalysts apparently increased the product selectivity toward either THF or BA. Particularly, the second group catalysts selectively promoted the formation of THF with 85–90% yield via further hydrogenation of GBL. The best catalytic performance toward THF was achieved over the Cu-rich Cu_8Pd_2/γ-Al_2O_3, affording a selectivity of 90% at a quantitative conversion of SA. On the other hand, under the influence of Pd as a dominant component in the third group catalysts, BA was observed as a major product with yields of 45–78%. The highest BA yield of 78% was obtained over the Pd-rich Cu_2Pd_8/γ-Al_2O_3 catalyst. Compared to the catalytic performance of the Pd-rich CuPd NPs on HAP support (Figure 2.1A, Chapter 2) where BA and GBL were mainly formed, the formations of BuOH and THF as apparent products over the third group catalysts here can possibly be ascribed to the contributory factor of Lewis acid sites of the γ-Al_2O_3 support [16].

It is noted that the Cu-rich CuPd NPs on weakly acid and neutral supports such as SiO_2, hydroxyapatite, TiO_2, and montmorillonite generally show high selectivities toward BDO and GBL (Table 4.2). Therefore, the formation of THF with excellent selectivity over the Cu-rich Cu_8Pd_2/γ-Al_2O_3 catalyst can plausibly be attributed to the effect of strong Lewis acid sites of γ-Al_2O_3 in combination with the essential role of CuPd metal

Table 4.2: Hydrogenation of different substrates over different Cu_8Pd_2/support catalysts[a]

Substrate	Catalyst	Conv. /%	Product yield /%				
			GBL	BDO	THF	BA	BuOH
SA	Cu_8Pd_2/HAP[b]	100	5	82	3	3	3
SA	Cu_8Pd_2/SiO_2	100	2	86	2	0	0
SA	Cu_8Pd_2/TiO_2	73	66	1	2	0	0
SA	Cu_8Pd_2/Mont[b]	100	82	0	6	5	0
SA	$Cu_8Pd_2/\gamma\text{-}Al_2O_3$[c]	100	3	0	90	0	1
SA	$\gamma\text{-}Al_2O_3$	39	0	0	0	0	0
GBL	$\gamma\text{-}Al_2O_3$[d]	23	-	0	0	0	0
GBL	$Cu_8Pd_2/\gamma\text{-}Al_2O_3$[e]	80	-	34	32	0	0
GBL	$Cu_8Pd_2/\gamma\text{-}Al_2O_3$[d]	100	-	0	93	0	0
GBL	$Pd_{10}/\gamma\text{-}Al_2O_3$[d]	100	-	0	2	52	22
BDO	$\gamma\text{-}Al_2O_3$[f]	96	0	-	82	0	0
BDO	$Cu_8Pd_2/\gamma\text{-}Al_2O_3$[f]	100	0	-	93	0	0

[a] Reaction condition: SA (0.1 g), catalyst (0.1 g), 1,4-dioxane (10 mL), temperature (200 ℃), H_2 pressure (8 MPa), reaction time (96 h).

[b] Hydroxyapatite (HAP), Mont (Montmorillonite)

[c] Reaction time (48 h)

[d] Reaction time (24 h)

[e] Reaction time (1 h)

[f] Reaction time (2 h)

species species which facilitated the further reduction of GBL to THF. To further clarify the reaction pathways, the reactions using GBL and BDO as starting materials have been performed and demonstrated in Table 4.2. Accordingly, the hydrogenation of GBL over the $Cu_8Pd_2/\gamma\text{-}Al_2O_3$ catalyst produced both BDO and THF, affording yields of 34% and 32% after 1 h reaction. After elongating the reaction time to 24 h, no BDO was detected, while THF increased significantly, reaching a yield of 93%. These results suggest that BDO may act as the intermediate in the production of THF from GBL. It should be noted that the hydrogenation of GBL over the bare $\gamma\text{-}Al_2O_3$ support, however, failed to produce THF, which emphasizes the prerequisite role of CuPd species in this conversion. In contrast, it was observed that the dehydration of BDO to THF can easily proceed using both the catalyst and the bare support. Therefore, it is highly plausible that BDO was formed under the influence of metal species, while the high selectivity of THF can be attributed to the role of acid sites in the $\gamma\text{-}Al_2O_3$ support itself.

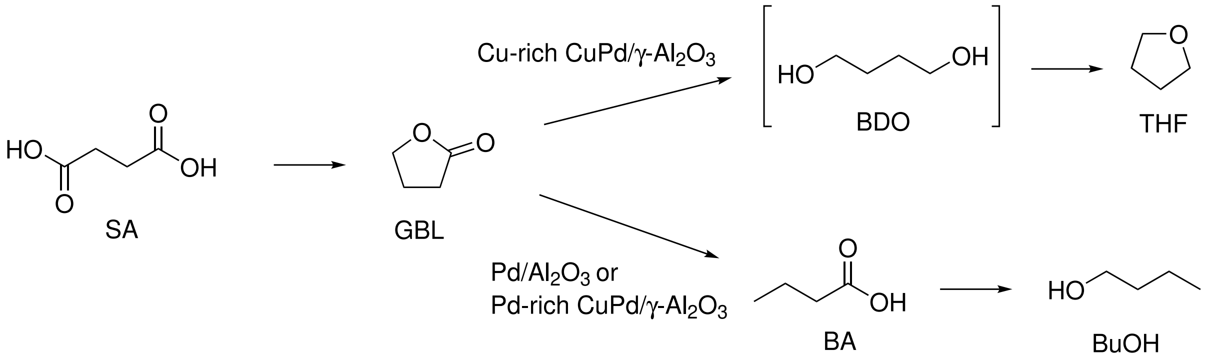

Scheme 4.1: Reaction routes for the SA hydrogenation over the $Cu_xPd_y/\gamma\text{-}Al_2O_3$ catalysts

Considering the results herein, it is worth emphasizing that for complex reactions i.e., containing multiple reaction steps or directions, controlling the sphere of the influence of several active species toward a target product is of utmost importance. In this catalyst system, there exists a limited range where a suitable metal ratio promotes the synergy generating active sites for GBL productions while at the same time constrains the strong influence of Pd which favors the formation of BA. Under this favorable circumstance, the Cu-rich CuPd species further reduce GBL to BDO which immediately undergoes dehydration over the strong Lewis acid sites of $\gamma\text{-}Al_2O_3$ to form THF. On the other hand, the reaction from GBL over the $Pd_{10}/\gamma\text{-}Al_2O_3$ confirmed that the formations of BA and BuOH are favorable under the influence of Pd sites and proceeded via the intermediate GBL (Table 4.2). Accordingly, the overall reaction pathways of SA hydrogenation over the present $Cu_xPd_y/\gamma\text{-}Al_2O_3$ catalysts can be proposed as demonstrated in Scheme 4.1.

4.3.2 Structure–activity relationship

Figure 4.2A represents the diffraction patterns of calcined samples together with their metal oxide references. Characteristic peaks of the $\gamma\text{-}Al_2O_3$ support can be observed at 2θ of about 32.4° 37.4° 39.4°, 45.5°, 60.5°, and 67.0° which represent the reflections of the (220), (311), (222), (400), (511), and (440) planes of a cubic structure. The impregnation of metals resulted in significant changes in the diffraction peaks at lower 2θ while those at the larger values remained the same. The calcined monometallic $Cu_{10}/\gamma\text{-}Al_2O_3$ clearly exhibits sharp peaks at 35.5° and 38.7° corresponding to the reflections upon the (002) and (111) planes of the CuO (PDF #00-041-0254). The interaction upon coordination with Pd modified the crystal structure of Cu inducing broader peaks with shifts to lower angles, which might be contributed to a better deposition of bimetallic metals onto the support compared to that of the monometallic Cu metal. The most "finest" deposition among these calcined samples can be predicted for Cu_2Pd_8/γ-Al_2O_3 since its diffraction patterns represent exactly the same as those of the host γ-Al_2O_3. Nevertheless, the XRD patterns of monometallic Pd emerges with a distinct peak at about 34.6° which is close to the diffraction peak of the (002) plane of the tetragonal PdO reference (PDF #01-075-0200). Thus, this result further confirms that the interaction between these two metals, i.e., alloying, can enhance the dispersion in comparison to that of both the monometallic Cu and Pd catalysts.

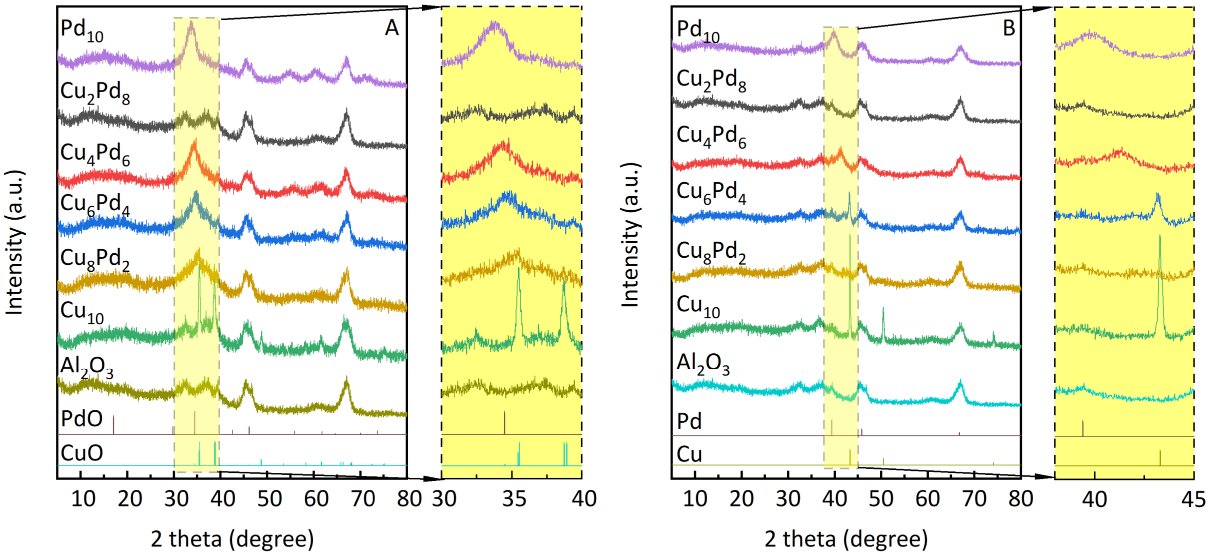

Figure 4.2: XRD patterns of (A) the calcined and (B) the reduced Cu_xPd_y/γ-Al_2O_3 catalysts

The XRD patterns of the samples after reduction under hydrogen are demonstrated in Figure 4.2B. The tetragonal-cubic phase transformation was observed upon reduction of the Pd_{10}/γ-Al_2O_3 since the peaks at 39.7°, 45.9°, and 67.1° are respectively assigned to the diffraction onto the (111), (200), and (220) planes of face-centered cubic (*fcc*) structure of metallic Pd (PDF #01-087-0641). While the diffraction peaks at 43.3°, 50.4°, and 74.1° of the Cu_{10}/γ-Al_2O_3 were generated by the incidence on the (111), (200), and (220) planes of the *fcc* structure of the metallic Cu (PDF #01-071-4610). As similar as the calcined sample, the reduced Cu_2Pd_8/γ-Al_2O_3 exhibits the diffraction line that is well-matched with the support. In comparison with the reduced monometallic Cu, there is no apparent diffraction peak related to the metallic Cu and CuPd species that can be observed in the Cu_8Pd_2/γ-Al_2O_3 sample. However, further replacement of Cu by Pd into the bimetallic structure of the Cu_6Pd_4/γ-Al_2O_3 resulted in the appearance of a clear peak at 43.1°, indicating the segregation of bulky Cu species in this sample. On the other hand, the presence of dominant Pd species in the Cu_4Pd_6/γ-Al_2O_3 induced only the diffraction peak related to Pd–Cu, suggesting that with the same wt% of metal loading, Pd was better dispersed on the γ-Al_2O_3 than Cu.

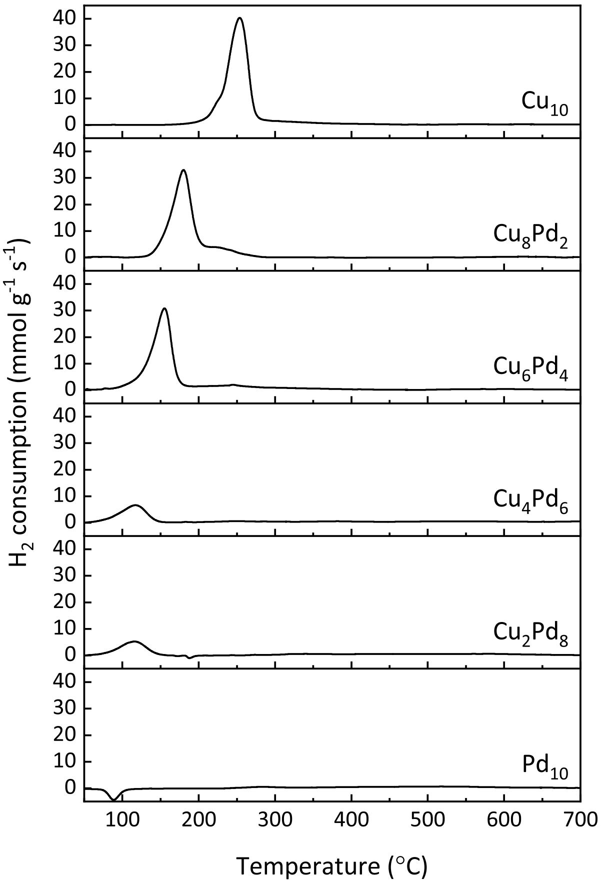

Figure 4.3: H_2-TPR profiles of the calcined Cu_xPd_y/γ-Al_2O_3 samples

H_2-TPR profiles for the calcined Cu_xPd_y/γ-Al_2O_3 samples were collected and shown in Figure 4.3. The Cu_{10}/γ-Al_2O_3 shows a great peak at 254 ℃ and a weak shoulder at a lower temperature, which can be assigned to the reduction of bulk and well-dispersed CuO species. In contrast, a negative peak at 88 ℃ is observed in the $Pd_{10}/\gamma\text{-}Al_2O_3$, which is known as the decomposition of β-phase of Pd hydride releasing H_2 [19, 20]. This negative peak disappeared in the bimetallic catalysts suggesting the strong interaction of Cu–Pd alloy which prevents the formation of Pd hydride [21]. In comparison with the Cu monometallic catalyst, the reduction peaks of the bimetallic ones shifted to lower temperatures. This is consistent with a previous report [22] that Pd aided the reduction of other oxides by hydrogen spillover [23], causing lower reduction peaks. It is noted that the major reduction peaks ranging from 115 ℃ to 180 ℃ might be attributed to mixture oxides including PdO and Cu_xPd_yO [24]. However, taking XRD results (Figure 4.2A) into account, it is believed that the Cu_xPd_yO exists as the prevalent phase. Also, it is worth mentioning that the peak related to the bulky Cu species, which shifted to lower temperatures, can be observed with a small minority in the Cu-rich CuPd catalysts (Cu $>$ 4wt%). The differences in the relative distance of these peaks to the mixed oxides could result in Cu species with different properties. For example, the close interaction with the mixed oxides in the $Cu_8Pd_2/\gamma\text{-}Al_2O_3$ may result in Cu species with better dispersion. In contrast, the weak interaction with the mixed oxides may induce Cu species with high crystallinity, leading to the sharp diffraction peak at 43.1° of the reduced $Cu_6Pd_4/\gamma\text{-}Al_2O_3$, as revealed by the XRD (Figure 4.2B).

TEM images of $\gamma\text{-}Al_2O_3$ supported Cu and Pd monometallic catalysts and the bimetallic catalyst $Cu_8Pd_2/\gamma\text{-}Al_2O_3$ are demonstrates in Figure 4.4. It is clear that the $\gamma\text{-}Al_2O_3$ supported monometallic Cu and Pd shows wide ranges of particle size distributions. Although having a similar average diameter of 5.0 nm, large particles of about 20 nm can be encountered in the $Cu_{10}/\gamma\text{-}Al_2O_3$ catalyst while the $Pd_{10}/\gamma\text{-}Al_2O_3$ exhibits a shorter range of particle size with less than 12 nm. These results suggest the tendency to the agglomeration of Cu is greater than that of Pd in these monometallic catalysts. The existence of the large particles in this catalyst can explain the sharp diffraction peaks revealed by XRD. In contrast, the $Cu_8Pd_2/\gamma\text{-}Al_2O_3$ bimetallic catalyst shows a narrow particle size distribution with the mean diameter of 3.0 nm. Accordingly, the better de-

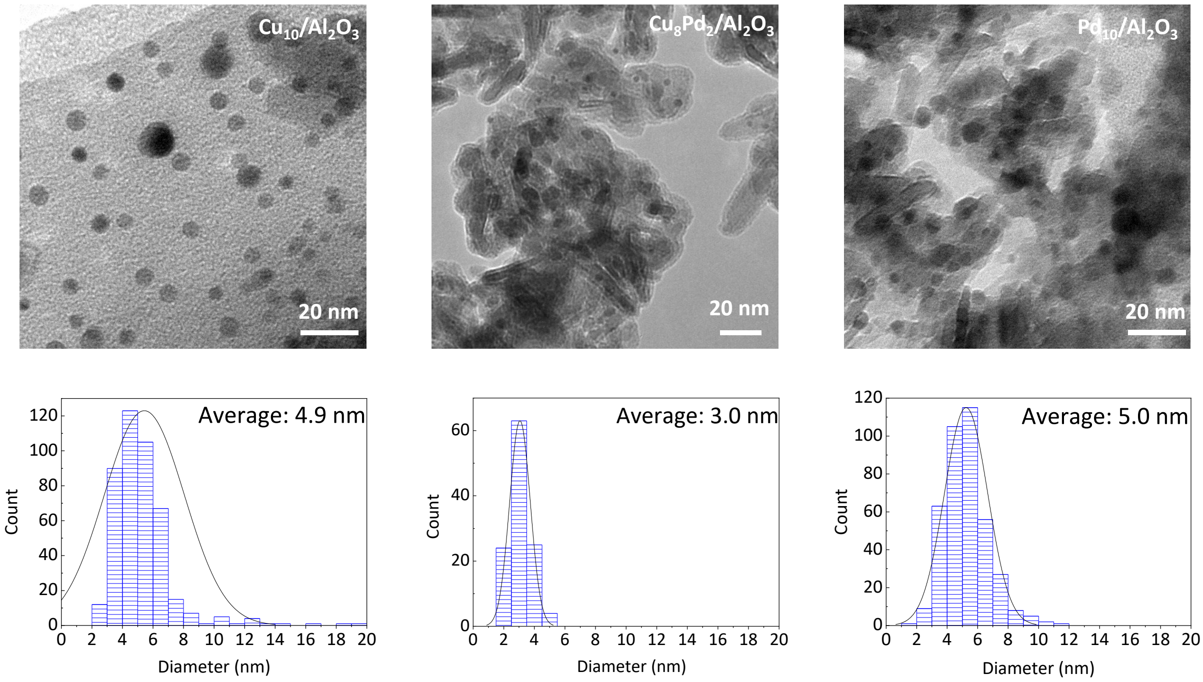

Figure 4.4: TEM images (upper) and particle size distributions (lower) of the reduced monometallic catalysts and the $Cu_8Pd_2/\gamma\text{-}Al_2O_3$ bimetallic catalyst

position of Cu onto the $\gamma\text{-}Al_2O_3$ was assisted by the co-existence of Pd, which resulted in the generation of small CuPd NPs.

XPS spectra of $\gamma\text{-}Al_2O_3$ supported CuPd catalysts are demonstrated in Figure 4.5 and the binding energies (BE) for the main components are listed in Table 4.3. Except for the Pd-rich CuPd bimetallic catalysts, the Cu $2p_{3/2}$ peaks (Figure 4.5A) can be deconvoluted into two components at 931.9–932.7 eV and 933.8–934.4 eV which closely correspond to the metallic Cu^0 and Cu^{2+} species, respectively [25, 26]. The increases in Cu concentrations of these bimetallic catalysts made them susceptible to oxidation which directly related to the presence of the Cu^{2+} satellite peaks at about 941–948 eV. The absence of Cu^{2+} peaks in the Cu_4Pd_6 and Cu_2Pd_8 catalysts can be attributed to the smaller loading amount of Cu or the prevalence of Pd on the surface which prevented Cu species from oxidizing. It is noted that the modification of the Cu structure by adding the Pd element led to the BE shifts at the Cu $2p$ regions of the CuPd bimetallic catalysts. The dependence of these shifts on the Pd contents can be visualized in Figure 4.6A. On the one hand, it can be observed that with regard to the BE shift of the monometallic Cu, there is no clear trend

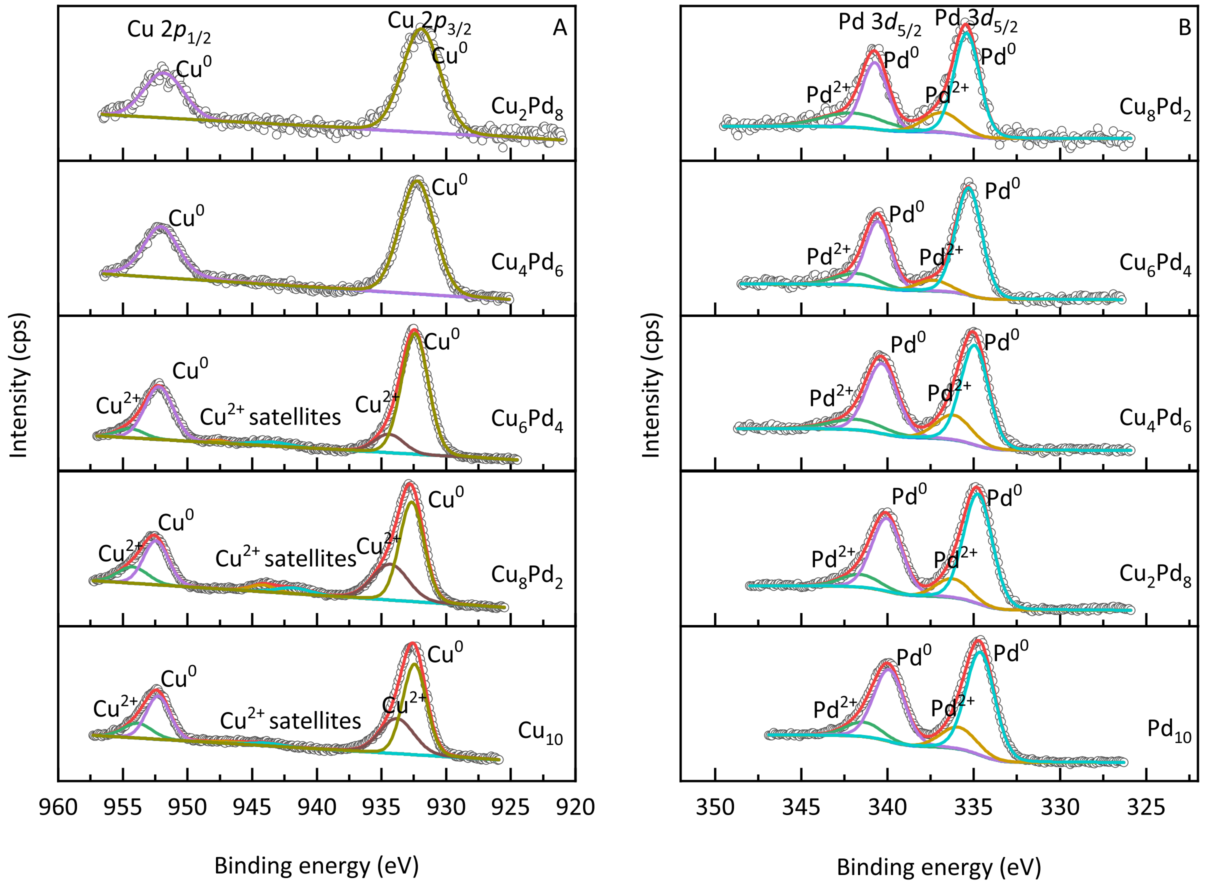

Figure 4.5: XPS spectra at (A) Cu $2p$ and (B) Pd $3d$ regions of the reduced Cu_xPd_y/γ-Al_2O_3 catalysts

in these shifts, especially when Cu contents are dominant. This can be attributed to the segregation of Cu on the surface. On the other hand, if comparing the chemical shifts among the bimetallic catalysts, a negative linear relationship ($R^2 = 0.96$) is observed, indicating that to some extent Pd–Cu interaction influenced the electronic structure of Cu.

The Pd $3d$ spectra of Cu_xPd_y/γ-Al_2O_3 catalysts are shown in Figure 4.5B. The deconvolution of Pd $3d_{5/2}$ spectra was performed involving Pd^0 and Pd^{2+} components. The former peak at 334.6–335.3 eV corresponds to BEs of Pd–Pd bonds while the latter peak at 335.9–337.3 relates to BEs of Pd–O coordinations [27]. Upon the addition of Cu, the core levels of Pd $3d_{5/2}$ peaks shifted to higher BEs. This further confirms the strong Cu–Pd interaction as a resulted of alloying formation [26, 27], inducing charge transfers between these two metals. The dependence of chemical shifts on the Cu content of the

Table 4.3: Binding energy of the $Cu_xPd_y/\gamma\text{-}Al_2O_3$ at Cu $2p_{3/2}$ and Pd $3d_{5/2}$ regions

Sample	Cu $2p_{3/2}$		Pd $3d_{5/2}$	
	Cu^0	Cu^{2+}	Pd^0	Pd^{2+}
$Cu_2Pd_8/\gamma\text{-}Al_2O_3$	931.9	-	334.8	336.2
$Cu_4Pd_6/\gamma\text{-}Al_2O_3$	932.3	-	335.0	336.2
$Cu_6Pd_4/\gamma\text{-}Al_2O_3$	932.4	934.4	335.3	337.3
$Cu_8Pd_2/\gamma\text{-}Al_2O_3$	932.7	934.2	335.4	336.8
$Cu_{10}/\gamma\text{-}Al_2O_3$	932.4	933.8	-	-
$Pd_{10}/\gamma\text{-}Al_2O_3$	-	-	334.6	335.9

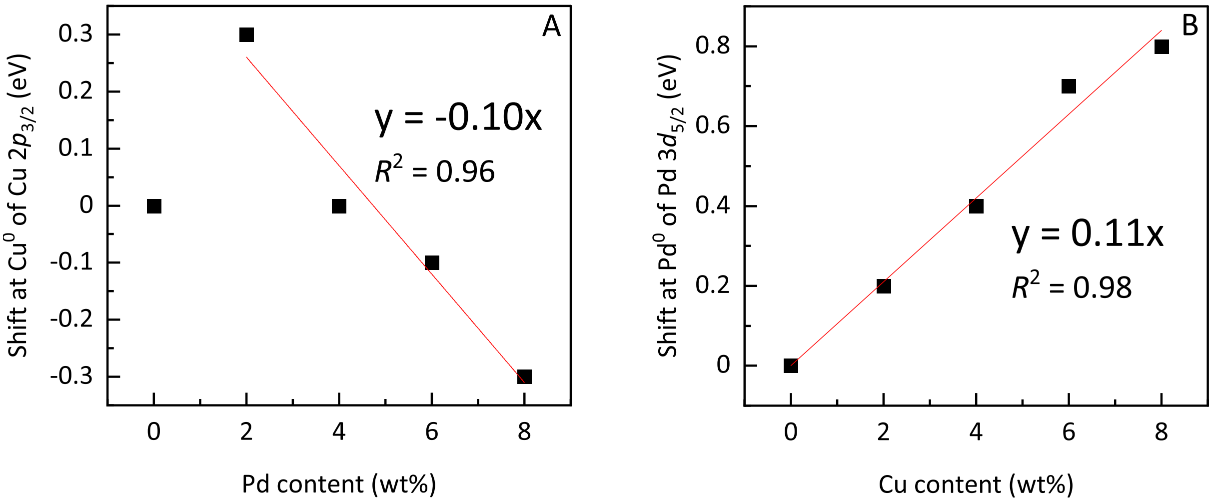

Figure 4.6: Dependence of chemical shifts at (A) Cu^0 of the Cu $2p_{3/2}$ on the Pd content and (B) Pd^0 of the Pd $3d_{5/2}$ on the Cu contents. The shifts are calculated relative to the BE of Cu_{10} and Pd_{10} monometallic catalysts

.

bimetallic catalysts with respect to the BE of the monometallic Pd_{10} is plotted in Figure 4.6B. In comparison with the BE shifts at Cu $2p_{3/2}$ which are scarcely affected by Pd if Cu is a prevalent component, a positive linear relationship ($R^2 = 0.98$) was observed at Pd $3d_{5/2}$. This result suggests a homogeneous distribution of Pd in CuPd nano surface.

XAFS was then performed to further investigate the structures of the $Cu_xPd_y/\gamma\text{-}Al_2O_3$ catalysts by examining the local environments at each target edge. The XANES features, k^3-weighted EXAFS, and Cu–O coordination fitting results at Cu K-edge of the catalysts and references were collected and respectively illustrated in Figure 4.7A and Figure 4.8. It can be observed from the XANES spectra that except for the $Cu_{10}/\gamma\text{-}Al_2O_3$, the bimetallic catalysts show intense white lines at 8.995 keV and shakedown like features at 8.980 keV,

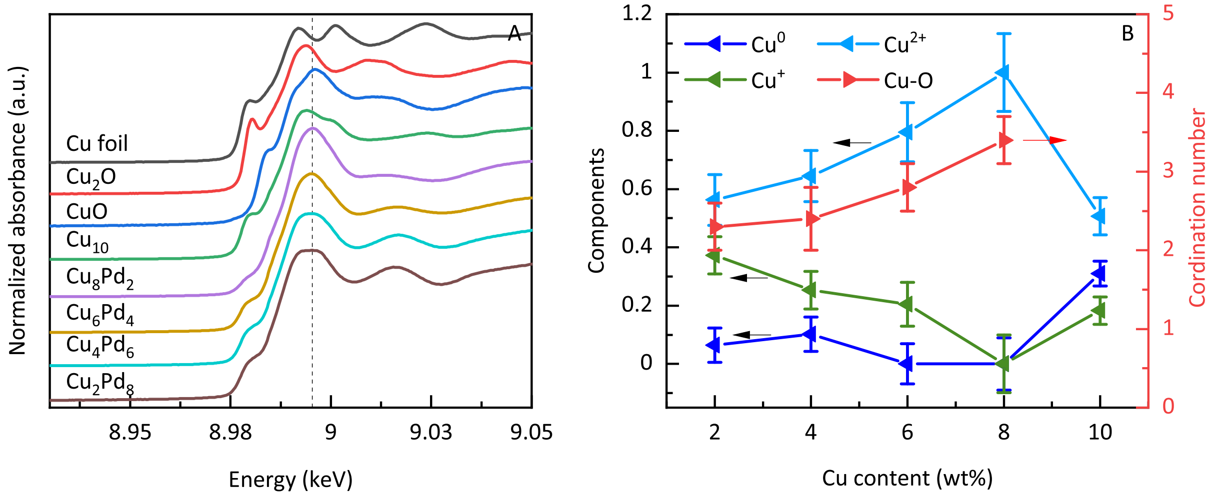

Figure 4.7: (A) XANES spectra and (B) LCF and Cu–O CNs at Cu K-edge for the reduced Cu_xPd_y/γ-Al_2O_3 catalysts

which can be assigned to the transitions of $1s \rightarrow 4p$ (continuum) and $1s \rightarrow 4p_{x,y}p_z$ transition in CuO and Cu_2O [28–30]. The positions of white line peaks in these catalysts shifted to lower photon energies along with the decreases in Cu contents indicating the increases in the Cu^+ components. These arguments are qualitatively demonstrated by performing linear combination fitting (LCF) and Cu–O coordination number (CN) fitting at Cu K-edge (Figure 4.7B). The results herein reveal that the more Pd coordinated with Cu by alloying formation, the fewer CuO species formed by being re-oxidized during the sampling steps for XAFS measurements. On the other hand, the increases in the Cu^+ components were observed in the bimetallic catalysts with increasing Pd contents. This suggests that under the influence of strong Cu–Pd interaction, the partial oxidation of Cu to Cu^+ is more favorable than the full oxidation to Cu^{2+}. Despite the fact that Pd can enhance the oxidation resistance of Cu, the Cu^{2+} components of the bimetallic catalysts are greater than that of the Cu monometallic catalyst. This can be explained by considering the existence of large particles in the latter which allowed lesser Cu–O coordination. Although the results at Cu K-edge might not reflect exactly the active phases of Cu due to the significant re-oxidation during the sampling steps in the air, the trend observed herein is valuable to support the results of XRD, XPS, and TEM with regards to Cu–Pd interaction, metal dispersion, and particle sizes.

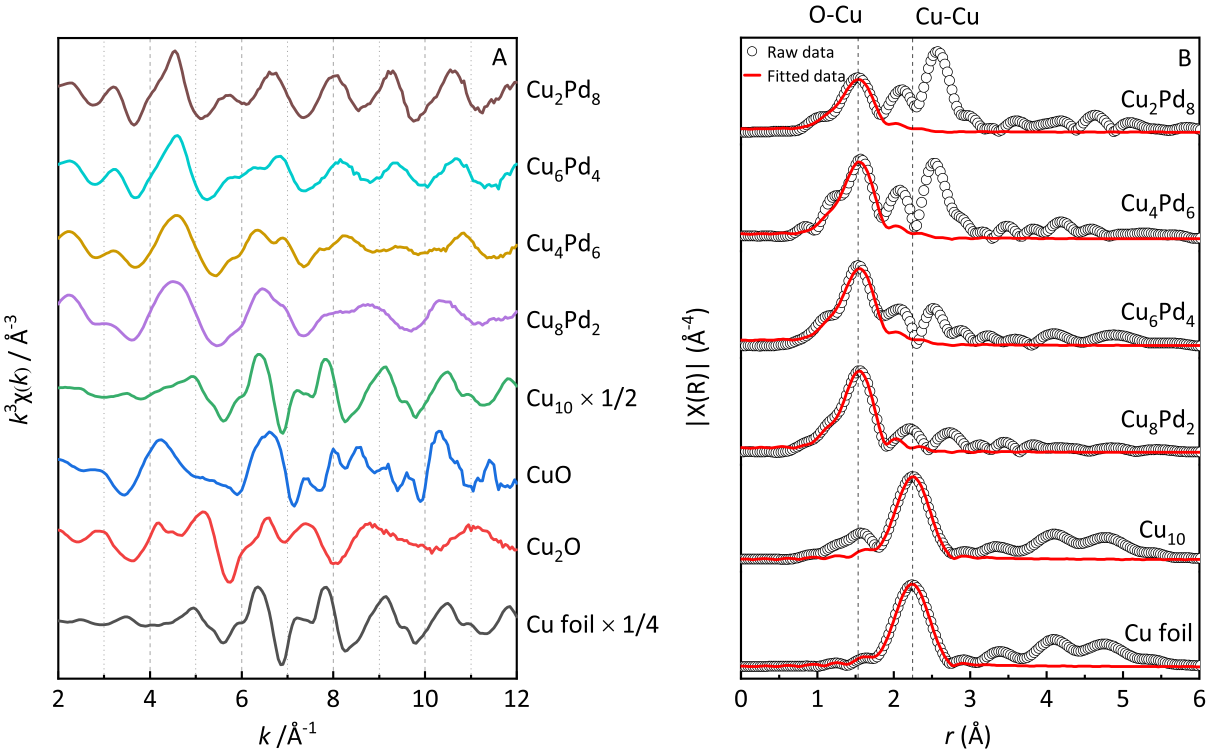

Figure 4.8: (A) k^3-weighted EXAFS and (B) FT EXAFS spectra of raw and fitted data at Cu K-edge for the reduced Cu_xPd_y/γ-Al_2O_3 catalysts

XANES features at Pd K-edge of the reduced Cu_xPd_y/γ-Al_2O_3 catalysts are demonstrated in Figure 4.9A. In general, the peak shapes of catalysts are similar to that of the Pd foil reference, indicating the prevalence of the Pd^0 state. However, in contrast with the trend observed at Cu K-edge, the addition of the Cu as a neighboring atom led to shifts toward higher photo energies at Pd K-edge suggesting the increase in the oxidation state of Pd. Considering the existence of more CuO content due to the re-oxidation in Cu-rich catalysts, it is believed that Pd at the CuO-Pd interface can also be partially re-oxidized due to the diffusion of oxygen into Pd lattice [31]. The k^3-weighted EXAFS spectra indicate the reductions in the $\chi(k)$ signal amplitude for the first two peaks of oscillations upon the increases of Cu contents (Figure 4.9B). These peaks were broadened and shifted to higher k values in comparison with the Pd_{10} monometallic catalyst. The observed phenomena suggest the decreases in the average Pd–Pd CNs which might be replaced by Pd–Cu and/or Pd–O coordinations.

The Fourier transformed (FT) EXAFS spectra and their simulated fits at Pd K-edge are

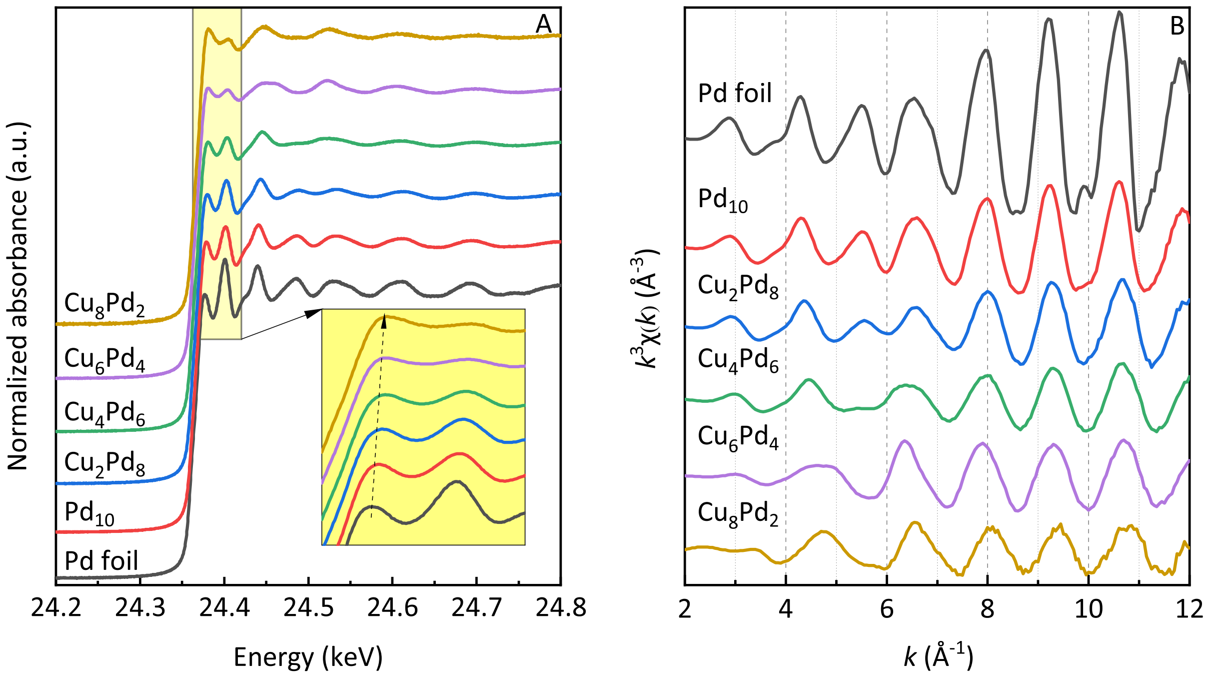

Figure 4.9: (A) XANES features and (B) k^3-weighted EXAFS spectra at Pd K-edge of the reduced Cu_xPd_y/γ-Al_2O_3 catalysts

Table 4.4: EXAFS fitting results at Pd K-edge for the reduced Cu_xPd_y/γ-Al_2O_3 catalysts

Sample	Pd–Pd	Pd–Cu	R_{Pd-Pd}	R_{Pd-Cu}
Pd foil	12.0	-	2.741	-
Pd_{10}/γ-Al_2O_3	8.3 ± 0.3	-	2.733	-
Cu_2Pd_8/γ-Al_2O_3	6.9 ± 0.4	2.0 ± 0.3	2.702	2.649
Cu_4Pd_6/γ-Al_2O_3	4.3 ± 0.4	3.2 ± 0.3	2.682	2.613
Cu_6Pd_4/γ-Al_2O_3	1.3 ± 0.6	4.2 ± 0.7	2.680	2.563
Cu_8Pd_2/γ-Al_2O_3	2.6 ± 0.5	3.3 ± 0.4	2.685	2.589
Cu_8Pd_2/γ-Al_2O_3 (used)	3.5 ± 0.9	4.2 ± 0.9	2.681	2.583

visualized in Figure 4.10. The Pd_{10} spectrum exhibits a single peak at 2.5 Å representing a Pd–Pd coordination. The addition of Cu in the bimetallic catalysts resulted in an additional peak at lower r values which can be attributed to the presence of Pd–Cu bonding. The fitting results are tabulated in Table 4.4 which show the decreases in Pd–Pd CNs and increases in Pd–Cu bonding as a result of alloying formation. Notably, the Cu_6Pd_4/γ-Al_2O_3 which shows only a single peak exhibits a greater Pd–Cu CN compared to that of others including the Cu_8Pd_2/γ-Al_2O_3 catalyst. The lesser extent in alloying with Cu of the Cu_8Pd_2/γ-Al_2O_3 can be attributed to the increase in CuO content, withdrawing Cu from coordinating with Pd. At the same time, the prevalence of the CuO component

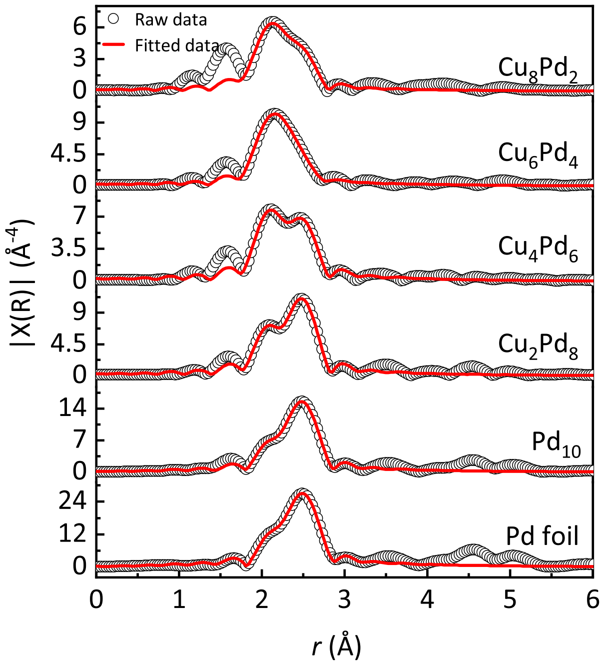

Figure 4.10: FT EXAFS spectra of raw and fitted data at Pd K-edge for the reduced Cu_xPd_y/γ-Al_2O_3 catalysts

also facilitates the oxidation of Pd which leads to an apparent Pd–O peak beneath the Pd–Cu peak in this catalyst. Whereas the greater alloying degree in Cu_6Pd_4/γ-Al_2O_3 made Pd more resistant to oxidation which is consistent with the smaller areas under Pd–O peaks revealed by both EXAFS and XPS (Figure 4.5B). Given the high activities of the CuPd bimetallic catalysts compared to the monometallic Cu, it is believed that a certain degree of Cu–Pd alloying is a prerequisite for the conversion of SA to the intermediate GBL. However, the Cu-rich CuPd NPs are crucial components since on the one hand it prevented the side reaction to BA; on the other hand, its interaction with the strong Lewis acid sites of γ-Al_2O_3 further drove GBL to THF with excellent selectivity.

4.3.3 Stability of the Potential Catalyst

The reusability of the Cu_8Pd_2/γ-Al_2O_3 was investigated and illustrated in Figure 4.11. It is obvious that the catalyst can maintain excellent activity and selectivity during the first three consecutive runs. It is noted that the fluctuation in the THF selectivity is within the uncertainty value (± 2%) which was determined by repeating the reaction over the

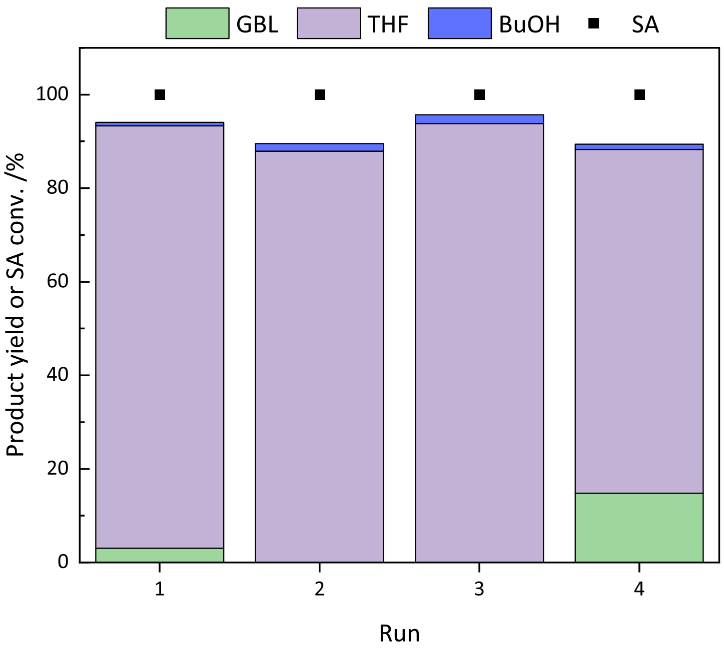

Figure 4.11: Recycling tests of the Cu_8Pd_2/γ-Al_2O_3 for the SA hydrogenation. Reaction conditions: catalyst (0.1 g), 1,4-dioxane (10 mL), temperature (200 ℃), H_2 pressure (8 MPa), reaction time (48 h).

fresh catalyst for three times. It is noted that the side reaction to BuOH was minimized throughout the recycling experiments, suggesting that Pd was stabilized by the strong Cu–Pd alloying interaction. The XPS at $2p$ region and XAFS at Cu K-edge comparing the fresh and used catalysts are respectively shown in Figure 4.12A which suggests a decrease in the Cu^{2+} component. Further evidence on this can also be found in the XAFS results, as illustrated in Figure 4.13A–C. At the same time, the XPS peak at Pd $3d_{5/2}$ region (Figure 4.12B) of the used catalysts shows a negative shift compared to the fresh one, indicating a stronger Pd–Cu interaction upon recycling tests. These results indicate that the decrease in the Cu^{2+} fraction of the used catalyst due to further reduction during the reaction allowed more Pd–Cu coordination in the used catalyst. The stabilization of Pd by Cu during the reaction can be viewed in the XAFS results at Pd K-edge (Figure 4.13D–F) where the used catalyst showed similar features to the fresh one. However, it should be noted that the FT EXAFS spectra of the used catalyst exhibits a higher intensity than that of the fresh one. This is qualitatively confirmed by its larger total CNs of Pd–M (M = Pd/Cu) (Table 4.4), suggesting an increase in the particle size. As a

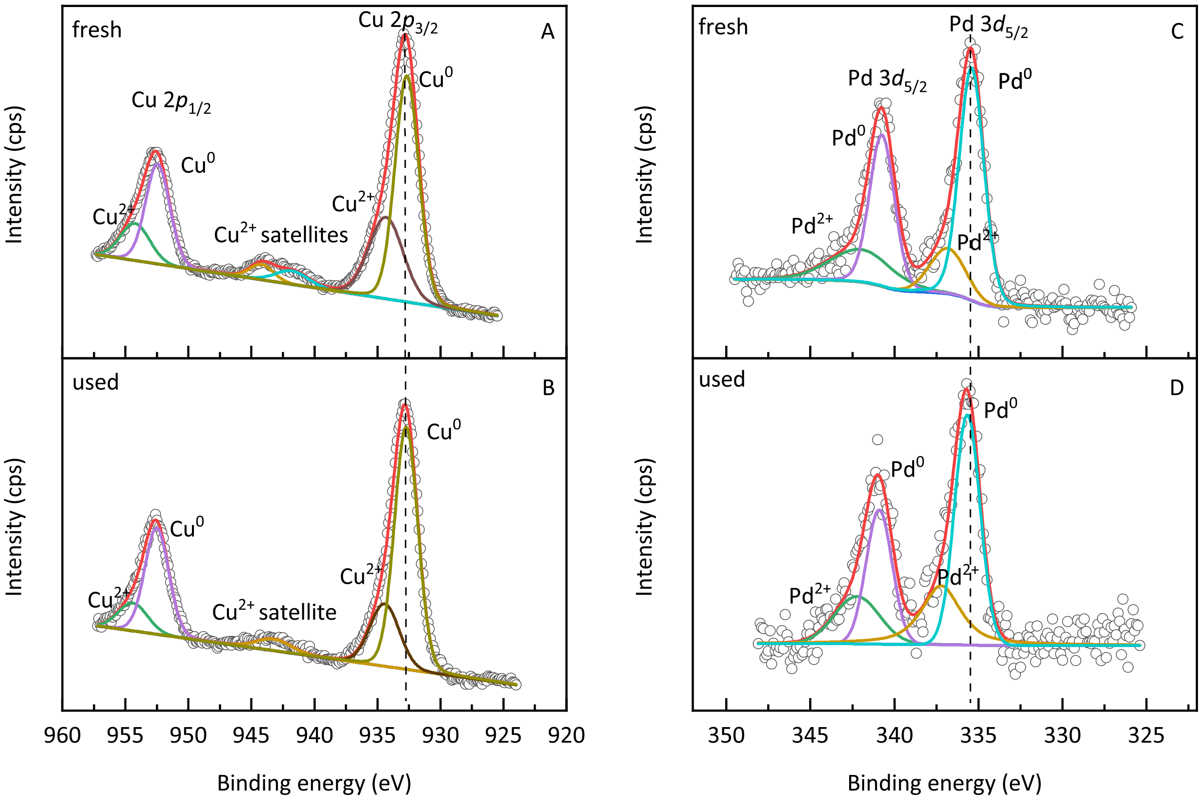

Figure 4.12: XPS spectra of the fresh and used $Cu_8Pd_2/\gamma\text{-}Al_2O_3$ (after 4 runs) at (A–B) Cu $2p$ and (C–D) Pd $3d$ regions

result, the used catalyst showed a slight decrease in the THF selectivity and the increase in the GBL selectivity in the fourth run.

4.4 Conclusion

This study demonstrates the effect of metal ratio on the activity of $\gamma\text{-}Al_2O_3$ supported CuPd NPs for SA hydrogenation. Excellent catalytic performance toward THF was achieved over the Cu-rich $Cu_8Pd_2/\gamma\text{-}Al_2O_3$, achieving the product yield and selectivity of 90%. In addition, the present catalyst can maintain its high activity and selectivity upon four recycling runs under the high temperature and pressure conditions. Extensive characterization methods revealed that major factors that were responsible for the superior performance and stability of this catalyst for THF production include CuPd alloy NPs with the isolated Cu species and strong Lewis acid sites of the $\gamma\text{-}Al_2O_3$ support. The strong interaction in CuPd alloy NPs led to the enhanced reactivity compared to

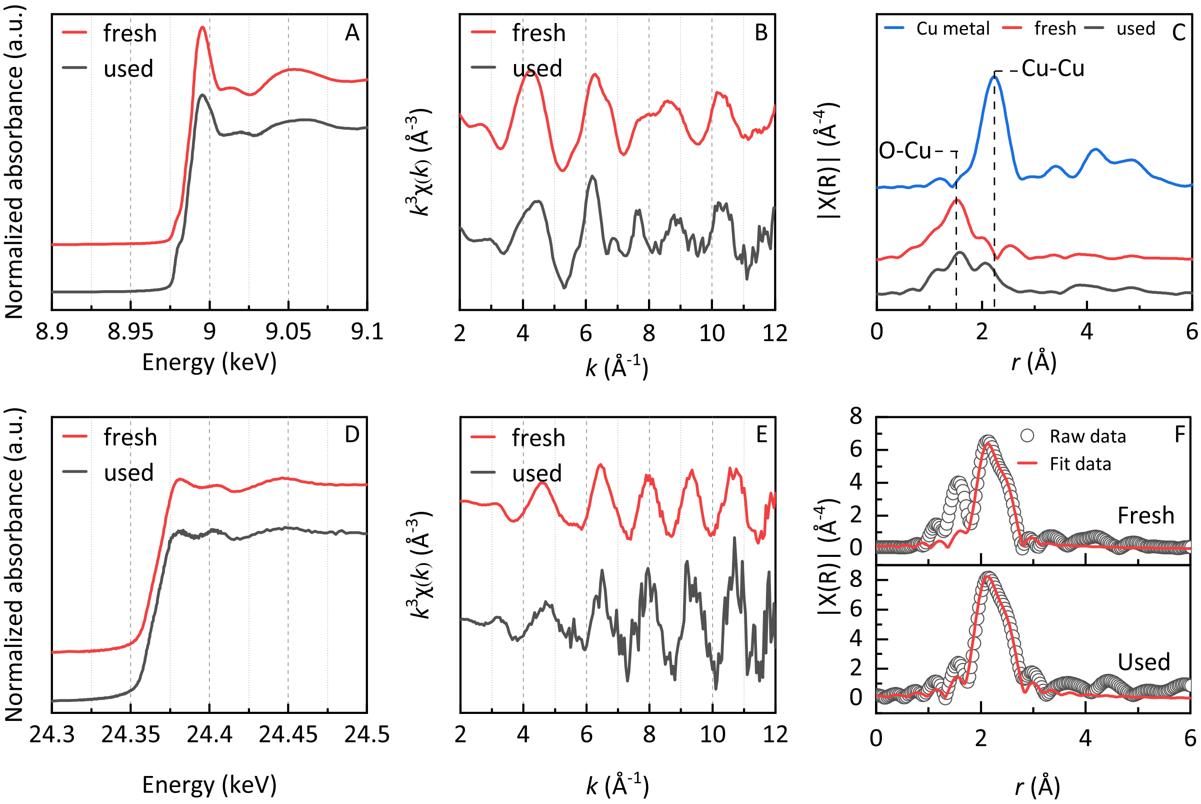

Figure 4.13: XANES features, k^3-weighted EXAFS and FT EXAFS spectra at (A–C) Cu K-edge and (D–F) Pd K-edge of the fresh and used Cu_8Pd_2/γ-Al_2O_3 catalysts

that of the monometallic Cu, while the Cu-rich component helped to restrain the strong reactivity of Pd species which favor the formation of BA. The presence of isolated Cu species enhanced the formation of the intermediate BDO, which was then converted to THF via cyclodehydration under the influence of strong Lewis acid sites in γ-Al_2O_3.

References

(1) Takkellapati, S.; Li, T.; Gonzalez, M. A. An overview of biorefinery-derived platform chemicals from a cellulose and hemicellulose biorefinery. *Clean Technol. Environ. Policy* **2018**, *20*, 1615–1630.

(2) Mazière, A.; Prinsen, P.; García, A.; Luque, R.; Len, C. A Review of Progress in (Bio)Catalytic Routes from/to Renewable Succinic Acid. *Biofuels, Bioprod. Biorefining* **2017**, *11*, 908–931.

(3) Delhomme, C.; Weuster-Botz, D.; Kühn, F. E. Succinic Acid from Renewable Resources as a C_4 Building-Block Chemical–a Review of the Catalytic Possibilities in Aqueous Media. *Green Chem.* **2009**, *11*, 13–26.

(4) Pritchard, J.; Filonenko, G. A.; Van Putten, R.; Hensen, E. J.; Pidko, E. A. Heterogeneous and Homogeneous Catalysis for the Hydrogenation of Carboxylic Acid Derivatives: History, Advances and Future Directions. *Chem. Soc. Rev.* **2015**, *44*, 3808–3833.

(5) Ly, B. K.; Minh, D. P.; Pinel, C.; Besson, M.; Tapin, B.; Epron, F.; Especel, C. Effect of Addition Mode of Re in Bimetallic Pd−Re/TiO_2 Catalysts Upon the Selective Aqueous-Phase Hydrogenation of Succinic Acid to 1,4-Butanediol. *Top Catal.* **2012**, *55*, 466–473.

(6) Liu, X.; Wang, X.; Xu, G.; Liu, Q.; Mu, X.; Liu, H. Tuning the Catalytic Selectivity in Biomass-Derived Succinic Acid Hydrogenation on FeO_x-Modified Pd Catalysts. *J. Mater. Chem. A* **2015**, *3*, 23560–23569.

(7) Takeda, Y.; Tamura, M.; Nakagawa, Y.; Okumura, K.; Tomishige, K. Hydrogenation of Dicarboxylic Acids to Diols over Re–Pd Catalysts. *Catal. Sci. Technol.* **2016**, *6*, 5668–5683.

(8) Di, X.; Li, C.; Zhang, B.; Qi, J.; Li, W.; Su, D.; Liang, C. Role of Re and Ru in Re-Ru/C Bimetallic Catalysts for the Aqueous Hydrogenation of Succinic Acid. *Ind. Eng. Chem. Res.* **2017**, *56*, 4672–4683.

(9) Shao, Z.; Li, C.; Di, X.; Xiao, Z.; Liang, C. Aqueous-Phase Hydrogenation of Succinic Acid to γ-Butyrolactone and Tetrahydrofuran over Pd/C, Re/C, and Pd–Re/C Catalysts. *Ind. Eng. Chem. Res.* **2014**, *53*, 9638–9645.

(10) Keels, J. M.; Chen, X.; Karakalos, S.; Liang, C.; Monnier, J. R.; Regalbuto, J. R. Aqueous-Phase Hydrogenation of Succinic Acid Using Bimetallic Ir–Re/C Catalysts Prepared by Strong Electrostatic Adsorption. *ACS Catal.* **2018**, *8*, 6486–6494.

(11) Hong, U. G.; Park, H. W.; Lee, J.; Hwang, S.; Yi, J.; Song, I. K. Hydrogenation of Succinic Acid to Tetrahydrofuran (THF) over Rhenium Catalyst Supported on H_2SO_4-Treated Mesoporous Carbon. *Appl. Catal. A Gen.* **2012**, *415*, 141–148.

(12) Chung, S.-H.; Park, Y.-M.; Kim, M.-S.; Lee, K.-Y. The Effect of Textural Properties on the Hydrogenation of Succinic acid Using Palladium Incorporated Mesoporous Supports. *Catal. Today* **2012**, *185*, 205–210.

(13) Sato, S.; Takahashi, R.; Sodesawa, T.; Yamamoto, N. Dehydration of 1,4-Butanediol into 3-Buten-1-ol Catalyzed by Ceria. *Catal. Commun.* **2004**, *5*, 397–400.

(14) Aghaziarati, M.; Kazemeini, M.; Soltanieh, M.; Sahebdelfar, S. Evaluation of Zeolites in Production of Tetrahydrofuran from 1,4-Butanediol: Performance Tests and Kinetic Investigations. *Ind. Eng. Chem. Res.* **2007**, *46*, 726–733.

(15) Mi, R.; Hu, Z.; Yi, C.; Yang, B. Catalytic Dehydration of 1,4-Butanediol over Mg–Yb Binary Oxides and the Mechanism Study. *ChemCatChem* **2020**, *12*, 2859–2871.

(16) Le, S. D.; Nishimura, S. Effect of Support on the Formation of CuPd Alloy Nanoparticles for the Hydrogenation of Succinic Acid. *Appl. Catal. B Environ.* **2020**, 119619.

(17) Vardon, D. R.; Settle, A. E.; Vorotnikov, V.; Menart, M. J.; Eaton, T. R.; Unocic, K. A.; Steirer, K. X.; Wood, K. N.; Cleveland, N. S.; Moyer, K. E.; Michener, W. E.; Beckham, G. T. Ru–Sn/AC for the Aqueous-Phase Reduction of Succinic Acid to 1,4-Butanediol under Continuous Process Conditions. *ACS Catal.* **2017**, *7*, 6207–6219.

(18) Le, S. D.; Nishimura, S. Highly Selective Synthesis of 1,4-Butanediol via Hydrogenation of Succinic Acid with Supported Cu–Pd Alloy Nanoparticles. *ACS Sustain. Chem. Eng.* **2019**, *7*, 18483–18492.

(19) Nag, N. K. A Study on the Formation of Palladium Hydride in a Carbon-Supported Palladium Catalyst. *J. Phys. Chem. B* **2001**, *105*, 5945–5949.

(20) Zhou, C.-H. C.; Beltramini, J. N.; Fan, Y.-X.; Lu, G. M. Chemoselective Catalytic Conversion of Glycerol as a Biorenewable Source to Valuable Commodity Chemicals. *Chem. Soc. Rev.* **2008**, *37*, 527–549.

(21) Molenbroek, A. M.; Haukka, S.; Clausen, B. S. Alloying in Cu/Pd Nanoparticle Catalysts. *J. Phys. Chem. B* **1998**, *102*, 10680–10689.

(22) Jabłońska, M. TPR Study and Catalytic Performance of Noble Metals Modified Al_2O_3, TiO_2 and ZrO_2 for Low-Temperature NH_3-SCO. *Catal. Commun.* **2015**, *70*, 66–71.

(23) Prins, R. Hydrogen Spillover. Facts and Fiction. *Chem. Rev.* **2012**, *112*, 2714–2738.

(24) Zhang, S.; Guo, Y. Effects of Large CuO Contents on the Performance of Pd/Al_2O_3-CuO Catalysts in Ethanol Oxidation Reaction. *Chem. Phys. Lett.* **2019**, *722*, 26–31.

(25) Fulajtárova, K.; Soták, T.; Hronec, M.; Vávra, I.; Dobročka, E.; Omastová, M. Aqueous Phase Hydrogenation of Furfural to Furfuryl Alcohol over Pd–Cu Catalysts. *Appl. Catal. A Gen.* **2015**, *502*, 78–85.

(26) Mhadmhan, S.; Franco, A.; Pineda, A.; Reubroycharoen, P.; Luque, R. Continuous Flow Selective Hydrogenation of 5-Hydroxymethylfurfural to 2,5-Dimethylfuran Using Highly Active and Stable Cu–Pd/Reduced Graphene Oxide. *ACS Sustain. Chem. Eng.* **2019**, *7*, 14210–14216.

(27) Castegnaro, M. V.; Gorgeski, A.; Balke, B.; Alves, M. C. M.; Morais, J. Charge Transfer Effects on the Chemical Reactivity of Pd_xCu_{1-x} Nanoalloys. *Nanoscale* **2016**, *8*, 641–647.

(28) Dupont, L.; Guillon, E.; Bouanda, J.; Dumonceau, J.; Aplincourt, M. EXAFS and XANES Studies of Retention of Copper and Lead by a Lignocellulosic Biomaterial. *Environ. Sci. Technol.* **2002**, *36*, 5062–5066.

(29) Khemthong, P.; Photai, P.; Grisdanurak, N. Structural Properties of CuO/TiO_2 Nanorod in Relation to Their Catalytic Activity for Simultaneous Hydrogen Production under Solar Light. *Int. J. Hydrog. Energy* **2013**, *38*, 15992–16001.

(30) Sharma, A.; Varshney, M.; Park, J.; Ha, T.-K.; Chae, K.-H.; Shin, H.-J. XANES, EXAFS and Photocatalytic Investigations on Copper Oxide Nanoparticles and Nanocomposites. *RSC Adv.* **2015**, *5*, 21762–21771.

(31) Steinhauer, S.; Zhao, J.; Singh, V.; Pavloudis, T.; Kioseoglou, J.; Nordlund, K.; Djurabekova, F.; Grammatikopoulos, P.; Sowwan, M. Thermal Oxidation of Size-Selected Pd Nanoparticles Supported on CuO Nanowires: The Role of the CuO–Pd Interface. *Chem. Mater.* **2017**, *29*, 6153–6160.

Chapter 5

Hydroxyapatite Supported Polyvinylpyrrolidone-Capped CuPd Nanoparticles for Highly Selective Lactonization of Succinic Acid

Abstract

Selectivity hydrogenation of succinic acid (SA) is no mean task especially toward γ-butyrolactone (GBL) which is ready to undergo further hydrogenation. Herein, poly(N-vinyl-2-pyrrolidone) capped CuPd nanoparticles (NPs) on hydroxyapatite, have been investigated for the production of highly selective GBL. The optimal catalyst exhibited remarkable activity and stability which preserved its efficiency even at a mild hydrogen pressure of 1 MPa and long recycling runs. Inhibition effects of PVP were proposed to play a key role in maintaining high selectivity of GBL in various conditions. While characterization techniques indicated strong interaction between Cu and Pd due to alloying formation which is supposed to generate new active sites to enhance the substrate adsorption. However, the GBL production can only be maximized if the alloy phase were surrounded by Pd–Pd sites which might be contributed to the enhancement of hydrogen

dissociation.

5.1 Introduction

Heterogeneous metal nanoparticles (NPs) have been extensively investigated for hydrogenation of succinic acid (SA) [1, 2]. The choice of metal was determined as a essential factor for the catalytic activity and selectivity of the target products. Shao et al. reported that monometallic Pd/C showed a low conversion of SA and high γ-butyrolactone (GBL) selectivity [3]. Depending on the amount of added Re in the Pd–Re bimetallic catalysts, the GBL yield can be improved or tetrahydrofuran (THF) can be observed as the final product. Whereas, $Pd-5\,FeO_x$ was reported as an efficient catalyst for the production of 1,4-butanediol (BDO) [4]. The presence of FeO_x species enhanced the SA conversion and modulated the product distribution. The structures and properties of metal NPs can be influenced by not only additional metal species but also the catalyst support [5]. For example, Chapter 3 revealed that the nature of support and metal–support interaction played an essential role in the construction of CuPd NPs, inducing tunable activity and selectivity for the SA hydrogenation.

Since the efficient hydrogenation of SA to GBL is generally difficult to accomplish due to excessive hydrogenation or hydrolysis reactions, the present chapter focuses on designing an effective catalyst that can minimize the rate of non-target reactions. In fact, various research focused on Pd-based catalysts for highly selective GBL had been done [6–9]. For example, Zhang et al. reported that boehmite nanosheets supported Pd can promote SA hydrogenation to afford GBL with excellent selectivity [8]. Even with very low metal loadings from 0.1 to 1 wt% Pd, conversion of SA up to 97% can be achieved. A study from Yakabi et al. revealed that the SA hydrogenation can proceed at relatively mild conditions (140–170 ℃ and 1.5–3 MPa). Particularly, >90% selectivity of GBL and <70% conversion of SA can be attained over the Pd/Al_2O_3 catalyst [9].

As discussed in Chapter 2, the hydrogenation of SA over the Cu/HAP monometallic catalysts can be used to afford GBL with excellent selectivity. However, less than 20%

conversion of SA can be achieved which can be attributed to the low reactivity of Cu for hydrogen activation and dissociation [10]. The use of TiO_2 supported CuPd bimetallic catalyst, as discussed in Chapter 3, facilitated the reaction affording GBL of 90% selectivity at 73% conversion of SA. However, it is noted that the use of high loading amounts of metals might raise several issues regarding metal leaching which decreases the catalytic efficiency and product selectivity. The issues can be addressed by using a capping agent which is generally used in preparing and stabilizing well-defined metal NPs [11, 12]. In addition, selectivity toward a certain product can be tuned in the presence of a capping agent which is presumably due to the inhibition of substrate accessibility to specific sites [13].

Given the potential of CuPd NPs for the hydrogenation of SA to GBL, as discussed in the previous work [14, 15], the effect of a capping agent, i.e., poly(*N*-vinyl-2-pyrrolidone) (PVP) on the catalytic performance of HAP supported CuPd NPs has been investigated in the present study. The catalysts were prepared using extremely low metal loadings (0.1 mmol) with the aim of enhancing the atom efficiency which is an important factor in industrial applications. The most promising catalyst was found by optimizing the Cu:Pd molar ratio at 40:60 and stabilizing by a suitable average molecular weight (M_w) of 40000 g mol^{-1}. The catalyst offered excellent activity and GBL selectivity even at very low hydrogen pressure (1 MPa) while maintaining its productivity up to 5 continuous runs. Extensive investigation on catalytic performance and characterization has been conducted and the roles of PVP and metal species are properly discussed.

5.2 Experimental Section

5.2.1 Materials

All the chemicals used in the current chapter are tabulated in Table 5.1 below:

Table 5.1: List of chemicals used in Chapter 5

Chemical name	Formula	Mw /g mol^{-1}	Supplier
Butyric acid	$C_4H_8O_2$	88.11	Aldrich
Copper (II) acetate monohydrate	$Cu(CO_2CH_3)_2 \cdot H_2O$	199.65	Wako
γ-Butyrolactone	$C_4H_6O_2$	86.09	Aldrich
Palladium acetate	$Pd(CH_3COO)_2$	224.51	Wako
Polyvinyl alcohol (PVA)	$(C_2H_4O)_n$	3500	Wako
Polyvinylpyrrolidone (PVP, K12)	$(C_6H_9NO)_n$	3500	Acros Org.
PVP (K16–18)	$(C_6H_9NO)_n$	8000	Acros Org.
PVP (K30)	$(C_6H_9NO)_n$	40000	Kanto
PVP (K29–32)	$(C_6H_9NO)_n$	58000	Acros Org.
PVP (K90)	$(C_6H_9NO)_n$	360000	Acros Org.
Starch, soluble	$(C_6H_{10}O_5)_n$	-	Kanto
Succinic acid	$C_4H_6O_4$	118.09	Kanto
1,4-Butanediol	$C_4H_{10}O_2$	90.12	Wako
1,4-Dioxane	$C_4H_8O_2$	88.11	Wako
1-Ethyl-2-pyrrolidone	$C_6H_{11}NO$	113.16	Acros Org.
1-Vinyl-2-pyrrolidone	C_6H_9NO	111.14	Aldrich
2-Ethoxyethanol	$C_4H_{10}O_2$	90.12	Wako

5.2.2 Catalyst Preparation

Poly(N-vinyl-2-pyrrolidone) (PVP)-capped Cu_xPd_y supported on hydroxyapatite (HAP), denoted as Cu_xPd_y-PVP/HAP, were prepared by polyol reduction method using PVP as a capping agent and 2-ethyoxyethanol as a reducing agent [16, 17]. In a typical procedure, $Cu(OAc)_2 \cdot H_2O$ (x mmol) and $Pd(OAc)_2$ (y mmol) with $x + y = 0.1$ mmol are dispersed with PVP in 2-ethyoxyethanol (50 mL) and refluxed at 140 ℃ for 2 h. Subsequently, HAP (1.0 g) is added into the suspension which is further refluxed for another 1 h. The obtained solid is filtered and washed with deionized water (3 L) before being dried under a vacuum at room temperature.

5.2.3 Catalyst Characterization

The crystal structures of catalysts were studied by using Powder X-ray diffraction (XRD) which was operated on a Rigaku Smart Lab X-ray diffractometer (Rigaku Co.) with a Cu Kα radiation ($\lambda = 0.154$ nm) at 40 kV and 30 mA. The database of the Joint Committee of Powder Diffraction Standard was used as references for analyzing observed diffraction patterns. The morphologies of catalysts were acquired by transmission electron microscopy (TEM) using H-7100 and H-7650 microscopes (Hitachi) operated at 100 kV. X-ray photoelectron spectra (XPS) were performed on an Axis-Ultra DLD spectrometer (Shimadzu Co. and Kratos Analytical Ltd.) with a monochromatic Al Kα (1486 eV) X-ray resource. The binding energies (BE) were calibrated using the C 1s spectrum of adventitious carbon contamination as an internal standard. XPS spectra were processed and analyzed by using the XPSPEAK4.1 software.

X-ray absorption fine structure (XAFS) spectra were recorded at the BL07 (for Pd K-edge) and BL11 (for Cu K-edge) stations of the SAGA light source under the proposal nos. 1910092R and 2010105R. The storage ring was operated at 1.4 GeV where Si (220) and Si (111) single crystals were used to obtain monochromatic X-ray beams at Pd K-edge and Cu K-edge measurements, respectively. The catalysts and references were measured in fluorescence and transmission modes, respectively. Analyses of X-ray absorption near-edge spectra (XANES) and extended X-ray absorption fine structure (EXAFS) were processed on the Athena and Artemis software of the Demeter suite version 0.9.26.

5.2.4 Catalyst Evaluation

Reaction in batch system

A solution containing 1,4-dioxane (10 mL), SA (0.1 g), and the reduced catalyst (0.1 g) was mixed in an inner glass vessel and placed in a stainless-steel autoclave reactor (Taiatsu Technol., Japan). Before reaction the reactor was purged from the remaining air, followed by pressurizing to a certain pressure by pure H_2 (99.999%) at room temperature. The reactor was then placed into an aluminum block heated prior at 200 ℃ under vigorous stirring. After reaction the reaction mixture was centrifugated and the products were analyzed by gas chromatography (GC, Shimadzu GC-2014) with a polar column (DB-FFAP, Agilent). The GC column program was increased from initial temperature of 50 ℃ (keep for 2 min) to 240 ℃ (keep for 5 min) at a rate of 20 ℃ min^{-1}. Whereas the temperatures at the injection port and detector were 250 ℃ and 280 ℃, respectively. The

SA conversion was analyzed by high-performance liquid chromatography (HPLC, Water 2414) equipped with a refractive index detector. An aqueous solution of H_2SO_4 (10 mM) was used as an eluent, which was pumped at a flow rate of 0.5 mL min^{-1} through an Aminex HPX-87H column (Bio-Rad) operated at 50 ℃.

Reaction in continuous-flow system

Continuous reactions were carried out in a down-flow fixed-bed reactor system (MCR-1000, EYELA, Tokyo, Japan). The catalyst (0.5 g) was loaded into a stainless steel tube ($\phi = 5$mm) and secured in place by bed filters at both ends. The liquid and hydrogen flow rates were set at 0.3 and 10 mL min^{-1}, respectively. The reactor was pressurized with pure H_2 (99.999%) to 0.5 MPa and then the temperature of the furnace was increased to 200 ℃. The reaction mixture was collected at hourly intervals and analyzed by GC and HPLC as mentioned earlier.

5.3 Results and Discussion

5.3.1 Influence of Capping Agents on the Performances of HAP supported CuPd catalysts

In an attempt to search for a suitable capping agent, common polymers including PVP, PVA, and starch were used to prepare HAP supported CuPd catalysts. The prepared catalysts were employed for the hydrogenation of SA and the results are shown in Figure 5.1A. PVP, which is a weakly adsorbing stabilizer, was emerged as a potential capping agent since the resulting catalyst can accelerate the SA hydrogenation to GBL with excellent yield. Whereas the catalyst prepared without capping agent or with other stabilizing polymers exhibited extremely low activities, which probably can be contributed to the metal agglomeration during the catalyst preparation.

The effect of molecular weight (Mw) of PVP on the catalyst activity and stability of various metals including Cu and Pd NPs has been widely reported [18–21]. However,

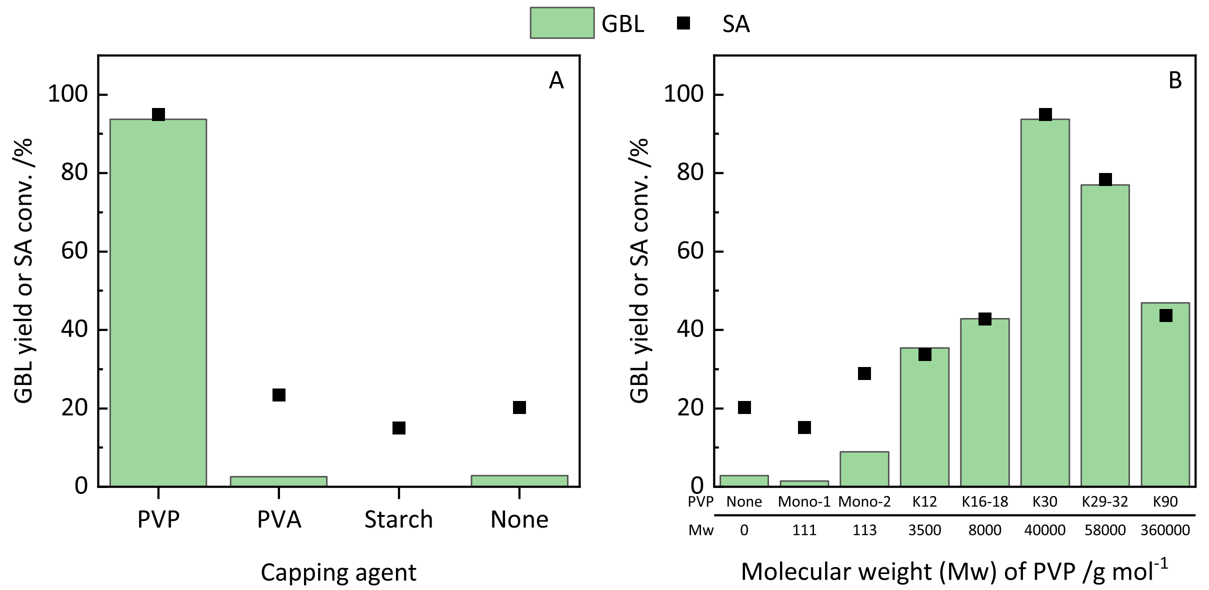

Figure 5.1: (A) Effect of capping agent and (B) molecular weight of PVP on the hydrogenation of SA over HAP supported CuPd catalysts. Reaction conditions: SA (0.1 g), $Cu_{40}Pd_{60}$−Polymer/HAP (0.1 g), 1,4-dioxane (10 mL), temperature (200 ℃), H_2 pressure (8 MPa), reaction time (48 h). Note: Mono-1 (1-vinyl-2-pyrrolidone), Mono-2 (1-ethyl-2-pyrrolidone).

the influence of the chain length of stabilizing polymer on the CuPd NPs remains elusive. Therefore, herein, the catalytic activity of CuPd NPs as a function of PVP Mw for the SA hydrogenation has been examined (Figure 5.1B). It is observed that the increase in PVP chain length resulted in better catalytic performance. Linear correlation between GBL yield and PVP can be fitted for Mw of less than 40000 g mol^{-1} (PVP K30) as shown in the inset. This enhancement in the catalytic activity might be attributed to the presence of CuPd NPs of well-defined morphologies. Further increasing the chain length of PVP, however, caused adverse effects on the activity since the GBL started to decrease and lost 50% in the case of PVP K90 (Mw = 360000), compared to that observed over the PVP K30. The negative impact of long-chain polymers on the CuPd NPs can be explained by the blockage of active sites from the accessibility of the substrate, which is typically encountered in polymer capped metal catalysts [22].

5.3.2 Effect of Metal Ratio on the Catalytic Activity

It is noted that the none capped CuPd NPs supported on HAP catalyzed SA hydrogenation toward butyric acid (BA) or BDO with high selectivities, as discussed in Chapter 2. However, with the use of a capping agent, the catalytic behavior fundamentally changed since only GBL was observed. As also revealed in the previous chapter that the Cu monometallic catalysts yielded GBL as a major product (Figure 2.1), the high selectivity of GBL over PVP capped CuPd NPs suggests a partial inhibition of Pd and/or Cu sites. Therefore, it is desirable to investigate the influence of metal ratio on the catalytic activity of the Cu_xPd_y−PVP(K30)/HAP. Figure 5.2A confirms the low activity of monometallic Cu as less than 5% yield of GBL can be observed. Upon addition of Pd, the formation of GBL increased and reached its peak at a yield of 94% over the $Cu_{40}Pd_{60}$−PVP/HAP. Further increasing Pd contents lead to the decreases in catalytic activity and selectivity since GBL yield dropped dramatically to 30% over the monometallic Pd catalyst. These results first indicate the importance of bimetallic catalysts for the enhancement in catalytic activity and GBL selectivity, compared to the monometallic ones. Second, the high selectivities of GBL point out the significance of PVP in controlling the catalytic selectivity by preventing both Cu and Pd sites from further reduction to BDO and hydrolysis to BA, respectively.

The reactions over catalysts with higher metal loading were performed as indicated in Figure 5.2B. It is observed that PVP can maintain its impact even at relatively high metal loading. Since the $Cu_{40}Pd_{60}$−PVP/HAP, which contains the greater fraction of Pd, was used, BA with small quantities can be observed at higher metal loadings ($\leq$ 0.5 mmol). However, a small fraction of BDO was only formed over the $Cu_{40}Pd_{60}$−PVP/HAP with a significantly high metal loading of 1 mmol. This result can be attributed to the low reactivity of Cu species in comparison with the precious metal Pd. A doubled amount of catalyst can yield BDO with greater selectivity, however, GBL is still maintained as the dominant product. It is also noted that when metal loading was greatly increased, Cu seemed to take over the role of Pd since no BA was detected. This might suggest changes

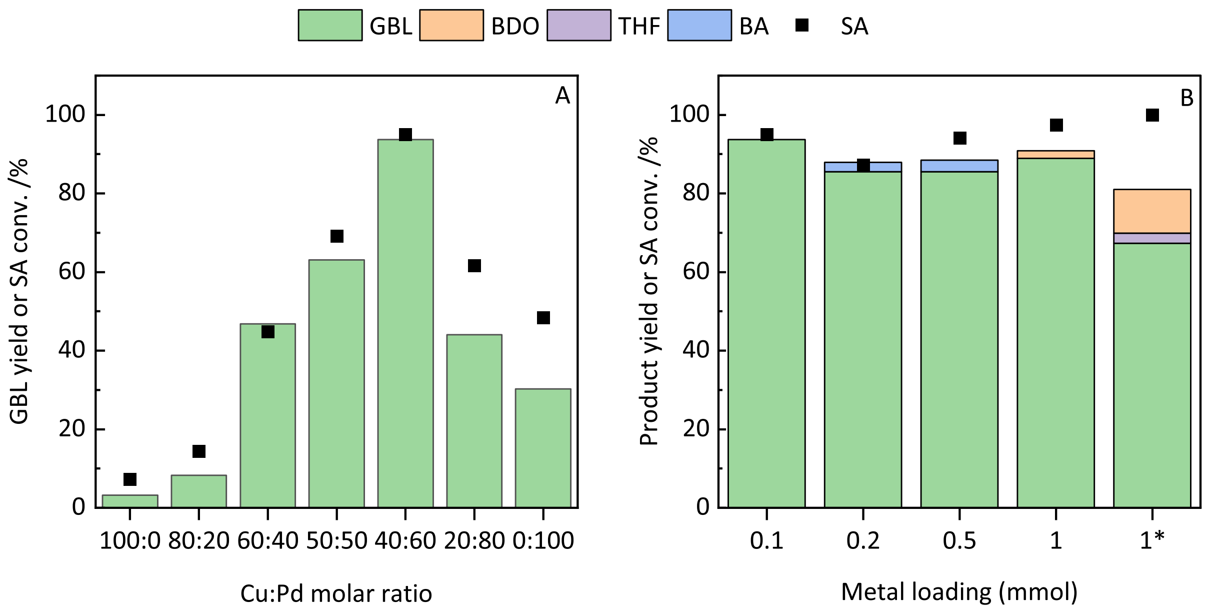

Figure 5.2: Influences of (A) metal ratio on the activities of Cu_xPd_y−PVP/HAP catalysts and (B) metal loading on the activities of the $Cu_{40}Pd_{60}$−PVP/HAP catalyst. Reaction conditions: SA (0.1 g), catalyst (0.1 g), 1,4-dioxane (10 mL), temperature (200 ℃), H_2 pressure (8 MPa), reaction time (48 h), *catalyst (0.2 g).

in the CuPd structures or morphologies.

5.3.3 Influences of Reaction Conditions or Other Factors

Time-based progression reaction

SA, in comparison to its analogous acid, for example, levulinic acid, is less reactive for the hydrogenation reaction [23]. It is therefore required longer reaction time and harder reaction conditions. The GBL progression over time is plotted in Figure 5.3. It can be observed that GBL formation increases steadily in the first 24 h. After that, the reaction rate of GBL production was slowed down as a result of the low concentration of SA. The GBL reached its maximum after 48 h when SA was almost consumed and reaction media contained mainly the product. It is worth referring that in the reaction over HAP supported CuPd without capping agent (Figure 2.1B), the consumption of GBL began right after its yield was about 60%. In the present catalyst, excellent selectivity of GBL can be maintained even at a high yield and longer reaction time. Even though after a 72 h reaction period, only a minor amount of BA can be observed, whereas GBL remains

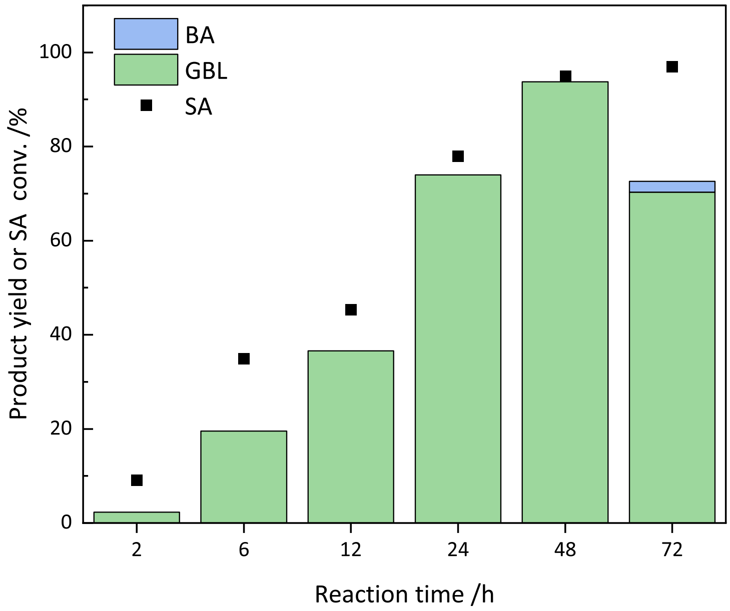

Figure 5.3: Time-based progression of SA hydrogenation over $Cu_{40}Pd_{60}$−PVP/HAP catalyst. Reaction conditions: SA (0.1 g), catalyst (0.1 g), 1,4-dioxane (10 mL), temperature (200 ℃), H_2 pressure (8 MPa).

as the primary product. This result again confirms the vital role of PVP in preventing GBL from over reduction and hydrolysis. Also, it suggests the formation of well-dispersed CuPd NPs with a minimized amount of Pd or Cu aggregation, which benefits from the use of PVP as a capping and stabilizing agent.

Influences of reaction conditions

The hydrogenation of SA is a complex reaction consisting of several pathways towards different products, which depends not only on the choice of the metal, support, and solvent but also the choice of reaction conditions such as temperature and H_2 pressure. Therefore, the effect of temperature on the overall reaction performance was investigated and the results are demonstrated in Figure 5.4A. A review from Delhomme et al. summarized that temperatures above 150 ℃ are generally required to obtain optimal performance of SA hydrogenation [1]. On the other hand, according to the results from previous chapters, for example, Figure 2.1C in Chapter 2, the GBL formation was favorable at a lower temperature than 200 ℃. Thus, reaction temperatures in a range of 150–200 ℃ were used to carry out the reaction over the present catalyst. The results, however, show

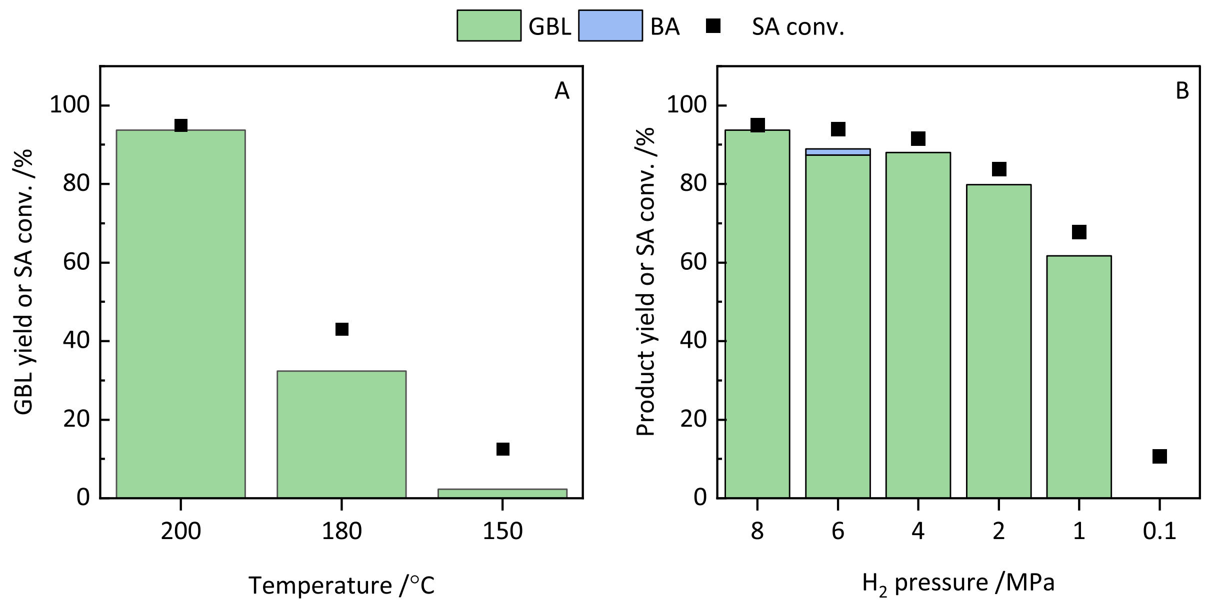

Figure 5.4: (A) effects of temperature and (B) H_2 pressure on the SA hydrogenation over the $Cu_{40}Pd_{60}$−PVP/HAP catalyst. Reaction conditions: SA (0.1 g), catalyst (0.1 g), 1,4-dioxane (10 mL), H_2 pressure (8 MPa) for (A) temperature (200 ℃) for (B), reaction time (48 h).

that at the lower reaction temperature, the GBL yield reduced significantly to just above 30% and less than 5% at 180 ℃ and 150 ℃, respectively. This might be ascribed to the small amount of metal loading and the negative impact of PVP on the active site, which requires greater activation energy, compared to that over the CuPd catalysts without capping agent.

The influence of H_2 pressure for the current reaction was examined and the results are shown in Figure 5.4B. In comparison with the productions of BDO and THF which typically require high pressures of H_2 due to the needs of 8 hydrogen atoms for 2-step hydrogenation from SA, the formation of GBL require only a half of the hydrogen consumption. As a result, lower H_2 pressure might be sufficient for the GBL production. So far, 3 MPa of hydrogen has been reported as a mildest pressure over alumina supported Pd NPs which catalyzed SA hydrogenation to afford GBL with greater than 90% selectivity and less than 70% SA conversion [9]. The present work has recorded even milder hydrogen pressure, i.e, 2 MPa, which efficiently converted SA to GBL with 95% selectivity at 84% SA conversion. The excellent selectivity can be maintained at a lower pressure of 1 MPa, however, the SA conversion slightly decreased to about 70%. An attempt to further reduce the H_2 pressure to as low as the atmospheric pressure has been made but was unsuccessful since no GBL can be detected. To explain the efficiency of catalytic performance at relatively low hydrogen pressure, two important factors, i.e, H_2 dissociation and diffusion, are needed to be taken into account. The presence of PVP first can help to enhance the metal dispersion which subsequently increases the hydrogen adsorption and diffusion in the metal surface. Second, as reported in both practical [24] and theoretical [25] methods, PVP can also serve as an electron donor which increases the electron density around the Pd atoms, facilitating the H_2 dissociation step.

Preliminary results on the application of flow reactor

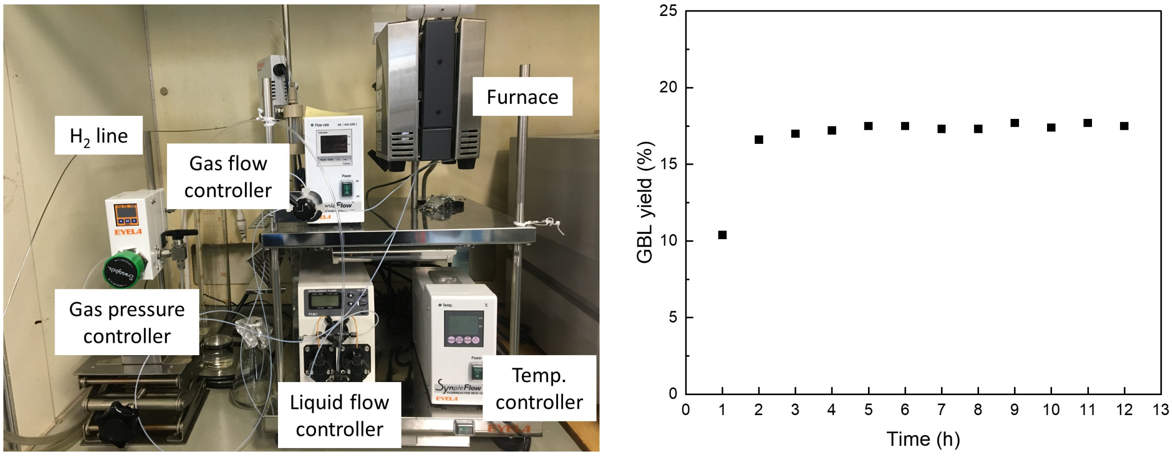

Figure 5.5: Experiment set up and preliminary results for SA hydrogenation in the continuous flow reactor. Reaction conditions: SA (0.05 M), catalyst bed (0.5 g), liquid flow rate (0.3 mL min^{-1}), H_2 flow rate (10 mL min^{-1}), H_2 pressure (0.5 MPa), temperature (200 ℃).

The reaction under low hydrogen pressure that is available in the batch reaction opens up a possibility to carry out the SA hydrogenation using a flow reaction system (Figure 5.5 (left)). Notably, under this flow system show that the GBL yield of about 18% can be maintained for 12 h at 0.5 MPa (Figure 5.5 (right)). According to the results obtained in the batch system, the GBL yield might be improved after appropriate optimization of reaction parameters shortly.

Influence of catalyst supports

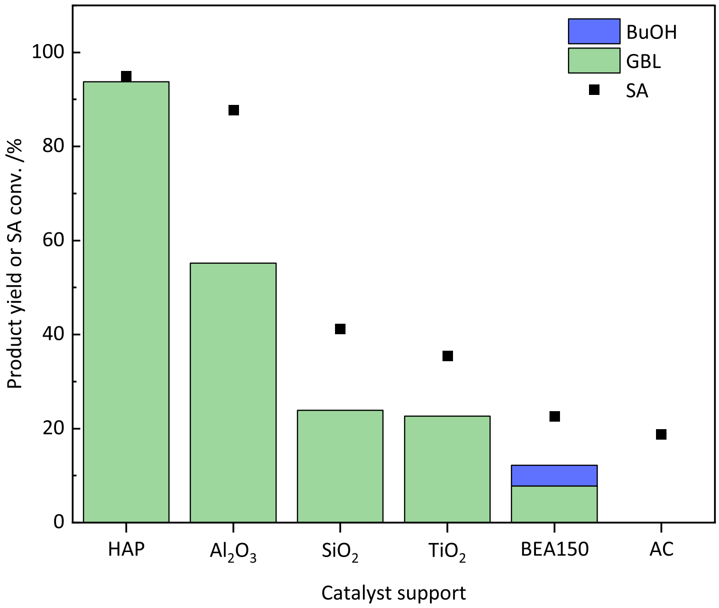

Figure 5.6: Effects of catalyst supports on the performances of PVP capped CuPd NPs

Various common supports have been used to investigate their impacts on the activity of the PVP-capped CuPd NPs (Figure 5.6). The results indicate that HAP is the most suitable support for achieving the superior performance of CuPd NPs. As discussed earlier in Chapter 2, HAP is one of the potential catalyst supports for SA hydrogenation due to its unique properties. For instance, the coexistence of weakly acidic and basic sites help to prevent mass transfer limitations and side reactions. In addition, the possession of high a specific area and superior exchangeability make it an ideal catalyst support where the metal can not only be immobilized on its surface but also incorporated into the apatite framework [26, 27].

5.3.4 Catalyst Characterization and Structure–Activity Relationship

Effect of metal ratio on the sizes of CuPd NPs

As indicated in Figure 5.7, the CuPd NPs show small sizes ranging from 1.9 to 3.7 nm. NPs with larger diameters of 3.8 nm and 4.7 nm can be observed in the monometallic

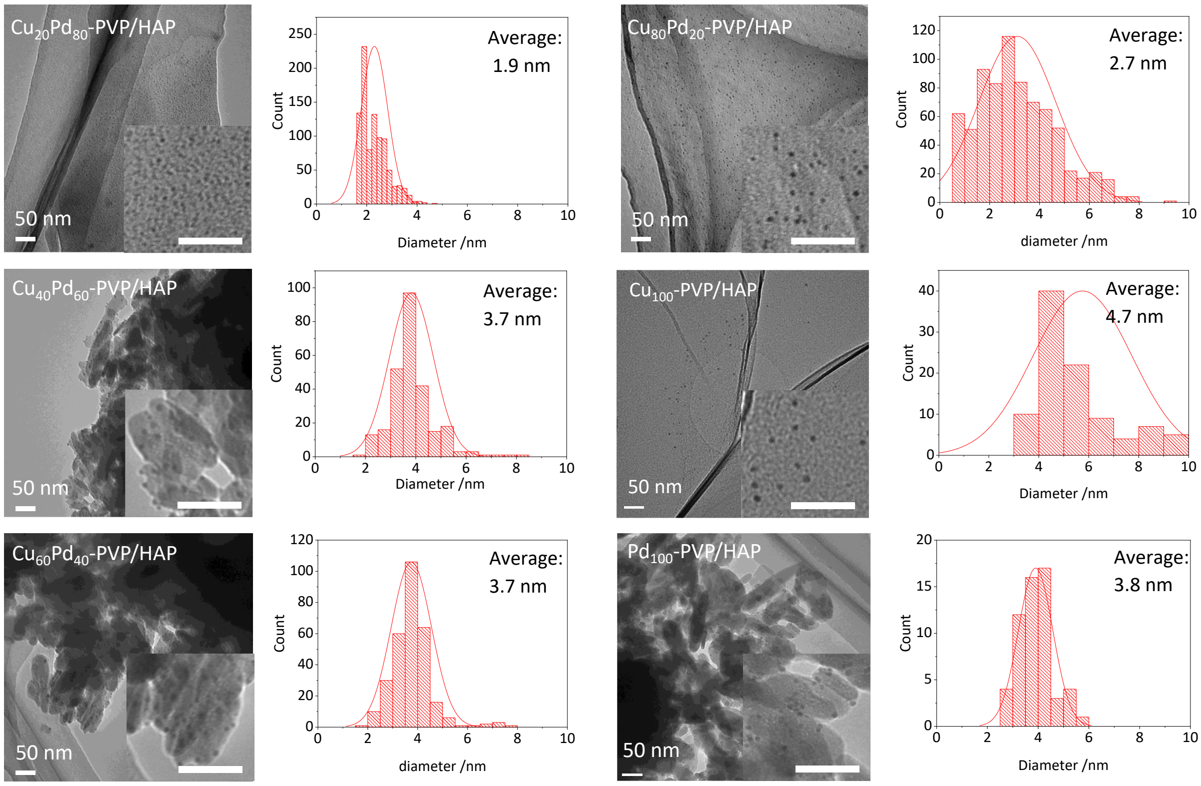

Figure 5.7: Effect of metal ratio on the sizes of CuPd NPs

catalysts Pd and Cu, respectively. The variation in sizes among these samples suggests that NP size depends mainly on the nature of metals and the ratio between them. To some extent, PVP can enhance the immobilization efficiency due to the binding affinity to the metal surface [28], which resulted in well-dispersed NPs in the prepared catalysts. However, the influence of PVP in the metal growing step might not significant due to steric effects of the PVP heads which prevent them from approaching and constraining small NPs. Nonetheless, PVP might be able to minimize the metal agglomeration when the particle grows to a certain size; for examples, restraining the sizes of Cu_{100} and $Cu_{80}Pd_{20}$ to be less than 5 nm on average. The results herein also suggest that the metal size is not a crucial factor for the catalytic performance because, for example, the $Cu_{60}Pd_{40}$ and $Cu_{20}Pd_{80}$ which show similar or even small NP sizes gave lower activities compared to that over the $Cu_{40}Pd_{60}$.

The XRD patterns of the catalysts and references were plotted in Figure 5.8. It is observed that the diffraction lines of all the samples resemble the pattern of HAP. No

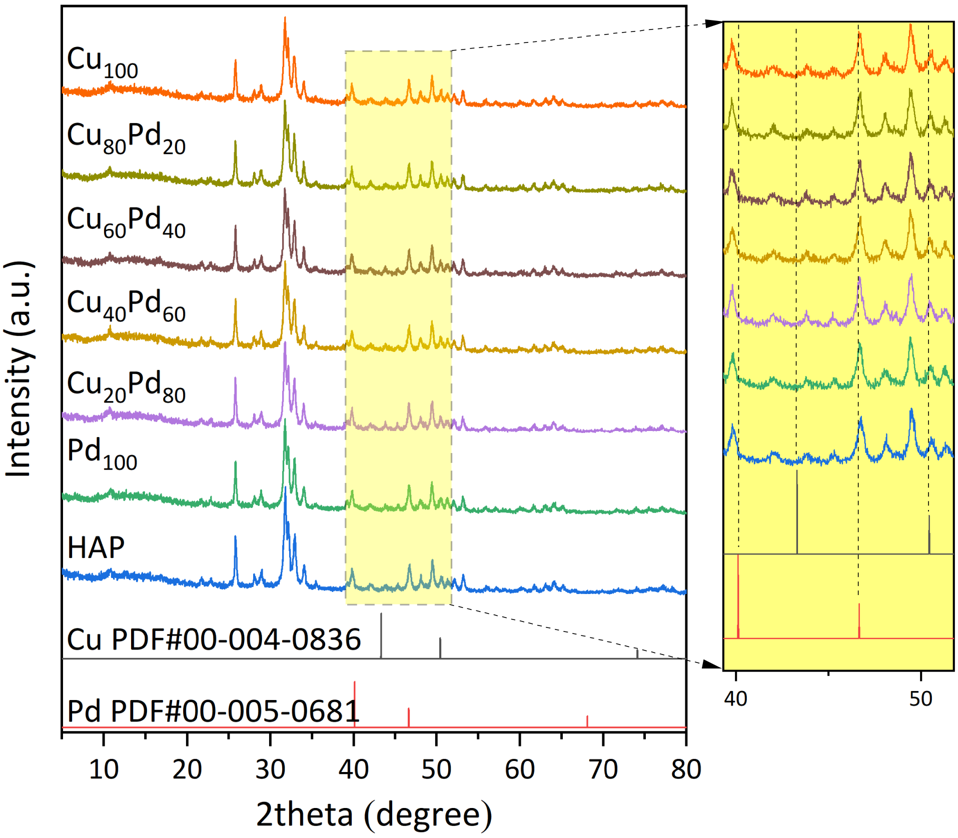

Figure 5.8: XRD patterns of the $\mathrm{Cu}_x\mathrm{Pd}_y$−PVP/HAP catalysts

diffraction peaks corresponding to the Cu or Pd metal references can be detected even in the cases of monometallic catalysts. These results can be contributed to the low loading amount of metal and the strong intensity of the support. Another possible reason is the uniform distribution of small NPs on the support as also suggested by the TEM results.

Electronic structures and metal interactions in $\mathbf{Cu}_x\mathbf{Pd}_y$−PVP/HAP catalysts

XPS was performed to determine the surface composition, electronic properties, and the interaction between Cu and Pd. Figure 5.9A demonstrates the spectra at Cu 2p region where Cu $2p_{3/2}$ and Cu $2p_{1/2}$ components can be observed at 933 eV and 953 eV, respectively, due to spin-orbit splitting. The deconvoluted peak at Cu $2p_{3/2}$ indicates the presence of Cu^0 ($\sim$933 eV) as a dominant phase. While in some cases, Cu^{2+} ($\sim$935 eV) can be involved in the fits due to partial oxidations during the XPS sampling. Similarly, XPS spectra at $3d$ region can be characterized by Pd $3d_{5/2}$ and Pd $3d_{3/2}$ components at about 335 eV and 340 eV, respectively (Figure 5.9B). The XPS peak at Pd $3d_{5/2}$ region can be fitted with Pd^0 and Pd^{2+} components at about 335 eV and 336–337 eV, respectively. Core level shifts of 0–0.4 to lower BE eV can be observed in the bimetallic catalysts with respect to the monometallic Cu catalyst. Whereas positive BE shifts of 0.3–0.4 eV were estimated at Pd $3d_{5/2}$ core level. These shifts suggest charge transfers from Pd to Cu resulting from strong interaction, i.e., alloying, between these two metals [29, 30].

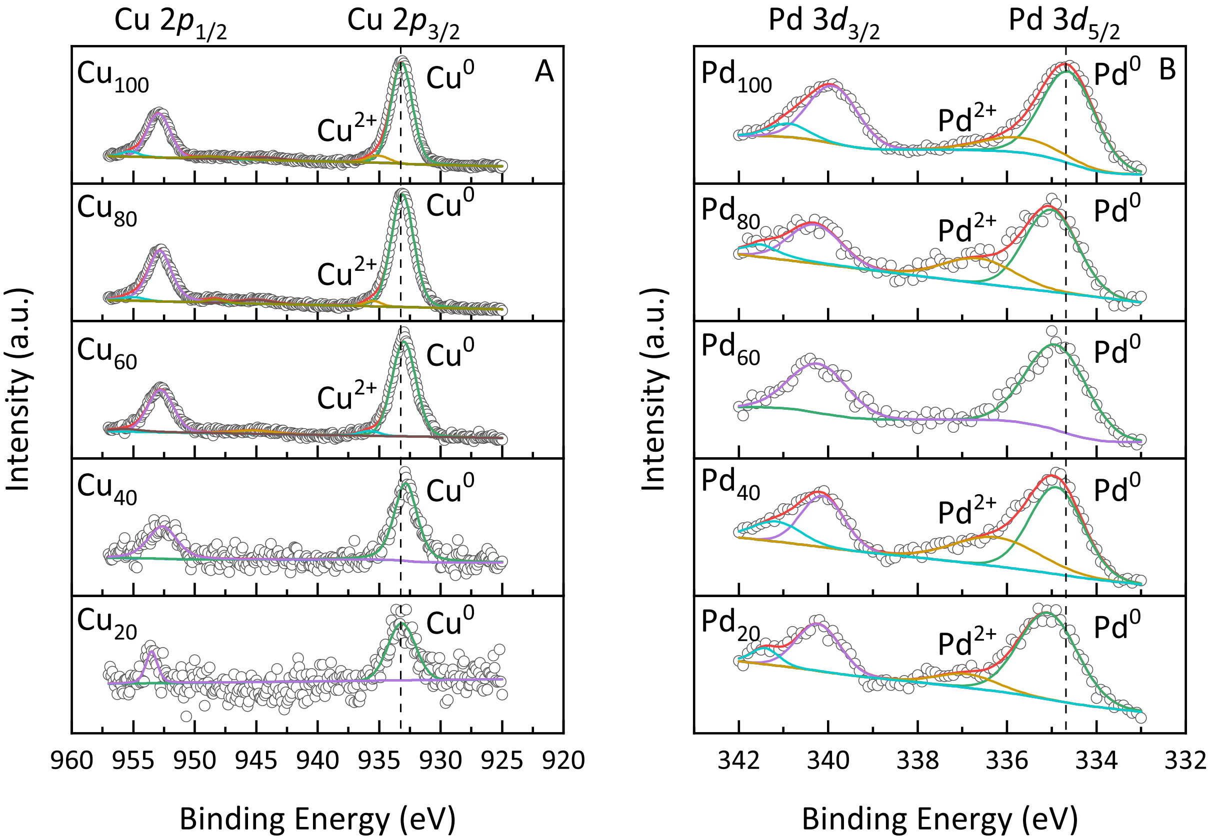

Figure 5.9: Deconvoluted XPS spectra of Cu_xPd_y–PVP/HAP catalysts at (A) Cu $2p$ and (B) Pd $3d$ regions

Figure 5.10A describes XANES spectra of Cu_xPd_y–PVP/HAP catalyst at Pd K-edge. In all samples, white lines are not observed indicating the prevalence of Pd in the metallic state. However, the first neighboring peaks in these catalysts are lower in intensity compared to that of the Pd foil, suggesting the existences of Pd^{2+} components. Linear combination fitting (LCF) was then performed to qualitatively determine the oxidation states of Pd (Figure 5.10B). The fraction of Pd^{2+} in the Pd_{80} is substantially larger than that of the others. These results seem to be unexpected when strong interaction with Cu

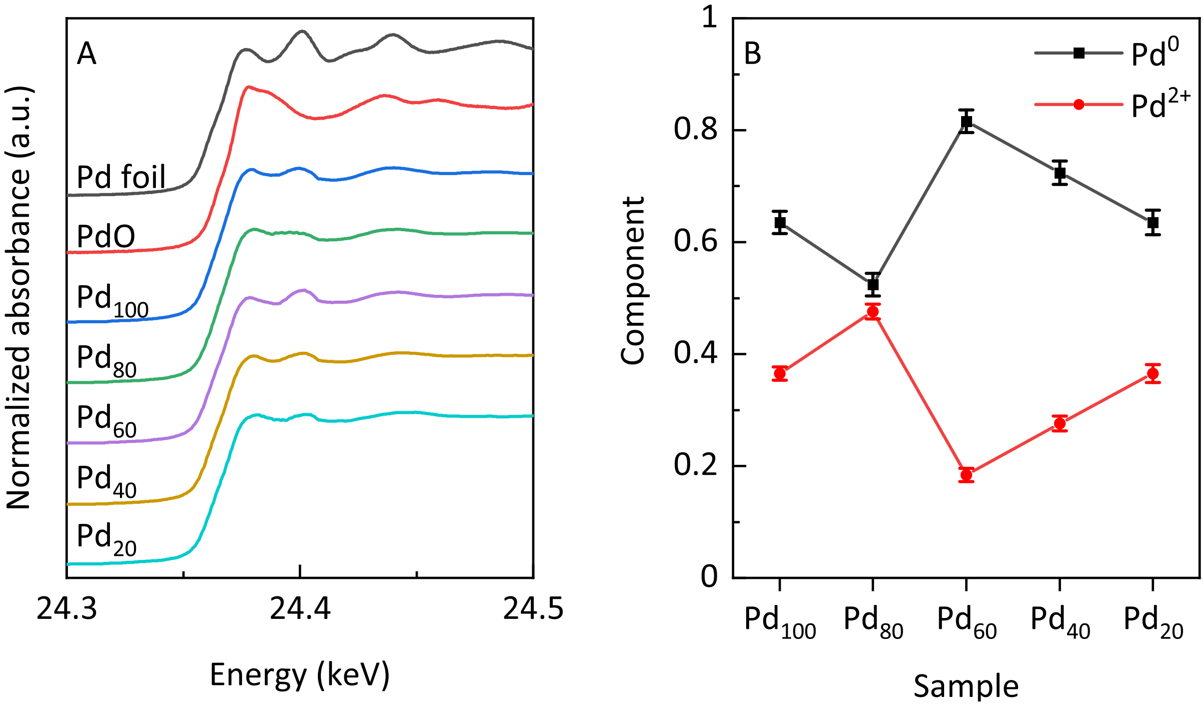

Figure 5.10: (A) XANES spectra and (B) LCF results for Cu_xPd_y–PVP/HAP at Pd K-edge

might lead to strong resistance to oxidation. However, it can be rationalized by referring to the NP size of this sample. As revealed by TEM (Figure 5.7), the constructed NPs in this sample is extremely small compared to others resulted in the enhancements of specific surface area and metal–oxygen coordination. Therefore, the lowest fraction of Pd^{2+} in Pd_{60} can be attributed to not only the stability of Pd–Cu bonding but also the larger NPs. Despite the fact that more Pd–Cu bonds can be formed upon addition of Cu, the dominance of Cu contents in the bimetallic catalysts can result in larger Pd^{2+} components due to the migration of oxygen from CuO–Pd interface to Pd [31]. As a result, the metallic contents of Pd decreased in the Pd_{40} and Pd_{20} catalysts.

Table 5.2: Fitting results at Pd K-edge for Cu_xPd_y–PVP/HAP

Sample	CN_{Pd-Pd}	CN_{Pd-Cu}	R_{Pd-Pd}	R_{Pd-Cu}
Pd foil	12	-	2.74	-
Pd_{100}-PVP/HAP	6.1 ± 0.9	-	2.74	-
$Cu_{20}Pd_{80}$-PVP/HAP	3.2 ± 0.4	-	2.72	-
$Cu_{40}Pd_{60}$-PVP/HAP	4.7 ± 0.6	1.4 ± 0.5	2.71	2.66
$Cu_{60}Pd_{40}$-PVP/HAP	3.0 ± 0.2	2.1 ± 0.2	2.68	2.59
$Cu_{80}Pd_{20}$-PVP/HAP	2.5 ± 0.7	2.2 ± 0.7	2.69	2.61

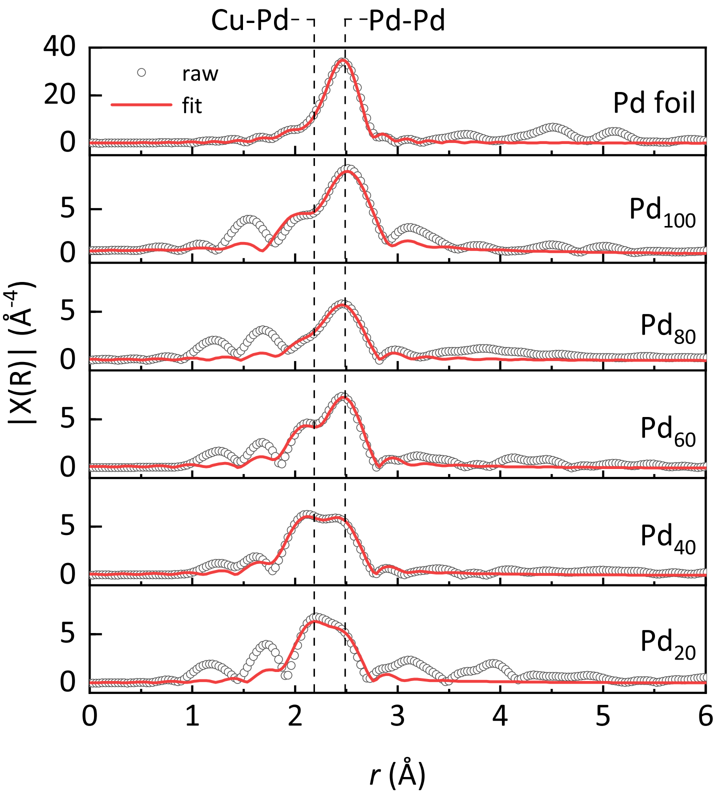

Figure 5.11: FT EXAFS spectra of Cu_xPd_y−PVP/HAP at Pd K-edge

The Fourier transform (FT) EXAFS spectra of raw and fitted data at Pd K-edge for the Cu_xPd_y−PVP/HAP catalysts are visually demonstrated in Figure 5.11. While the details on the coordination number (CN) and atomic distance (R) are listed in Table 5.2. The peaks corresponding to Pd–Pd appeared at about 2.5 Å, whereas adjacent peaks at about 2.2 Å representing Pd–Cu bonding can be observed in the bimetallic catalysts. Except for the $Cu_{20}Pd_{80}$-PVP/HAP which contains a small amount of Cu, Cu can be involved in the fits of other bimetallic catalysts. The fitting results indicate that CN of Pd–Cu increased with the addition of Cu content, which confirms the strong interaction between Cu and Pd as a result of alloying formation.

Given the superior catalytic performances of bimetallic catalysts compared to the monometallic ones (Figure 5.2A), CuPd alloying are proposed to be a prerequisite factor. In particular, the charger transfers from Pd to Cu might lead to positive Pd sites which enhanced the adsorption of SA. However, it seems that it is not sufficient to obtain an excellent yield of GBL because, for example, greater alloying degrees in Pd_{40} and Pd_{20}

cannot help them to improve the GBL yield. Therefore, there must be another factor that is responsible for this. It is worth noting that the Pd–Pd ensembles remained as a comparable phase to the Pd–Cu. The decreases of Pd–Pd from 4.7 to 2.5 are found to be aligned with the reduction of GBL in the bimetallic catalysts. According to Yang et al., the adsorption energy of hydrogen on the $Pd_1Cu_3(111)$ is lower than on the Pd(111) [32], which can be attributed to the unsuitable geometries due to larger Pd–Pd distance [33]. In other words, the efficiencies of hydrogen adsorption and dissociation might be lower on the CuPd alloying sites than the Pd sites, which is possibly responsible for the decreases in catalytic activity. Therefore, it is suitable to propose that in terms of the catalytic activity, Pd rich CuPd alloying NPs are necessary and sufficient conditions for the optimum efficiency of GBL production.

Catalyst stability

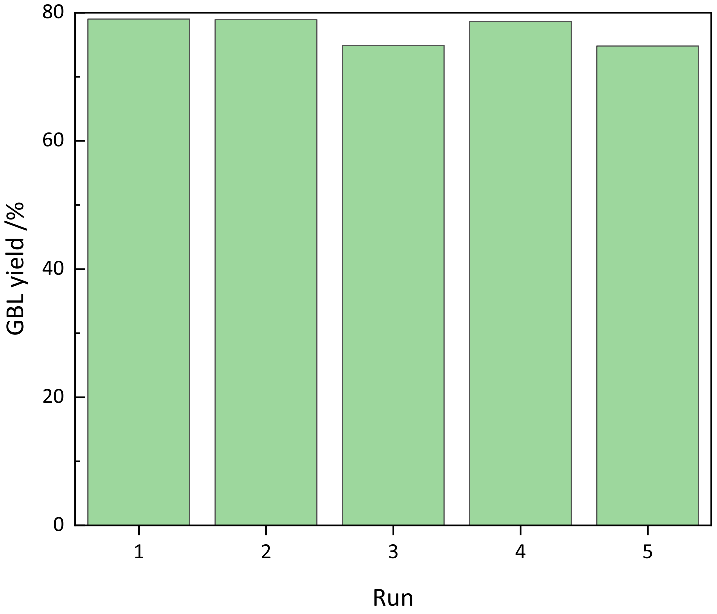

Figure 5.12: Reusability tests for the $Cu_{40}Pd_{60}$-PVP/HAP catalyst. Reaction condititons: SA (0.1 g), catalyst (0.1 g), 1,4-dioxane (10 mL), H_2 pressure (8 MPa), temperature (200 ℃), reaction time (24 h).

To evaluate the catalyst stability, the used catalyst was washed with 1,4-dioxane (4 × 5 mL) and dried in a vacuum before using for the subsequent run. Figure 5.12 shows excellent reusability of the $Cu_{40}Pd_{60}$-PVP/HAP for up to 5 consecutive runs. The AAS was performed to determine the metal contents of the catalyst after recycling runs. The used catalyst showed a slight decrease in the metal loading of approximately 0.01 mmol per gram catalyst compared to that of the fresh one. Since the Cu:Pd molar ratio was maintained the same after uses, the decrease in the total amount of metal loading might not come from the metal leaching to the reaction media but an agglomeration of PVP which lowered the metal loading per catalyst amount. To further clarify this point, the determination of metal contents in reaction media after recycling experiments is considered in future work.

5.4 Conclusion

In conclusion, highly efficient PVP-capped CuPd NPs constructed on HAP was discovered for selective hydrogenation of SA to GBL. The capping agent PVP played an important role in controlling the GBL selectivity by preventing further hydrogenation or other side reactions. While low activities could be observed in the monometallic catalysts, the reaction over the optimized $Cu_{40}Pd_{60}$-PVP/HAP catalyst exhibited remarkable enhancement in the production of GBL. XPS revealed a strong interaction between Cu and Pd leading to unique properties of the bimetallic catalysts. XAFS suggested the Pd–Pd phase that exists closely to Cu–Pd alloying phase as a prominent factor to afford remarkable activity in the optimized catalyst. The catalyst was able to perform at low hydrogen pressure from 1 MPa while maintaining high selectivity of GBL (>90%). Also, together with the remarkable reusability, the present catalyst is potentially available for hydrogenation of not only SA but also other oxygen-rich biomass resources from laboratory to industrial scale.

References

(1) Delhomme, C.; Weuster-Botz, D.; Kühn, F. E. Succinic Acid from Renewable Resources as a C_4 Building-Block Chemical–a Review of the Catalytic Possibilities in Aqueous Media. *Green Chem.* **2009**, *11*, 13–26.

(2) Mazière, A.; Prinsen, P.; García, A.; Luque, R.; Len, C. A Review of Progress in (Bio)Catalytic Routes from/to Renewable Succinic Acid. *Biofuels, Bioprod. Biorefining* **2017**, *11*, 908–931.

(3) Shao, Z.; Li, C.; Di, X.; Xiao, Z.; Liang, C. Aqueous-Phase Hydrogenation of Succinic Acid to γ-Butyrolactone and Tetrahydrofuran over Pd/C, Re/C, and Pd–Re/C Catalysts. *Ind. Eng. Chem. Res.* **2014**, *53*, 9638–9645.

(4) Liu, X.; Wang, X.; Xu, G.; Liu, Q.; Mu, X.; Liu, H. Tuning the Catalytic Selectivity in Biomass-Derived Succinic Acid Hydrogenation on FeO_x-Modified Pd Catalysts. *J. Mater. Chem. A* **2015**, *3*, 23560–23569.

(5) Liu, L.; Corma, A. Metal Catalysts for Heterogeneous Catalysis: From Single Atoms to Nanoclusters and Nanoparticles. *Chem. Rev.* **2018**, *118*, 4981–5079.

(6) You, C.; Zhang, C.; Chen, L.; Qi, Z. Highly Dispersed Palladium Nanoclusters Incorporated in Amino-Functionalized Silica Spheres for the Selective Hydrogenation of Succinic Acid to γ-Butyrolactone. *Appl. Organomet. Chem.* **2015**, *29*, 653–660.

(7) Hong, U. G.; Hwang, S.; Seo, J. G.; Lee, J.; Song, I. K. Hydrogenation of Succinic Acid to γ-Butyrolactone (GBL) over Palladium Catalyst Supported on Alumina Xerogel: Effect of Acid Density of the Catalyst. *Ind. Eng. Chem. Res.* **2011**, *17*, 316–320.

(8) Zhang, C.; Chen, L.; Cheng, H.; Zhu, X.; Qi, Z. Atomically Dispersed Pd Catalysts for the Selective Hydrogenation of Succinic Acid to γ-Butyrolactone. *Catal. Today* **2016**, *276*, 55–61.

(9) Yakabi, K.; Jones, A.; Buchard, A.; Roldan, A.; Hammond, C. Chemoselective Lactonization of Renewable Succinic Acid with Heterogeneous Nanoparticle Catalysts. *ACS Sustain. Chem. Eng.* **2018**, *6*, 16341–16351.

(10) Cao, K.; Füchsel, G.; Kleyn, A. W.; Juurlink, L. B. Hydrogen Adsorption and Desorption from Cu(111) and Cu(211). *Phys. Chem. Chem. Phys.* **2018**, *20*, 22477–22488.

(11) Tao, A. R.; Habas, S.; Yang, P. Shape Control of Colloidal Metal Nanocrystals. *Small* **2008**, *4*, 310–325.

(12) Heuer-Jungemann, A.; Feliu, N.; Bakaimi, I.; Hamaly, M.; Alkilany, A.; Chakraborty, I.; Masood, A.; Casula, M. F.; Kostopoulou, A.; Oh, E., et al. The Role of Ligands in the Chemical Synthesis and Applications of Inorganic Nanoparticles. *Chem. Rev.* **2019**, *119*, 4819–4880.

(13) Liu, P.; Qin, R.; Fu, G.; Zheng, N. Surface Coordination Chemistry of Metal Nanomaterials. *J. Am. Chem. Soc.* **2017**, *139*, 2122–2131.

(14) Le, S. D.; Nishimura, S. Highly Selective Synthesis of 1,4-Butanediol via Hydrogenation of Succinic Acid with Supported Cu–Pd Alloy Nanoparticles. *ACS Sustain. Chem. Eng.* **2019**, *7*, 18483–18492.

(15) Le, S. D.; Nishimura, S. Effect of Support on the Formation of CuPd Alloy Nanoparticles for the Hydrogenation of Succinic Acid. *Appl. Catal. B Environ.* **2020**, 119619.

(16) Guy, K. A.; Xu, H.; Yang, J. C.; Werth, C. J.; Shapley, J. R. Catalytic Nitrate and Nitrite Reduction with Pd–Cu/PVP Colloids in Water: Composition, Structure, and Reactivity Correlations. *J. Phys. Chem. C* **2009**, *113*, 8177–8185.

(17) Nishimura, S.; Yoshida, N.; Ebitani, K. Bimetallic PdCu nanoparticle catalyst supported on hydrotalcite for selective aerobic oxidation of benzyl alcohol. *MRS Proc.* **2015**, *1760*, mrsf14-1760-yy05–32.

(18) Tsuji, M.; Nishizawa, Y.; Matsumoto, K.; Kubokawa, M.; Miyamae, N.; Tsuji, T. Effects of Chain Length of Polyvinylpyrrolidone for the Synthesis of Silver Nanostructures by a Microwave-Polyol Method. *Mater. Lett.* **2006**, *60*, 834–838.

(19) Haesuwannakij, S.; Kimura, T.; Furutani, Y.; Okumura, K.; Kokubo, K.; Sakata, T.; Yasuda, H.; Yakiyama, Y.; Sakurai, H. The Impact of the Polymer Chain Length on the Catalytic Activity of Poly(N-vinyl-2-pyrrolidone)-supported Gold Nanoclusters. *Sci. Rep.* **2017**, *7*, 1–8.

(20) Upadhyay, L. S. B.; Kumar, N. Green Synthesis of Copper Nanoparticle using Glucose and Polyvinylpyrrolidone (PVP). *Inorg. Nano-Met. Chem.* **2017**, *47*, 1436–1440.

(21) Han, G.-H.; Lee, S.-H.; Seo, M.-g.; Lee, K.-Y. Effect of Polyvinylpyrrolidone (PVP) on Palladium Catalysts for Direct Synthesis of Hydrogen Peroxide from Hydrogen and Oxygen. *RSC Adv.* **2020**, *10*, 19952–19960.

(22) Rossi, L. M.; Fiorio, J. L.; Garcia, M. A.; Ferraz, C. P. The Role and Fate of Capping Ligands in Colloidally Prepared Metal Nanoparticle Catalysts. *Dalton Trans.* **2018**, *47*, 5889–5915.

(23) Sun, D.; Sato, S.; Ueda, W.; Primo, A.; Garcia, H.; Corma, A. Production of C_4 and C_5 Alcohols from Biomass-Derived Materials. *Green Chem.* **2016**, *18*, 2579–2597.

(24) Sun, G.; An, J.; Hu, H.; Li, C.; Zuo, S.; Xia, H. Green Catalytic Synthesis of 5-Methylfurfural by Selective Hydrogenolysis of 5-Hydroxymethylfurfural over Size-Controlled Pd Nanoparticle Catalysts. *Catal. Sci. Technol.* **2019**, *9*, 1238–1244.

(25) Gupta, A.; Boekfa, B.; Sakurai, H.; Ehara, M.; Priyakumar, U. D. Structure, Interaction, and Dynamics of Au/Pd Bimetallic Nanoalloys Dispersed in Aqueous Ethylpyrrolidone, a Monomeric Moiety of Polyvinylpyrrolidone. *J. Phys. Chem. C* **2016**, *120*, 17454–17464.

(26) Sun, H.; Su, F.-Z.; Ni, J.; Cao, Y.; He, H.-Y.; Fan, K.-N. Gold Supported on Hydroxyapatite as a Versatile Multifunctional Catalyst for the Direct Tandem Synthesis of Imines and Oximes. *Angew. Chem. Int. Ed.* **2009**, *48*, 4390–4393.

(27) Tounsi, H.; Djemal, S.; Petitto, C.; Delahay, G. Copper Loaded Hydroxyapatite Catalyst for Selective Catalytic Reduction of Nitric Oxide with Ammonia. *Appl. Catal. B Environ.* **2011**, *107*, 158–163.

(28) Munnik, P.; De Jongh, P. E.; De Jong, K. P. Recent Developments in the Synthesis of Supported Catalysts. *Chem. Rev.* **2015**, *115*, 6687–6718.

(29) Yin, Z.; Zhou, W.; Gao, Y.; Ma, D.; Kiely, C. J.; Bao, X. Supported Pd–Cu Bimetallic Nanoparticles That Have High Activity for the Electrochemical Oxidation of Methanol. *Chem. Eur. J.* **2012**, *18*, 4887–4893.

(30) Castegnaro, M. V.; Gorgeski, A.; Balke, B.; Alves, M. C. M.; Morais, J. Charge Transfer Effects on the Chemical Reactivity of Pd_xCu_{1-x} Nanoalloys. *Nanoscale* **2016**, *8*, 641–647.

(31) Steinhauer, S.; Zhao, J.; Singh, V.; Pavloudis, T.; Kioseoglou, J.; Nordlund, K.; Djurabekova, F.; Grammatikopoulos, P.; Sowwan, M. Thermal Oxidation of Size-Selected Pd Nanoparticles Supported on CuO Nanowires: The Role of the CuO–Pd Interface. *Chem. Mater.* **2017**, *29*, 6153–6160.

(32) Yang, Q.; Hou, R.; Sun, K. Tuning Butene Selectivities by Cu Modification on Pd-Based Catalyst for the Selective Hydrogenation of 1,3-Butadiene. *J. Catal.* **2019**, *374*, 12–23.

(33) Litovchenko, V.; Efremov, A. The Enhanced Catalytic Dissociation of Adsorbed Hydrogen Containing Molecules. *Condens. Matter Phys.* **1999**, *19*, 561.

Chapter 6

General Conclusion

In this doctoral dissertation, a comprehensive study on the CuPd bimetallic catalysts for selective hydrogenation of succinic acid has been presented. In the present chapter, a brief overview of the significant findings and a general conclusion are provided. Also, the limitations that existed in this research are pointed out which suggest various lines of research for pursuing in the future.

6.1 Summary

Chapter 2 studied the effect of the Cu:Pd ratio on the structure and activity of CuPd/HAP catalysts for selective hydrogenation of SA. The Cu_8Pd_2/HAP catalyst has successfully accelerated the hydrogenation of SA toward BDO with high selectivity (>80%) at a quantitative SA conversion. The Cu-rich CuPd alloy structure has been revealed by extensive characterization techniques. Synergistic effects between Cu and Pd inducing unique properties of the CuPd bimetallic catalysts in comparison with the monometallic ones have been examined. Accordingly, the strong interaction between Cu and Pd, on the one hand, resulted in the enhancement of catalytic activity to the intermediate GBL, compared to that over the Cu/HAP monometallic catalyst. While on the other hand, it suppressed the high reactivity of Pd, preventing the side reaction to butyric acid, which is typically encountered in the Pd/HAP monometallic catalyst. The Cu species that existed closely to CuPd alloying sites subsequently promoted further hydrogenation of GBL, affording BDO with high yield.

Chapter 3 investigated the influences of various supports i.e., SiO_2, TiO_2, and γ-Al_2O_3, on the construction of CuPd alloy nanoparticles (NPs). The study revealed that the metal–support interaction played a central role in controlling the structure of CuPd alloy NPs. In-depth characterizations indicated that randomly homogeneous CuPd NPs were prevalently constructed on TiO_2 and SiO_2, whereas the heterogeneous CuPd alloy NPs with a great extent of Cu segregation were dominantly formed on γ-Al_2O_3. Variations in the CuPd NPs construction led to dramatic changes in catalytic activity and selectivity among these catalysts. Particularly, GBL with high selectivity (90%) can be attained over the CuPd/TiO_2 catalyst at 73% conversion of SA, which was attributed to the presence of large CuPd NPs preventing further hydrogenation of GBL and lowering the catalytic activity. On the other hand, the higher activity and selectivity toward BDO of CuPd/SiO_2 were rationalized by the small CuPd NPs and the presence of Cu sites which promoted the formation of BDO at a high yield of 86%. Notably, the strong Lewis acid sites in the CuPd/γ-Al_2O_3 was revealed as the decisive factor in the formation of highly selective THF with 97% at a quantitative conversion of SA.

Chapter 4 demonstrated the effect of metal ratio on the activity of γ-Al_2O_3 supported CuPd NPs for SA hydrogenation. Excellent selectivity toward THF was achieved over the Cu-rich CuPd/γ-Al_2O_3, i.e., the Cu_8Pd_2/γ-Al_2O_3 and Cu_6Pd_4/γ-Al_2O_3. In addition, the present catalyst can maintain its high activity and selectivity for several recycling runs under high temperature and pressure conditions. Characterization methods revealed that major factors that are responsible for the superior performance of this catalyst for THF production include CuPd alloy NPs with Cu-rich sites and strong Lewis acid sites of the support. The strong interaction in CuPd alloy NPs led to the enhanced reactivity compared to that of the monometallic Cu, while the Cu-rich component helped to restrain the strong reactivity of Pd species which favor the formation of BA. Alternatively, the Cu-rich CuPd NPs enhanced the formation of the intermediate BDO which was easily converted to THF *via* cyclodehydration under the influence of strong Lewis acid sites in

γ-Al_2O_3.

Chapter 5 examined the influence of the capping agent on the catalytic performance of CuPd NPs. A highly efficient PVP-capped CuPd NPs constructed on HAP was discovered for selective hydrogenation of SA to GBL. The inhibition effect of the capping agent PVP was revealed to play a key role in the formation of GBL with excellent selectivity. The catalyst was able to proceed at extremely low hydrogen pressure from 1 MPa while maintaining high selectivity of GBL (>90%). Besides, the catalyst showed remarkable reusability, offering the catalyst with enormous potential for applying to the hydrogenation of not only SA but also other oxygen-rich biomass resources from laboratory to industrial scale.

6.2 Key Findings and Conclusion

6.2.1 Key Findings

CuPd NPs-Tunable catalyst for selective hydrogenation of SA

The importance of SA hydrogenation which generates the key intermediates including GBL, BDO, and THF for the polymer industry is unquestionable. Also, recent breakthroughs in biotechnology made bio-SA more abundant and competitive supply for further transformations. Despite its great potential, the development in the catalytic hydrogenation of SA in the last decade is admittedly modest. In addition, the heavy dependence on rare-earth metals in previous studies probably restrains them from practical applications. The discovery of CuPd bimetallic catalysts in the present research, therefore, provides not only cheaper catalysts but also effective and feasible methods to tune the product selectivity for the SA hydrogenation (Table 6.1). Furthermore, in terms of productivity, the present catalyst system showed excellent performances, which closely approach or even greatly superior to the highest records for BDO or THF and GBL productions so far. On the other hand, in the context of reaction conditions, the PVP-capped $Cu_{40}Pd_{60}$ catalyst promoted the SA hydrogenation to highly selective GBL even at low hydrogen

Table 6.1: The development of bimetallic catalysts for SA hydrogenation in the last decade including the present studies

Catalyst	Temp. /°C	P H_2 /MPa	Conv. /%	Selectivity /%			Ref.
				BDO	GBL	THF	
Cu_8Pd_2/HAP or SiO_2	200	8	100	82–86	<5	≤3	This thesis
$Cu_8Pd_2/\gamma\text{-}Al_2O_3$	200	8	100	0	0	97	This thesis
Cu_8Pd_2/TiO_2	200	8	73	2	90	3	This thesis
$Cu_{40}Pd_{60}$−PVP/HAP	200	1–4	68–92	0	92–96	0	This thesis
Ir−Re/C	240	8	100	<5	0	75	[123]
Pd−Cu/AX	190	7	72	0	94	0	[124]
Pd/Al_2O_3	170	3	<70	<1	95	0	[118]
Re−Ru/C	160	8	99	70	6	6	[125]
Re3−Ru/C	240	8	99	3	5	60	[125]
Pd−Re/AC	180	10	100	67	0	14	[126]
Re−Ru/BMC	200	8	100	65	34	3	[127]
Re−Pd/SiO_2	140	8	100	89	3	0	[128]
Pd−5 FeO_x/C	200	5	100	70	-	-	[114]
Re−Ru/MC	200	8	100	71	18	11	[129]
Pd−Re/C	240	8	89	4	-	73	[130]
Pd−Re/TiO_2	160	15	100	83	0	-	[131]
Pd−Re/C	160	15	100	66	0	-	[132]

Further information regarding the previous reports can be found in Tables 1.1 and 1.2 and the discussions therein. The reference numbers displayed in this Table 6.1 are consistent with those of Chapter 1.

pressure, from 1 MPa. In addition, the extremely low concentration of metal loading (0.1 mmol) in combination with the excellent reusability made this catalyst suitable for flow reactor and thus open up a possibility for industrial application.

Revealing mechanism of SA hydrogenation over CuPd catalysts

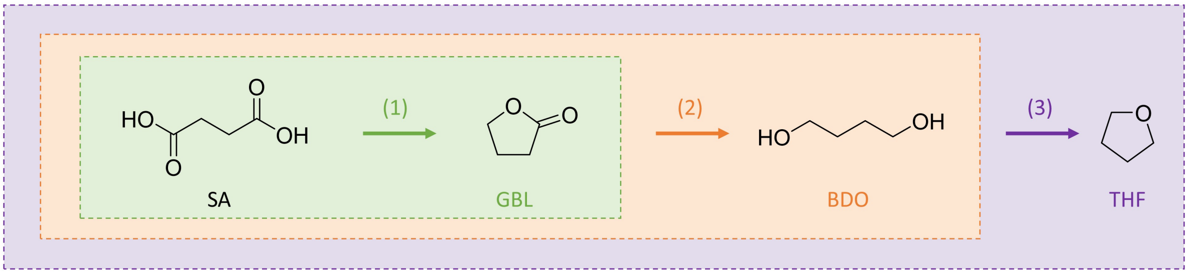

Scheme 6.1: Simple reaction scheme for SA hydrogenation

A simple reaction scheme illustrated the SA hydrogenation to GBL (1), BDO (2), and THF (3) is shown in Scheme 6.1. It should be noted that the present dissertation focuses on direct hydrogenation of SA, the use of the intermediate GBL or BDO as starting material in some cases is just for clarifying the roles of metal components in the investigated catalysts.

(1) SA → GBL: First, according to the catalytic performances of monometallic Cu and Pd observed in Figures 2.1A, 4.1, and 5.2A, it is clear that both Cu and Pd can reduce SA to GBL. However, Cu catalysts showed poor catalytic performance for SA hydrogenation which can be attributed to the limited capability of Cu for H_2 activation. On the other hand, as a precious metal, Pd holds great potential for H_2 dissociation, which turned out not to be suitable for SA hydrogenation since it directed the reaction via hydrogenolysis pathway to the side products BA and BuOH. The strong Cu–Pd interaction due to alloy formation, which enhanced the reducibility of Cu (Figures 2.2 and 3.10), therefore, resulted in better GBL yield in the case of Cu_8Pd_2/TiO_2 and $Cu_{40}Pd_{60}$−PVP/HAP (Table 6.1). The reactions were terminated at GBL without further hydrogenation because (i) the absence of isolated Cu and/or large CuPd NPs of the former catalyst (Chapter 3) and (ii) the inhibition effect of PVP in the latter (Chapter 5).

(2) SA → BDO: The reaction using GBL as a starting material showed that Cu can reduce GBL to afford BDO with excellent yield and selectivity (Table 2.3). This is because the transformation from GBL requires only 4 hydrogen atoms compared to the total 8 atoms that are required for direct transformation of SA to BDO (Scheme 1.4). Therefore, the presence of isolated Cu in Cu_8Pd_2/HAP and Cu_8Pd_2/SiO_2 can further reduce the intermediate GBL to BDO with high yield and selectivity (Table 6.1). It should be emphasized that the close interaction between Cu and Pd is important because the physical mixture of Cu_8/HAP and Pd_2/HAP was unable to produce BDO with the comparable yield to that over the bimetallic catalyst (Figure 2.1A).

(3) SA → THF: The reaction using BDO as starting material revealed that strong Lewis acid site in γ-Al_2O_3 is one of the crucial factors for the production of THF (Table

3.6). However, the CuPd alloy is the prerequisite factor for direct hydrogenation of SA to THF since reaction over the bare support was failed to produce any THF (Table 3.2). The hydrogenation of GBL over $Cu_8Pd_2/\gamma\text{-}Al_2O_3$ indicated that in the preliminary step of this reaction, BDO was formed as an intermediate, which immediately converted to THF under the influence of the strong Lewis acid site (Table 4.2). Therefore, the highly selective hydrogenation of SA toward THF is the combination and working in concert of (i) the Cu-rich CuPd NPs and (ii) strong Lewis acid sites of $\gamma\text{-}Al_2O_3$.

6.2.2 Conclusion

In conclusion, the present thesis provides feasible and versatile methods to design effective CuPd bimetallic catalysts for selective hydrogenation of SA. Depending on the certain purpose, the SA hydrogenation could be directed toward a specific product including GBL, BDO, and THF by adjusting the Cu:Pd ratio, changing the catalyst support, and stabilizing with a capping agent. The roles of individual metals, CuPd alloy, supports, and the capping agent have been revealed. In addition, the reaction pathways and optimized reaction conditions for each integrated reaction have been clarified and examined. The mentioned understanding of the current catalyst system allows us to control the SA hydrogenation and other related reactions from various angles.

6.3 Limitations

Despite the benefits and strength stated earlier, there are various issues and limitation existed in the present thesis:

- *Leaching issues*: As demonstrated in Chapters 2 and 4, although the catalysts can be recycled for several runs, Cu leaching is one of the issues causing the gradual descent in the BDO selectivity. The PVP capped CuPd NPs can enhance the catalyst stability, however, it limited the hydrogenation within the formation of GBL.

- *Lack of kinetic studies*: Despite the fact that the reaction parameters could be optimized for enhancing the reaction performance, the studies in this thesis did not pursue to provide kinetic models due to several technical issues regarding the high-pressure reactor and difficulties inherently existed in complex reaction like SA hydrogenation.

6.4 Recommendations

6.4.1 Recommendations Relating to the Present Study

Based on the mentioned limitations, further understanding of the present catalyst system can be achieved by pursuing the following subjects.

(1) **Building a catalyst model for the CuPd–PVP/HAP by either practical or computational method.** This research may clarify where and what types of active sites that the reactant was preferably adsorbed on. Furthermore, it may answer how the steric effect of PVP prevent further hydrogenation of GBL or whether the competitive adsorptions between H_2 and SA/GBL occur.

(2) **Preparing the CuPd bimetallic catalysts with capping agent by a different approach to enhance both the catalyst activity and stability.** For example, using the post-synthesis ligand exchange process to apply for the catalyst prepared by impregnation-reduction method or combining the ligand and CuPd externally.

(3) **Carrying out the kinetic studies to build a reaction model for the hydrogenation of SA over the CuPd-PVP/HAP catalyst under a flow reactor.** This kind of research may provide preliminary data to build up and optimize the reaction conditions at a larger scale.

6.4.2 Recommendations Relating for Further Studies

Since the great potential of Cu-based bimetallic catalysts for SA hydrogenation has been recognized and proved in the current study, the first question should be to what extent the present catalyst system is applicable for other dicarboxylic acids.

Second, although excellent yield and selectivity of target products were achieved, it is admitted that the current catalyst system requires hard reaction conditions and a long reaction time. What would happen if instead of H_2, the transfer hydrogen (non-H_2 hydrogen source) is used for SA hydrogenation?

Third, it was pointed out earlier that Cu holds the great potential for the BDO production from GBL but the low reactivity for hydrogen dissociation, possibly due to the electron deficiency of supported Cu catalysts, limited it from the direct SA hydrogenation. However, as discussed in Chapter 1 that the H_2 dissociation can be enhanced by using electronegative heteroatom from the support or additive to activate the cleavage of H_2 via heterolytic pathway (e.g., Formenti D. et al., *Catal. Sci. Technol.*, **2016**, *6*, 4473 and *J. Catal.*, **2017**, *351*, 79). Is it possible that Cu with the aid of a suitable support/additive catalyzes the SA hydrogenation?

By pointing out these possibilities, the following lines of research may be beneficially pursued.

(1) **Hydrogenation of similar dicarboxylic acids to lactones and diols using supported CuPd bimetallic catalysts**

(2) **Hydrogenation of succinic acid using transfer hydrogen approach.**

(3) **Supported Cu-based heterogeneous for hydrogenation of succinic acid**

(4) **Cu single atoms-catalyzed hydrogenation of succincic acid**

Publications and Awards

Academic Journals

[1] Son Dinh Le, Shun Nishimura, Hydroxyapatite Supported Polyvinylpyrrolidone-Capped CuPd Nanoparticles for Highly Selective Lactonization of Succinic Acid. (In preparation)

[2] Son Dinh Le, Shun Nishimura, Influence of metal ratio on alumina-supported CuPd catalysts for the production of tetrahydrofuran from succinic acid, Appl. Catal. A: Gen., 616 (2021), 118063.

[3] Son Dinh Le, Shun Nishimura, Effect of support on the formation of CuPd alloy nanoparticles for the hydrogenation of succinic acid, Appl. Catal. B: Environ., 282 (2021), 119619.

[4] Son Dinh Le, Shun Nishimura, Highly selective synthesis of 1,4-butanediol via hydrogenation of succinic acid with supported Cu–Pd alloy nanoparticles, ACS Sustain. Chem. Eng., 7 (2019), 18483–18492.

Patent Application

[5] Shun Nishimura, Son Dinh Le, Catalysts for 1,4-butanediol, butyric acid and tetrahydrofuran productions, Japanese Patent Application Nos. 2020-115838 (filed Jul 3, 2020) and 2019-148506 (filed Aug 13, 2019).

Conferences Presentation

[6] Son Dinh Le, Shun Nishimura, Supported CuPd bimetallic nanoalloys as highly efficient and tunable catalysts for succinic acid hydrogenation, 5th International Conference on Catalysis and Chemical Engineering, Feb 22–26, 2021, California, USA (virtually oral presentation, accepted).

[7] Son Dinh Le, Shun Nishimura, Hydroxyapatite supported polyvinylpyrrolidone-capped CuPd bimetallic catalysts for highly selective γ-butyrolactone via hydrogenation of succinic acid, 50th Petroleum-Petrochemical Symposium of Japan Petroleum Institute, Nov 12–13, 2020, Kumamoto, Japan (virtually oral presentation, 1E08).

[8] Son Dinh Le, Shun Nishimura, Tunable catalytic activity of supported Cu–Pd nanoparticles for hydrogenation of bio-derived succinic acid, 126th Catalyst Society of Japan Annual Meeting, Sep 16–18, 2020, Shizuoka, Japan (virtually oral presentation, 1J11 A2).

[9] Son Dinh Le, Shun Nishimura, Polyvinylpyrrolidone-capped CuPd catalyst for highly selective lactonization of succinic acid, 11th International Conference on Environmental Catalysis, Sep 6–9, 2020, Manchester, UK (virtually oral presentation, 2B-135).

[10] Son Dinh Le, Shun Nishimura, Synergistic effect between Cu and Pd in Cu–Pd nanoparticles for direct synthesis of 1,4-butanediol via hydrogenation of succinic acid, 17th International Congress on Catalysis, Jun 14–19, 2020 California, USA (published abstract #22851).

[11] Son Dinh Le, Shun Nishimura, Hydrogenation of bio-derived succinic acid to 1,4-butanediol using supported bimetallic catalysts, 14th European Congress on Catalysis, Aug 18–23, 2019, Aachen, Germany (poster presentation, B4-176).

Honors & Awards

[12] JAIST Grant (Houga) for A Potential Research Project · June 2019

[13] JAIST Grants for Attending International Conferences · 2018 – 2021 (4 times)

[14] JAIST Doctoral Research Fellowship Scholarship · April 2018 – March 2021

Achievements not included in this thesis

Academic Journals

[15] Shun Nishimura, Junya Ohyama, Takaaki Kinoshita, Son Dinh Le, Keisuke Takahashi, Revisiting machine learning predictions for oxidative coupling of methane (OCM) based on literature data, ChemCatChem, 12 (2020), 5888–5892. (Selected as Cover Feature)

[16] Abdallah I.M. Rabee, Son Dinh Le, Koichi Higashimine, Shun Nishimura, Aerobic oxidation of 5-hydroxymethylfurfural into 2,5-furandicarboxylic acid over gold stabilized on zirconia-based supports, ACS Sustain. Chem. Eng., 8 (2020), 7150–7161.

[17] Abdallah I.M. Rabee, Son Dinh Le, Shun Nishimura, MgO-ZrO_2 mixed oxides as effective and reusable base catalysts for glucose isomerization into fructose in aqueous media, Chem. Asian J., 15 (2020), 294–300.

[18] Son Dinh Le, Shun Nishimura, Kohki Ebitani, Direct esterification of succinic acid with phenol using zeolite beta catalyst, Catal. Commun., 122 (2019), 20–23.

Conferences

[19] Xueting Chu, Son Dinh Le, Shun Nishimura, Oxidative Conversion of Methane over Montmorillonite Catalysts, 101st CSJ Annual Meeting, Mar 19–22, 2021, Japan (virtually oral presentation, accepted).

[20] Sho Inuduka, Son Dinh Le, Shun Nishimura, Hydroxymethylation of furoic acid with zeolite catalysts, 101st CSJ Annual Meeting, Mar 19–22, 2021, Japan (virtually oral presentation, accepted.

[21] Shun Nishimura, Yusaku Asai, Natsuki Takahashi, Son Dinh Le, Shintaro Ohmatsu, Effect of calcination temperature on Boehmite for cyclization of 2,5-hexanedione, 50th Petroleum-Petrochemical Symposium of Japan Petroleum Institute, Nov 12–13, 2020, Kumamoto, Japan (virtually poster presentation, P22).

[22] Xueting Chu, Son Dinh Le, Shun Nishimura, Methane oxidation by metal cation exchanged montmorillonite, 50th Petroleum-Petrochemical Symposium of Japan Petroleum Institute, Nov 12–13, 2020, Kumamoto, Japan (virtually poster presentation, P15).

[23] Sho Inuduka, Son Dinh Le, Shun Nishimura, Hydroxymethylation of furoic acid by solid scid catalyst, 50th Petroleum-Petrochemical Symposium of Japan Petroleum Institute, Nov 12–13, 2020, Kumamoto, Japan (virtually poster presentation, P21).

[24] Xinyue Li, Son Dinh Le, Shun Nishimura, Reductive amination of HMF over beta zeolite-supported ruthenium bimetallic catalyst, 50th Petroleum-Petrochemical Symposium of Japan Petroleum Institute, Nov 12–13, 2020, Kumamoto, Japan (virtually oral presentation, 1E05).

[25] Son Dinh Le, Shun Nishimura, Transformation of succinic acid into value-added chemicals using solid Acid and base Catalysts, International Congress on Pure & Applied Chemistry Langkawi, Oct 30–Nov 2, 2018, Langkawi, Malaysia (oral presentation, PCC-37).

[26] Son Dinh Le, Shun Nishimura, Kohki Ebitani, Direct esterification of succinic acid with phenol using zeolite beta catalyst, 8th Tokyo Conference on Advanced Catalytic Science and Technology (TOCAT8), Aug 5–10, 2018, Yokohama, Japan (poster presentation, P3189).